

NORTHWESTERN UNIVERSITY

Linear and Nonlinear Optical Spectroscopy on Two-Dimensional Arrays of Silver Nanoparticles

A DISSERTATION

SUBMITTED TO THE GRADUATE SCHOOL  
IN PARTIAL FULFILLMENT OF THE REQUIREMENTS

for the degree

DOCTOR OF PHILOSOPHY

Field of Chemistry

By

Jiha Sung

EVANSTON, ILLINOIS

December 2007

© Copyright by Jiha Sung 2007

All Rights Reserved

**ABSTRACT**

## Linear and Nonlinear Optical Spectroscopy on Two-Dimensional Arrays of Silver Nanoparticles

Jiha Sung

The work presented in this thesis describes investigations into linear and nonlinear optical properties of two-dimensional silver nanoparticle arrays. The linear optical measurements – extinction measurements were performed on two-dimensional square arrays of L-shaped silver nanoparticles fabricated by electron beam lithography in order to study the effect of dipole coupling to the plasmon resonance of the arrays. A single L-shaped nanoparticle localized surface plasmon resonance (LSPR) had two polarized components which independently coupled to create plasmon resonances in the arrays. The resonance location and bandwidth of the arrays were dependent on grid spacing and number of particles in the array. The array plasmon resonance had a minimum bandwidth of  $700 - 800 \text{ cm}^{-1}$  at a grid spacing  $\sim 75 \text{ nm}$  smaller than the grid having the largest red shift of the plasmon resonance. The birefringence property of the arrays was also investigated. The maximum phase difference of  $30^\circ$  for two orthogonal optical axes was observed in between two main dipole resonance wavelengths. The observation suggested the possible application of the two-dimensional nanoparticle arrays as wavelength-tunable, extremely thin birefringence materials. The nonlinear optical measurements – frequency-scanned excitation profiles of coherent second harmonic generation (SHG) were measured for silver nanoparticle arrays prepared by nanosphere lithography. The second harmonic (SH) emission from the arrays was compared with a smooth silver film to identify an enhancement of SH emission efficiency. The polarization and orientation dependence of the enhancement suggested that it is related to a dipolar LSPR mode polarized normal to the plane of the substrate. In-plane dipoles that dominate linear extinction spectra did not contribute to the

SHG process because of the centrosymmetric orientation of arrays which allowed observation of the weak out-of-plane component. Laser power stability of  $\text{Al}_2\text{O}_3$  coated silver nanoparticles was tested. It was demonstrated that the atomic layer deposited  $\text{Al}_2\text{O}_3$  layers provide enhanced stability of the silver nanoparticles against femtosecond laser exposure, therefore the  $\text{Al}_2\text{O}_3$  coated nanoparticles can serve as a stable platform for surface enhanced laser spectroscopy, including nonlinear spectroscopy.

## Acknowledgements

I would like to thank my advisors Prof. Richard P. Van Duyne and Prof. Kenneth G. Spears for giving me a chance to work in this fantastic group with fantastic members and for their guidance for last five years of my life as a Ph.D. student in Northwestern University. I also thank Prof. Tamar Seideman for supporting me for last two months, and my committee members, Prof. George C. Schatz, Prof. Peter C. Stair, and Prof. Franz M. Geiger (QE).

I owe many people while I was doing my research presented in this thesis. For Chapter 2, I thank Prof. Tamar Seideman, Dr. Maxim Sukharev, and Prof. George C. Schatz for helpful discussions. Leif Sherry taught me how to take dark field scattering spectrum using inverted microscope setup and he took AFM images for me. Nilam Shah and Olga Lyandres gave me advice for flow cell system setup, and Erin M. Hicks fabricated e-beam samples and took SEM images for me. I thank Dr. Shengli Zou for primary DDA calculations. For Chapter 3, I thank Prof. Tamar Seideman and Dr. Jeffrey Anker for helpful discussions and Dr. Maxim Sukharev for helpful discussions and FDTD calculations. For Chapter 4, Dr. Andrew Moran was my coworker and I thank Erin M. Hicks for NSL sample fabrication during the early stage of the research and for AFM imaging. I thank Leif Sherry for DDA calculations. For Chapter 5, I thank Kathryn Kosuda for ALD and Jing Zhao for helpful discussions and SEM imaging. For the Appendix 1, Jing Zhao was my coworker and I thank Prof. Joseph T. Hupp, Dr. Ryan Bailey, and Stacey Standridge for letting me use their integrating sphere. For Appendix 2, I thank Erin M. Hicks for sample fabrication and SEM imaging.

I thank Dr. Adam McFarland and Dr. Andrew Moran for their help and advice when I was starting my research here and when I was preparing for qualifying exam. I thank Dr. Kallie Willets for Matlab instruction and for her advice for my research proposal. I enjoyed

“Fundamental spectroscopy and plasmonics subgroup meeting” and thank the subgroup members; Matt Young, Jon Dieringer, Dave Andrews, Dr. Jeffrey Anker, Dr. Kallie Willets, Dr. Jon Camden, and Dr. Paul Stiles, for interesting discussions and their feedbacks for my research presentations. I thank my office mates; George Chan, Hua Yu, Jing Zhao, and Dr. Aravindan Ponnu. I enjoyed all the discussions with George not only about LSPR but also about life. I also enjoyed afternoon tea time with Aravindan and his Indian snacks. I acknowledge senior group members for help and guidance for my lab life: Dr. Christy Haynes, Dr. Amanda Haes, Dr. Adam McFarland, Dr. Xiaoyu Zhang, and Dr. Chanda R. Yonzon. I thank Matt Young, Dr. Jon Camden, Jon Dieringer, Dr. Jeffrey Anker, Dr. Paul Stiles, and George Chan for checking English grammar for this thesis. I also thank all previous and current Van Duyne group; Dr. Doug Stuart, Alyson Whitney, Kevin Biggs, Julia Bingham, Paige Hall, Jennifer Roden, and Dr. Rebecca Wolfe.

I enjoyed many friendships outside of the lab: Ralph Rose and his family, Myung-Han Yoon and his wife, Dr. Hyonseok Hwang, Dr. Joonkyung Jang, Dr. Sang Woo Han, Dr. Doo Young Kim and his family, Dr. YounJoon Jung, Dr. Jong Kuk Lim and his wife, Choongik Kim, and Paul Lee. I love and will miss the times that I had with them. I also thank Director Hayao Miyazaki, Director Junichi Sato, GAINAX, the late Izumi Sakai, and Wolfgang Amadeus Mozart for impressive movies and music with which I had a sweet break during my research.

Finally, I thank my parents, grandmother and brother. Without their support and encouragement, I could not be standing here today.

Jiha Sung  
Evanston, IL  
August 2007

아버지, 어머니, 그리고 할머니께 이 논문을 바칩니다.

To my parents and grandmother

## Table of Contents

<b>Abstract</b>	<b>3</b>
<b>Acknowledgements</b>	<b>5</b>
<b>List of Figures</b>	<b>11</b>
<b>List of Tables</b>	<b>15</b>
<b>Chapter 1 Introduction to Linear and Nonlinear Optical Spectroscopy on Noble Metal Nanoparticles</b>	<b>16</b>
0 <i>Anni Mirabilēs</i>	17
1.1 Optical Properties of Noble Metal Nanoparticles	19
1.1.1 Surface Plasmon Polariton and Localized Surface Plasmon Resonance	19
1.1.2 Coupling of Localized Surface Plasmon	22
1.2 Nonlinear Optical Spectroscopy on Noble Metal Nanoparticles	28
1.2.1 Introduction to Nonlinear Optics	28
1.2.2 Second Harmonic Generation (SHG) from Noble Metal Nanoparticles	30
1.3 Goals and Organization	33
<b>Chapter 2 Dipole Coupling in Two-Dimensional Arrays of L-Shaped Silver Nanoparticles</b>	<b>35</b>
2.1 Introduction	36
2.2 Experimental Methods	39
2.2.1 Sample Fabrication	39
2.2.2 Extinction Measurements	44
2.2.3 Dark-Field Scattering Measurement	46
2.2.4 Structural Characterization of Nanoparticle Arrays	46
2.3 Results	46
2.3.1 Structural Characterization	47
2.3.2 Plasmon Resonance Position and Bandwidth in an Isolated Particle and 2D arrays	47
2.3.3 Range of Dipole Coupling	51
2.3.4 Solvent Effect on the Plasmon Resonance of 2D arrays	55
2.4 Discussion	61
2.5 Conclusion	65
<b>Chapter 3 Birefringence in Two-Dimensional Arrays of L-Shaped Silver Nanoparticles</b>	<b>67</b>
3.1 Introduction	68
3.2 Experimental Methods	70
3.2.1 Sample Fabrication and Structural Characterization	70
3.2.2 White Light Spectroscopy	72
3.3 Results and Discussion	76
3.3.1 Perpendicularly Induced Component Measurements	76
3.3.2 Inadequacy of a Dichroism Model	78

		9
	3.3.3	Birefringence Model 81
	3.3.4	Transmission with Resolved Linear Polarization 82
	3.3.5	Phase Difference Predicted from the Complex Index of Refraction 87
	3.3.6	2D Array of L-Shaped Nanoparticles as a Birefringence Material 90
	3.4	Conclusion 92
<b>Chapter 4</b>	<b>Second Harmonic Excitation Spectroscopy of Silver Nanoparticle Arrays</b>	<b>94</b>
	4.1	Introduction 95
	4.2	Experimental Methods 97
	4.2.1	Sample Preparation 97
	4.2.2	Structural Characterization of NSL-fabricated Nanoparticle Arrays 98
	4.2.3	Extinction Measurements 101
	4.2.4	SHG Measurements 101
	4.2.5	Theoretical Calculations 106
	4.3	Results and Discussion 106
	4.3.1	Extinction Measurements 106
	4.3.2	Nanoparticle Annealing 108
	4.3.3	SHG Excitation Spectra 111
	4.3.4	Polarization Dependent SHG 117
	4.4	Conclusion 121
<b>Chapter 5</b>	<b>Stability of Silver Nanoparticles Fabricated by Nanosphere Lithography and Atomic Layer Deposition to Femtosecond Laser Excitation</b>	<b>123</b>
	5.1	Introduction 124
	5.2	Experimental Methods 126
	5.2.1	Materials 126
	5.2.2	Preparation of Silver Nanoparticle Samples 126
	5.2.3	Measurement of the Stability of Silver Nanoparticles upon Laser Exposure 127
	5.3	Results and Discussion 130
	5.3.1	Laser Induced LSPR Change of the Bare Silver Nanoparticles 130
	5.3.2	Laser Induced LSPR Change of ALD Al <sub>2</sub> O <sub>3</sub> Coated Nanoparticles 136
	5.3.3	Change in LSPR Bandwidth after the Laser Exposure 142
	5.4	Conclusion 145
	<b>References</b>	<b>147</b>
<b>Appendix 1</b>	<b>Absorption Measurement of Dyes Adsorbed on Silver Film</b>	<b>161</b>
	A1.1	Introduction 162
	A1.2	Integrating Sphere Theory 164
	A1.2.1	Radiance Equation 164

		10	
	A1.2.2	Reflectance Measurement – Substitution and Comparison Methods	166
	A1.2.3	Reflectance Measurement Geometry	169
A1.3		Experimental Methods	171
	A1.3.1	Sample Preparation	171
	A1.3.2	Geometry of Integrating Sphere	171
	A1.3.3	Collection Optics Alignment	174
	A1.3.4	Surface Absorption Measurement	176
	A1.3.5	Solution Absorption Measurement	176
A1.4		Results	177
	A1.4.1	2',7'-Dibromo-5'-(hydroxymercurio)fluorescein Disodium Salt (merbromin)	177
	A1.4.2	Rhodamine 6G (R6G)	177
	A1.4.3	[2,3,7,8,12,13,17,18-Octakis-(propyl)porphyrazinato]magnesium(II) (MgPz)	180
	A1.4.4	Tris(2,2'-bipyridyl)dichlororuthenium(II) Hexahydrate (Ru(bpy) <sub>3</sub> <sup>2+</sup> )	180
A1.5		Conclusion	180
<b>Appendix 2</b>		<b>Plasmon Coupling in Finite Two-Dimensional Arrays of Cylindrical Silver Nanoparticles – Effect of Number of Interacting Nanoparticles</b>	<b>184</b>
	A2.1	Introduction	185
	A2.2	Experimental Methods	187
	A2.2.1	Sample Fabrication and Structural Characterization	187
	A2.2.2	Extinction Measurements	191
A2.3		Results and Discussion	193
	A2.3.1	Semi-Infinite Arrays	193
	A2.3.2	Gap Arrays	196
A2.4		Conclusion	205
<b>Vita</b>			<b>207</b>

## List of Figures

Figure 1.1	Simple dipole-dipole interaction model	24
Figure 1.2	Reciprocal space representation of the 2D square array of grid spacing $D$	26
Figure 2.1	SEM images of 2D arrays of L- and V-shaped nanoparticles	41
Figure 2.2	Experimental setup for extinction measurements	45
Figure 2.3	LSPR spectra of isolated L-shaped nanoparticles and 2D L arrays	46
Figure 2.4	Resonant wavelength and bandwidth of LSPR versus grid spacing for 2D L and V arrays	50
Figure 2.5	Resonant wavelength and bandwidth of LSPR versus the number of particles per block edge for gap array	53
Figure 2.6	Resonant wavelength and bandwidth of LSPR band scanned from one edge to the other edge of 2D L array	54
Figure 2.7	Resonant wavelength and bandwidth of LSPR in two different dielectric media; nitrogen and benzene	56
Figure 2.8	Energy difference between X- and Y-polarized bands in nitrogen and benzene	58
Figure 2.9	Extinction spectra of the 2D V arrays in nitrogen and benzene	59
Figure 2.10	Resonant wavelength of X-polarized band and grating-induced modes	60
Figure 3.1	SEM image of 2D array of L-shaped Ag nanoparticles and definition of axes	71
Figure 3.2	Experimental setup for extinction and transmission measurements	73
Figure 3.3	Polarizer setup	75
Figure 3.4	Extinction spectra and perpendicularly polarized component spectra	77
Figure 3.5	Extinction spectra for A-polarized beam; comparison between experimental data and modeling	80
Figure 3.6	Wavelength dependent phase difference	83
Figure 3.7	Collection polarizer angle dependent signal intensities; comparison between experimental data and modeling	84

		12
Figure 3.8	Polarization of the beam after the nanoparticle array	86
Figure 3.9	Diagram of the refractive index (imaginary and real part) of the nanoparticle array and phase difference	88
Figure 3.10	Diagram of refractive index (real part) of conventional birefringence materials and electron cloud bound to a nucleus	91
Figure 4.1	Nanosphere lithography (NSL)	99
Figure 4.2	AMF image of a NSL sample	100
Figure 4.3	Experimental design used for angle dependent extinction measurements	102
Figure 4.4	Schematic of the femtosecond laser system	103
Figure 4.5	Configuration used for SHG measurements	105
Figure 4.6	Polarization and orientation dependent extinction spectra	107
Figure 4.7	Experimentally obtained LSPR $\lambda_{\max}$ versus nanoparticle height	109
Figure 4.8	LSPR $\lambda_{\max}$ calculated by DDA method versus nanoparticle height	110
Figure 4.9	Extinction spectra and the SHG enhancement profiles for $D = 510$ nm and 590 nm samples	113
Figure 4.10	Extinction spectra and the SHG enhancement profiles for $D = 390$ nm samples	114
Figure 4.11	SHG enhancement maxima versus nanoparticle height	115
Figure 4.12	Out-of-plane dipole resonance calculated by DDA method versus nanoparticle height	118
Figure 4.13	Normalized SHG intensity detected in p polarization at $10^\circ$ and $45^\circ$ incidence for both the nanoparticle arrays and smooth film	119
Figure 5.1	Experimental setup used for laser irradiation and extinction measurements	129
Figure 5.2	LSPR change after the laser exposure to the bare silver nanoparticles in the case of the resonant condition	131
Figure 5.3	LSPR change after the laser exposure to the bare silver nanoparticles in the case of the off-resonant condition	133
Figure 5.4	LSPR shift versus laser exposure time for bare nanoparticles	134

		13
Figure 5.5	LSPR shift versus laser exposure time for nanoparticles coated with 4 ALD layers	138
Figure 5.6	LSPR shift versus laser exposure time for nanoparticles coated with 10 ALD layers	139
Figure 5.7	LSPR shift after 120 sec laser exposure versus laser pulse intensity	140
Figure 5.8	Percent change in LSPR bandwidth after 120 sec laser exposure versus laser pulse intensity	144
Figure A1.1	Substitution method for reflectance measurement	167
Figure A1.2	Comparison method for reflectance measurement	168
Figure A1.3	Reflectance measurement geometry	170
Figure A1.4	Integrating sphere model RSA-HP-84 (labsphere)	173
Figure A1.5	Collection optics alignment for surface absorption measurement with integrating sphere	175
Figure A1.6	Absorption spectra of merbromin aqueous solution, merbromin adsorbed on 200 nm Ag film, and merbromin adsorbed on 50 nm Au film	178
Figure A1.7	Absorption spectra of R6G ethanol solution and R6G adsorbed on 200 nm Ag film	179
Figure A1.8	Absorption spectra of MgPz ethanol solution and MgPz adsorbed on 200 nm Ag film	181
Figure A1.9	Absorption spectra of Ru(bpy) <sub>3</sub> <sup>2+</sup> aqueous solution and Ru(bpy) <sub>3</sub> <sup>2+</sup> adsorbed on 270 nm Ag film	182
Figure A2.1	SEM images of two-dimensional square arrays of cylindrical nanoparticles	189
Figure A2.2	Nanoparticle area normalized extinction spectra of 2D square arrays of $d = 339$ nm nanoparticles.	194
Figure A2.3	Resonant wavelength and bandwidth versus grid spacing for 2D semi-infinite arrays of $d = 339$ nm nanoparticles (large cylinders)	195
Figure A2.4	Resonant wavelength and bandwidth versus grid spacing for 2D semi-infinite arrays of $d = 163$ nm nanoparticles (small cylinders)	197
Figure A2.5	Extinction spectra of gap array 1 ( $d = 339$ nm)	200

Figure A2.6	Resonant wavelength and band width of gap array samples ( $d = 339$ nm) versus the number of particles per block edge.	201
Figure A2.7	Extinction spectra of gap array 2 ( $d = 163$ nm)	202
Figure A2.8	Resonant wavelength and band width of gap array 2 samples ( $d = 163$ nm, $D = 450$ nm) versus the number of particles per block edge	204

**List of Tables**

Table 2.1	Characteristics of 2D Ag nanoparticle square arrays	42
Table 2.2	Characteristics of Ag nanoparticle gap arrays	43
Table A2.1	Characteristics of semi-infinite square arrays	190
Table A2.2	Characteristics of gap arrays	192

## **Chapter 1**

### **Introduction to Linear and Nonlinear Optical Spectroscopy on Noble Metal Nanoparticles**

## 0 *Anni Mirabilēs*

The first observation of surface-enhanced Raman scattering (SERS) was made by Fleischmann et al. in 1974.<sup>1</sup> They reported that the Raman signal of pyridine is enhanced by a factor of  $10^5$ - $10^6$  through adsorption at a roughened silver electrode, and they believed that the signal enhancement came from the increase in silver electrode surface area. Jeanmaire and Van Duyne<sup>2</sup> recognized that the enhancement cannot be explained just by the increased surface area alone, and in 1977 they proposed that the local electric field enhancement caused by the roughened silver surface accounts for the large Raman enhancement. The electromagnetic model has explained the surface enhanced spectroscopy successfully, and according to this model, the field enhancement is the consequence of the optical resonance of nano-sized structures or particles, called localized surface plasmon resonance (LSPR).

In Van Duyne group, a highly SERS-active substrate fabrication technique, called nanosphere lithography (NSL), has been developed.<sup>3,4</sup> By this technique, a two-dimensional (2D) array of truncated tetrahedron-shaped nanoparticles or a roughened film, called film over nanosphere (FON), can be fabricated with high reproducibility, high throughput, and low cost.<sup>4</sup> These substrates have been utilized for SERS studies and sensor developments. McFarland et al.<sup>5</sup> monitored the surface-enhanced Raman excitation spectroscopy (SERES) profile from NSL-fabricated nanoparticle arrays and correlated the SERS enhancement to the LSPR of the nanoparticle arrays. They showed that the strongest SERS enhancement occurs under conditions where the incident and Raman scattered photons are both strongly enhanced, which is consistent with prediction of the electromagnetic enhancement model. How then is the nonlinear response, especially second harmonic generation (SHG) of the NSL-fabricated nanoparticle arrays

correlated to their LSPR? This question was my first research topic in the Van Duyne and Spears groups, and my results on this topic will be presented in Chapter 4.

Another research interest in the Van Duyne group has been developing chemo/bio sensors from NSL-fabricated substrates. SERS and LSPR sensors for various biomolecules, such as glucose,<sup>6</sup> calcium dipicolinate which is an anthrax biomarker,<sup>7</sup> amyloid-derived diffusible ligand known as an Alzheimer's disease biomarker,<sup>8</sup> and concanavalin A,<sup>9</sup> have been demonstrated successfully. The latter two among listed above are examples of an LSPR sensor. In the case of noble metal nanoparticles, the LSPR red-shifts as the refractive index of the surrounding increases, and this refractive index sensitivity of LSPR is the key feature of LSPR sensor development. The LSPR shift should be large in order to be a good sensor, and LSPR wavelength shift per refractive index unit ( $\text{nmRIU}^{-1}$ ) has been used to determine the sensitivity of the system. However, not only the amount of shift but also the LSPR bandwidth is also important for the resolution, and Sherry et al.<sup>10</sup> proposed new figure of merit (FOM). In this unit, the LSPR shift is normalized by LSPR bandwidth. Then how can we make LSPR bandwidth narrow? Schatz and coworkers<sup>11-13</sup> predicted theoretically that a remarkably narrow plasmon resonance is possible for one-dimensional (1D) and two-dimensional (2D) silver nanoparticle arrays through dipole coupling when certain conditions are met, and it is shown that the sensing capability of the narrow band is larger than the corresponding single particle.<sup>12</sup> Hicks et al.<sup>14</sup> demonstrated the prediction of Schatz and coworkers partly for a 1D array of cylindrical nanoparticles. As a sensing platform, however, 2D arrays, rather than 1D arrays, are commonly used because higher signal level is expected for 2D arrays. The bandwidth narrowing had not been shown for 2D arrays, which lead me to a second research topic: investigation of the effect of dipole coupling to the surface plasmon of 2D silver nanoparticle arrays.

This thesis is not organized in chronological order. The dipole coupling study precedes the SHG study, so that the linear spectroscopies are presented before nonlinear spectroscopy. Backgrounds for understanding following chapters will be briefly introduced in this chapter. Section 1.1 describes dipole coupling. LSPR will be introduced briefly in first subsection, and detailed discussion of dipole coupling will be presented in second subsection. Section 1.2 is about nonlinear spectroscopy. A brief introduction to the nonlinear spectroscopy and overview of SHG studies that have been done on noble metal surfaces and nanoparticles will be discussed in two continuing subsections.

## **1.1 Optical Properties of Noble Metal Nanoparticles**

### **1.1.1 Surface Plasmon Polariton and Localized Surface Plasmon Resonance**

The physical entities that have particle-like properties are usually named with the words ending in –ON.<sup>15</sup> Electron, neutron, proton, photon, boson, fermion, phonon, exciton, polaron, polariton, and plasmon are examples. Among all those –ON’s, plasmon, especially, localized surface plasmon is the main interest of this thesis.

In 1940’s Ruthemann<sup>16</sup> and Lang<sup>17</sup> reported the characteristic energy loss of fast electrons when those electrons pass through thin beryllium and aluminum film.<sup>18</sup> There had been debate on the origin of this energy loss. Various workers tried to explain this observation with interband transitions of individual conduction electrons, but the origin turned out to be a coupling of the electron charge to a surface plasmon.<sup>19,20</sup> The surface plasmon is coherent oscillation of the surface conduction electrons, and it is distinct from unbounded bulk plasmon because electrons are confined in the metal surface.<sup>21</sup> The surface plasmon can couple with electromagnetic waves to create a surface plasmon polariton (SPP). If the single boundary of a metal and dielectric medium is considered, the dispersion relation of the SPP is given by<sup>22</sup>

$$k_x = \frac{\omega}{c} \left[ \frac{\varepsilon_1(\varepsilon_{2r} + i\varepsilon_{2i})}{\varepsilon_1 + \varepsilon_{2r} + i\varepsilon_{2i}} \right], \quad (1.1)$$

where  $k_x$  is the wave vector of the SPP,  $\omega$  is angular frequency,  $c$  is speed of light,  $\varepsilon_1$  is dielectric function of the dielectric medium, and  $\varepsilon_{2r}$  and  $\varepsilon_{2i}$  are real and imaginary component of metal dielectric function, respectively. A propagating mode with a sharp resonance (small damping) requires a large negative  $\varepsilon_{2r}$  and a small  $\varepsilon_{2i}$ .<sup>22</sup> This condition is well satisfied by noble metals, lithium, aluminum, indium and sodium in the visible wavelength region. However, the surface plasmon cannot be directly coupled to the electromagnetic field from the external dielectric media. The maximum surface-parallel wave vector that can be achieved from the electromagnetic wave in the dielectric media with same angular frequency,  $\omega$ , is  $k_{\max, \varepsilon_1} = (\omega/c)\sqrt{\varepsilon_1}$  which is smaller than the wave vector of the SPP ( $k_x$ ). Thus, it is clear from each dispersion relation that the wave vector matching condition cannot be achieved. For the optical excitation of the SPP, prism coupling or grating coupling is necessary.<sup>23</sup> In the case of thin metal films, the SPP modes form at two metal-dielectric boundaries, and there is coupling between them, resulting in two mixed modes; short-range and long-range SPP mode.<sup>24,25</sup> The short-range SPP mode has antisymmetric surface charge, and it results in large electric field within metal, so, it is strongly attenuated through Joule heating. The long-range SPP mode has symmetric surface charge, very weak electric field within metal, and a longer propagation distance,<sup>22,24,25</sup> therefore this mode is of potential practical application in a plasmonic band gap laser.<sup>26,27</sup> The SPP of the metal film has also been employed in various sensing techniques.<sup>23</sup>

Now let me move from metal surfaces and films to metal nanoparticles. There is more confinement of the conduction electrons in metal nanoparticles than those in metal surfaces or films, and this makes the optical properties of metal nanoparticles distinct from those of bulk

metal or metal film. An electromagnetic field satisfying the resonance condition can cause the collective oscillation of conduction electrons of the metal nanoparticles, and it is called a localized surface plasmon resonance (LSPR). Because of this resonance, small colloidal particles of some metals, such as gold, show varied colors in absorption or scattering within the visible wavelength range. In 1908, Mie reported the rigorous analytical solution of the Maxwell equations for a homogeneous spherical particle of arbitrary size,<sup>21,28-30</sup> and in 1912, Gans extended the Mie theory to spheroids.<sup>30,31</sup> The scattering and absorption, therefore extinction, which is the sum of scattering and absorption, of homogeneous spherical and spheroidal particles can be described with this theory.<sup>21,29</sup> If the particle diameter is much smaller than the wavelength of incident light (electrostatic dipole approximation), the extinction spectrum  $E(\lambda)$  of the metal sphere or spheroid can be given by following equation:<sup>30</sup>

$$E(\lambda) = \frac{2\pi N}{\ln(10)} \frac{(1 + \chi)^2 \varepsilon_1^{3/2} V}{\lambda} \left[ \frac{\varepsilon_{2i}(\lambda)}{(\varepsilon_{2r}(\lambda) + \chi \varepsilon_1)^2 + \varepsilon_{2i}(\lambda)^2} \right], \quad (1.2)$$

where  $N$  is number of nanoparticles in unit area,  $\lambda$  is wavelength of electromagnetic field,  $V$  is the volume of nanoparticle,  $\varepsilon_1$  is dielectric constant of dielectric medium,  $\varepsilon_{2r}$  and  $\varepsilon_{2i}$  are real and imaginary component of metal dielectric function, and  $\chi$  is a shape factor. For a spherical particle,  $\chi$  is two, and  $\chi$  is larger than two for spheroids. Here, again, the requirement for a sharp resonance is a large negative value of  $\varepsilon_{2r}$  and small  $\varepsilon_{2i}$ . From Equation 1.2, it is clear that the LSPR of the noble metal nanoparticle imbedded in dielectric medium depends on the composition of the nanoparticle ( $\varepsilon_{2r}$  and  $\varepsilon_{2i}$ ), the dielectric constant of environment ( $\varepsilon_1$ ), and the nanoparticle shape ( $\chi$ ). When the nanoparticles form a particle pair, cluster, one-dimensional (1D) array or two-dimensional (2D) array, the dipole coupling of nanoparticles also affects the plasmon resonance of whole cluster or array.<sup>11,12,32-34</sup> This aspect will be discussed in section 1.1.2. Two remarkable consequences of this optical phenomenon are (1) an enhanced light

scattering and absorption which is sensitive to the external refractive index and (2) a large local electromagnetic field enhancement. LSPR sensors for chem/bio detection and quantitation can be developed utilizing the former feature.<sup>35,36</sup> The latter feature enables surface enhanced spectroscopies.<sup>37</sup> Molecules near a noble metal nanoparticle or nanostructure feel an enhanced local electric field when excited at the LSPR wavelength, therefore their response to the electric field is greatly enhanced compared to without the metal surface. For example, Raman scattering of a molecule is enhanced greatly when the molecule is adsorbed on roughened metal surface,<sup>1,2,38,39</sup> and it is called Surface-enhanced Raman scattering (SERS). In the ensemble-averaged system, Raman enhancements up to  $10^8$  have been observed<sup>5,40</sup> and in the case of single molecule SERS, a Raman enhancement factor on the order of  $10^{14}$ - $10^{15}$  was reported.<sup>41</sup> Surface-enhanced hyper-Raman scattering (SEHRS)<sup>42-44</sup>, fluorescence,<sup>45-47</sup> second harmonic generation (SHG)<sup>48,49</sup>, and two-photon absorption<sup>50</sup> from the molecules adsorbed on metal electrode or nanoparticles have also been studied. When the external electromagnetic field impinging on a metal nanoparticle is resonant with the LSPR of the nanoparticle, fluorescence and the nonlinear response of the metal nanoparticle itself is also enhanced. This aspect will be discussed in section 1.2.2 in more detail.

### 1.1.2 Coupling of Localized Surface Plasmons

In the previous section, the emphasis was on the factors that determine the LSPR of single noble metal nanoparticle. Under the electromagnetic field, each nanoparticle can be considered as a single dipole, and if two or more nanoparticles are brought together, the LSPR of the system can be modified by the interaction of the dipoles. There are two types of interactions between metal nanoparticles; one is short range dipolar coupling due to the evanescent field and the other is long range dipolar coupling due to radiative dipolar fields.<sup>33,34,51</sup>

The short range coupling becomes dominant if the particle spacing is the order of a particle radius. The system of two adjacent nanoparticles<sup>34,52-55</sup> and 1D nanoparticle arrays<sup>56</sup> with various particle spacing have been explored by various research groups. They monitored the resonance wavelength of the system while the particle spacing was tuned and they compared their observations with theoretical calculations. Both experiment and theory<sup>57,58</sup> have shown that for the incident beam polarization parallel to the array axis, the resonance of the system red-shifts as particles get closer, and for the incident beam polarization perpendicular to the array axis, the resonance blue-shifts as particles get closer. This observation can be explained qualitatively by a simple dipole-dipole interaction model.<sup>52</sup> The incident electromagnetic field creates positive and negative charges on the metal nanoparticle surface at opposite sides, and the charges on each side feel a repulsive force (Figure 1.1A). Imagine that another particle is brought nearby. By the electromagnetic field, the same charge separation will take place for the second particle. If the second particle is placed to form an array with its axis parallel to the polarization of driving field (Figure 1.1B), opposite charges are facing within particle gap and the repulsive forces within each particle will be weakened, leading to a lower resonance frequency. However, if the second particle is placed to form an array with its axis perpendicular to the polarization of the field (Figure 1.1C), the same charges are facing within particle gap to enhance the repulsive forces within each particle, leading to a higher resonance frequency.<sup>52</sup> A molecular ruler utilizing this sensitivity of resonance to the particle spacing has been demonstrated by Alivisatos and coworkers.<sup>59,60</sup> The short range coupling leads to a large enhancement of the local electric field in the gap between the particles<sup>34</sup> and it is considered as an origin of spectroscopic “hot spots”. Since Nie and Emory<sup>41</sup> reported Raman scattering from a single rhodamine 6G molecule adsorbed on aggregated silver colloids, which requires Raman

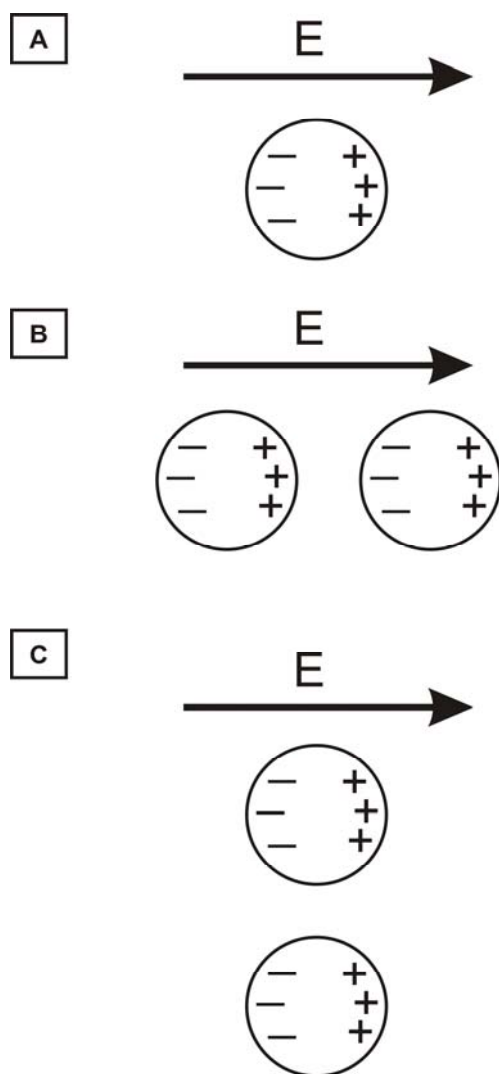


**Figure 1.1** Simple dipole-dipole interaction model. (A) Single particle, (B) a pair of particles with polarization parallel to the array axis, and (C) a pair of particles with polarization perpendicular to the array axis.

enhancements of the order  $10^{14}$ - $10^{15}$ , electromagnetic “hot spots” have drawn attention. There have been much experimental and theoretical work to design<sup>61-63</sup> and fabricate<sup>64-68</sup> “hot spots”.

Long range dipolar coupling becomes more important if the interparticle distance exceeds the order of a particle radius. Wokaun and coworkers<sup>69,70</sup> modeled the dipolar interaction between the metal particles in 2D arrays. They also simulated the shifts and broadening of the particle plasmon resonances and field enhancement for a regular 2D array of particles. Retarded dipolar interactions between the particles are explicitly taken into account in their model and the incident field was plane wave. They showed that the dipolar interactions among particles exhibit a large dependence on both the wavelength and the grid spacing ( $D$ ) of the array.<sup>69</sup> The total field can be written as a Fourier series of plane and evanescent waves, which represent the radiating and evanescent grating orders. When the grid spacing is smaller than the wavelength (Figure 1.2A), all the grating orders are evanescent, except zero order. In this case, large shifts of the plasmon resonance arise. The dipolar interactions exhibit a strong variation when the grid spacing matches the wavelength, i.e. when the particular order crosses the light circle in reciprocal space (Figure 1.2B). At this critical grid spacing ( $D_{crit}$ ), the grating order changes from evanescent to radiating, and it radiates at grazing angle. Once the grid spacing becomes larger than the wavelength (Figure 1.2C), strong damping occurs because of radiative grating order. Their model was used by Aussenegg and coworkers<sup>33</sup> to explain data for 2D square arrays of cylindrical silver nanoparticles. They performed extinction and plasmon decay time measurements on the arrays with variable grid spacing, and they observed a red shift of the plasmon resonance when the grating order was evanescent. When the grating order became radiative by increased grid spacing, an enhanced plasmon damping was observed, which is thought to result from the strongly enhanced radiative damping.<sup>33</sup> More recently, Schatz and

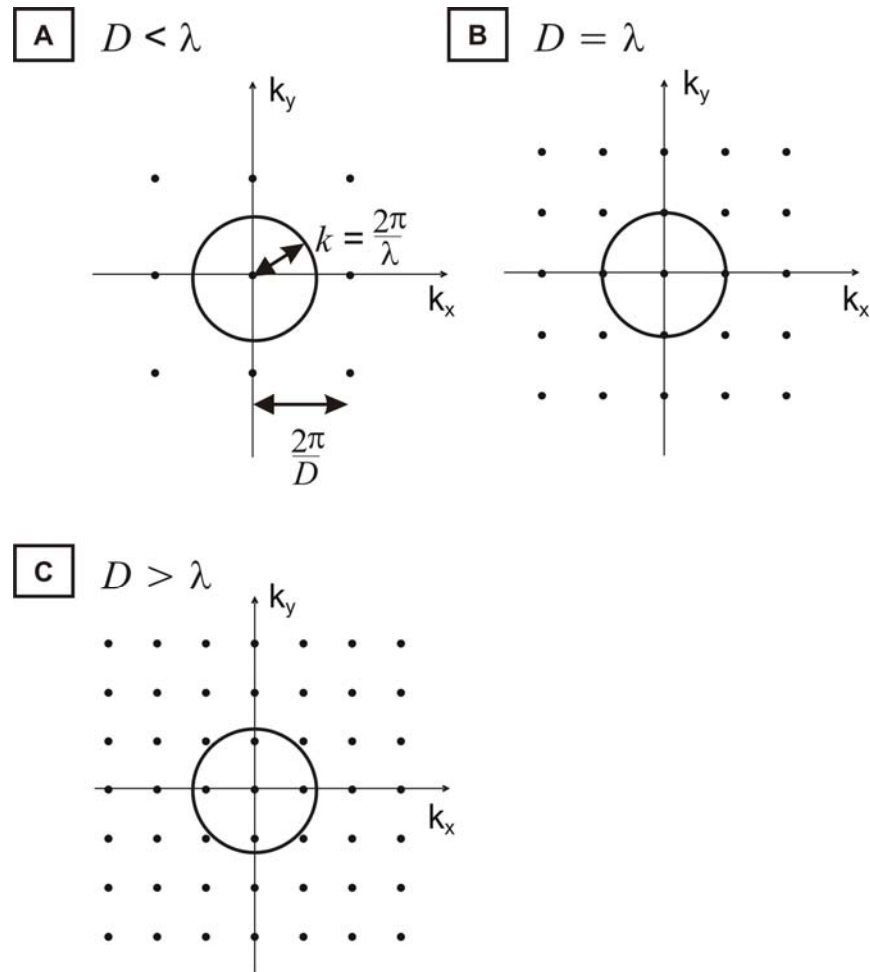


**Figure 1.2** Reciprocal space representation of the 2D square array of grid spacing  $D$ . Beam propagation is normal to the array surface. The grating orders are represented by dots and the circle represents the light circle with wavelength  $\lambda$ . (A)  $D < \lambda$ , (B)  $D = \lambda$ , and (C)  $D > \lambda$ .

coworkers<sup>11,12</sup> performed theoretical calculations on 1D and 2D arrays of silver nanoparticles, and reported that a remarkably narrow plasmon line can be achieved at certain grid spacing. They used the coupled dipole (CD) method for the modeling. For a small spherical particle close to resonance, the polarizability  $\alpha_s$  is approximately  $-A/(\omega - \omega_p + i\gamma)$ , where  $A$  is a positive real constant,  $\omega_p$  is surface plasmon frequency for the isolated particle, and  $\gamma$  is its half-width.<sup>11,12</sup> Then the polarization ( $P$ ) of the spherical particle is

$$P = \alpha_s E_0 = \frac{-AE_0}{\omega - \omega_p + i\gamma}, \quad (1.3)$$

where  $E_0$  is the amplitude of incident field. In the case of an infinite array, the polarization of each particle turns out to be:<sup>11,12</sup>

$$P = \frac{-AE_0}{\omega - \{\omega_p - \text{Re}(AS)\} + i\{\gamma + \text{Im}(AS)\}}, \quad (1.4)$$

where  $S$  is the retarded dipole sum given by

$$S = \sum_{j \neq i} \left[ \frac{(1 - ikr_{ij})(3 \cos^2 \theta_{ij} - 1)e^{ikr_{ij}}}{r_{ij}^3} + \frac{k^2 \sin^2 \theta_{ij} e^{ikr_{ij}}}{r_{ij}} \right], \quad (1.5)$$

where  $k$  is wave vector of incident field,  $r_{ij}$  is the distance between dipole  $i$  and  $j$ , and  $\theta_{ij}$  is the angle between  $r_{ij}$  and the polarization direction. From Equation 1.4, the real part of  $AS$  determines the shift of the plasmon resonance frequency and the imaginary part determines the change in bandwidth. It was shown that there is a condition where the width factor  $\gamma + \text{Im}(AS)$  vanishes. The 1D array of 50 nm silver nanoparticles showed 3.5 nm (20 meV) bandwidth with a peak wavelength of 471.4 nm, for 470 nm particle spacing.<sup>11</sup> In the case of 2D arrays constructed from the same particle, the bandwidth is always broader than 1D arrays, but the minimum bandwidth is still much narrower than that of an isolated single particle.<sup>11</sup> There is a difference between Wokaun's model and Schatz's model in describing the origin of change in

plasmon bandwidth. In Wokaun's model, the radiative damping, i.e. the plasmon life time was the factor that determines the plasmon bandwidth. However, in Schatz's model, the origin of bandwidth narrowing is attributed as a destructive interference within a small window of wavelengths, so it is not because of the increased plasmon life time. Van Duyne and coworkers<sup>14</sup> reported the observation of plasmon line shape that is similar to that of Schatz's model for the 1D arrays of cylindrical silver nanoparticles. For the observation, the refractive index of the dielectric media that is surrounding the silver nanoparticle arrays should be matched.

## 1.2 Nonlinear Optical Spectroscopy on Noble Metal Nanoparticles

### 1.2.1 Introduction to Nonlinear Optics

*'Physics would be dull and life most unfulfilling if all physical phenomena around us were linear'* – from *'The Principles of Nonlinear Optics'* by Y. R. Shen

The nonlinear optical properties have been known since Maxwell's time. However, the first observation of nonlinear optical process was made after the pulsed ruby laser was developed in 1960.<sup>71-73</sup> Since Franken et al.<sup>74</sup> reported second harmonic generation (SHG) of a ruby laser beam ( $\lambda = 694.3$  nm) through crystalline quartz in 1961, various nonlinear optical processes have been experimentally observed. They have drawn particular attention, because nonlinear optical measurements enable obtaining optical properties that are not observable with linear optical measurement. For example, high surface-specificity of the second order process makes the SHG and sum frequency generation (SFG) a powerful tool for surface or interface study.

For all but exceptional circumstances, the induced polarization  $P(t)$  can be expressed with power series of electric field strength  $E(t)$ ; <sup>73,75,76</sup>

$$\begin{aligned} P(t) &= \chi^{(1)} E(t) + \chi^{(2)} E^2(t) + \chi^{(3)} E^3(t) + \dots \\ &\equiv P^{(1)}(t) + P^{(2)}(t) + P^{(3)}(t) + \dots \end{aligned} \tag{1.6}$$

where  $\chi^{(1)}$ ,  $\chi^{(2)}$ , and  $\chi^{(3)}$  are linear, second-order, and third-order susceptibility, respectively.

High-order nonlinear optical susceptibilities are naturally much weaker than the linear susceptibility, therefore, when the electric field strength is small, the second-order and higher-order terms can be neglected and only the linear polarization term  $P^{(1)}(t) = \chi^{(1)}E(t)$  is important.

Absorption, reflection, and refraction under the weak electric field are related to  $P^{(1)}(t)$ .

However, as the electric field strength becomes large, high-order terms become important.

$P^{(2)}(t) = \chi^{(2)}E^2(t)$  is the second-order polarization, and it describes the three-wave mixing process, such as SHG, SFG, difference frequency generation (DFG) and optical parametric amplification. If the incident optical field consists of two frequency components  $\omega_1$  and  $\omega_2$ , it can be expressed as;

$$E(t) = E_1 e^{-i\omega_1 t} + E_2 e^{-i\omega_2 t} + c.c. \quad (1.7)$$

Then the second-order polarization in Equation 1.6 becomes<sup>75</sup>

$$\begin{aligned} P^{(2)}(t) &= \chi^{(2)} E^2(t) \\ &= \chi^{(2)} [E_1^2 e^{-2i\omega_1 t} + E_2^2 e^{-2i\omega_2 t} + 2E_1 E_2 e^{-i(\omega_1 + \omega_2)t} + 2E_1 E_2^* e^{-i(\omega_1 - \omega_2)t} + c.c.] \\ &\quad + 2\chi^{(2)} [E_1 E_1^* + E_2 E_2^*]. \end{aligned} \quad (1.8)$$

The first two polarization terms with frequency of  $2\omega_1$  and  $2\omega_2$  in Equation 1.8 are related to SHG, and next two terms with frequency of  $\omega_1 + \omega_2$  and  $\omega_1 - \omega_2$  are related to SFG and DFG, respectively. The last two polarization terms with zero frequency are related to optical rectification. Under the electric dipole approximation, second-order optical processes are forbidden in a medium with inversion symmetry, such as liquids, gases, amorphous solids, and even many crystals. The inversion symmetry is broken at the surface or interface between two media with inversion symmetry, therefore the second-order optical process is highly surface or interface-specific.<sup>73,77</sup> A variety of surface/interface studies are performed by SHG and SFG

spectroscopy. Electrochemical processes at liquid/solid interface,<sup>78,79</sup> molecular orientation on a surface,<sup>80,81</sup> optical imaging microscopy,<sup>82-85</sup> vibrational spectroscopy of surface/interface,<sup>86-89</sup> molecular chirality,<sup>90</sup> surface adsorption kinetics,<sup>91,92</sup> bare semiconductor and metal surfaces,<sup>93-95</sup> and surface/membrane potential<sup>96,97</sup> have been studied by SHG and SFG spectroscopy.

Third-order polarization,  $P^{(3)}(t) = \chi^{(3)} E^3(t)$ , describes four-wave mixing process. Third harmonic generation, coherent anti-Stokes Raman spectroscopy (CARS), transient grating, and photon echo are spectroscopic techniques related to  $P^{(3)}(t)$ . Also the nonlinear contribution to the refractive index (intensity-dependent refractive index) is governed by  $\chi^{(3)}$ .<sup>75</sup>

Other than those mentioned above, a variety of nonlinear optical spectroscopy have been developed and applied for a variety of research areas, but introducing each of them is demanding and beyond the scope of this thesis. Let me close this introduction with a brief review of SHG studies that have been done on noble metal nanoparticles in following section which is related to work presented in this thesis.

### **1.2.2. Second Harmonic Generation (SHG) from Noble Metal Nanoparticles**

As discussed at the beginning of this chapter, the great enhancement of Raman scattering by roughened silver surfaces was reported in the 1970's and the origin of the enhancement is attributed to the local field enhancement from the surface plasmon of the roughened metal surface. This observation attracted great interest from many researchers, and they tried to achieve an enhancement of other optical processes from the local field enhancement. SHG spectroscopy was not an exception. SHG enhancement from the surface roughness of a metal is studied experimentally<sup>79,98-100</sup> and theoretically<sup>79,99</sup>, but this section will be focused on the SHG studies performed on noble metal nanoparticles rather than on roughened metal films.

SHG enhancement of the dye molecules conjugated to gold nanoparticle was reported by Clark et al.<sup>48</sup> JPW4041 dye conjugated to the 100 nm gold nanoparticle showed 100 times enhanced SHG signal compared to the dye conjugated to a latex bead with same size. Chen et al.<sup>49</sup> demonstrated that the SHG of an ionic self-assembled multilayer film is enhanced 200 times by silver nanoparticles deposited on the film. These experiments clearly show that the local field enhancement by noble metal nanoparticles LSPR enhances the SHG from the molecule adsorbed on the nanoparticle surface.

The LSPR also enhances the SHG of the noble metal nanoparticle itself. Sandrock et al.<sup>101</sup> fabricated noncentrosymmetric gold nanocylinder pairs in a porous anodic alumina host. The SHG signal resulting from this structure was collected with 780 nm incident wavelength that corresponds to the dipolar plasmon resonance of long particle axis. They changed the incidence angle of the 780 nm beam to change the component of the incident electric field parallel to the long particle axis, and they observed the increase in SHG intensity as the field component increased. This observation is consistent with local field enhancements arising from a long-axis dipolar plasmon resonance. Podlipensky et al.<sup>102</sup> reported strongly enhanced SHG in thin layers of uniformly oriented ellipsoidal silver nanoparticles in a glass matrix. These measurements were performed while the incident beam polarization and incidence angle was varied while the incident laser wavelength was fixed.

There also have been wavelength-scanned measurements on spherical noble metal nanoparticles. Antoine et al. reported surface plasmon enhanced second harmonic (SH) response of gold nanoparticles at the air/toluene interface<sup>103</sup> and gold clusters embedded in an alumina matrix.<sup>104</sup> In their research, the incident laser wavelength was scanned while the resulting SHG intensity was monitored. The SHG wavelength was scanned through the interband transition and

surface plasmon wavelength region. SH response from the surface plasmon dominated that from the interband transitions. Hupp and coworkers<sup>105-107</sup> studied the hyper-Rayleigh scattering (HRS) from colloidal noble metal nanoparticles while the incident laser wavelength was scanned. Their experiment was also performed with a two-photon resonance condition. Their study demonstrated the existence of distinguishable contributions to HRS intensities from 32 nm silver nanoparticles arising from electric dipole and quadrupole plasmon resonances at the emitted wavelength.<sup>105</sup> However, Russier-Antoine et al.<sup>108</sup> reported no contribution from the electric quadrupolar term in HRS response for 11 nm gold nanoparticles since retardation effects are much smaller in 11 nm particles. Strong enhancement of gold nanoparticle HRS is observed for harmonic frequencies in resonance with the dipolar surface plasmon excitation and no contribution of the interband transition is observed,<sup>108</sup> which agrees with the report of Antoine et al.<sup>104</sup>

There also have been efforts to correlate SH responses of noble metal nanoparticles with their morphology. Scherer and coworkers<sup>109</sup> obtained SHG signals from colloidal silver nanoparticles deposited onto a substrate and correlated their SHG signal to the STM image. Strong SHG signal was observed from dimers with nonspherical particles and trimers, and detectable SHG signal was not yielded from single spherical particles.

The review in this section have been focused on the studies that investigate the factors that govern noble metal nanoparticle SHG enhancement, but there have been many SHG studies on metal nanoparticles for many other purposes. For example, Aussenegg and coworkers<sup>110-112</sup> studied plasmon dephasing in gold and silver nanoparticles by SHG autocorrelation measurements. Canfield et al.<sup>113</sup> studied the chirality arising from small defects in gold nanoparticle arrays by both linear and SHG measurements. They showed that the chiral

responses from SHG are enormous compared to linear measurements and demonstrated that the SHG measurement can be an excellent tool for studying nanoparticle chirality.

### **1.3 Goals and Organization**

The goal of the work described in this thesis is to provide further understanding of linear and nonlinear optical properties of two-dimensional square arrays of silver nanoparticles, which is essential for the application of these arrays for sensing and laser spectroscopy. As discussed in previous sections, noble metal nanoparticle exhibit remarkable optical properties which result from the LSPR. The main interest in this thesis is about LSPR properties that are modified by dipole coupling within nanoparticle arrays and the SHG enhancement originating from the LSPR of nanoparticles.

In Chapter 2 and 3, linear optical properties of two-dimensional arrays of L-shaped silver nanoparticles fabricated by electron beam lithography are presented. All the measurements were performed with continuous wave white light from the tungsten-halogen light source. Chapter 2 describes the dipole coupling in two-dimensional arrays of L-shaped silver nanoparticles. The effect of grid spacing, array size and refractive index to the plasmon resonance of the array is discussed. Chapter 3 discusses the birefringence property of the L-shaped silver nanoparticle arrays and experimental observations are rationalized with several models. In Chapter 4 and 5, nonlinear optical properties and femtosecond laser stability of NSL-fabricated silver nanoparticle arrays are presented. Chapter 4 presents the frequency-scanned excitation profile of coherent second harmonic generation of silver nanoparticle arrays and the origin of the second harmonic enhancement is proposed. Chapter 5 describes the stability of the NSL-fabricated silver nanoparticle arrays to a femtosecond laser pulse. The femtosecond laser stability of bare nanoparticles and  $\text{Al}_2\text{O}_3$  coated nanoparticles were studied by monitoring the LSPR extinction

spectra during laser illumination. The Appendix 1 demonstrates the absorption measurements of the dye molecules that are adsorbed on smooth silver film, performed by an integrating sphere. The absorbance of surface-adsorbed dyes is compared with that of dye solution. Finally, the appendix 2 summarizes the optical measurements performed on the gap arrays of cylindrical silver nanoparticles and discusses the effect of number of interacting nanoparticles of plasmon resonance.

## **Chapter 2**

### **Dipole Coupling in Two-Dimensional Arrays of L-Shaped Silver Nanoparticles**

## 2.1 Introduction

Nanomaterials are of current interest in a wide variety of fields from medicine to microelectronics. The optical properties of nanoscale-fabricated noble metal nanoparticles have drawn particular interest both experimentally and theoretically because of their impact in technological applications such as bio/chemosensors,<sup>114-117</sup> optical filters,<sup>118,119</sup> plasmonic waveguides,<sup>23,120-122</sup> and substrates for surface-enhanced spectroscopy.<sup>5,123,124</sup> The property behind all of these applications is the localized surface plasmon resonance (LSPR), which is a collective oscillation of the conduction electrons that occurs when light impinges on a nanoparticle at a specific wavelength. The resonance peak position and shape of the LSPR is governed by the nanoparticle shape, size, composition, and dielectric environment. The LSPR creates enhanced light scattering, absorption, and local enhancement of the electromagnetic field. For arrays of nanoparticles the optical properties become dependent on the array interactions to create a modified plasmon resonance that is characteristic of the whole array; therefore, one needs to understand nanoparticle coupling versus grid spacing, effects of shape and size, and the nanoparticle dielectric environment.

To effectively study a wide variety of arrays, a fabrication method is needed that has precise, user-defined placement of the nanoparticles. Current fabrication techniques include natural lithography, such as nanosphere lithography (NSL),<sup>3,4</sup> and direct-write methods, such as photolithography,<sup>125,126</sup> electron beam lithography (EBL),<sup>32,127</sup> and dip-pen nanolithography.<sup>128</sup> Each type has its own advantages and disadvantages, but for experiments involving the precise control of nanoparticles on a surface, a direct-write method is an excellent tool. Specifically, EBL can be used to create nanoparticles with different shapes, sizes, spacing, and orientation in

two-dimensional (2D) arrays. A partial review of nanoparticle fabrication by EBL is given by Canfield, et al.<sup>129</sup>

Optical properties of one- or two-dimensional noble metal nanoparticle arrays have been studied experimentally<sup>14,32,33,130-133</sup> and theoretically<sup>11,12,51,69,70</sup> by several groups. Short-range coupling effects in EBL fabricated hexagonal and square arrays of triangular and circular Au and Ag nanoparticles were studied by Van Duyne and coworkers.<sup>32</sup> They observed a shift of the LSPR dependent on lattice spacing, and related theoretical work explained these effects in terms of radiative dipolar coupling between the nanoparticles and retardation effects.<sup>32,134</sup> For one-dimensional (1D) chains, they were able to experimentally find a narrower shoulder on the plasmon resonance due to long-range dipole interactions along the chain,<sup>14</sup> which was predicted by Schatz and co-workers.<sup>11,12</sup> Others have looked in more detail at 2D arrays with large grid spacing. Aussenegg and co-workers have studied extinction spectra of 2D Au nanoparticle arrays with a variety of nanoparticle geometries such as cylinders,<sup>33,131,132</sup> nanorods,<sup>131,132</sup> and nanowire gratings.<sup>133</sup> In one study of Au arrays<sup>33</sup> this group monitored the resonance peak with white light spectroscopy and the plasmon lifetime with time-resolved collinear autocorrelation measurements. They observed a red shift with increasing grid spacing and a dramatic increase in the plasmon damping at critical grid spacing. Their physical explanation for these effects relied on the models of Meier and Wokaun,<sup>69,70</sup> and the experiments showed the importance of coherent scattering into a substrate as the means to enhance dipole coupling and thereby increase the radiative component of bandwidth. In a related recent work,<sup>132</sup> they showed a predicted grating-induced resonance<sup>69,70</sup> in an array of Au nanorods having large transition dipoles. Others have looked into different shapes and lattice structures as well.<sup>56,135,136</sup>

In this work an L-shaped nanoparticle without a center of inversion symmetry was studied to provide optical characterization of linear optical properties prior to nonlinear optical studies of the same particles. For a nanoparticle or a lattice with in-plane center of inversion symmetry, the centrosymmetry of the in-plane dipole results in the cancellation of second order nonlinear response such as second harmonic generation (SHG).<sup>111,137</sup> Aussenegg and co-workers have studied the SHG response from a square lattice of Au nanoparticles created from three coalesced discs in a rough L shape. This work measured the plasmon dephasing time in the nanoparticles by interferometric autocorrelation methods.<sup>110,111</sup> Tuovinen, Canfield and co-workers<sup>129,138,139</sup> studied the linear and second order nonlinear optical properties of a two-dimensional array of L-shaped Au nanoparticles having rounded arms. They observed polarization dependence in the linear and SHG response of L-shaped nanoparticle arrays. The extinction spectra were shown to have two optical transitions with independent polarizations along the mirror plane and perpendicular to the mirror plane. In their SHG studies, the incident laser wavelength was fixed at 1060 nm and they scanned the plasmon resonance of the array by changing the grid spacing.

There also have been efforts to theoretically predict and explain the modification of the optical properties of noble metal nanoparticles in 1D and 2D arrays. Wokaun and co-workers<sup>69,70</sup> explained the resonant shift and bandwidth change of the plasmon of periodic nanoparticle arrays by dipolar interaction. With a coupled dipole model, Schatz and co-workers<sup>32,134</sup> demonstrated that for the 1D and 2D periodic nanoparticle arrays the plasmon wavelength shift is determined by the real part of the retarded dipole sum, while the bandwidth is determined by the imaginary part of this sum. They also have shown that the bandwidth can reach a minimum for 1D and 2D arrays, and especially for 1D arrays the polarization

perpendicular to the arrays gives exceptional opportunity for extremely narrow plasmon bandwidths<sup>11,12,140</sup> when the chain is in a uniform dielectric environment.

While the prior results give a conceptual basis for understanding some of the features of nanoparticle interactions in an array, more complete experimental data are required to provide data sets for more accurate testing of theoretical models and optimizing arrays for applications. A study with a fine set of grid spacings and comparison to isolated nanoparticles is presented here to explore how resonance positions and bandwidths depend on such parameters. In addition, the first study of different sized arrays having varying nanoparticle gaps in extended structures is presented to show how resonances and bandwidths evolve with nanoparticle number and spacing. All of these studies are a prerequisite for understanding nonlinear optical properties of L-shaped particles, and motivating new theory for linear and nonlinear optical properties of arrays. In this work we emphasize larger grid spacing and long-range dipole coupling effect.

In the following sections, our optical studies of 2D arrays of Ag nanoparticles and the effects of grid spacing, dielectric environment, and gaps within a 2D structure on the peak position and bandwidth of the plasmon resonance are described. Some discussion of theoretical models is used to rationalize the results, but more detailed theoretical modeling is in progress.

## **2.2 Experimental Methods**

### **2.2.1 Sample Fabrication**

The samples were prepared by EBL on an indium-tin-oxide (ITO) conducting layer of 40 nm on 750  $\mu\text{m}$  thick glass substrates (Thin Film Devices, Anaheim, CA). The substrates were first cleaned by sonication for 5 min in each of the following solvents: acetone, isopropyl alcohol, and DI water. The clean substrates were then baked at 170  $^{\circ}\text{C}$  for 1 min to remove any excess water from the surface. Each substrate was then spin-coated with a 70 nm film of an electron-

sensitive resist, ZEP 520 (Nippon ZEON Ltd.) diluted 1:2 in anisole. Each sample was then soft-baked at 170 °C in a convection oven overnight. A Jeol 9300 FS was used to expose resist; the resolution of the Jeol 9300 FS is approximately 6 nm, at an accelerating voltage of 100 kV. After exposure of the ZEP 520, the nanoparticle patterns were developed in hexyl acetate to create areas for deposition of Ag metal in a high-vacuum thin-film vapor deposition system (AVAC HVC 600). For all samples the metal thickness was 30 nm, as measured by a quartz crystal microbalance. In the last step of the sample preparation, the lift-off step, the resist was dissolved in a strong solvent (Shipley remover 1165), which also removes the metal deposited on top of the resist. To ensure that the metal film on top of the resist does not have any physical contact with the metal deposited directly on the substrate, samples were prepared with an “undercut” in the resist film. This is accomplished by overdeveloping the resist slightly. In this work, nanoparticles shaped like an L, with equal arms, were used in two orientations, which are called L or V depending on their orientation relative to lines of nanoparticles (see Figure 2.1A,B). Both continuous arrays over large areas of  $\sim 100 \times 100 \mu\text{m}^2$  and arrays with gaps were studied. Gap arrays are those where different unit cells were repeated with “missing” nanoparticles or gaps; this gives translational symmetry to the whole array. Scanning electron microscopic (SEM) images to clarify this structure can be seen in Figure 2.1C,D. For the L structure, arm length was used to refer to the extension past the thickness of the arm, which is  $63 \pm 5 \text{ nm}$ ; for example, an  $82 \pm 5 \text{ nm}$  arm length has a full edge length of 145 nm in both directions. Figure 2.1E shows the definition of arm length and arm width of L-shaped nanoparticle. Tables 2.1 and 2.2 summarize all the arrays reported in this paper. In each sample, duplicate and triplicate arrays were prepared, and data for two or three duplicate samples are shown in Figures 2.4, 2.5, 2.7, and 2.8. These

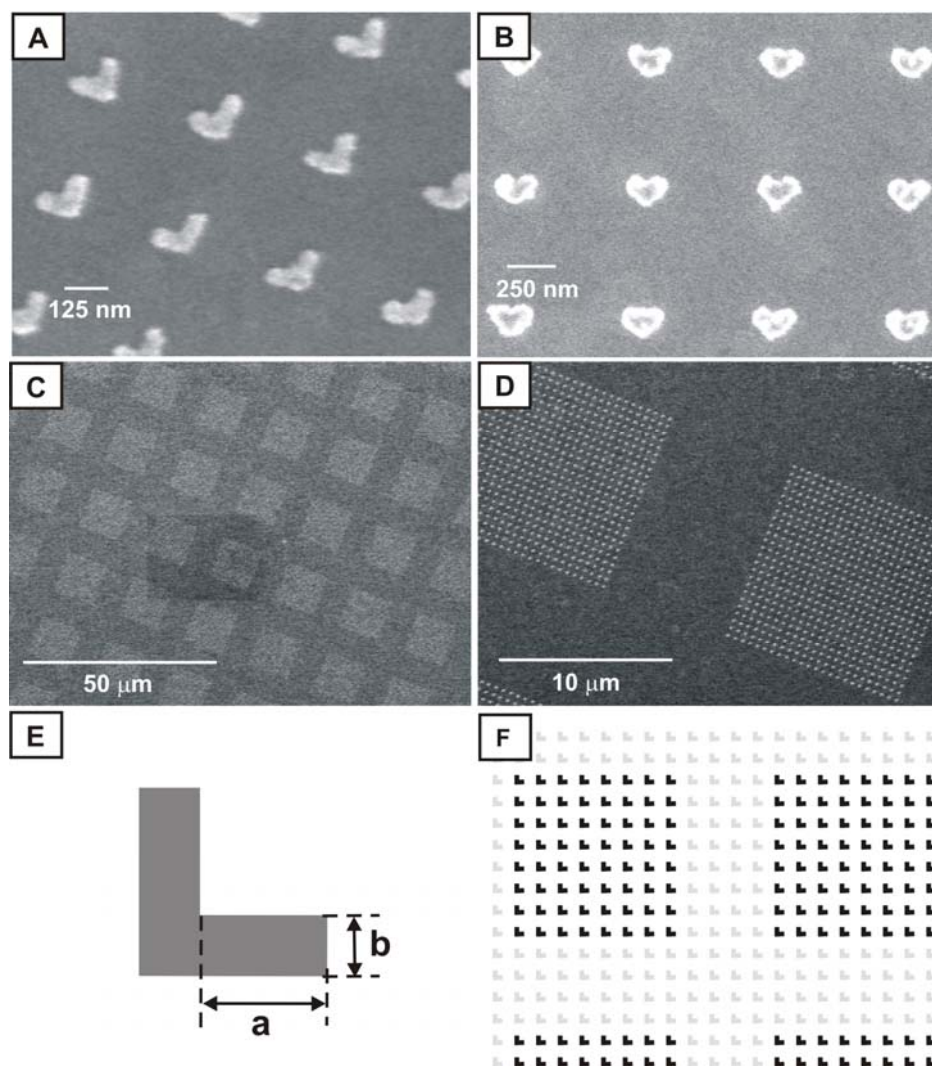


**Figure 2.1** SEM images of two-dimensional arrays of L- and V-shaped nanoparticles. (A) L-shaped nanoparticle arrays (82 nm arm length, 250 nm grid spacing). (B) V-shaped nanoparticle arrays (83 nm arm length, 675 nm grid spacing). (C) Gap array with 82 nm arm length and 450 nm grid spacing (24 particles per block edge and gap of 17 particles). (D) Enlarged view of panel C. (E) Diagram of L-shaped nanoparticle. Dimension  $a$  is defined as the arm length and  $b$  is defined as arm thickness. (F) Diagram of gap arrays with  $8 \times 8$  blocks and gap size of 4. Gray particles in the diagram stand for vacant sites.

orientation	arm length <sup>a</sup> (nm)	arm width <sup>a</sup> (nm)	grid spacing (nm)
L	82	63	250, 300, 350, 400, 420, 440, 450, 460, 500, 550, 600, 650, 5000
L	92	63	250, 300, 350, 400, 420, 440, 450, 460, 500, 550, 600, 650, 5000
V	83	93	400, 450, 475, 500, 525, 550, 575, 600, 625, 650, 675, 700, 725, 750, 5000
V	103	93	400, 450, 475, 500, 525, 550, 575, 600, 625, 650, 675, 700, 725, 750, 5000

<sup>a</sup> Error is  $\pm 5$  nm

**Table 2.1** Characteristics of 2D Ag Nanoparticle Square Arrays

orientation	arm length <sup>a</sup> (nm)	arm width <sup>a</sup> (nm)	grid spacing (nm)	block size <sup>b</sup>	gap size <sup>b</sup>
L	82	63	450	24 × 24	17
L	92	63	400	8 × 8	4, 9, 17
L	92	63	400	12 × 12	4, 9, 17
L	92	63	400	16 × 16	9, 17
L	92	63	400	24 × 24	9, 17, 25

<sup>a</sup> Error is ± 5 nm

<sup>b</sup> Numbers of particles

**Table 2.2** Characteristics of Ag Nanoparticle Gap Arrays

duplicates show reproducibility of the EBL method. EBL fabrication was performed at the MC2 process lab at Chalmers University of Technology.

### 2.2.2 Extinction Measurements

Extinction spectra were collected on an Ocean Optics USB2000 fiber-coupled spectrometer for the 400 – 1000 nm region and a fiber-coupled near-infrared (NIR) spectrometer (NIR 128L-1.7T1-USB, Control Development) for the 900 – 1700 nm region. The Ocean Optics spectrometer had low noise to 950 nm. The spectra over this wide region have a slight mismatch near 900 nm, signifying where one spectrometer ends and the other begins. The optics arrangement is shown schematically in Figure 2.2. White light from a tungsten-halogen lamp light source was fiber-coupled with a 100  $\mu\text{m}$  fiber to a +40 mm focal length achromatic collimating lens. The collimated beam was then polarized by a Glan-Taylor calcite polarizer with 5 mm aperture and focused onto the sample by a +12.7 mm focal length achromatic lens with the optic axis normal to the sample surface. Transmitted light was collected by an infinity corrected 10 $\times$  Nikon microscope objective (NA = 0.30) at a working distance of 16.0 mm and focused into a 600  $\mu\text{m}$  fiber that couples into the spectrometer. The white light spot size on the sample was scanned with a straight edge and was close to Gaussian with a 20  $\mu\text{m}$  diameter at full width at half-maximum (FWHM).

The sample was mounted on two computer-controlled microtranslational stages (M-111.1DG, Physik Instrumente) to form an x–y system with a 50 nm step size. The x–y stage system is fixed on the manual vertical linear stage (MVN50, Newport Corp.) and manual rotational stage (M-UTR120A, Newport Corp.). Rotation of the incident beam polarization relative to the sample geometry was achieved by rotating the sample stage with fixed incident beam polarization. The white light axis was coincident with the rotational axis of a rotational

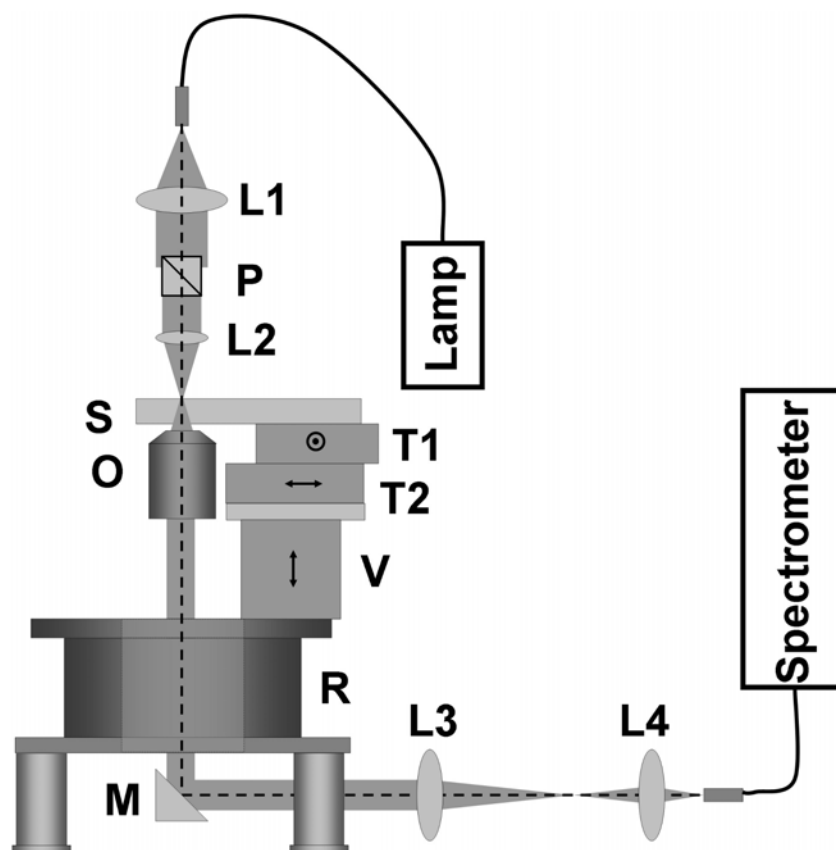


**Figure 2.2** Experimental setup for extinction measurements. Symbols represent achromatic lenses (L1-L4), polarizer (P), sample mount or flow cell (S), 10× Nikon microscope objective (O), computer-controlled microtranslational stages (T1 and T2), vertical stage (V), rotational stage (R), and a mirror (M). The focal lengths of achromatic lenses are +40 mm, +12.7 mm, +200 mm, and +30 mm respectively. The microscope objective is attached to its own manual xyz-translational stage, which is not shown in this figure.

stage to make the beam position fixed on the sample during sample rotation. All the samples were studied under a stream of dry nitrogen, with some additional samples being tested in benzene as well. The extinction measurement was done approximately at the center of the  $100 \times 100 \mu\text{m}^2$  pads and the reference measurement was obtained by scanning into a nearby region of the glass substrate.

### **2.2.3 Dark-Field Scattering Measurement**

A single nanoparticle scattering spectrum of the high-energy band was obtained by resonant Rayleigh dark-field optical microscopy with an inverted microscope (Eclipse TE300, Nikon Instruments) equipped with a dark-field condenser (NA = 0.95 – 0.80) for illumination and a 40 $\times$  objective (NA = 0.60) for collection. White light from the tungsten-halogen lamp in the microscope was polarized by a linear polarizer (cutoff  $\sim$ 800 nm) before the dark-field condenser. The dark-field condenser system was modified to improve transmitted polarization by a mask having a wide slit along a radius aligned with the input polarization, but the transmitted polarization still shows a weak component from orthogonal polarized transitions. Collected light was directed to an imaging spectrograph (SpectraPro 300i, Roper Scientific) coupled with a liquid nitrogen-cooled charge-coupled device (CCD) camera (Spec-10:400B, Roper Scientific).

### **2.2.4 Structural Characterization of Nanoparticle Arrays**

The EBL patterns were characterized with scanning electron microscopy. Accelerating voltages used for imaging were 5 – 10 kV with a working distance of 7 mm. In Figure 2.1, images of different shapes and arrangements are shown. Imaging was performed in the EPIC center at Northwestern University with a Hitachi 4500.

## **2.3 Results**

### 2.3.1 Structural Characterization

The shape of nanoparticles in 2D L-shaped nanoparticle arrays (L arrays) is sharper than that of 2D V-shaped nanoparticle arrays (V arrays), and these variations are according to each particular run of the EBL machine (see Figure 2.1). Grid spacing is varied from 250 to 650 nm for L arrays and from 400 to 750 nm for V arrays. A 2D array with 5  $\mu\text{m}$  grid spacing was also fabricated to provide spectra of “isolated” nanoparticles due to negligible dipole interactions at this spacing. For most studies, sample pads with  $100 \times 100 \mu\text{m}^2$  dimension were fabricated, and a  $300 \times 300 \mu\text{m}^2$  pad was fabricated to explore edge effects from the dipole coupling (see section 2.3.3). Gap arrays of smaller array size were created by isolating smaller blocks with gaps within the same  $100 \times 100 \mu\text{m}^2$  pad. These were fabricated to study the range of dipole coupling in finite arrays; the samples maintain translational symmetry for fixed grid spacing and fixed nanoparticle parameters with variable gaps and variable numbers of nanoparticles in each block.

### 2.3.2 Plasmon Resonance Position and Bandwidth in an Isolated Nanoparticle and 2D Arrays

The polarization dependent spectra of isolated L-shaped nanoparticles and a 400 nm spaced square array of L-shaped nanoparticles are shown in Figure 2.3A,B. Two independent bands can be observed in the isolated nanoparticle spectra (Figure 2.3A) with orthogonal incident beam polarization. The high-energy band in these spectra was studied with a dark-field scattering method on a single nanoparticle in a pad with 5  $\mu\text{m}$  grid spacing, and the low-energy band was obtained by extinction measurement on a pad with 5  $\mu\text{m}$  grid spacing. These two transitions are maintained in the 2D arrays (Figure 2.3B). The inset in Figure 2.3A is a definition of the polarizations used for these experiments. For both 2D L and 2D V arrays, as well as for

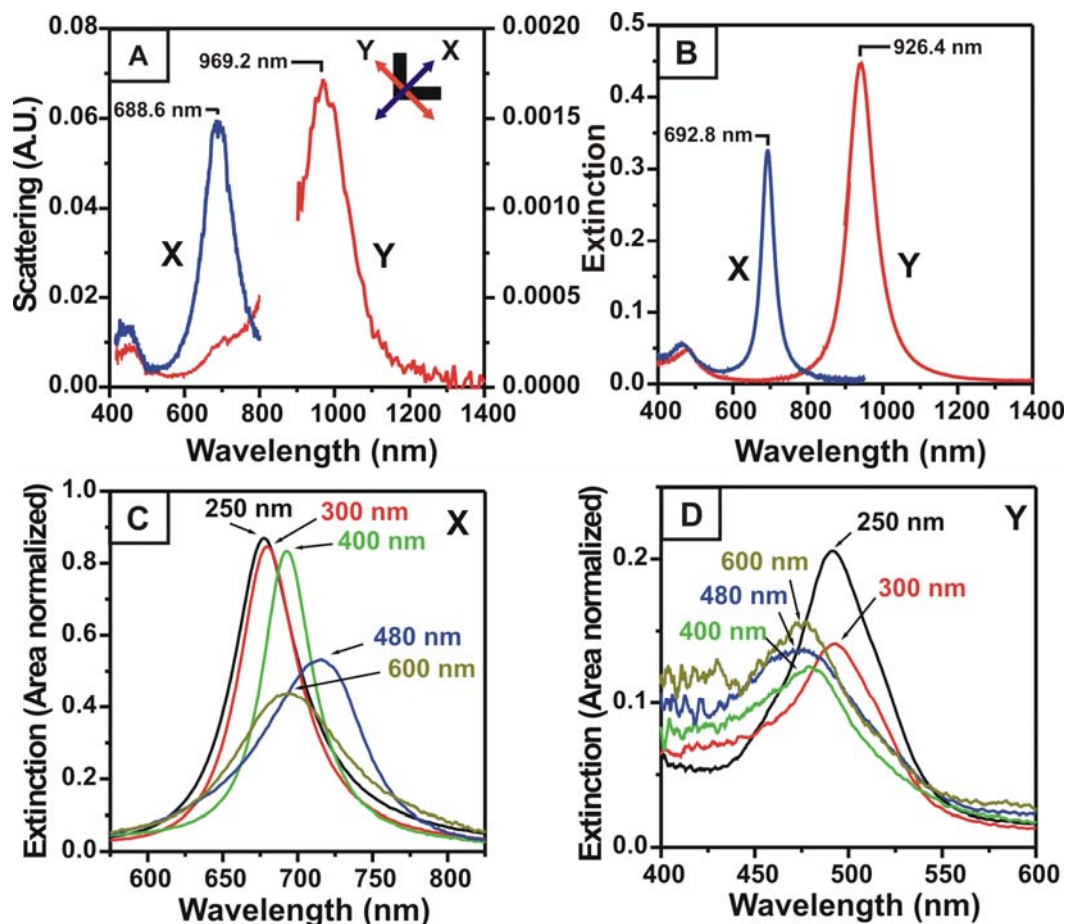


**Figure 2.3** (A) Dark-field scattering spectrum (400-800 nm) of a single nanoparticle and extinction spectrum (>900 nm) of isolated nanoparticles of 82 nm arm length L-shaped nanoparticles in 5  $\mu\text{m}$  grid spacing array. Inset shows a definition of the incident beam polarizations used for these experiments. (B) Extinction spectra of 2D array of 82 nm arm length L-shaped nanoparticles with 400 nm grid spacing. (C) Spectra of the high-energy dipole band for selected grid spacing; 250 nm (black), 300 nm (red), 400 nm (green), 480 nm (blue), and 600 nm (dark yellow). (D) Spectra of the nonpolarized band with a Y-polarized incident beam for selected grid spacings.

isolated nanoparticles, when the polarization is along the mirror symmetry plane of the nanoparticle (X polarization), a high-energy band is observed, and when the polarization is perpendicular to the symmetry plane (Y polarization), a low-energy band is observed. When the polarization is in between, both bands are observed. However, the resonant wavelength and bandwidth of the isolated nanoparticles are different from those of the 2D array, and the resonant wavelength and bandwidth of the 2D array also changes for other grid spacings. In Figure 2.3C, the narrowest bandwidth is shown at 400 nm grid spacing and the resonant wavelength of the spectrum shows the most red shift at 480 nm grid spacing. Note that the spectrum at 480 nm grid spacing is quite distorted from a Lorentzian line shape.

In Figure 2.3A,B, there is a weak band at  $\sim 450$  nm; it does not change by rotation of the incident beam polarization and is not very dependent on grid spacing. These features suggest that this band might be a more complex resonance, and it will be referred to as the nonpolarized extinction band. Figure 2.3D shows the nonpolarized band of the 2D L arrays with Y-polarized incident beam. A similar spectrum is observed for the X-polarized incident beam, which is not shown. At more closely spaced grids of 250 and 300 nm, the amplitude of this band increases with a slight red shift, and this effect is shown for all 2D L arrays with different arm lengths.

Samples were systematically prepared to study the grid spacing effect, and the results are shown in Figure 2.4A,B. Two data points are often visible for duplicate arrays made in the same preparation, although most are overlapping. The isolated particle parameters are obtained from the data with 5  $\mu\text{m}$  grid spacing. As the grid spacing changes, the resonant wavelength of the absorption changes for both array types. The resonant wavelength red shifts with increasing grid spacing, and reaches a maximum red shift at a critical grid spacing ( $D_{crit}$ ). At larger grid spacing the resonance wavelength begins to blue shift.  $D_{crit}$  is observed at the grid spacing where the

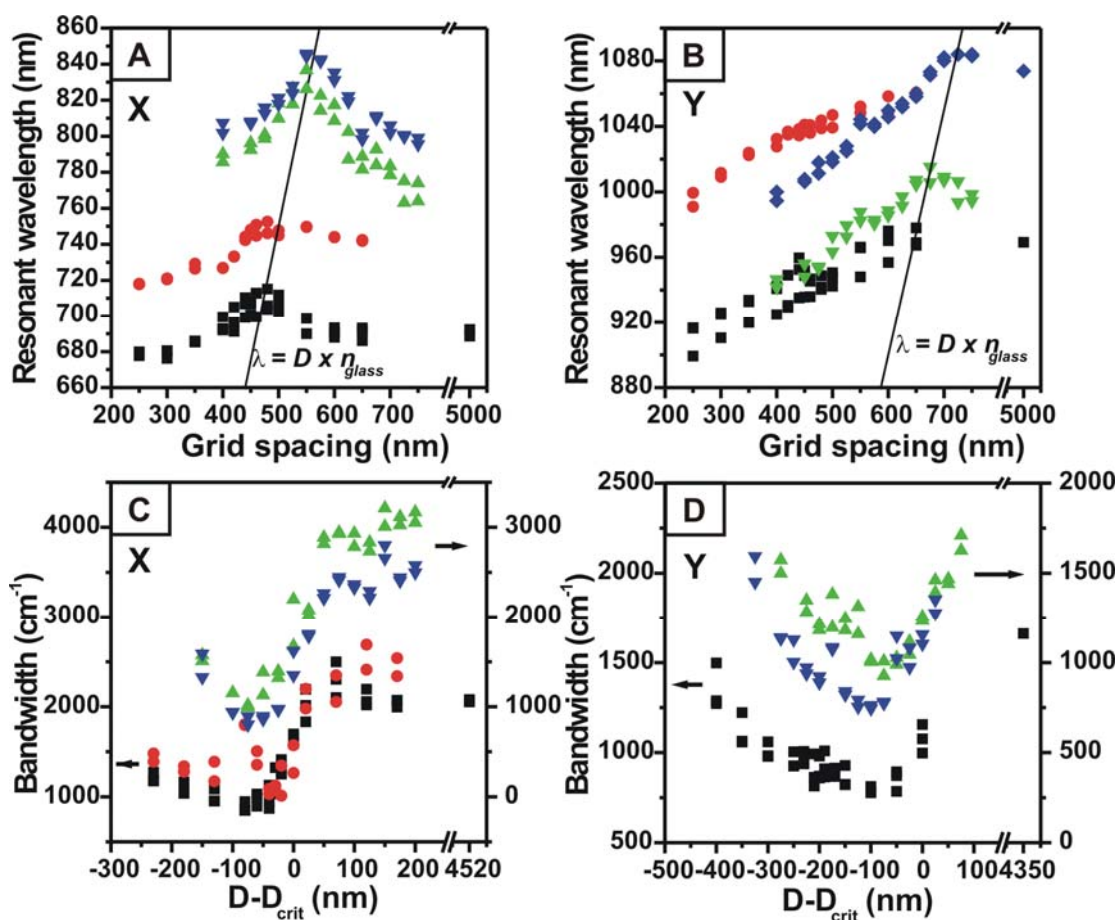


**Figure 2.4** Resonant wavelength and bandwidth versus grid spacing for high-energy band (A, C) and low-energy band (B, D) for 2D nanoparticle arrays of L and V orientation. L arrays with 82 and 92 nm arm length are plotted with black squares and red circles, respectively, and V arrays with 83 and 103 nm arm length are plotted with green triangles and blue inverted triangles, respectively. Duplicate and triplicate (82 nm L, black) arrays are shown for different array pads prepared on the same chip. The light line  $\lambda = D n_{glass}$  is shown with a black solid line in panels A and B. The bandwidth is plotted versus  $(D - D_{crit})$ , where  $D$  is the actual grid spacing and  $D_{crit}$  is the critical grid spacing where the resonant wavelength shows maximum red shift. Plots for L arrays follow the left axis, and the plots for V arrays follow the right axis.

resonant wavelength is coincident with  $Dn_{glass}$  where  $D$  is grid spacing and  $n_{glass}$  is the refractive index of glass ( $n_{glass} = 1.5$ ). Not only the peak position but also the bandwidth varies as the grid spacing is changed. Figure 2.4C,D depicts the plots of the resonance bandwidth versus ( $D - D_{crit}$ ). For both high-energy (X-polarized) and low-energy (Y-polarized) dipole bands, the bandwidth decreases as the grid spacing increases until the grid spacing about 75 nm smaller than the  $D_{crit}$  of each band. After the grid spacing, the bandwidth starts increasing. The minimum bandwidth achieved with an optimized 2D array is about half of the single nanoparticle resonance.

The resonance band shape of most grid spacings is a Lorentzian function except when the grid spacing is near  $D_{crit}$ . The spacings with Lorentzian line shapes indicate that there is no large inhomogeneous broadening in these nanoparticles. When the grid spacing is close to  $D_{crit}$ , the line shape of the resonance band starts deviating from Lorentzian, and this distortion lasts until  $\sim 100$  nm larger spacing than  $D_{crit}$ . When the grid spacing is just larger than the turnover of bandwidth, the band shape becomes distorted significantly and forms a broad shoulder on the high-energy side, as can be seen in the 480 nm grid of Figure 2.3C. In the case of bands with Lorentzian shape, the product of lifetime in time domain and bandwidth in frequency domain is  $1/2\pi$ . The minimum bandwidth observed was around  $700 - 800 \text{ cm}^{-1}$  ( $\sim 0.1 \text{ eV}$ ), and it corresponds to a plasmon lifetimes of  $7.6 - 6.6 \text{ fs}$ .

### 2.3.3 Range of Dipole Coupling

To explore the plasmonic coupling in these arrays,  $100 \times 100 \text{ }\mu\text{m}^2$  gap arrays were fabricated with different unit sizes and gap sizes between the units (each unit is a smaller square block of nanoparticles, and in the discussion these are referred as blocks). The pattern is shown in Figure 2.1C,D for a specific case, and in Figure 2.1F, a detailed diagram of gap-arrays with 8

$\times 8$  blocks and a gap size of 4 is shown. Gray particles in Figure 2.1F stand for vacant sites. All the gap-arrays tested have L orientation and are summarized in Table 2.2. The resonant wavelength of each gap array is shown in Figure 2.5A,B for each high-energy (X-polarized) and low-energy (Y-polarized) band. For the smallest block size, an  $8 \times 8$  nanoparticle block, the high-energy and low-energy bands are red shifted from that of a semi-infinite array, which is a continuous particle array over a  $100 \times 100 \mu\text{m}^2$  area ( $250 \times 250$  nanoparticles). The magnitude of the shift is different for each band, with a shift of  $\sim 50$  nm for the low-energy band and  $\sim 10$  nm for the high-energy band. As the number of nanoparticles in a block is systematically increased from  $8 \times 8$  to  $24 \times 24$ , the plasmon peak position blue shifts and approximately converges to the peak position of a semi-infinite nanoparticle array.

The resonance bandwidth also shows a large change according to the block dimension. Figure 2.5C,D shows a plot of the bandwidth versus block dimension. As the block size increases, the bandwidth decreases and it converges to that of semi-infinite nanoparticle array. However, the gap dimension does not seem to play a significant role in either the resonant wavelength or the bandwidth. There is no systematic trend in resonant wavelength and bandwidth according to the change of gap dimension. Furthermore, for some nanoparticle blocks such as  $16 \times 16$  blocks, different gaps show almost the same resonant wavelength and bandwidth. This suggests that four or more nanoparticle gaps isolate the unit blocks. These results are shown for a grid spacing of 400 nm; a similar set of results was found for a spacing of 450 nm, which is not shown.

To explore the consistency of the resonant wavelength and the bandwidth of the LSPR across a nanoparticle array, large arrays ( $300 \times 300 \mu\text{m}^2$ ; grid spacing = 250 nm) were fabricated and spectra were taken at various positions throughout the array. These results are in Figure 2.6

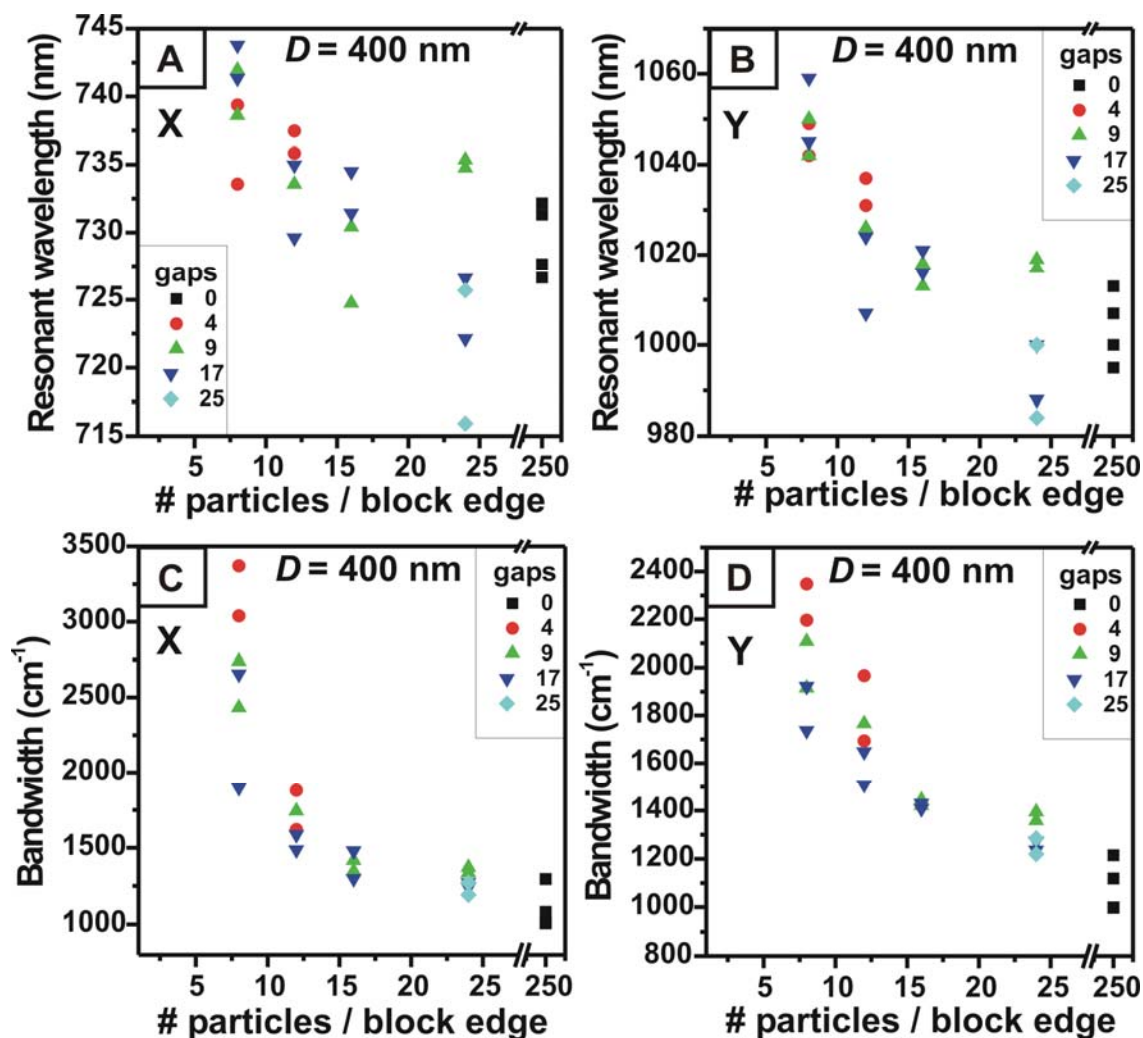


**Figure 2.5** Resonant wavelength and bandwidth of high-energy bands (A, C) and low-energy bands (B, D) of gap array samples (92 nm arm length, 400 nm grid) versus the number of particles per block edge. Data for semi-infinite particle arrays are plotted with black squares, and data with gaps corresponding to 4, 9, 17, and 25 particles are plotted with red circles, green triangles, blue inverted triangles, and cyan diamonds, respectively. Duplicate arrays are shown for different array pads prepared on the same chip.

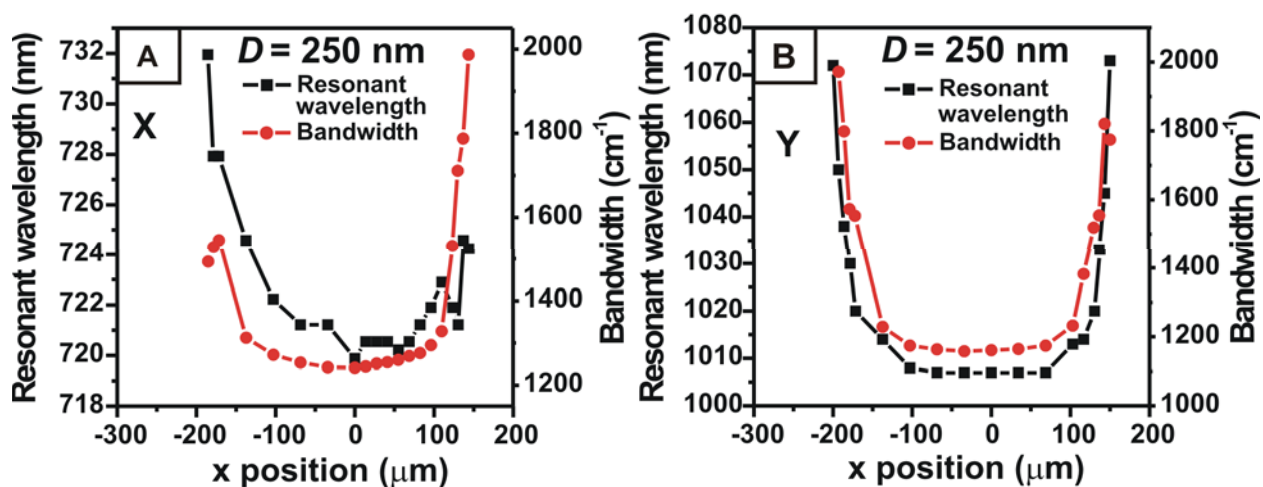


**Figure 2.6** Resonant wavelength and bandwidth of (A) high-energy band and (B) low-energy band scanned from one edge to the other edge of the two-dimensional L-shaped nanoparticle array. The array dimension was  $300 \times 300 \mu\text{m}^2$ . The arm length of the particle was 92 nm, the grid spacing was 250 nm, and the focal spot radius for 99% of the energy was  $\sim 19 \mu\text{m}$ .

where one observes that as the probe beam gets closer to the edge of the pad, the peak position red shifts and the bandwidth becomes broader. The origin ( $x, y = 0$ ) is arbitrarily set in both directions, and the data were not rescaled to be symmetric.

### 2.3.4 Solvent Effect on the Plasmon Resonance of 2D Arrays

As stated in the beginning of the paper, the LSPR resonance position is a function of many parameters, including the refractive index of the medium surrounding the nanoparticles. Mie theory for spherical nanoparticles<sup>28</sup> and the experimental measurements and theoretical calculations of various types of nanoparticles<sup>134,141,142</sup> describe the plasmon shift in dielectric media other than vacuum.

The two dipole bands of V arrays with 83 nm arm length were monitored in nitrogen and benzene. The change in resonance wavelength and bandwidth for different grid spacing in nitrogen and benzene is shown in Figure 2.7. Figure 2.7A,B shows the resonant wavelength versus grid spacing plots for both high and low-energy bands in two different dielectric media for the same sample. In benzene ( $n = 1.5$ ), the resonant wavelength shifted to the red compared to nitrogen ( $n = 1.0$ ), as expected from the increase in refractive index. The  $D_{crit}$  of the high-energy band shifted from  $\sim 575$  nm in nitrogen to  $\sim 650$  nm in benzene. The  $D_{crit}$  of the low-energy band is  $\sim 700$  nm in nitrogen; however, in benzene, it is not observed within our grid spacing range.

Figure 2.7C,D shows the bandwidth versus grid spacing plot for both high and low-energy bands. In the high-energy band (Figure 2.7C) the nitrogen case has a minimum in bandwidth at about 525 nm grid spacing, or 50 nm below the  $D_{crit}$ . However, the case of benzene shows no clear minimum in bandwidth until about 625 nm, which is slightly below its  $D_{crit}$ . In the low-energy band (Figure 2.7D), the bandwidth of the LSPR in two different environments is

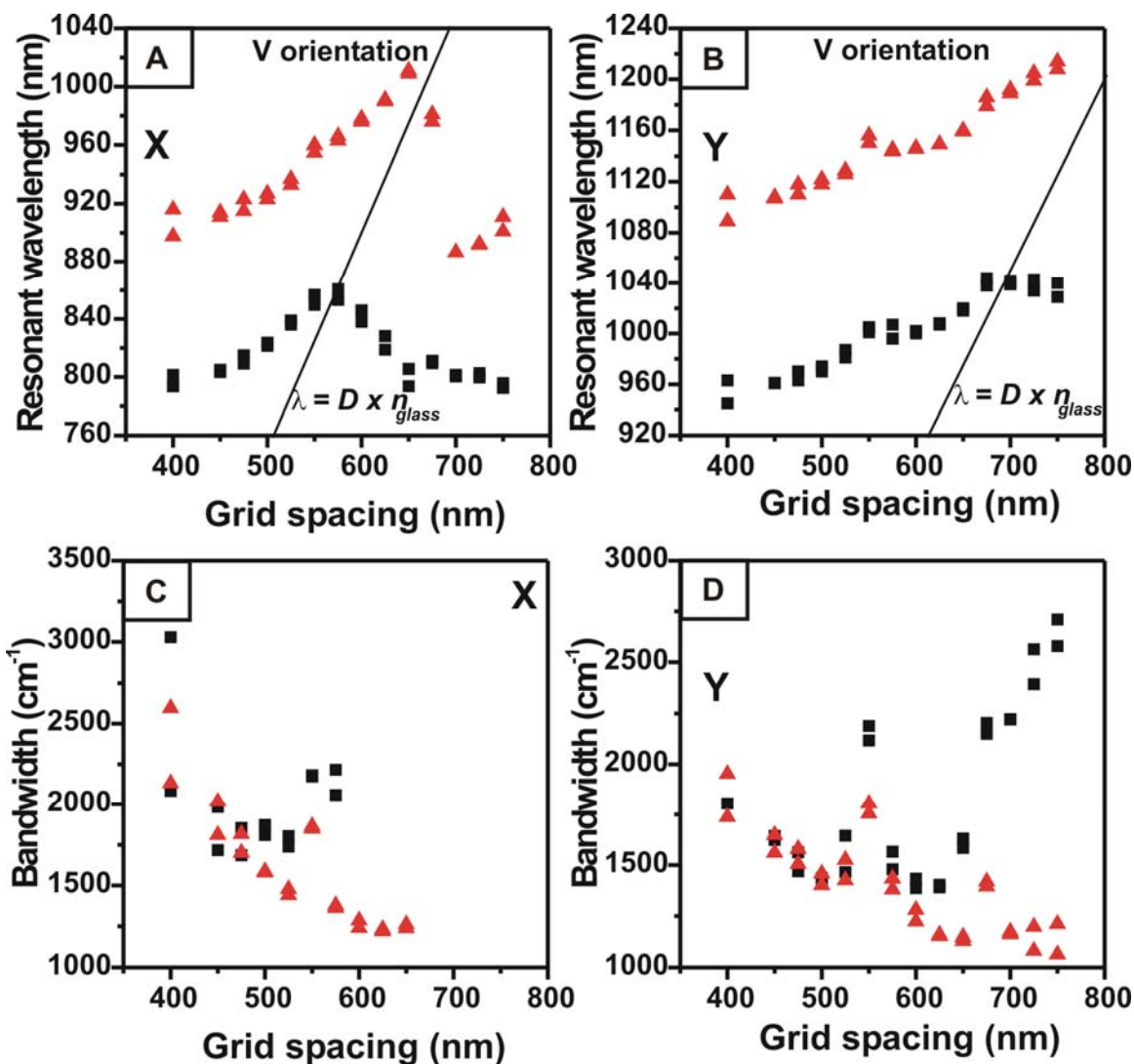


**Figure 2.7** Resonant wavelength and bandwidth of the high-energy band (A, C) and low-energy band (B, D) in two different dielectric media; nitrogen ( $n = 1.0$ ) and benzene ( $n = 1.5$ ). The sample was 2D V arrays with 83 nm arm length. Duplicate arrays are shown for different array pads prepared on the same chip. The plot with black squares is in nitrogen, and the plot with red triangles is in benzene. The light line  $\lambda = Dn_{glass}$  is shown with a black solid line.

similar to each other at grids smaller than 600 nm. However, in nitrogen it starts increasing after 600 nm grid spacing, while in benzene it keeps decreasing because  $D_{crit}$  is moved to larger grid spacing.

An alternative way to examine the data is to plot the difference between the high-energy and low-energy resonances in nitrogen and benzene. In Figure 2.8, the energy difference between the high-energy and low-energy bands in nitrogen is the same up to 575 nm grid spacing which is  $D_{crit}$  for the high-energy band in the nitrogen.

When benzene was introduced as a dielectric medium, additional bands were observed that were not seen under nitrogen; they are plotted in Figure 2.9A,B that shows normalized extinction spectra for X-polarized beam. These features shifted to red as the grid spacing increased, and they are assigned as grating-induced plasmon modes as seen previously by Félidj et al.<sup>132</sup> These modes were not observed under nitrogen because 40 nm ITO cannot support a waveguide mode with a low index on one side.<sup>143,144</sup> When the refractive index of the medium on top of the 40 nm ITO layer is close to 1 (the refractive index of nitrogen), the cutoff frequency for waveguide operation is located in the UV range. However, as the refractive index of the medium approaches that of glass substrate, the cutoff frequency moves to low frequency. Therefore, in benzene, the ITO waveguide mode can support visible and near-IR wavelengths, and this creates additional features in the extinction spectrum. In Figure 2.10A, the grating-induced plasmon mode (bands marked as  $c$  in Figure 2.9B) is plotted with black squares and marked as  $c$  while the high-energy band resonance (bands marked as  $d$  in Figure 2.9B) is plotted with red circles and marked as  $d$ . The grating-induced mode follows the  $\lambda = Dn_{glass}$  light line and it corresponds to orders on the light circle of  $k = 2\pi / D$  in the reciprocal lattice (Figure 2.10B). This agrees with the observation reported by Félidj et al.<sup>132</sup> It is also observed for the Y-

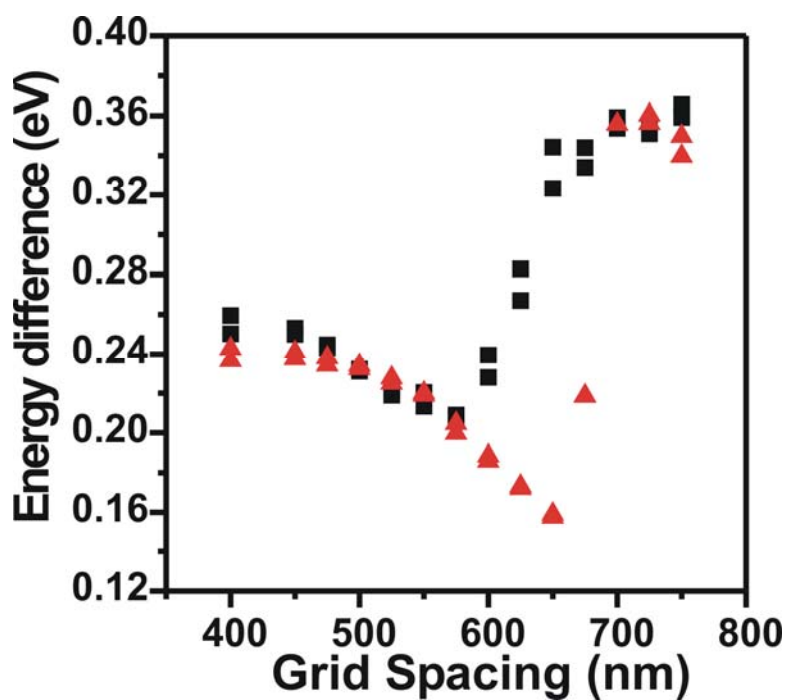


**Figure 2.8** The energy difference between X- and Y-polarized bands in nitrogen (black square plot) and in benzene (red triangle plot). Duplicate arrays are shown for different array pads prepared on the same chip.

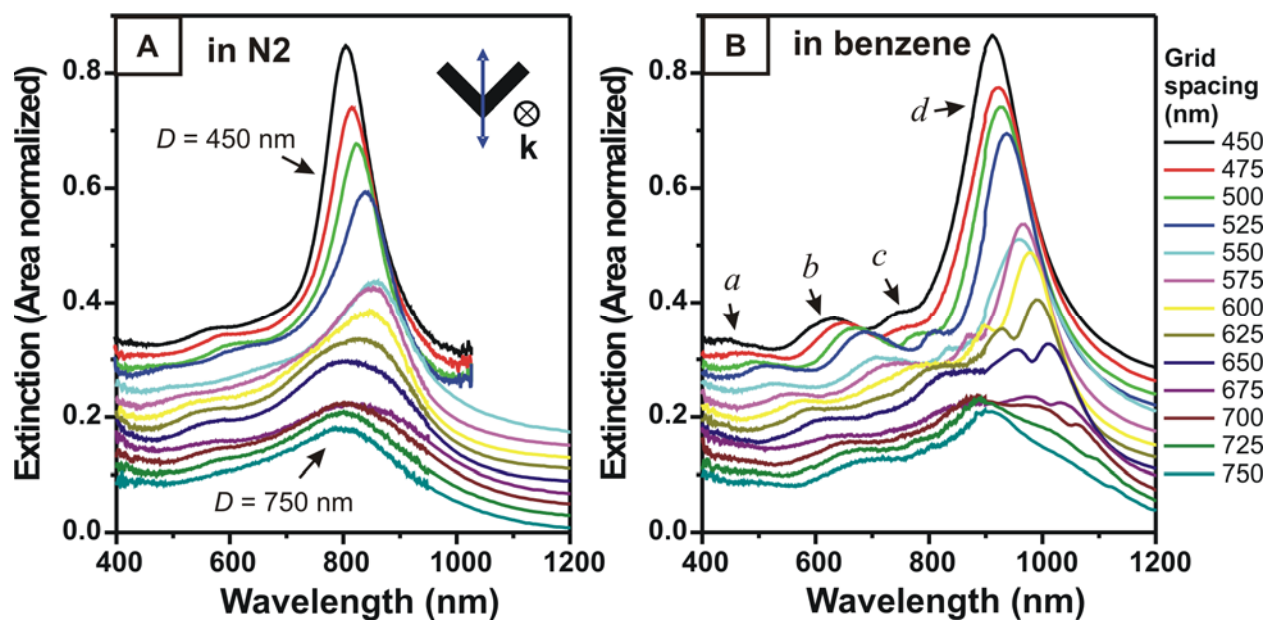


**Figure 2.9** (A) Nanoparticle area normalized extinction spectra of the 2D V arrays with different grid spacings in nitrogen. Grid spacing ranges from 450 nm to 750 nm in 25 nm increment from top to bottom. All the spectra are shown with an offset for clarity. The arm length of the V nanoparticle was 83 nm. (B) Area normalized extinction spectra of the 2D V arrays in benzene. Grid spacing is the same as panel A. The wave vector and polarization of the incident beam are shown in inset of panel A.

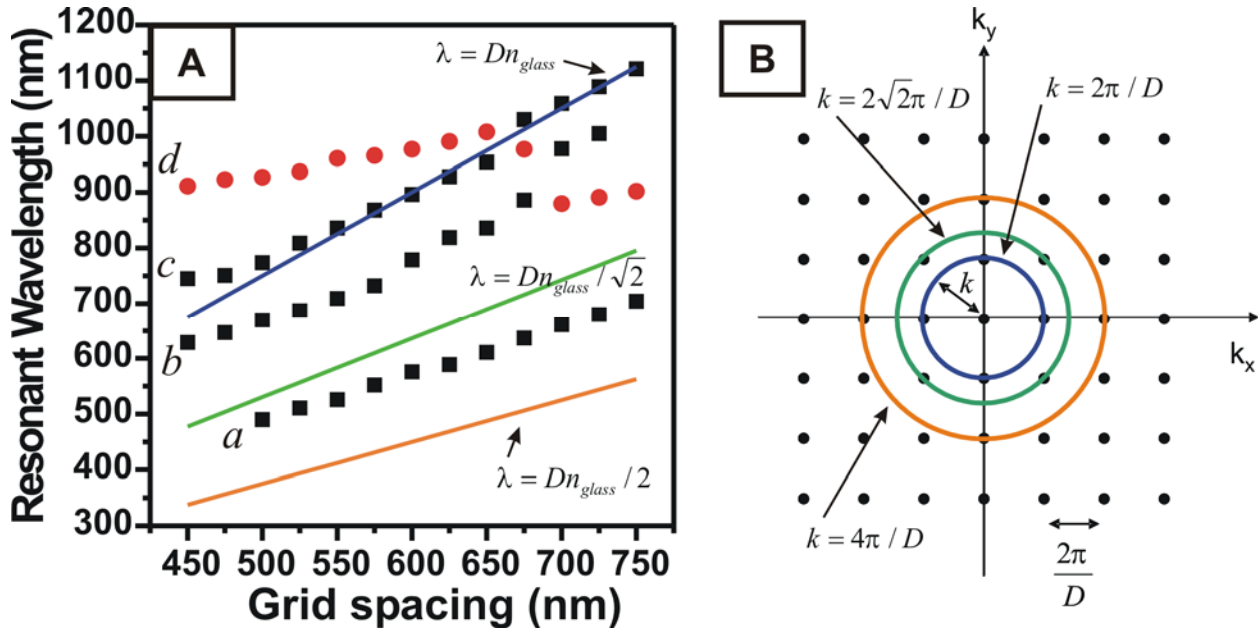


**Figure 2.10** (A) Resonant wavelength of X-polarized band, that is marked as  $d$  in Figure 2.9B is plotted with red circles and grating-induced plasmon mode that is marked as  $c$  in Figure 2.9B is plotted with black squares and marked as  $c$ . The grating-induced mode follows  $\lambda = Dn_{glass}$  line. Another resonance that is marked with  $a$  and  $b$  in Figure 2.9B, is plotted with black squares and marked as same letter. (B) Reciprocal lattice of 2D square array with grid spacing  $D$ . All the grating orders are marked with black dots. Light circles of  $k = 2\pi / D$ ,  $k = 2\sqrt{2}\pi / D$ , and  $k = 4\pi / D$  are marked with blue, green, and orange circles, respectively. The light lines  $\lambda = Dn_{glass}$ ,  $\lambda = Dn_{glass} / \sqrt{2}$ , and  $\lambda = Dn_{glass} / 2$  in panel A correspond to the light circles  $k = 2\pi / D$ ,  $k = 2\sqrt{2}\pi / D$ , and  $k = 4\pi / D$  in panel B, respectively.

polarized beam, which is not shown here. The origin of the bands marked with  $a$  and  $b$  in Figure 2.9B can be the grazing angle scattering through the orders on the light circles of  $k = 2\sqrt{2}\pi/D$  and  $k = 4\pi/D$  in Figure 2.10B. However the plot of band  $a$  and  $b$  in Figure 2.10A do not follow the light lines of those  $k$ 's, so the origin of those bands is not clear.

## 2.4 Discussion

Resonances having polarization properties similar to those shown in Figure 2.3 have been reported for arrays of Au nanoparticles of a rounded L shape<sup>129,138,139,145</sup> but not for isolated nanoparticles. Our fabrication procedure often resulted in less rounded arms for individual L nanoparticles and these Ag nanoparticles have two main polarized transitions with a small nonpolarized transition to the blue of the main transitions. The position of the nonpolarized transition is not sensitive to grid spacing, but it increases in amplitude at close spacings of 250 and 300 nm and it also exists in the isolated nanoparticle. Preliminary theoretical results confirm that small nonpolarized extinction is expected to the blue of the two polarized resonances.

The shifts in location of the polarized resonances as a function of grid spacing have been seen previously for close-spaced grids<sup>32</sup> and for grids having similar spacing ranges to this work.<sup>33</sup> Figure 2.4 shows a variety of L sizes and two orientations for both the high-energy and low-energy resonances of nanoparticles. The results in Figure 2.4A,B show the same grid spacing dependence as was seen previously,<sup>33</sup> with a resonance peak position shifting red as the grid spacing increases. This shift reverses at some critical grid spacing  $D_{crit}$ , and then returns to a value similar to the isolated nanoparticle resonance at larger spacing. The limiting value at very large spacing is expected to be identical to the average isolated nanoparticle resonance. The maximum resonance shift has been discussed previously<sup>33</sup> as being defined by the wavelength where scattering can propagate in the substrate with grazing angle, which for normal incidence

geometry is at the glass index of refraction ( $n_{glass} \sim 1.5$ ) times the grid spacing ( $D$ ). In prior theoretical work<sup>69,70</sup> this type of shifting was predicted as due to dipole interactions with enhancement from scattering into the substrate. This model provides a qualitative understanding of why the bandwidth is also changing dramatically<sup>33</sup> as shown in Figure 2.4C,D. The physical interpretation of this model shows that the greatest bandwidth should be at a grid where maximum radiation into the substrate is present, which enhances radiation damping and shortens the lifetime below the intrinsic electron-hole relaxation time. When the grid spacing is small compared to the wavelength of the plasmon resonance, radiative damping and intrinsic relaxation define the bandwidth. As the grid spacing times the glass refractive index ( $Dn_{glass}$ ) approaches the plasmon resonance wavelength, maximum dipole interactions between particles shift the peak resonance due to coherent interactions. These interactions near the wavelength  $Dn_{glass}$  provide increased radiative damping, which broadens the Lorentzian line shape. All of the samples give the narrowest bandwidth at a similar value of  $\sim 75$  nm for  $(D - D_{crit})$ . However, specific computation is required to predict how narrow the minimum bandwidth might become, and the origin of the 75 nm offset for minimum bandwidth.

Another type of model has identified how the dipole coupling explains red or blue shifts in the resonances.<sup>32,134</sup> A simple semianalytical model of coupled dipoles<sup>134</sup> shows how summing all of the dipole interactions on an infinite lattice can be modeled with optical constants of the metal and computation of the extinction. While this study did not extend to larger grid spacing, they showed that the bandwidth is controlled by the imaginary part of the sum of all dipole contributions and the resonance is controlled by the real component. Red shifting was shown to be expected for grid spacing similar to the isolated nanoparticle resonance and blue shifts for closer spacing. By analyzing the polarization of the whole array in this fashion they

showed that long-range dipole contributions dominate for 2D lattices. The simplified model was also used to examine 2D array data at relatively close spacings.<sup>32</sup> The resonance shifts are qualitatively consistent with the data; however, the simplified model was not extended to large grid spacings. More recently, an electrodynamic calculation was done for 400 spherical Ag nanoparticles of 50 nm diameter on 2D arrays.<sup>11-13</sup> This calculation shows a progressive narrowing of the resonance with increasing grid spacing, along with the red shift. The grid spacing of minimum bandwidth is 500 nm, with a bandwidth of 0.084 eV for hexagonal arrays and 420 nm with a bandwidth of 0.105 eV for square arrays, which is similar to the narrowest bandwidth observed in our research. However, the line shape for resonances is different from our experiments. In the theoretical work, as the grid becomes larger the line shapes look like an interference dip plus a red resonance adding to the broad resonance of an isolated nanoparticle. We have used the simplified coupled dipole model<sup>134</sup> to show that this general form is also present at larger grid spacings with no substrate; we find the interference dip for ellipses at the wavelength of the grid spacing. Therefore, the experimental line shapes do not agree with the theoretical line shape that has been predicted for arrays of spherical nanoparticles,<sup>11,12</sup> although the minimum bandwidth is close to our data. However, our experiments on an ITO glass interface do not follow the theoretical conditions of uniform refractive index, even in benzene. Our work and the prior work on Au nanoparticles<sup>33</sup> find a Lorentzian line shape for most wavelengths, except when the grid is near the grid of maximum red shift  $D_{crit}$ . Additional theoretical work on nonspherical particles that includes substrate effects is required to model these changes in line shape as a function of grid spacing, and the location of the minimum bandwidth point.

The data on gap arrays relate to the basic interpretation of dipole interaction discussed in the prior paragraph. Figure 2.5A,B shows how the resonance position shifts as the number of nanoparticles in the 2D arrays increases. The resonance position data show significant fluctuation so that any dependence of the trend on gap size is not obvious. However, the size of the array clearly correlates with the resonance position, with larger numbers of nanoparticles having a resonance that approaches the limiting semi-infinite array value. Figure 2.5C,D shows that the number of nanoparticles greatly affects the bandwidth. As the number of nanoparticles increases bandwidth reduces dramatically. For the smaller gap arrays of  $8 \times 8$  and  $12 \times 12$  nanoparticles, the data suggest that gaps of four nanoparticles have greater bandwidth than larger gaps, but this might be due to sample variations, and more study with even smaller gaps is in progress. The greater bandwidth of smaller arrays is clear from these data, and  $24 \times 24$  nanoparticles is approaching the number of dipole interactions required to give similar effects to a full array. For this particular grid spacing of 400 nm, the full array has a bandwidth near the minimum value, which is achieved at 450 nm grid spacing. The dependence of bandwidth on nanoparticle number suggests that the minimum bandwidth is a consequence of many dipole interactions reducing the natural radiative scattering probability. Additional theory is required to explain the nanoparticle number dependence of the bandwidth and define the ultimate minimum bandwidth. The range of nanoparticle interaction in these experiments exceeds 25 nanoparticles with 400 nm spacing, or 10  $\mu\text{m}$ . While not tested, one might expect the coupled nanoparticle range of 40 nanoparticles might closely approach the infinite limit, or 16  $\mu\text{m}$ .

Figure 2.6 shows how the range of dipole interactions depends on the experimental setup. For an optical focus of 20  $\mu\text{m}$  FWHM, which is smaller than the array size of  $300 \times 300 \mu\text{m}^2$ , we can clearly see the effects of approaching an edge. As shown in Figure 2.6B, about 200 – 220

$\mu\text{m}$  out of the  $300\ \mu\text{m}$  size have the limiting bandwidth. The beam focus radius to the 99% energy level is  $18.7\ \mu\text{m}$ , although the sharpness of the focus in this particular experiment was not immediately measured and might be slightly different. If we use this radius and a nanoparticle interaction range of  $16\ \mu\text{m}$  to define a reasonable approximation to an infinite lattice, then the sum of these effects is about  $35\ \mu\text{m}$ . This would predict a constant range of  $230\ \mu\text{m}$  in the data for Figure 2.6B, which is slightly larger than we measured. This shows that optical scanning of arrays requires careful attention to edge effects in the probe beam and the range of dipole interactions, and is important for designing sensing applications.

The solvent experiments shown in Figure 2.7 have the effect of approximately immersing the nanoparticles into a constant refractive index environment. The red shifts of resonances were similar to other types of nanoparticle arrays, and the bandwidth changes in benzene are similar to data in nitrogen. Figure 2.8 shows that the splitting between the resonances is almost constant up to  $D_{crit}$ . These results show that the minimum bandwidth effects can be maintained in solvents, which might be important for sensing applications. The effect of a constant refractive index environment at enhancing waveguide effects was shown in Figure 2.9. For a study of dipole coupling of nanoparticles in solution it would be better to not use ITO, although it makes the fabrication easier.

## 2.5 Conclusion

The LSPR extinction spectra of 2D arrays of Ag nanoparticles having an L shape were obtained for various grid spacings and nanoparticle sizes. Single nanoparticles had two independent extinction resonances with orthogonal polarization, and the two resonances were maintained in the 2D arrays. A small resonance to the blue of the main resonances was not polarized, and it suggests a more complex optical transition that had changes in amplitude and

resonance at close grid spacing of 250 and 300 nm. Each polarized resonance had its resonance wavelength and bandwidth modified by the grid spacing of 2D arrays. The maximum resonance red shift was shown at a critical grid spacing,  $D_{crit}$ , defined previously<sup>33</sup> as the spacing where scattering launches into the substrate. The minimum bandwidth was observed at  $\sim 75$  nm smaller grid spacing than the critical grid spacing for each high- and low-energy band. The minimum bandwidth of  $700 - 800 \text{ cm}^{-1}$  is half the single nanoparticle resonance and corresponds to 7.6 – 6.6 fs lifetime. The number of interacting nanoparticles also determined the resonant wavelength and bandwidth, with bandwidth most sensitive. As the number of interacting nanoparticles increased from an  $8 \times 8$  to a  $24 \times 24$  array, the resonant wavelength red-shifted and bandwidth decreased to near the semi-infinite array limit. However changing the gap between adjacent 2D blocks from 4 to 25 nanoparticles did not play a discernible role in resonant wavelength and bandwidth, although fabrication issues create noise in the data. More experiments are needed with gaps from 1 to 4 particles. The effect of dipole coupling range was also shown by scanning a larger array, where edge effects in resonance position and bandwidth could be clearly shown. When the refractive index of the environment was increased by adding solvent, the resonant wavelength shifted to the red. The critical grid spacing and the spacing for minimum bandwidth shifted accordingly. This solvent effect shows that specific grid spacing can achieve minimum bandwidth, which is important for sensing applications in solvents. The energy difference between the high- and low-energy band was approximately constant in nitrogen and benzene. The refractive index similarity of benzene to a glass substrate enables a waveguide mode to be supported by a 40 nm ITO layer. Therefore, in benzene a small grating-induced resonance was observed, which was not observed in a nitrogen environment.

## **Chapter 3**

### **Birefringence in Two-Dimensional Arrays of L-Shaped Silver Nanoparticles**

### 3.1 Introduction

Nanomaterials have drawn particular interest in a wide variety of fields because their optical properties are different from bulk properties. The optical properties of metal nanoparticles or nanostructures can be modified and controlled by changing the shape, size, composition, and the refractive index of dielectric media.<sup>4,21,142,146,147</sup> The development of flexible nanofabrication techniques to adjust those parameters has enabled wavelength tuning of the optical functions of these nanomaterials. Various types of nanostructures including sub-wavelength grating, sub-wavelength hole arrays, and nanoparticle arrays are fabricated as optical elements such as reflective and transmission polarizers,<sup>148-150</sup> optical filters,<sup>118,119,148,151</sup> antireflection surfaces,<sup>152-154</sup> wave plates,<sup>154,155</sup> and binary lenses.<sup>156</sup>

Sub-wavelength grating patterns etched on dielectric material or semiconductor shows a birefringence property that arises from anisotropy on a scale much larger than molecular scale. It is called form birefringence<sup>157</sup> and such a grating produces only zero-order diffraction.<sup>158,159</sup> The optical properties of the structure have been modeled,<sup>160-162</sup> and it has been shown that the birefringence property can be adjusted by variation of the duty cycle (filling factor) and the shape of the structure. By using these properties, applications have been demonstrated with sub-wavelength gratings as polarizers,<sup>160,163,164</sup> antireflection surfaces,<sup>152-154,160</sup> wave plates,<sup>154,155</sup> and binary lenses.<sup>156</sup> Typical fabrication methods were holographic lithography or electron-beam lithography (EBL) followed by ion-beam etching.

Metal nanostructures offer another means to fabricate ultra thin optical elements; for example, the metal wire-grid is one of the most studied structures. An optical model to estimate the transmittance and reflectance of a wire-grid is suggested by Yeh,<sup>165</sup> and polarizers<sup>149,150,166</sup> as well as extreme-ultraviolet filters<sup>148,151</sup> have been fabricated with gold, aluminum, and chromium

wire-grids. Their polarization dependent resonance behavior also has been studied by Chen et al.<sup>167</sup> On the other hand, Ebbesen and coworkers demonstrated the transmission wavelength selectivity of sub-wavelength hole arrays on noble metal film.<sup>119,168,169</sup> The transmission wavelength can be tuned by changing the period of array and hole diameter, therefore the array acts like a tunable color filter. In the case of metal nanoparticle arrays, pearl-necklace-type arrays of silver nanoparticles embedded in flexible film have been demonstrated as a polarization-dependent color filter.<sup>118</sup> However, there have been few studies that use metal nanoparticle arrays as far-field optical elements, and their birefringence properties have not been analyzed.

Depolarized scattering from nonspherical particles have been studied since long ago.<sup>29,170-173</sup> Recently, the depolarized scattering from metal nanoparticles also has been reported by Bazhan and coworkers, where they studied the depolarization of light scattered by a sodium nanoparticle trapped in an electro-optical trap.<sup>174</sup> Calander, Gryczynski, and coworkers reported the depolarized light scattering from colloidal silver nanoparticles.<sup>175-177</sup> They observed strong depolarized scattering around the resonant wavelength of the silver nanoparticles<sup>175,176</sup> and the observation was explained by the interference of surface plasmon resonances.<sup>177</sup> Their model showed that the maximum depolarization occurs between two surface plasmon resonances of anisotropic particles. Khlebtsov and coworkers studied the depolarized light scattering from gold nanorods.<sup>178,179</sup> All their work has been performed on randomly oriented colloidal samples.

In this work, we present studies on the birefringent properties of two-dimensional (2D) ordered arrays of L-shaped silver nanoparticles. The birefringence is discussed from the optical properties of single silver nanoparticle, briefly. A macroscopic birefringent transmission model is also used to rationalize the experimental observations. Presented work suggests that 2D

nanoparticle arrays can provide extremely thin birefringence materials for a designed wavelength region.

## 3.2 Experimental Methods

### 3.2.1 Sample Fabrication and Structural Characterization

EBL was used to fabricate the sample. Detailed fabrication steps are described elsewhere.<sup>180</sup> Briefly, The sample was prepared on 40 nm indium-tin-oxide (ITO) conducting layer on 750  $\mu\text{m}$  thick glass substrates (Thin Film Devices, Anaheim, CA). The 2D nanoparticle pattern was written by a Jeol 9300 FS on the spin-coated resist. After the exposure, the nanoparticle patterns were developed in hexyl acetate, and then Ag metal was deposited through the mask. For all samples the Ag metal thickness was 30 nm, as measured by a quartz crystal microbalance. After the Ag metal deposition, the resist was dissolved in Shipley remover 1165. Two samples were fabricated for this study; one had  $82 \pm 5$  nm arm length with 63 nm arm width and the other had  $92 \pm 5$  nm arm length with 63 nm arm width. The definition of arm length and arm width is illustrated in Figure 3.1B. The samples were fabricated over areas of  $100 \times 100 \mu\text{m}^2$ . EBL fabrication was performed at the MC2 process lab at Chalmers University of Technology.

The structure of the sample was characterized with scanning electron microscopy (SEM). Imaging was performed in the EPIC center at Northwestern University with a Hitachi 4500. Figure 3.1A shows the SEM image of the 82 nm arm length sample. Figure 3.1B describes the axis definition that is used in this paper. The axes along each arm of the nanoparticle are defined as A and B-axis, respectively. The axis along the mirror plane of the L-shaped nanoparticle, i.e.  $45^\circ$  off of the arms of L, is defined as X-axis and the axis perpendicular to the X-axis is defined as Y-axis. The angle  $\theta$  is defined in Figure 3.1B as the angle between X-axis and the

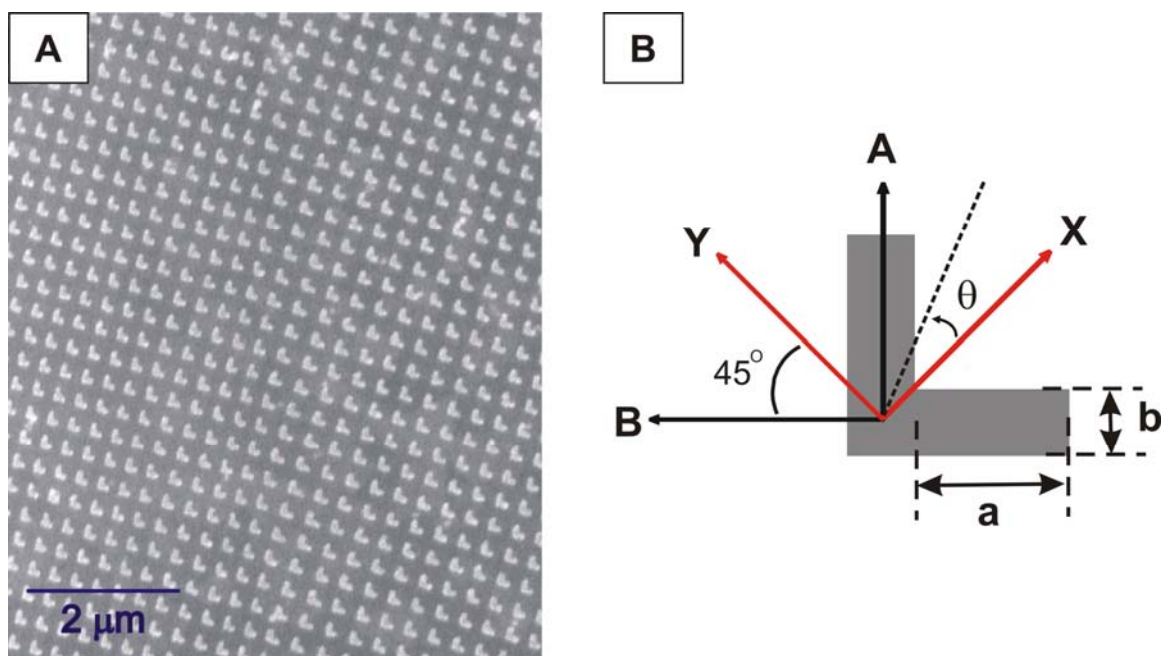


**Figure 3.1** (A) SEM image of two-dimensional array of L-shaped Ag nanoparticles (82 nm arm length, 63 nm arm width, 30 nm height, and 250 nm grid spacing). (B) Definition of each axis (X, Y, A, and B), angle of transmission axis of second polarizer ( $\theta$ ), arm length (a), and arm width (b).

transmission axis of the wire-grid polarizer (P2); where  $\theta$  increases to the counterclockwise as shown in Figure 3.1B.

### 3.2.2 White Light Spectroscopy

Extinction spectra and the intensity of an induced beam with a polarization perpendicular to the incident beam were collected by a spectrometer (SpectraPro 2300i, Roper Scientific) coupled with a liquid nitrogen-cooled charge-coupled device (CCD) camera (Spec-10:400LN, Roper Scientific) for the 600-1100 nm region. Spectra were also obtained with Ocean Optics USB2000 fiber-coupled spectrometer for the 400-950 nm region and a fiber-coupled near-IR spectrometer (NIR 128L-1.7T1-USB, Control Development) for the 900-1700 nm region. The optics arrangement is shown schematically in Figure 3.2. White light from a tungsten-halogen lamp light source was fiber-coupled with a 100  $\mu\text{m}$  fiber to a +40 mm focal length achromatic collimating lens. The collimated beam was then polarized by a Glan-Taylor calcite polarizer (P1) with 5 mm aperture and focused onto a sample by a +12.7 mm focal length achromatic lens with the optic axis normal to the sample surface. Transmitted light was collected by an infinity-corrected 10 $\times$  Nikon microscope objective (NA = 0.30) at a working distance of 16.0 mm and again polarized by VersaLight wire-grid polarizer (P2) before it was focused into a 600  $\mu\text{m}$  fiber that couples into the spectrometer. The white light spot size on the sample was scanned with a straight edge and was close to Gaussian with 20  $\mu\text{m}$  diameter at full width at half-maximum (FWHM).

The sample was mounted on two computer-controlled micro translational stages (M-111.1DG, Physik Instrumente) to form an x-y system with a 50 nm step size. The x-y stage system is fixed on the manual vertical linear stage (MVN50, Newport Corporation) and manual rotational stage (M-UTR120A, Newport Corporation). Rotation of the incident beam

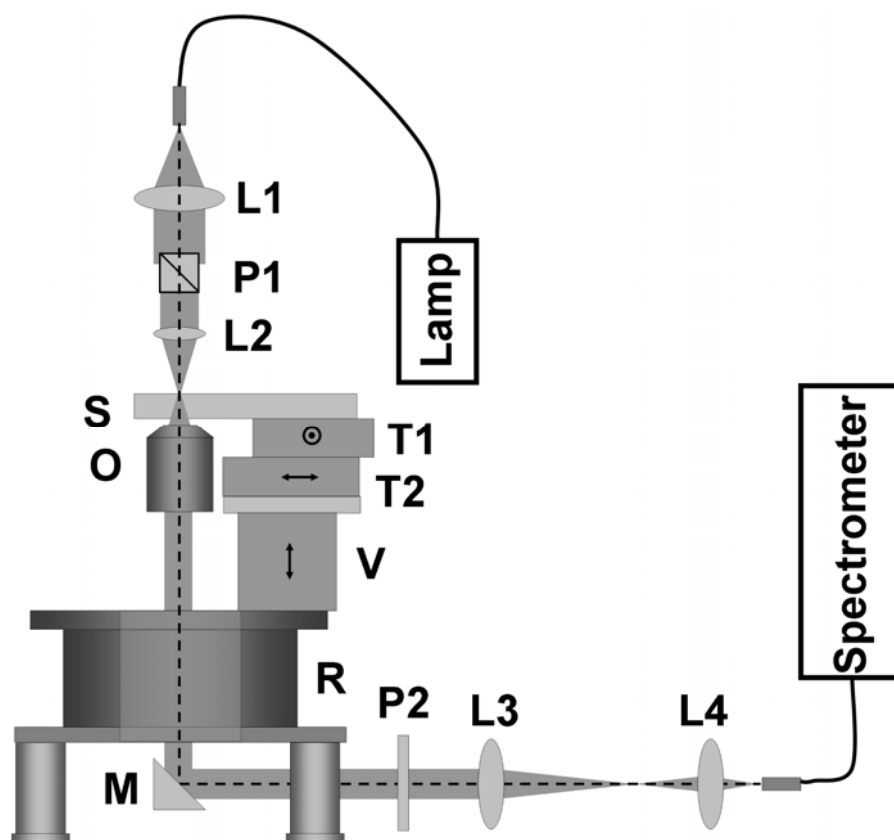


**Figure 3.2** Experimental setup. Symbols represent achromatic lenses (L1-L4), Glan-Taylor calcite polarizer (P1), VersaLight wire-grid polarizer (P2), sample mount and flow cell (S), 10× Nikon microscope objective (O), computer-controlled microtranslational stages (T1 and T2), vertical stage (V), rotational stage (R), and a mirror (M). The focal lengths of achromatic lenses are +40 mm, +12.7 mm, +200 mm, and +30 mm, respectively. The microscope objective is attached to its own manual xyz-translational stage, which is not shown in this figure.

polarization relative to the sample geometry was achieved by rotating the sample stage with fixed incident beam polarization. The white light axis was coincident with the rotational axis of a rotational stage to make the beam position fixed on the sample during sample rotation. All the samples were studied under a stream of dry nitrogen in a flow cell.

To acquire extinction spectra, the transmission axis of the second polarizer (P2) was set parallel to the incident beam polarization. The polarizer setup for this measurement is shown in Figure 3.3A. The transmitted beam intensity through the sample ( $I_{\theta}^{\theta}$ ) was measured and a reference measurement ( $I_{\theta,ref}^{\theta}$ ) was obtained by scanning into a nearby region of the glass substrate. In this section and following sections, the superscript and subscript used with  $I$  and  $T$  are for incident beam (superscript) and detection (subscript) polarization angle or axis. If the signal is obtained on the glass substrate (reference), it is specified in the subscript as *ref*, otherwise, the signal is obtained on the nanoparticle arrays (sample). Extinction ( $E$ ) is defined by  $E = -\log_{10} T_{\theta}^{\theta}$ , where  $T_{\theta}^{\theta} = I_{\theta}^{\theta} / I_{\theta,ref}^{\theta}$ . To measure the intensity of perpendicularly induced components,  $I_{\theta+90}^{\theta}$ , P2 was set perpendicular to the incident beam polarization. The polarizer setup for this measurement is shown in Figure 3.3B. In order to remove the artifacts that come from the imperfection of the polarizers from the perpendicularly induced beam measurements, the following formula is used to obtain transmission with perpendicular component. We correct the signal as  $T_{\theta+90}^{\theta} = (I_{\theta+90}^{\theta} - (I_{\theta+90,ref}^{\theta} \times T_{\theta+90}^{\theta+90})) / I_{\theta,ref}^{\theta}$ , where  $I_{\theta,ref}^{\theta}$  is the intensity measured when the incident beam was on the bare glass substrate and P2 was parallel to P1. The  $I_{\theta+90,ref}^{\theta}$  is the intensity obtained when the incident beam was on bare glass substrate and P2 was perpendicular to P1, and  $T_{\theta+90}^{\theta+90}$  is the transmittance of the nanoparticle array for +90° rotated incident beam polarization.

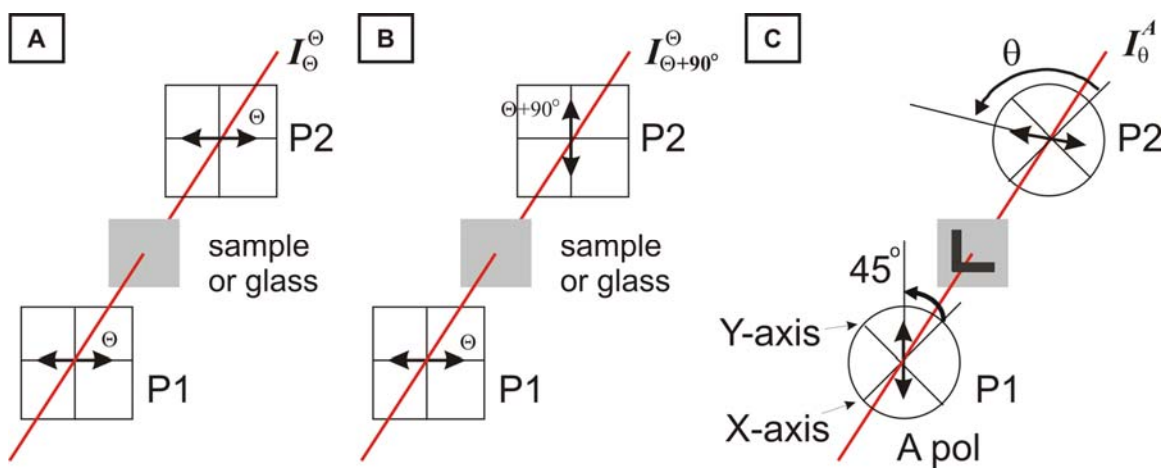


**Figure 3.3** Polarizer setup for (A)  $I_{\theta}^{\theta}$ , (B)  $I_{\theta+90}^{\theta}$ , and (C)  $I_{\theta}^A$  measurements.

### 3.3 Results and Discussion

#### 3.3.1 Perpendicularly Induced Component Measurements

The extinction spectra ( $E = -\log_{10} T_{\theta}^{\theta}$ ) are shown in Figure 3.4 with black solid lines. Incident beam polarization ( $\theta$ ) was X, Y, and A as shown in Figure 3.4A, B, and C respectively. For the extinction measurements, collection beam polarizer (P2) was set parallel to the incident beam polarization. The extinction spectra show high and low energy resonances for X and Y incident beam polarization and this spectrum shows both resonances for in between polarization (A polarization), which is already shown in previous work.<sup>111,113,180</sup> The high and low-energy resonances are at 738 nm and 1029 nm, respectively. The transmission with perpendicularly induced beam ( $T_{\theta+90}^{\theta}$ ) is shown in Figure 3.4 with red solid lines. When the incident beam has either X and Y polarization,  $T_{\theta+90}^{\theta}$  is negligible (<0.3 % of the incident beam intensity). However, when the incident beam has A polarization, significant  $T_{\theta+90}^{\theta}$ , i.e.  $T_B^A$  is observed between 600 and 1500 nm. At 993 nm, the ratio of the induced field intensity ranges up to 6.2 % of the incident field intensity. A similar observation was made for the B polarization (data is not shown).

The observation of perpendicularly induced field can be rationalized as following. The L-shaped nanoparticles have two dipole resonances, one is along the X-axis (high-energy resonance) and the other is along the Y-axis (low-energy resonance). When the incident field impinges on the nanoparticle with the polarization along the X or Y-axis, it only excites the dipole oscillation along X or Y-axis, which results in the induced field oscillation parallel to the incident field polarization. However, when the incident field is along the A or B-axis, it creates dipole oscillation that is a superposition of both X and Y-axis oscillations. The field oscillation along the X and Y-axis has both A and B components, so induced field oscillation by incident

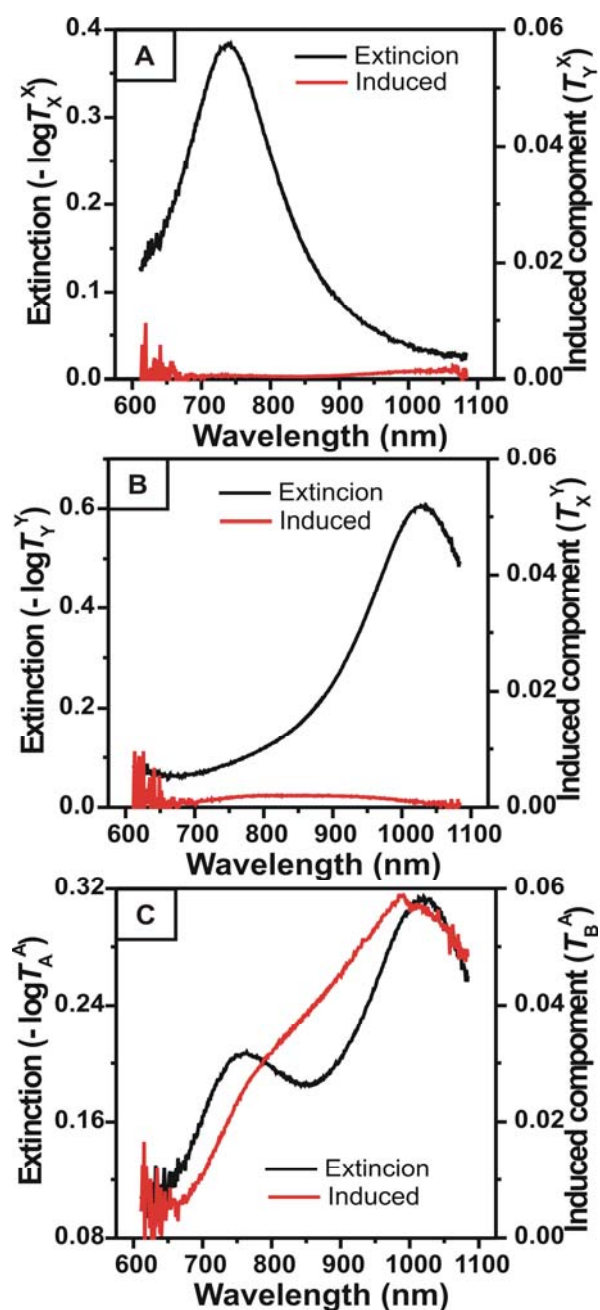


**Figure 3.4** Extinction spectra  $E = -\log_{10} T_{\theta}^{\theta}$  (black line, left axis) and the perpendicularly induced component  $T_{\theta+90}^{\theta}$  (red line, right axis) of 92 nm arm length sample. The polarization of incident beam was along (A) X-axis, (B) Y-axis, and (C) A-axis.

beam polarization along A and B-axis can have perpendicular components of the polarization to the incident beam. The individual nanoparticles are the origin of the effect. However the dipole interactions of nanoparticles in arrays can modify the optical properties of 2D arrays that consist of the nanoparticles, such as resonant wavelength and bandwidth, and this aspect was already discussed in previous paper, in detail.<sup>180</sup>

### 3.3.2 Inadequacy of a Dichroism Model

A dichroism model can be used to test the experimental observations. Here, the nanoparticle array is treated as a single optical element, and all the microscopic information, such as particle shape, size, composition, and array structure, are not taken into consideration. In this section and the following section, the data are obtained from a 92 nm arm length L array with 250 nm grid spacing. The high-energy and low-energy resonances of the sample are located at 738 nm and 1029 nm, respectively, and the intersection of those two bands occurs at 844 nm (Figure 3.5A).

The Jones matrix formalism<sup>181,182</sup> is used for calculating the propagation of polarized light by optical elements. Complex vector amplitude and optical elements are expressed by  $2 \times 1$  column vector and  $2 \times 2$  matrices respectively, and the propagation of the beam polarization by the optical elements is calculated by matrix algebra. The normalized Jones vector for the incident beam with A polarization is  $\frac{1}{\sqrt{2}} \begin{pmatrix} 1 \\ 1 \end{pmatrix}$ .

The Jones matrices of the linear polarizer with a transmission axis along the A and B-axis are  $\frac{1}{2} \begin{pmatrix} 1 & 1 \\ 1 & 1 \end{pmatrix}$  and  $\frac{1}{2} \begin{pmatrix} 1 & -1 \\ -1 & 1 \end{pmatrix}$ , respectively. The Jones

matrix of the nanoparticle array is  $\begin{pmatrix} \sqrt{T_X^X} & 0 \\ 0 & \sqrt{T_Y^Y} \end{pmatrix}$  for the simple dichroism-based model, where

$T_X^X$  and  $T_Y^Y$  are the transmittance for X and Y-polarized incident beam, respectively. Here the

particle is assumed to be perfectly symmetric so there are no off-diagonal terms. Electric fields after the beam passes through the nanoparticle array and the polarizer P2 along the A-axis ( $\vec{\mathbf{E}}_A$ ) and along the B-axis ( $\vec{\mathbf{E}}_B$ ) are as follows:

$$\vec{\mathbf{E}}_A = \frac{1}{2} \begin{pmatrix} 1 & 1 \\ 1 & 1 \end{pmatrix} \begin{pmatrix} \sqrt{T_X^X} & 0 \\ 0 & \sqrt{T_Y^Y} \end{pmatrix} \frac{1}{\sqrt{2}} \begin{pmatrix} 1 \\ 1 \end{pmatrix} = \frac{(\sqrt{T_X^X} + \sqrt{T_Y^Y})}{2\sqrt{2}} \begin{pmatrix} 1 \\ 1 \end{pmatrix}, \quad (3.1a)$$

$$\vec{\mathbf{E}}_B = \frac{1}{2} \begin{pmatrix} 1 & -1 \\ -1 & 1 \end{pmatrix} \begin{pmatrix} \sqrt{T_X^X} & 0 \\ 0 & \sqrt{T_Y^Y} \end{pmatrix} \frac{1}{\sqrt{2}} \begin{pmatrix} 1 \\ 1 \end{pmatrix} = \frac{(\sqrt{T_X^X} - \sqrt{T_Y^Y})}{2\sqrt{2}} \begin{pmatrix} 1 \\ -1 \end{pmatrix}, \quad (3.1b)$$

and transmittances for each system are:

$$T_A^A = |\vec{\mathbf{E}}_A|^2 = \frac{1}{4} (T_X^X + T_Y^Y + 2\sqrt{T_X^X T_Y^Y}), \quad (3.2a)$$

$$T_B^A = |\vec{\mathbf{E}}_B|^2 = \frac{1}{4} (T_X^X + T_Y^Y - 2\sqrt{T_X^X T_Y^Y}). \quad (3.2b)$$

The extinction along A-axis ( $-\log T_A^A$ ) and the perpendicularly induced component  $T_B^A$  calculated by this model are compared with the experimental data in Figure 3.5A and 3.5B, respectively. In Figure 3.5A, the extinction along A-axis ( $-\log T_A^A$ ) calculated by the model (red line) crosses the intersection of extinction of the extinction along X-axis ( $-\log T_X^X$ , black line marked as X) and along Y-axis ( $-\log T_Y^Y$ , black line marked as Y); however the experimental data (black line marked as A) does not. In Figure 3.5B, the induced component along the B-axis,  $T_B^A$  shows a node at 844 nm where the extinction along the A and B-axis crosses (Figure 3.5A), but the experimental data does not show such a node.

The simple dichroism-based model accounts for some of the observed features, but it deviates from experiment at predicting the property of the light transmission where the two dipole bands cross.

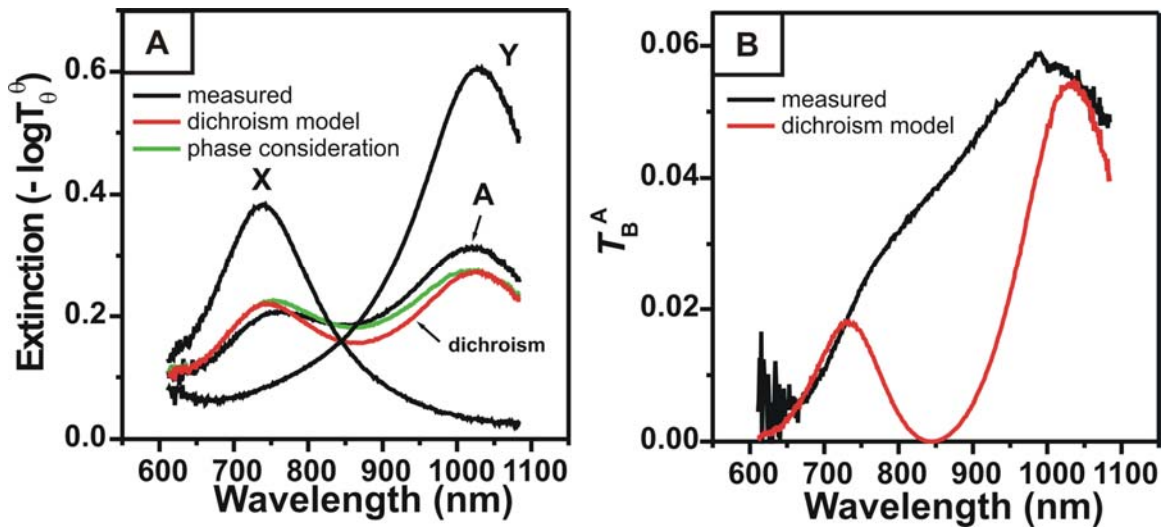


**Figure 3.5** (A) Experimentally obtained extinction spectra  $E = -\log_{10} T_{\theta}^{\theta}$  for X, Y, and A-polarized incident beam (black lines), and extinction spectra for A-polarized incident beam obtained by simple dichroism-based model (red line) and by birefringence model (green line). (B) Perpendicularly induced component  $T_{\theta+90}^{\theta}$  that is obtained experimentally (black line) and by dichroism-based model (red line).

### 3.3.3 Birefringence Model

In the previous section, when the Jones matrix for the nanoparticle array is constructed, the phase retardation was not considered or it was assumed that the phase retardation for both X and Y-axis was same, therefore the light was still linearly polarized after it passed through the nanoparticle array as shown in Equation 3.1. The phase retardation can be introduced in the Jones matrix. If the phase retardation along X-axis is  $\varphi_x$  and along the Y-axis is  $\varphi_y$ , the Jones

matrix for the nanoparticle array becomes  $\begin{pmatrix} \sqrt{T_X^X} e^{i\varphi_x} & 0 \\ 0 & \sqrt{T_Y^Y} e^{i\varphi_y} \end{pmatrix}$ . The Jones vector after the X-

polarized incident beam pass through the nanoparticle array becomes  $\frac{1}{\sqrt{2}} \begin{pmatrix} \sqrt{T_X^X} e^{i\varphi_x} \\ \sqrt{T_Y^Y} e^{i\varphi_y} \end{pmatrix}$ , and in case

$\varphi_x \neq \varphi_y$ , it is no longer a linearly polarized beam. If the transmission axis of P2 is set  $\theta$ , after the beam passes P2 the electric field vector becomes

$$\vec{\mathbf{E}}_{\theta} = \frac{1}{\sqrt{2}} \begin{pmatrix} \sqrt{T_X^X} \cos^2 \theta e^{i\varphi_x} + \sqrt{T_Y^Y} \sin \theta \cos \theta e^{i\varphi_y} \\ \sqrt{T_X^X} \sin \theta \cos \theta e^{i\varphi_x} + \sqrt{T_Y^Y} \sin^2 \theta e^{i\varphi_y} \end{pmatrix}. \quad (3.3)$$

Then the transmittance of whole system ( $T_{\theta}^A$ ) is:

$$T_{\theta}^A = |\vec{\mathbf{E}}_{\theta}|^2 = \frac{1}{2} \left[ T_X^X \cos^2 \theta + T_Y^Y \sin^2 \theta + 2\sqrt{T_X^X T_Y^Y} \sin \theta \cos \theta \cos \varphi \right], \quad (3.4)$$

where  $\varphi = \varphi_x - \varphi_y$ . Note that if  $\varphi$  is zero, Equation 3.4 becomes identical to Equation 3.2. When

$\theta$  is  $+45^\circ$  (A-axis) and  $-45^\circ$  (B-axis), it becomes Equation 3.2a and 3.2b, respectively.  $T_X^X$ ,  $T_Y^Y$ ,

and  $T_{\theta}^A$  are experimentally measurable parameters, and  $\theta$  is experimentally controlled by

adjusting the P2 transmission axis, therefore the phase difference for two axis  $|\varphi|$  can be

obtained by Equation 3.4. For  $\theta = -45^\circ$  (B-axis), where the transmission axis of P2 is set

perpendicular to the incident beam polarization along A-axis ( $\theta = +45^\circ$ ), the transmittance

becomes  $T_{-45}^A = T_B^A = \frac{1}{4} \left[ T_X^X + T_Y^Y - 2\sqrt{T_X^X T_Y^Y} \cos \varphi \right]$ , therefore the phase difference  $|\varphi|$  can be obtained as follows:

$$|\varphi| = \arccos \left[ \frac{T_X^X + T_Y^Y - 4T_B^A}{2\sqrt{T_X^X T_Y^Y}} \right]. \quad (3.5)$$

The red solid line in Figure 3.6A shows the phase difference  $|\varphi|$  versus wavelength plot obtained by Equation 3.5. The two main dipole bands are shown with black lines for comparison. The significant phase difference is obtained between two main dipole bands, and the maximum phase difference ranges up to 28°.

From the  $|\varphi|$  obtained here, the extinction along A-axis can be calculated from Equation 3.4 ( $\theta = +45^\circ$ ) and the result is plotted in Figure 3.5A with green line. It does not cross the intersection of the two dipole bands, which agrees with the experimental observation (black line) better than the plot based on the simple dichroism-based model (red line).

### 3.3.4 Transmission with Resolved Linear Polarization

To characterize the beam after the nanoparticle array, the beam intensity was monitored by the Ocean Optics spectrometer while the transmission angle of the P2 ( $\theta$ ) was rotated for an incident beam polarization fixed along the A-axis. This polarizer setup is shown in Figure 3.3C. For this measurement, the 82 nm arm length L array with 250 nm grid spacing was tested. The high-energy and low-energy resonance of this array is located at 704 nm and 929 nm respectively, and the intersection of those two bands happens at 789 nm (not shown in this paper). The  $\theta$ -dependent beam intensity ( $T_\theta^A$ ) is plotted in Figure 3.7 with red square and it is compared with the calculation based on Equation 3.4 (black line) for selected wavelengths; 450, 701, 720, and 770 nm. The calculation used a phase difference  $|\varphi|$  of 0°, 14°, 23°, and 32°, respectively.

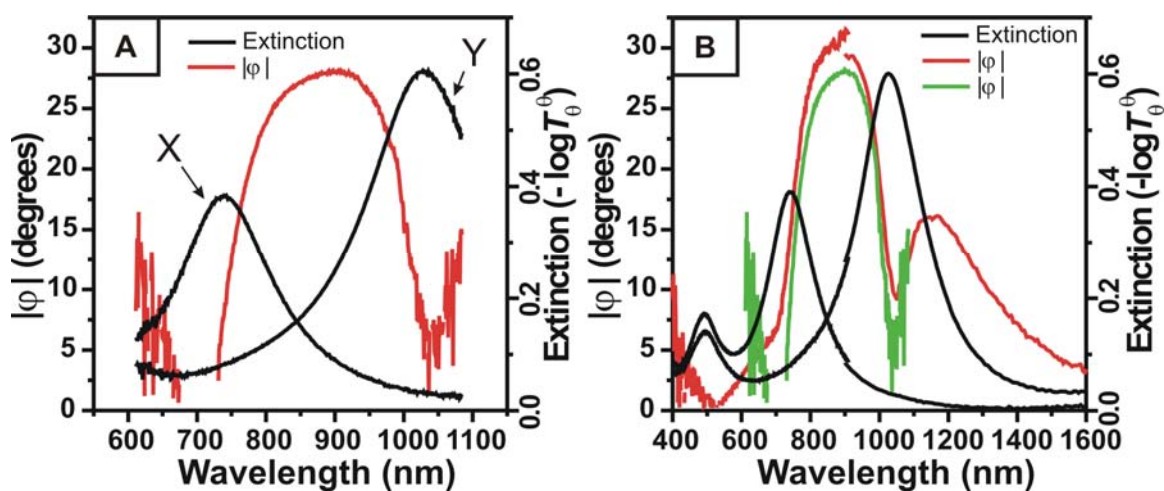


**Figure 3.6** The wavelength dependent phase difference ( $|\varphi|$ ) is plotted with red line (left axis). Extinction spectra for the X and Y-polarized incident beam are shown with black lines for comparison, plotted to right axis. The measurements are performed by (A) spectrometer coupled with liquid nitrogen-cooled CCD detector and (B) UV-vis and near-IR spectrometers.  $|\varphi|$  plot of panel A is shown in panel B again with green line for comparison.

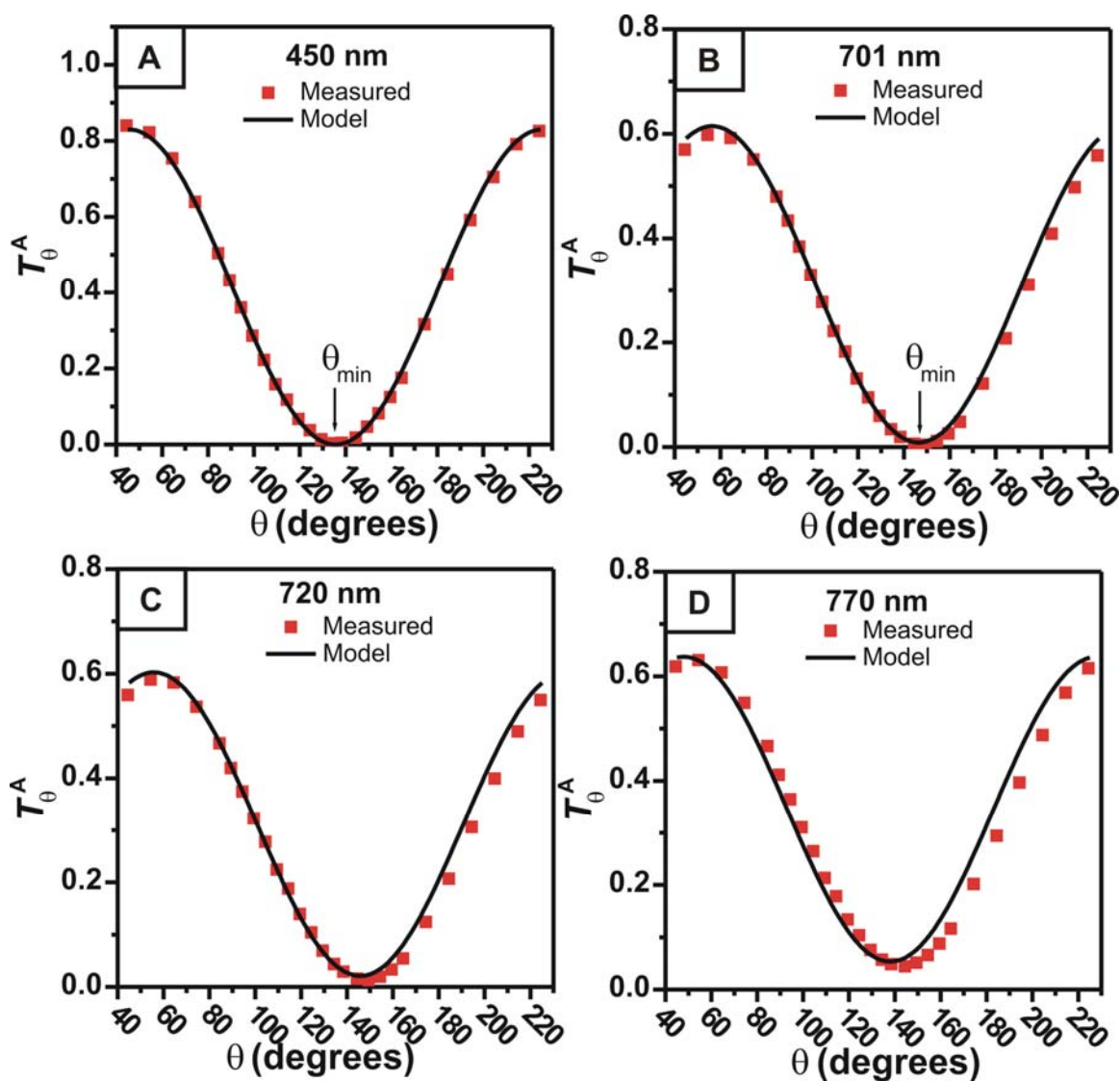


**Figure 3.7** Experimentally obtained collection polarizer angle ( $\theta$ )-dependent signal intensities ( $T_{\theta}^A$ ) from 82 nm arm length sample are plotted with red dots for (A) 450 nm, (B) 701 nm, (C) 720 nm, and (D) 770 nm wavelengths. Calculations by birefringence model are plotted with black line.

$\theta = 45^\circ$  is achieved when the transmission axis of the P2 is along the A-axis (parallel to the incident beam polarization) and  $\theta = 135^\circ$  corresponds to when the transmission axis of the P2 is along B-axis (perpendicular to the incident beam polarization). There is a little deviation of the experimental plot from the calculation, but their behavior is quite close each other. A slight difference in arm length of the particle that came from the imperfection of the fabrication is thought to be the source of the observed deviation.

The  $\theta$  that shows the minimum transmission ( $\theta_{min}$ ) for fixed wavelength, as marked in Figure 3.7, is determined by the ratio between the transmission for X and Y-axis;  $T_X^X$  and  $T_Y^Y$ . If their ratio is unity, the angle should be  $135^\circ$ ; as the ratio deviates from unity,  $\theta_{min}$  moves to higher angle. At 450 nm, where  $T_X^X$  and  $T_Y^Y$  are similar, the minimum transmittance is observed at about  $135^\circ$  polarizer angle. The wavelength of 701 nm is close to the high-energy band resonance, therefore the transmission for X and Y-polarization shows a large difference at this wavelength and the  $\theta_{min}$  moves to larger angle. However, as the wavelength is moved to 720 nm and 770 nm, the difference between  $T_X^X$  and  $T_Y^Y$  decreases, and the  $\theta_{min}$  moves back toward  $135^\circ$ . The minimum transmission is correlated to the phase difference  $|\varphi|$ . If  $|\varphi|$  is zero, the beam is still linearly polarized after it passes through the nanoparticle array, therefore the minimum transmission after P2 becomes zero (Figure 3.7A). If  $|\varphi|$  is nonzero, the beam becomes elliptically polarized after the nanoparticle array and the minimum transmission deviates from zero as shown both in experimental plot and calculation in Figure 3.7B,C,D.

The polarization of the beam after the sample is graphically represented in Figure 3.8. As  $|\varphi|$  decreases, the polarization becomes close to linear and as it increases, the polarization

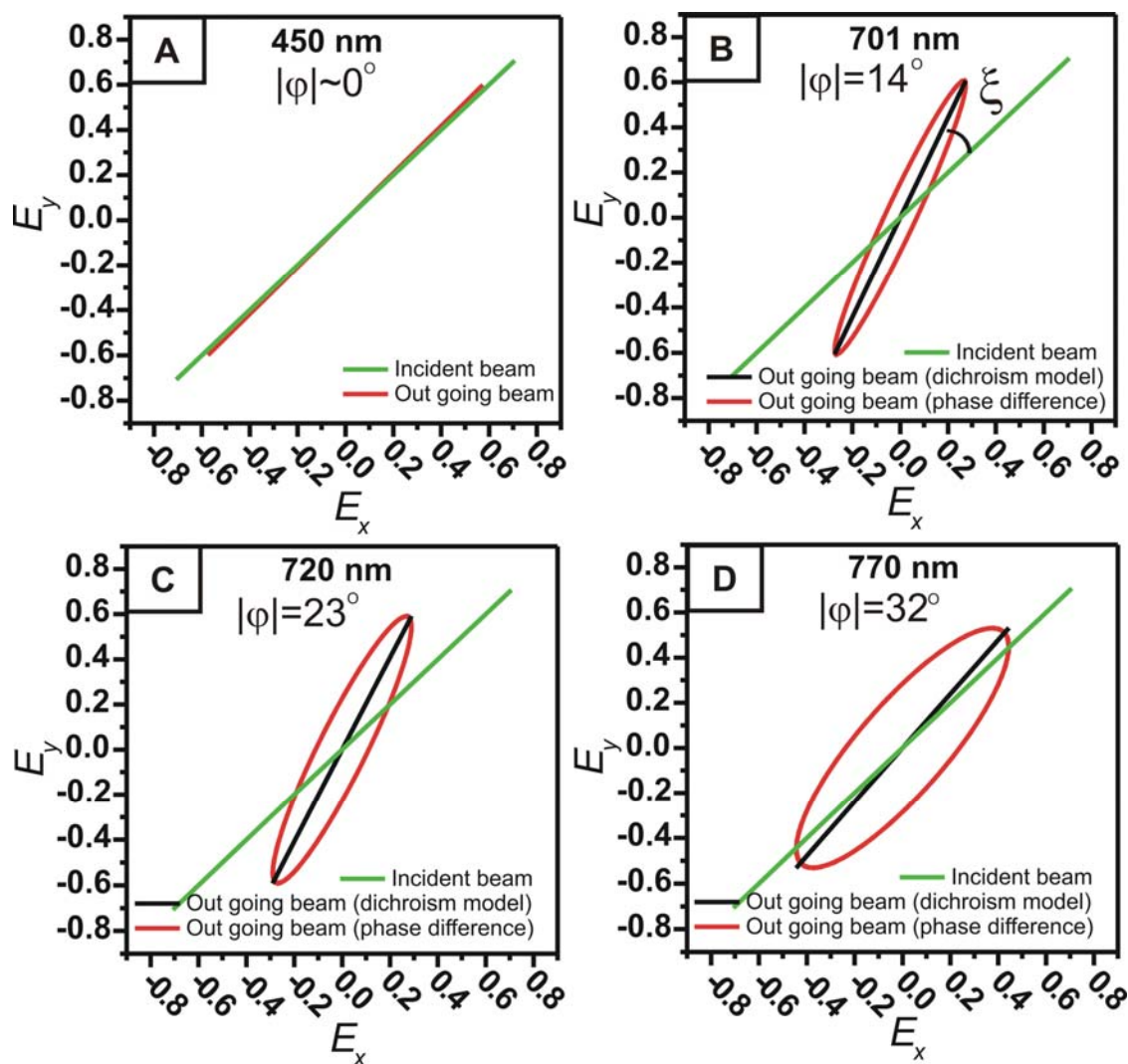


**Figure 3.8** The polarization of the beam after the nanoparticle array is calculated by simple dichroism-based model (black plot) and birefringence model (red plot) for (A) 450 nm, (B) 701 nm, (C) 720 nm, and (D) 770 nm wavelength beam. The polarization of the incident beam is shown with green line for comparison.  $\xi$  is the rotation angle of the polarization axis after the beam pass through the nanoparticle arrays.

becomes closer to circular. As discussed previously, the angle  $\xi$  that is shown in Figure 3.8 is determined by the ratio between  $T_X^X$  and  $T_Y^Y$ , and they are related by following equation:

$$\xi = \left| \arctan \sqrt{\frac{T_Y^Y}{T_X^X}} - \frac{\pi}{4} \right|. \quad (3.6)$$

### 3.3.5 Phase Difference Predicted from the Complex Index of Refraction

In Figure 3.6A, the phase difference  $|\varphi|$  shows minima near 700 nm and 1050 nm, but they are not resolved well because of the low signal to noise ratio. To resolve these features,  $T_X^X$ ,  $T_Y^Y$ , and  $T_A^A$  are obtained by Ocean Optics USB2000 fiber-coupled spectrometer for the 400-950 nm region and a fiber-coupled near-IR spectrometer for the 900-1700 nm region.  $|\varphi|$  and extinction are obtained based on the measurements and the results are plotted in Figure 3.6B. The extinction spectra for X and Y polarized beam is plotted with black lines and  $|\varphi|$  is plotted with red line. A slight mismatch near 900 nm signifies where one spectrometer ends and the other begins.  $|\varphi|$  in Figure 3.6A is plotted with green line for comparison. The local  $|\varphi|$  minimum near 1050 nm is clearly shown and another local maximum of  $|\varphi|$  is shown near 1200 nm.

These local minimum and maximum can be qualitatively explained by considering the complex index of refraction of the nanoparticle array. An L-shaped nanoparticle has two strong dipole resonances that are perpendicular each other, and each dipole mode shows different extinction for each incident beam polarization, therefore the nanoparticle array has different refractive index for two orthogonal polarizations. The diagram of the imaginary and real part of the refractive index is shown in Figure 3.9A,B. The imaginary part,  $\kappa$  is related to the extinction and the peak position is determined by resonance frequency of both high and low energy band,

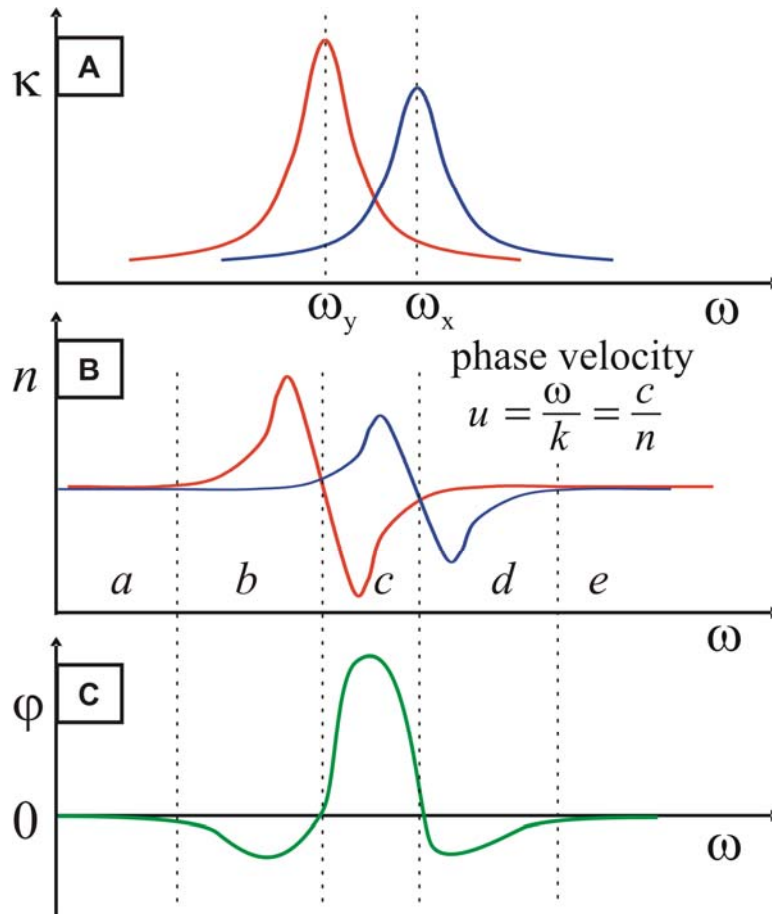


**Figure 3.9** Diagram of (A) imaginary part ( $\kappa$ ) and (B) real part ( $n$ ) of the refractive index of the nanoparticle array. Five distinct frequency areas are labeled with from  $a$  to  $e$ . (C) Estimated  $\phi$  from the panel B. Inset in panel B:  $u$  is phase velocity,  $\omega$  is angular frequency,  $k$  is wave vector, and  $c$  is speed of light.

$\omega_x$  and  $\omega_y$  respectively (Figure 3.9A). The corresponding real part,  $n$  is shown in Figure 3.9B, and it determines phase velocity,  $u$ , by the equation inset in Figure 3.9B. The difference in phase velocity between the two optical axes determines the phase difference  $\varphi$ . In frequency region  $a$  and  $e$  in Figure 3.9B, there is no phase difference because the phase velocity for X- and Y-polarized light are same. However, birefringence is shown in frequency region  $b$ ,  $c$ , and  $d$  because of the phase velocity difference for two orthogonal polarization axes. The polarity of phase difference in  $c$  is different from in  $b$  and  $d$ , therefore at the boundary between  $b$  and  $c$  and between  $c$  and  $d$ , the phase difference should be zero (Figure 3.9C). In our experiment,  $|\varphi|$  instead of  $\varphi$  is measured, therefore regions  $b$ ,  $c$ , and  $d$  should have each local maximum and there should be nodes between each maximum. The maximum  $|\varphi|$  is expected to be observed at region  $c$  because maximum difference in phase velocity is expected in the region. Above arguments explain some of the features in Figure 3.6B, such as maximum  $|\varphi|$  near 900 nm, local maximum near 1200 nm and a node near 1050 nm. However there are some disagreements. The local maximum expected at highest frequency region is not observed distinctly. A distinct node is observed near 1050 nm, but it does not hit zero value. A possible explanation of these discrepancies is the imperfection of the nanoparticles.  $|\varphi|$  is obtained under the assumption of perfect symmetry of the nanoparticle. However, there is slight asymmetry because of imperfection of the fabrication, which can cause the error in the estimation of  $|\varphi|$ . Furthermore, if there is a deviation in the nanoparticles size, each nanoparticle has slightly different refractive index, and the sharp node can be smeared out by average of all particles. Finally, small signal artifacts in  $T_X^X$ ,  $T_Y^Y$ , and  $T_A^A$  during the experimental measurements also can lead to the deviation of the modeled  $|\varphi|$  from the actual value. The modeling in Figure 3.9 considered only

two main dipole bands. However there is another spectral feature at 500 nm as shown in Figure 3.6B and it might interfere with the node at high energy side that is predicted by the simple model and obscure the node.

Even though this crude model does not match exactly with experimental observations, it qualitatively explains the feature of experimentally obtained  $|\varphi|$  and also provides insights into the birefringence of nanoparticle array.

### 3.3.6 2D Array of L-Shaped Nanoparticles as a Birefringence Material

In the case of conventional birefringence crystals, such as calcite and quartz, absorption is at UV region, therefore they have almost constant refractive index in visible region where we are interested in, as shown in Figure 3.10A. Because of the anisotropy of crystal structure (Figure 3.10B), birefringence crystals have different resonant frequencies along X- and Y-axis, which leads to the different refractive indices  $n_x$  and  $n_y$  along each axis. The phase difference  $|\varphi|$  is given by:<sup>181</sup>

$$|\varphi| = \frac{2\pi}{\lambda_0} d (|n_x - n_y|) \quad (3.7)$$

where  $\lambda_0$  is wavelength in vacuum and  $d$  is thickness of the crystal.  $|\varphi|$  can be tuned by changing  $d$  in order to obtain a quarter waveplate ( $|\varphi| = 90^\circ$ ) or a half waveplate ( $|\varphi| = 180^\circ$ ). In the case of nanoparticle arrays tested in this study, the maximum phase retardation was  $30^\circ$ , therefore quarter waveplate cannot be obtained. Furthermore, transmittance is low compared to the conventional birefringence crystals because there is strong absorption in the wavelength region where we are interested in. Even though there are some restrictions in using the nanoparticle arrays as birefringence materials, there are many interesting aspects. The nanoparticle arrays have high birefringence only within a particular wavelength range

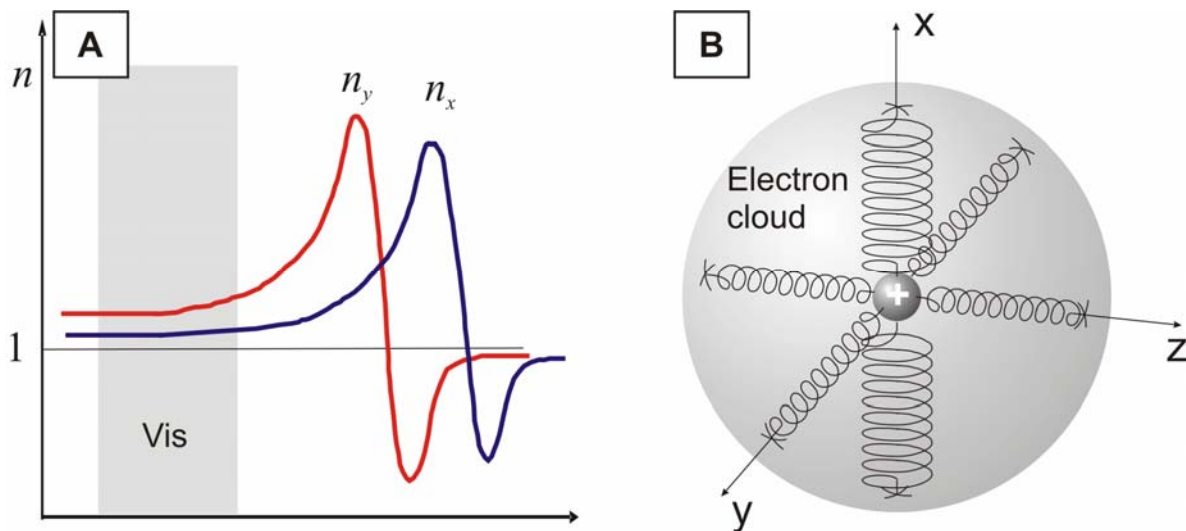


**Figure 3.10** (A) Diagram of the refractive index (real part) of conventional birefringence materials.  $n_x$  and  $n_y$  are refractive index along X- and Y-axis, respectively. (B) Electron cloud bound to a nucleus. The diagram depicts the different restoring force along X- and Y-axis for a birefringence crystal with single optic axis (X-axis).

characteristic of the overlapping resonances. Any particle shape that has two orthogonal dipole resonances such as an ellipse or rectangle is expected to show similar birefringence properties. The wavelength range of maximum phase difference can be tuned by varying the two dipole resonances. These dipole resonances can be varied by changing the size, aspect ratio, and composition of the nanoparticles.<sup>4,21,147</sup> In the case of noble metal nanoparticles, the dipole resonance red-shifts as the refractive index of surrounding increases,<sup>4,134,142</sup> therefore the dipole resonance position also can be tuned by varying the refractive index of surrounding media. In order to generate 30° phase difference between two orthogonal polarizations, at 590 nm wavelength, typical birefringence materials, such as quartz, calcite, and calomel requires 7.3 μm, 388 nm, and 98 nm, respectively. However, the silver nanoparticle arrays demonstrated in this paper show about 30° phase difference with 30 nm thickness silver nanoparticles with 92 nm and 82 nm arm length at 850 nm and 780 nm wavelength, respectively, which suggests the possibility of the nanoparticle arrays as a wavelength-tunable, extremely thin birefringence materials. Future work will be focused on improving birefringence properties of nanoparticle arrays. In order for real application, achievement of 90° of  $|\varphi|$  which gives quarter waveplate is important. Higher particle density, changing particle shape, and fabrication with different materials can be tried to increase  $|\varphi|$ . Further theoretical studies are also required to explore the optimum condition for the application.

### 3.4 Conclusion

The perpendicularly induced component from the incident beam polarization was measured for L-shaped nanoparticle arrays with height of 30 nm. A significant amount of perpendicularly induced component was observed for A-polarized incident beam between two main dipole resonances of nanoparticle array and the ratio was 6.2% of the incident beam at 993

nm. The A-polarized incident beam can excite dipole oscillations along both X and Y-axis, and as a result, induced field oscillation can have the component of polarization that is perpendicular to the incident beam polarization. However, the perpendicularly induced component was negligible when the incident beam polarization was along X and Y-axis, the direction of two main dipoles of the L-shaped nanoparticle, because the field oscillation along X-axis cannot excite dipole oscillation along Y-axis, and visa versa. The experimental observation was also modeled by a dichroism-based model and a birefringence model, and the birefringence model agrees well with the experimental data. The linearly polarized incident beam along the A-axis is changed to an elliptically polarized beam after it passes through the nanoparticle arrays as a consequence of phase retardation along X and Y-axis. This effect depends on wavelength. The polarization of the outgoing beam is determined by the transmittance along X and Y-axis ( $T_X^X$  and  $T_Y^Y$ ) and phase difference along each axis ( $|\phi|$ ). The maximum phase difference was observed in between two overlapping dipole resonance wavelengths, and it was about  $30^\circ$  for 2D arrays of L-shaped nanoparticle with thickness of 30 nm and this phase difference is high compared to the conventional birefringence materials with same thickness. This study is expected to provide a step toward the development of new plasmonic birefringence materials.

## **Chapter 4**

### **Second Harmonic Excitation Spectroscopy of Silver Nanoparticle Arrays**

## 4.1 Introduction

Current interest in the optical properties of nanoscale materials is driven by a broad spectrum of technological applications, including bio/chemosensors,<sup>114-117</sup> optical filters,<sup>118,119</sup> plasmonic waveguides,<sup>23,120-122</sup> and substrates for surface-enhanced molecular spectroscopy.<sup>5,123,124</sup> Noble metal nanoparticles are particularly well-suited for applications in a wide variety of fields due to their size, shape and environment sensitive localized surface plasmon resonance (LSPR) bands. Current fabrication methods allow LSPR energies and widths of individual particles<sup>134,183-187</sup> and ordered arrays<sup>3,125,126,188</sup> to be tuned with high precision. Many applications use the linear optical response of the LSPR modes. Fundamental studies of nonlinear optical properties represent a relatively new method of studying nanoparticle properties.

Experimental studies of second-order optical properties for metal nanoparticles were reported for colloids dispersed in solution,<sup>105,106,109,189-191</sup> embedded in a dielectric matrix,<sup>101,102,104</sup> and supported on a substrate.<sup>79,111,139,192-196</sup> These investigations include measurements of both hyper-Rayleigh scattering (HRS)<sup>105,106,189,190</sup> and coherent second harmonic generation (SHG).<sup>79,101-104,111,139,192-196</sup> Hupp and co-workers<sup>105</sup> reported the first experimental distinction between electric dipole and quadrupole contributions to HRS for solutions of spherical 32 nm silver nanoparticles by comparing angularly resolved emission to predictions of a theoretical model. In addition, nanoparticle enhanced SHG was recently studied for a fluorescent polymer adsorbed on 100 nm gold particles.<sup>48</sup>

Several theoretical studies have been reported for particles with simple geometric shapes.<sup>79,197-203</sup> Specific treatments include a hydrodynamic model for an electron gas,<sup>198</sup> a quantum size effect formulation for conduction electrons,<sup>199</sup> and an extension of the continuous

dipole model<sup>204</sup> to a sphere in an inhomogeneous longitudinal field.<sup>205</sup> Most predictions for complex shapes are made by assuming an intensity independent nonlinear response, which is expressed as the product of linear susceptibilities.<sup>134</sup> A general formalism for arbitrarily shaped particles in inhomogeneous dielectric environments is not yet available. The second harmonic (SH) signals from silver films are consistent with a general form of the second-order susceptibility and a tight-binding basis set.<sup>206-208</sup> The SH signals from the nanoparticle arrays are analyzed by considering general multipolar interaction mechanisms.

In this work, linear and nonlinear optical properties of silver nanoparticle arrays fabricated by nanosphere lithography (NSL)<sup>3,4,188,209</sup> are characterized. NSL is an inexpensive, simple to implement, inherently parallel, high throughput, materials general, and size-controllable fabrication technique capable of producing well-ordered two-dimensional nanoparticle arrays.<sup>4,147</sup> The NSL-fabricated substrates as a platform for bio/chemosensors<sup>8,35,114,134</sup> and a substrate for surface-enhanced spectroscopy<sup>5,210</sup> have been demonstrated. There have been studies to correlate the LSPR of the NSL-fabricated substrate to the surface-enhanced Raman excitation spectroscopy (SERES) profile by Van Duyne and co-workers.<sup>5,40</sup> They showed that the strongest surface-enhanced Raman scattering (SERS) enhancement occurs under conditions where the incident and Raman scattered photons are both strongly enhanced,<sup>5</sup> and it is consistent with prediction of the electromagnetic enhancement mechanism.<sup>211</sup>

In this study, extinction spectra and SHG were measured for various orientations and polarizations, and the coherent SHG was studied with a tunable femtosecond laser. The fundamental beam was not resonant with the material, whereas the emitted frequency was tuned in the region of the LSPR to identify resonance behavior. The SHG from a silver film was

measured to compare with the array SHG at every wavelength, which allows experimental parameter normalization. Experimental observations were compared with theoretical calculations that were performed by a discrete dipole approximation (DDA) method.

## 4.2 Experimental Methods

### 4.2.1 Sample Preparation

Fisher brand no. 2, 18 mm diameter glass coverslips (Fisher Scientific, Fairlawn, VA) were used as substrates. Glass substrates were cleaned by immersion in a boiling piranha solution (3:1 concentrated  $\text{H}_2\text{SO}_4$ : 30%  $\text{H}_2\text{O}_2$ ) for 30 min. (CAUTION: *Piranha reacts violently with organic compounds and should be handled with great care.*) After cooling, the substrates were thoroughly rinsed repeatedly with  $18.2 \text{ M}\Omega \text{ cm}^{-1}$  Millipore water (Marlborough, MA). The substrates were then sonicated for 1 h in 5:1:1  $\text{H}_2\text{O}:\text{NH}_4\text{OH}:30\%\text{H}_2\text{O}_2$ . Following sonication, the substrates were rinsed with copious amounts of Millipore water. Surfactant free, white carboxyl-substituted 390 nm diameter polystyrene latex nanospheres were received as a suspension in water from Duke Scientific (Palo Alto, CA), whereas 510 nm and 590 nm nanospheres were purchased from Interfacial Dynamics (Portland, OR). Absolute ethanol was purchased from Pharmco (Brookfield, CT). Silver (99.99%) was purchased from D.F. Goldsmith (Evanston, IL).

Single-layer nanoparticle arrays were prepared with the nanosphere lithography technique.<sup>3,4</sup> The nanoparticle geometry, and therefore the LSPR, can be controlled by the selection of the nanosphere diameter ( $D$ ) and the deposited metal thickness ( $d_m$ ). A suspension of nanospheres spontaneously self-assembled into hexagonally closed-packed two dimensional arrays after being coated on a clean glass substrate. Once the sphere masks were dry, half of the mask was removed to leave an area of bare glass where the film would be deposited. Silver was

deposited at a rate of  $0.1 \text{ nm s}^{-1}$  with a Consolidated Vacuum Corporation (Rochester, NY) deposition system or with a Kurt J. Lesker Axxis electron beam deposition system (Pittsburgh, PA) with a base pressure of  $10^{-6}$  Torr. The deposited height was monitored with a XTM/2 monitor quartz crystal microbalance (Leybold Inficon, East Syracuse, NY). The silver deposition had been made by two steps. In the first step, the area for the silver film where the sphere mask was removed was masked with aluminum foil and silver was deposited with desired particle height (30 – 60 nm). In the next step, the nanoparticle portion of the cover slip was masked and 50 nm of silver film was deposited. On the day of optical measurements, the nanosphere masks were removed by sonication in absolute ethanol for approximately 5 min. NSL fabrication procedure is illustrated in Figure 4.1.

#### 4.2.2 Structural Characterization of NSL-fabricated Nanoparticle Arrays

AFM images were collected with a Digital Instruments Nanoscope III microscope operated in tapping mode with etched Si nanoprobe tips (Digital Instruments, Santa Barbara, CA). These tips have resonance frequencies between 280 and 320 kHz, are conical in shape with a cone angle of  $20^\circ$ , and an effective radius of curvature at the tip of 10 nm. Figure 4.2 shows an AFM image of a typical sample prepared with  $D = 390$  nm nanospheres. This image and earlier studies by nanosphere lithography support the dimensional properties of each nanoparticle as a truncated tetrahedron. The triangular base of each tetrahedron has a perpendicular bisector of  $\sim 90 - 100$  nm, and the nanoparticles form hexagonal arrays around the 390 nm diameter of the nanosphere. The geometric relationships have been previously described<sup>4,188</sup> in terms of the nanosphere diameter,  $D$ . The triangular base has a perpendicular bisector  $a$  that equals  $0.233D$  and the interparticle center-to-center spacing,  $d_{ip}$ , equals  $0.577D$ . Figure 4.2 demonstrates that the pattern is composed of pairs of tetrahedra in defect free sections of the surface, which is

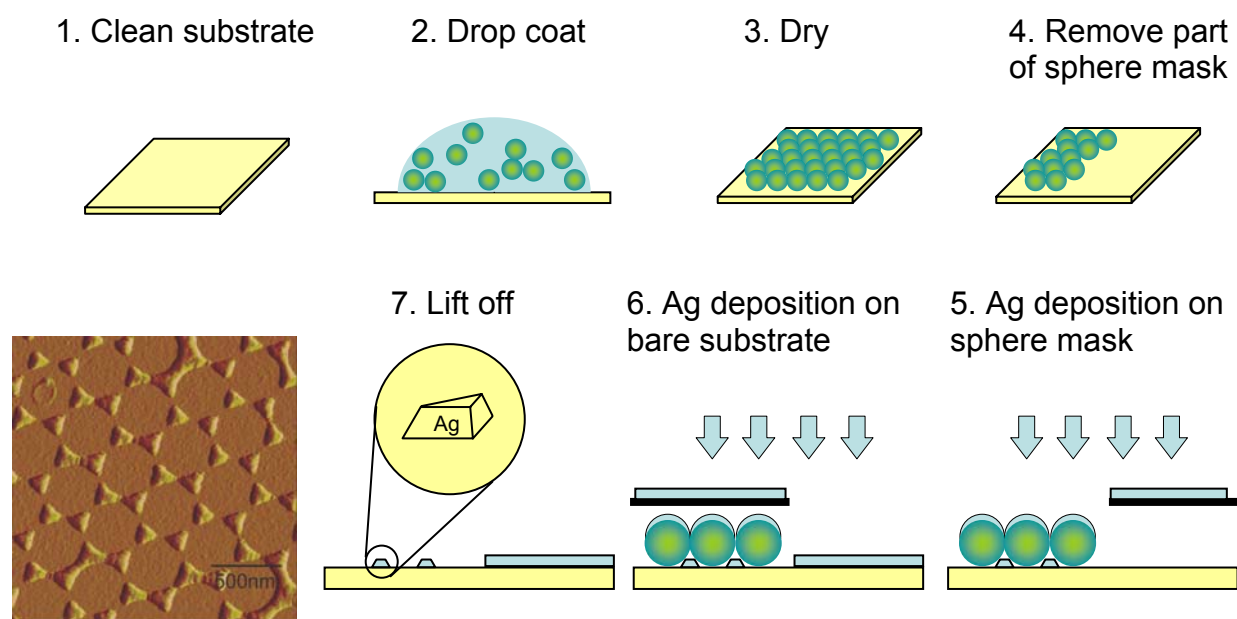


**Figure 4.1** Nanosphere lithography (NSL).

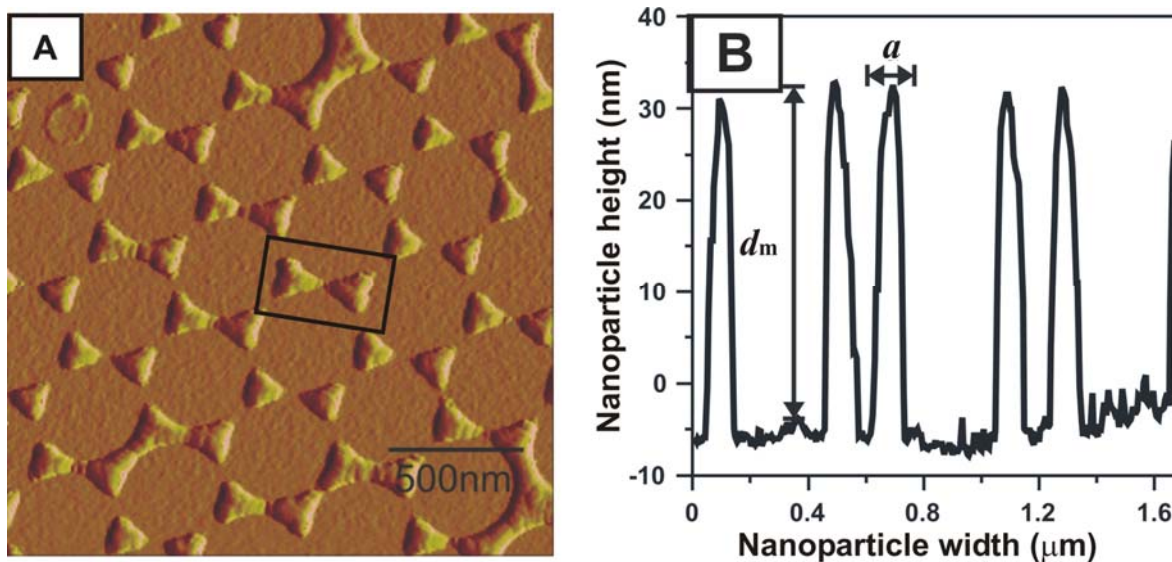


**Figure 4.2** (A) AFM image of a sample prepared with a nanosphere diameter ( $D$ ) of 390 nm. The perpendicular bisector,  $a$ , of the triangular base is 100 nm, and the interparticle distance is 294 nm. The box depicts the centrosymmetry of particle pairs present in the sample. (B) A line scan of the sample in panel A shows  $a = 104$  and  $d_m = 52$  nm.

important for discussing the SHG properties.<sup>4,212</sup> The particle arrays have a number of defects which have been described, but not correlated with optical properties. The size of defect free regions is unknown, but prior work suggests they are probably small ( $\sim 10 \mu\text{m}$ ) so that with a  $125 \mu\text{m}$  spot size in our experiments we cannot assume uniform symmetry through the whole area that is illuminated.

### 4.2.3 Extinction Measurements

The optical design used to measure extinction is shown in Figure 4.3. A continuum ( $\sim 400 - 900 \text{ nm}$ ) generated by a tungsten-halogen light source was focused to a spot size of  $600 \mu\text{m}$  (FWHM) at the sample with an achromatic lens. A Glan-Taylor calcite polarizer was used to control incident light polarization. Sample orientation (normal,  $45^\circ$ , and  $70^\circ$  incidence) was varied with a graduated manual rotational mount. Extinction spectra were collected with an optical-fiber-coupled Ocean Optics model USB2000 spectrometer. With a nominal height of  $50 \text{ nm}$  the  $390 \text{ nm}$ ,  $510 \text{ nm}$  and  $590 \text{ nm}$  sphere diameters gave extinctions peaking at  $620 - 630 \text{ nm}$ ,  $720 - 750 \text{ nm}$ , and  $840 - 850 \text{ nm}$ , respectively.

### 4.2.4 SHG Measurements

Experiments were carried out with an amplified Ti:Sapphire laser system.<sup>213</sup> Figure 4.4 shows the schematic of the instrumentation for SHG measurements. The laser system consists of a mode-locked femtosecond Ti:Sapphire oscillator<sup>214</sup> and a pulse stretcher/regenerative amplifier/pulse compressor<sup>215,216</sup> for producing high power ultrafast laser pulses. A continuous wave (CW) frequency-doubled diode pumped Nd:YVO<sub>4</sub> laser (Millennia, Spectra Physics) pumped the oscillator with  $2.80 \text{ W}$ . The oscillator output pulses were centered at  $800 \text{ nm}$  with a repetition rate of  $83 \text{ MHz}$  and  $85 \text{ mW}$  of average power ( $\sim 1.0 \text{ nJ/pulse}$ ). A faraday isolator was used before a grating pulse stretcher and then the stretcher output was injected into the

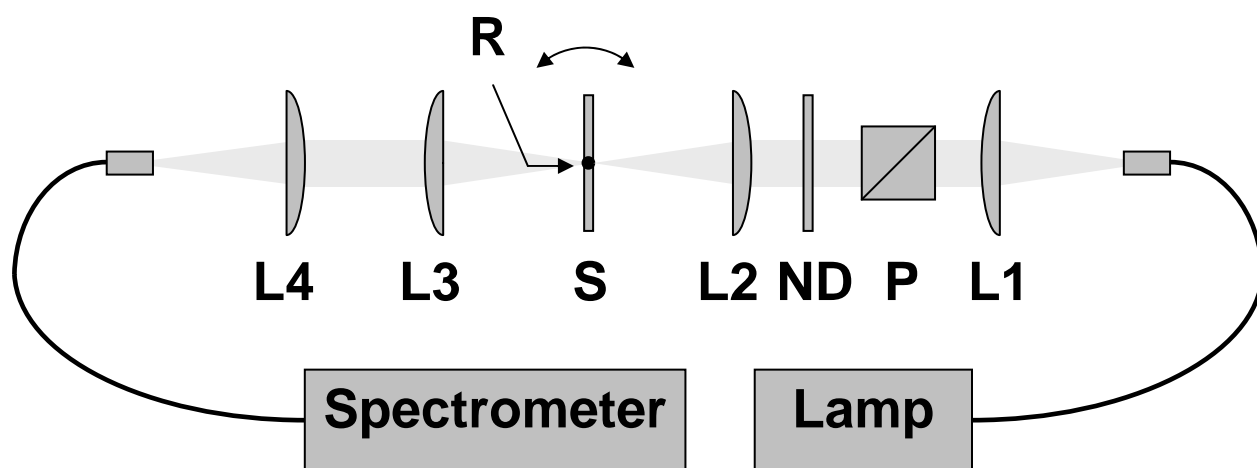


**Figure 4.3** Experimental design used for extinction measurements. Symbols represent achromatic lenses (L1-L4), polarizer (P), neutral density filter (ND), sample (S), and a rotational axis for the sample (R).

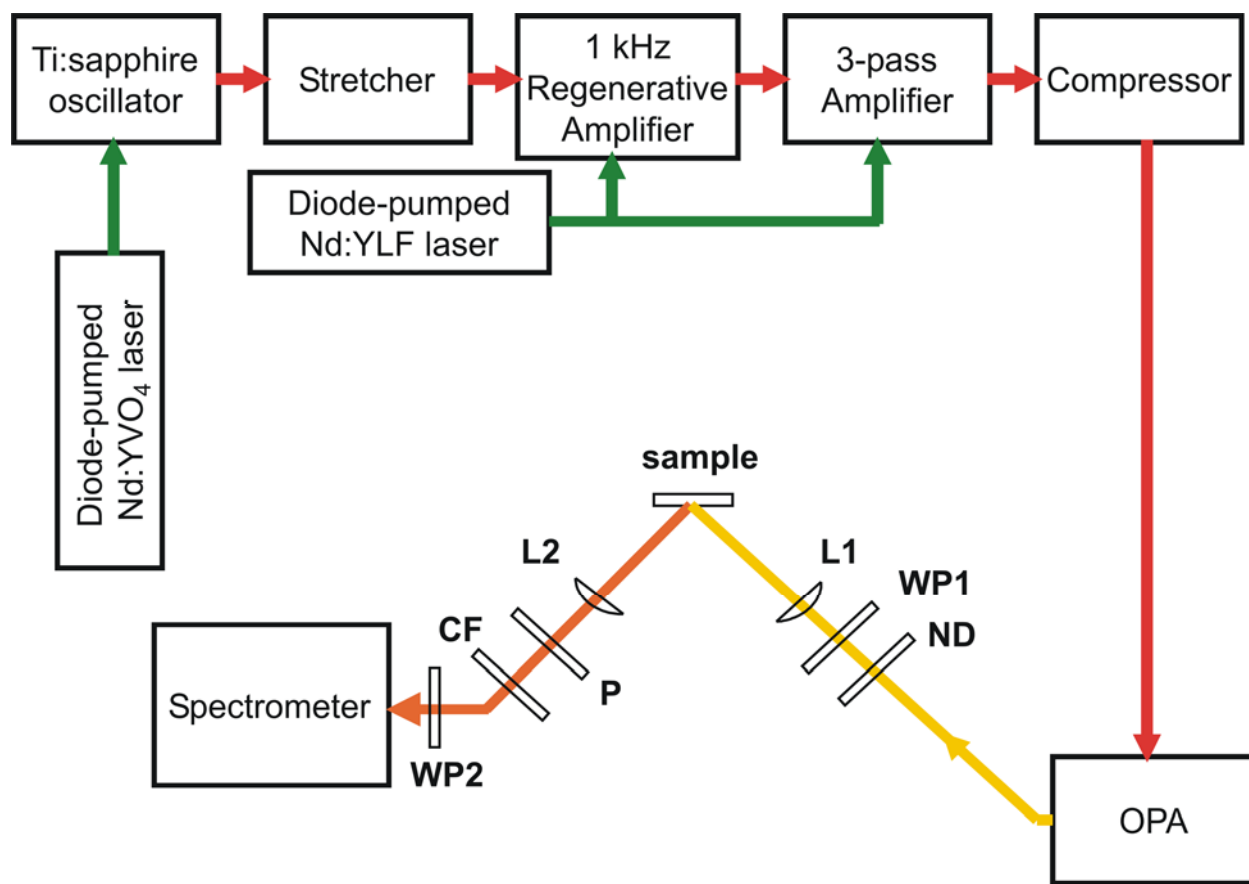


**Figure 4.4** Schematic of the femtosecond laser system. Symbols represent a neutral density filter (ND),  $\lambda/2$  waveplates (WP1, WP2), focusing and collimating lenses (L1, L2), and a short pass color filter (CF).

regenerative amplifier with a 10% reflection. The regenerative amplifier was pumped with an average power of 5.9 W split from a Q-switched, frequency-doubled, Nd:YLF laser (Evolution-30, Spectra Physics) with  $\sim 250$  ns pulses at 527 nm and a 1 kHz repetition rate. The amplifier cavity-switched output was 850 mW of 805 nm pulses at 1 kHz. A 3-pass amplifier (Photonics Industries) before the pulse compressor provided additional amplification with little added dispersion. The 3-pass amplifier was pumped with 9.66 W from the Nd:YLF laser to provide 1.8 W of 805 nm pulses at a 1 kHz repetition rate. The amplified beam was sent to a grating compressor. The output of the compressor was centered at 805 nm with a spectral bandwidth of 22 nm and pulse duration of 90 fs at 1 kHz. A tunable near-IR fundamental beam was generated with a laboratory-built optical parametric amplifier (OPA) pumped by 650  $\mu\text{J}/\text{pulse}$  of the amplified Ti:Sapphire laser beam. The total near-IR output of the OPA was 50  $\mu\text{J}/\text{pulse}$  (signal + idler). A polarizer separated the signal and idler pulses. The duration and bandwidth of the signal pulse is 125 fs and  $430\text{ cm}^{-1}$  (at  $1.3\ \mu\text{m}$ ). Pulse energy was controlled with neutral density filters.

The SHG experimental configuration is shown in Figure 4.5. The fundamental was focused to  $125\ \mu\text{m}$  ( $\sim 100,000$  particles) with a +20 cm focal length  $\text{CaF}_2$  lens at incident angles of  $10^\circ$  and  $45^\circ$ . Polarization was varied with an achromatic (1000 – 1600 nm)  $\lambda/2$  waveplate. The SHG signal was collected with a +10 cm focal length lens, and then passed through a thin film polarizer and a short-pass color filter (Schott KG-3 or Corning 1-69) before being focused into a spectrometer (SpectraPro 2300i, Roper Scientific) coupled with a liquid nitrogen-cooled charge-coupled device (CCD) camera (Spec-10:400LN, Roper Scientific). Apertures were used to prove that the output SHG signal was in a coherent beam.

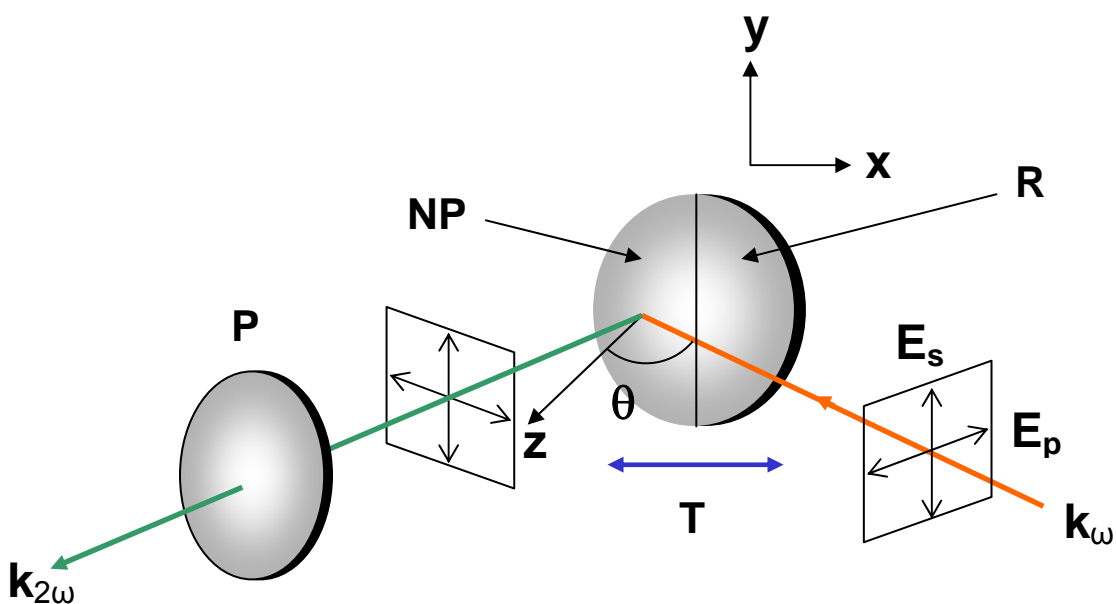


**Figure 4.5** Configuration used for SHG measurements. A coordinate system is also defined. Symbols represent the incidence angle ( $\theta$ ), Ag nanoparticle arrays (NP), Ag film reference (R), polarizer (P), and translational stage (T). Polarization notation as s:s or p:p is used to refer to input/output polarization.

Both p-polarized and s-polarized emissions were recorded while the fundamental beam was tuned from 1.16  $\mu\text{m}$  to 1.52  $\mu\text{m}$ . The fundamental beam was focused to four spots on the sample by translating the sample stage. The sample stage was oriented to translate parallel to the sample plane, so the detection alignment was equivalent for all positions on the sample. Two of the four spots were on the nanoparticle array, while the other two were on the smooth film. This procedure was designed to minimize changes in detection alignment between the nanoparticle array and silver film reference.

#### 4.2.5 Theoretical Calculations

The discrete dipole approximation (DDA) method<sup>57,217,218</sup> was utilized to model the in-plane and out-of-plane mode of Ag nanoparticles. The nanoparticle shape is assumed to be a truncated tetrahedron. Following parameters are used to perform the calculation;  $a = 118$  and  $137$  nm (in-plane perpendicular bisector),  $d_m = 30, 40, 50,$  and  $60$  nm (out-of-plane height), and DDA grid spacing =  $2$  nm. The in-plane perpendicular bisectors of  $118$  and  $137$  nm can be achieved when the diameter of sphere mask that is used in NSL fabrication is  $510$  and  $590$  nm, respectively. The effect of the glass on the LSPR was treated using the effective medium theory.<sup>219</sup> Incident fields with in-plane and out-of-plane polarization are tested.

### 4.3 Results and Discussion

#### 4.3.1 Extinction Measurements

Typical polarization and orientation dependent extinction measurements are shown in Figure 4.6. Spectra recorded at normal,  $45^\circ$  and  $70^\circ$  incidence are shown, but absolute magnitude comparisons are only approximate. Each preparation leads to slightly different results in shape and peak location as a function of angle, and different spots in the same sample are not exactly identical. The angle tuning changes the sample area illuminated, so we expect some

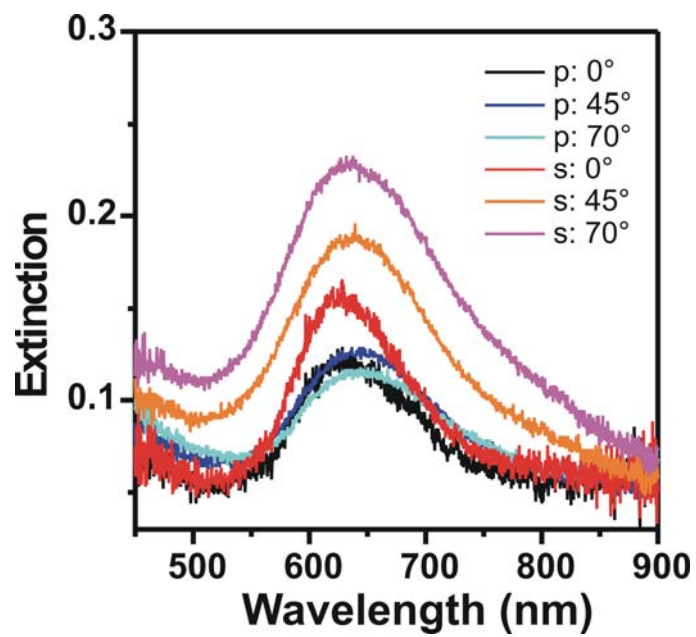


**Figure 4.6** Polarization and orientation dependent extinction spectra. The magnitudes are approximate.

spectral variation as a function of angle. The spectra in Fig 4.6 show no large changes in resonance wavelength, which is of interest for later discussion. The dominant feature at 630 nm in Figure 4.6 is assigned to an in-plane dipolar mode. An out-of-plane dipolar mode is not observed because of its weak extinction.

Figure 4.7 and Figure 4.8 shows the measured and calculated LSPR  $\lambda_{\max}$  as a function of nanoparticle height ( $d_m$ ). Extinction was measured for  $D = 390, 510,$  and  $590$  nm samples, and DDA calculation was performed for  $D = 510$  and  $590$  nm samples. All the measurements and calculations were performed with normal incident beam condition. Both measurement and calculation show that for the same in-plane dimension, the  $\lambda_{\max}$  blue-shifts as  $d_m$  is increased and for the same  $d_m$ , the  $\lambda_{\max}$  red-shifts as in-plane dimension increases, which is consistent with previous reports.<sup>146,147</sup> However, there is significant difference between measured and calculated  $\lambda_{\max}$ . In the case of  $D = 590$  nm (Figure 4.7C and 4.8B), the difference ranges up to 150 nm, and in all cases, the experimental data shows larger  $\lambda_{\max}$  than the calculation. A water layer formation on nanoparticle arrays during the experiment can be a plausible explanation for the red-shifted  $\lambda_{\max}$  in the experimental observation compared to the calculation. If the water layer is formed on nanoparticles the refractive index of nanoparticle surrounding increases, which leads to the red-shift of the LSPR.

### 4.3.2 Nanoparticle Annealing

Noble metal nanoparticles can be annealed with a high power laser beam,<sup>220-223</sup> so measurements were made to ensure that the fluence used for studying SHG was not within this regime. A 300  $\mu\text{m}$  pinhole was placed over a sample and extinction spectra were measured before and after irradiation with a near-IR beam ( $\lambda = 1300$  nm). A fraction (45 or 65 %) of the near-IR beam was allowed to pass through the pinhole. No change in the spectrum was observed

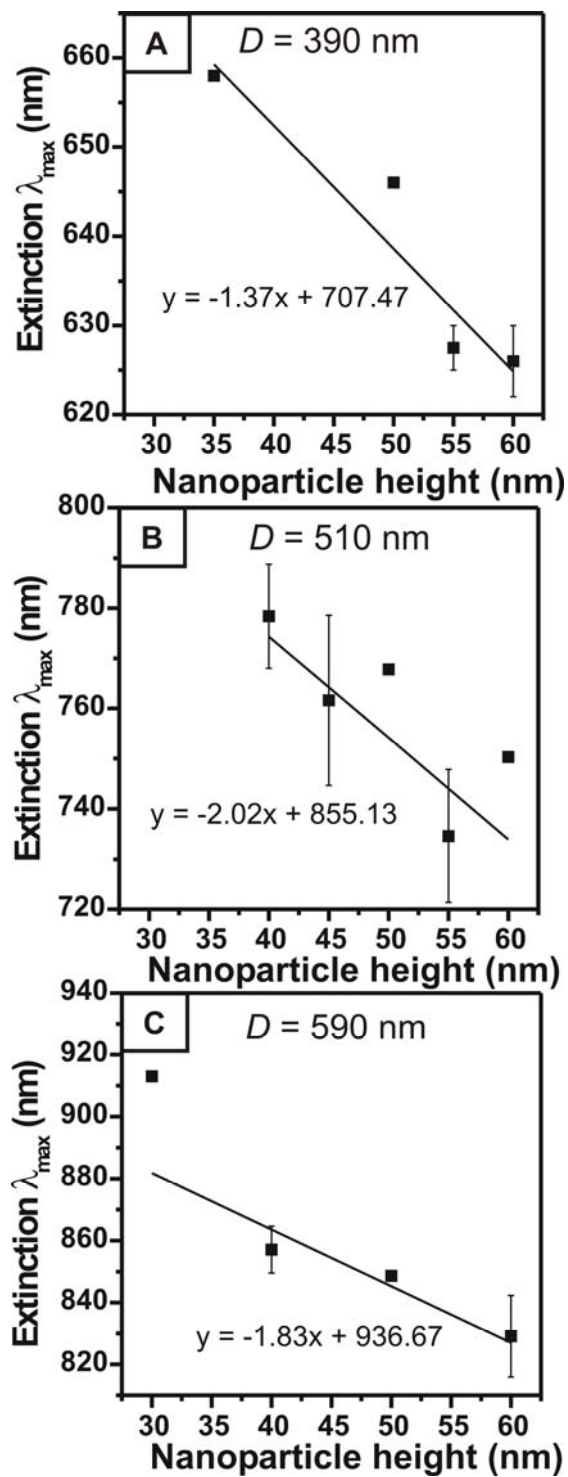


**Figure 4.7** Experimentally obtained LSPR  $\lambda_{\max}$  versus nanoparticle height ( $d_m$ ). Nanosphere diameter  $D$  was (A) 390 nm, (B) 510 nm, and (C) 590 nm.

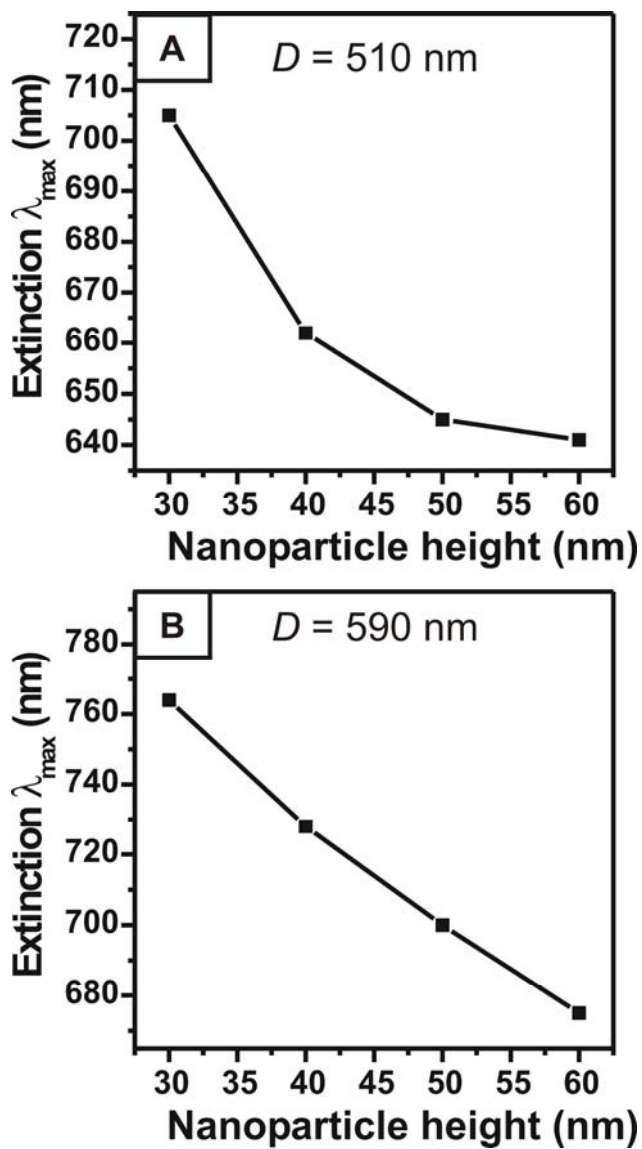


**Figure 4.8** LSPR  $\lambda_{\max}$  calculated by DDA method versus nanoparticle height ( $d_m$ ). Nanosphere diameter  $D$  was (A) 510 nm and (B) 590 nm.

at fluences below  $4.4 \text{ mJ cm}^{-2}$ , which corresponds to a power of  $300 \text{ }\mu\text{W}$  for our SHG experimental setup (beam spot size of  $125 \text{ }\mu\text{m}$  FWHM at the focus and  $1 \text{ kHz}$  repetition rate). However, the extinction peak blue shifted by  $\sim 20 \text{ nm}$  after irradiation at a fluence of  $7.00 \text{ mJ cm}^{-2}$ , corresponding to a power of  $750 \text{ }\mu\text{W}$ . SHG intensity versus incident power was also directly tested, and a logarithmic plot deviated from linearity after  $\sim 400 \text{ }\mu\text{W}$ . Both results assure that the sample is safe until  $300 \text{ }\mu\text{W}$  with a power threshold of about  $400 \text{ }\mu\text{W}$ . The power used for SHG measurements in following section was  $\sim 100 \text{ }\mu\text{W}$  (pulse energy of  $100 \text{ nJ}$ ), corresponding to a fluence of  $1.46 \text{ mJ cm}^{-2}$  through the central 25 % area of the focus spot.

### 4.3.3 SHG Excitation Spectra

We begin this section by briefly reviewing the resonance structure of the second-order response. The second-order susceptibility can be stated as a product of linear susceptibilities<sup>73,75</sup>

$$\chi_{ij}^{(2)}(2\omega; \omega, \omega) = -\frac{mb}{N^2 e^3} \chi_{ii}^{(1)}(2\omega) [\chi_{jj}^{(1)}(\omega)]^2 \quad (4.1)$$

where  $m$  is the electron mass,  $b$  is a nonlinear coefficient,  $N$  is the plasma electron density, and  $e$  is a unit charge. The linear susceptibilities,  $\chi_{ij}^{(1)}(\omega)$ , are written in tensor form with indices  $ij$  that represent electric field polarizations and frequency arguments that represent the fundamental ( $\omega$ ) and emitted waves ( $2\omega$ ). The frequency dependence of SHG enhancement can be predicted by Equation 4.1. In the absence of centrosymmetric SHG cancellation, the resonance enhancement in our case should result from the  $\chi_{ii}^{(1)}(2\omega)$  factor since the fundamental frequency is far from any linear resonance; the SHG excitation profiles should exhibit maxima at the peak positions seen in the linear extinction spectra.

SHG excitation profiles measured for p:p (fundamental/SH emission) polarization conditions at incidence angle of  $45^\circ$  and  $10^\circ$  for  $D = 510 \text{ nm}$  and  $d_m = 50 \text{ nm}$  sample are shown

in Figure 4.9A,B. Extinction spectra of the sample obtained by polarized beam with normal incidence are shown together. The SHG enhancement is plotted versus SH wavelength. The enhancement factor is the ratio of the SH signal from the nanoparticle array divided by SH from the silver film and is not normalized for the reduced particle area (~9.3 % coverage of the film). The measurements with 45° and 10° incidence angle shows similar profile, but the absolute signals (not shown) were 7-15 times stronger for 45° incidence angle measurement, although alignment variations made accurate quantification difficult. The SHG enhancement of 10° incidence angle is higher than 45° even though absolute SHG signal is small, because, when the incidence angle is varied from 45° to 10°, decrease in absolute SHG signal in film is larger than in nanoparticle arrays.

A peak in the p:p SHG efficiency was found for  $D = 510$  nm and 590 nm samples (Figure 4.9). The extinction maxima are located at longer wavelengths than the laser tuning range (SH of 1.16 – 1.52  $\mu\text{m}$ ) or at red end of the range. The peak was blue-shifted with respect to the extinction peak.  $D = 390$  nm samples have the extinction maxima within laser tuning range, however no distinct peak was found and overall SHG efficiency was small compared to  $D = 510$  nm and 590 nm samples (Figure 4.10). Figure 4.9A,B show that both 45 and 10° angles of incidence give similar SH profiles for the p:p experiment. There is greater opportunity at 10° than at 45° to excite in-plane dipole components, but the similar resonance behavior supports the hypothesis that this resonance is dominated by an out-of-plane transition.

Figure 4.11A,B shows the SHG enhancement profile versus nanoparticle height ( $d_m$ ) for  $D = 510$  nm and 590 nm, respectively. The wavelength, where the SHG enhancement maximum is observed, increases as the  $d_m$  increases for both nanoparticle sizes, which is opposite of the

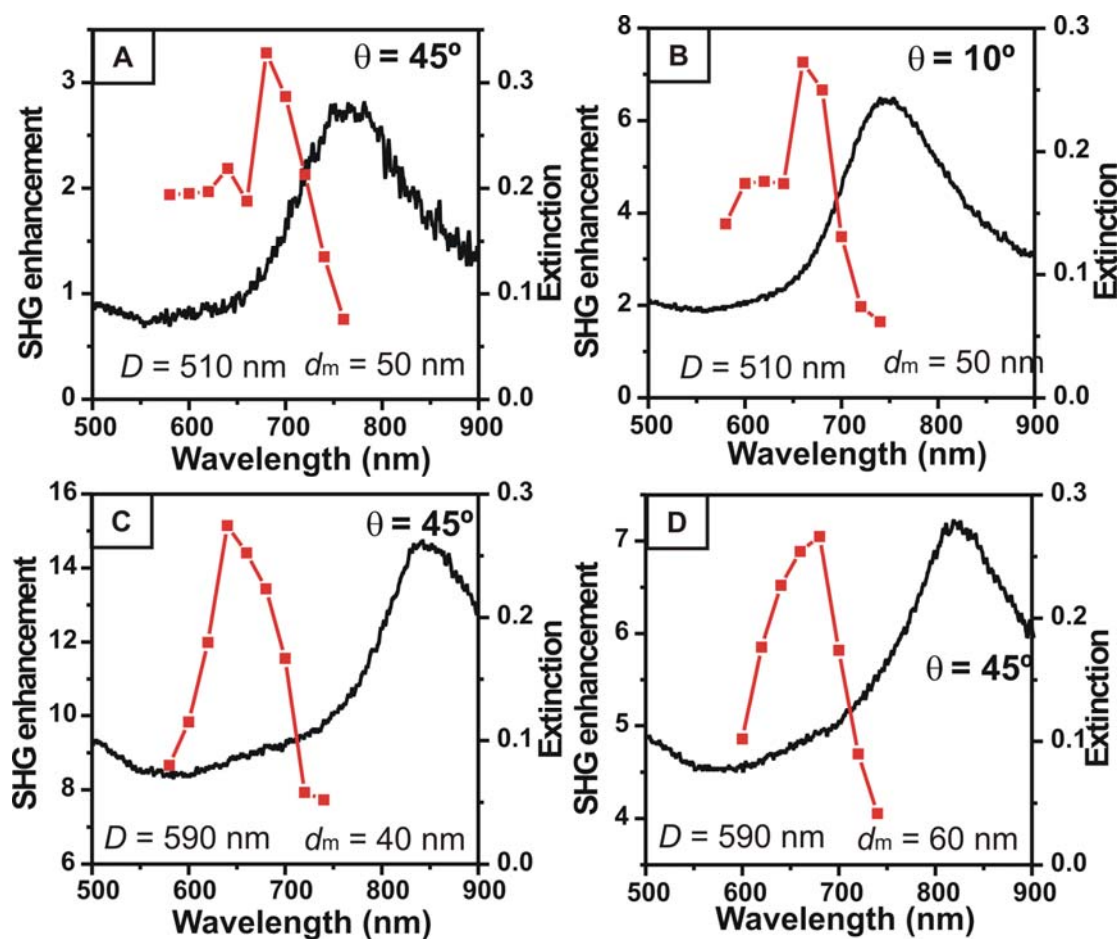


**Figure 4.9** The extinction spectra (black line) and the SHG enhancement profiles (red square plots) for  $D = 510$  nm and  $590$  nm samples. (A)  $D = 510$  nm,  $d_m = 40$  nm, incidence angle  $\theta = 45^\circ$ , (B)  $D = 510$  nm,  $d_m = 40$  nm,  $\theta = 10^\circ$ , (C)  $D = 590$  nm,  $d_m = 40$  nm,  $\theta = 45^\circ$ , and (D)  $D = 590$  nm,  $d_m = 60$  nm,  $\theta = 45^\circ$ .

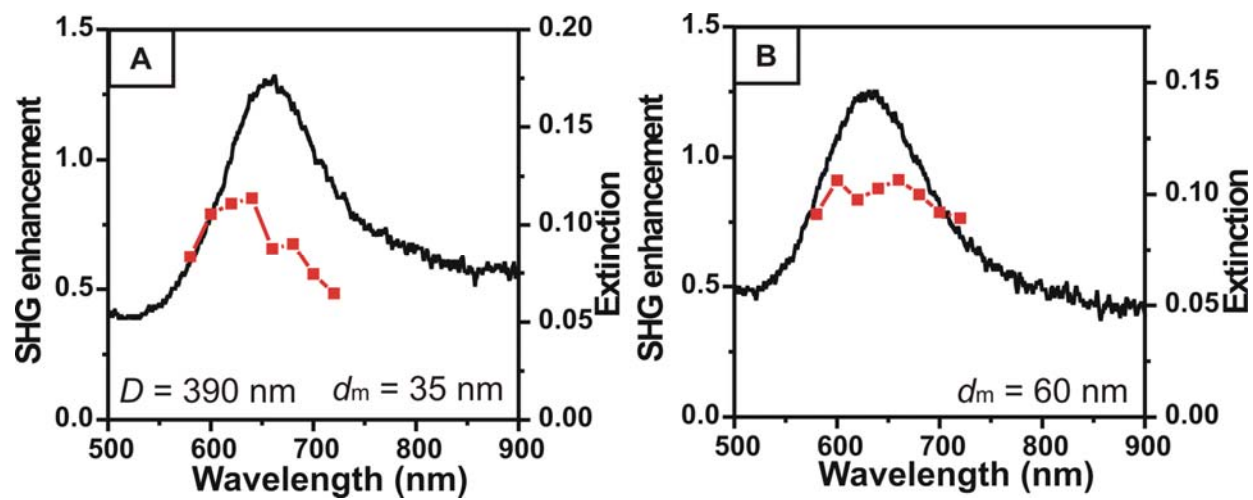


**Figure 4.10** The extinction spectra (black line) and the SHG enhancement profile (red plots) for  $D = 390$  nm samples. (A)  $d_m = 35$  nm and (B)  $d_m = 60$  nm.  $\theta = 45^\circ$  for all measurements.

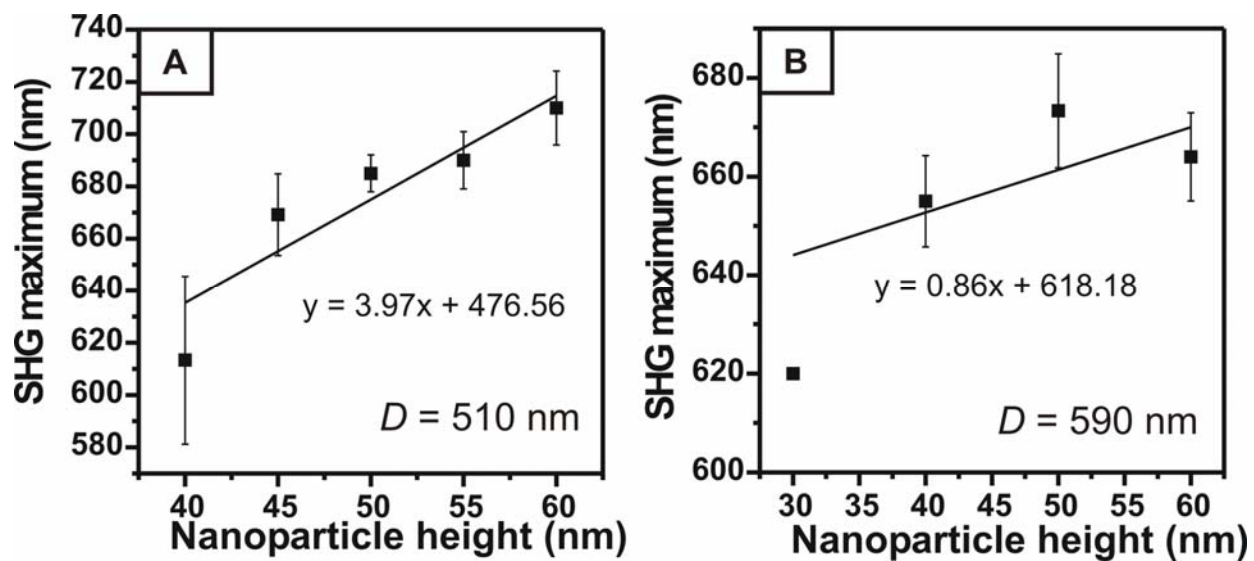


**Figure 4.11** SHG enhancement maxima versus nanoparticle height ( $d_m$ ). Nanosphere diameter  $D$  was (A) 510 nm and (B) 590 nm.

behavior of the extinction maxima. This observation also suggests that the in-plane dipole mode is not the main contribution to the observed SHG enhancement

The p:p SH emission was  $\sim 10$  times more intense than s:s emission. There was a sample dependent spectral response of the s:s signals. The usual case was a weak signal, but some samples showed weak signals with different profiles suggesting that these polarizations probe small differences in sample preparation.

A general consideration of SHG enhancement mechanisms provides physical insight for the present work. Three radiation-matter interactions occur for second-order processes. Local interactions occur by electric dipole (E1) coupling, whereas the electric quadrupole (E2) and magnetic dipole (M1) modes are the leading nonlocal contributions. All possible permutations of interaction mechanisms are allowed for noncentrosymmetric array of particles. However, electric dipole terms should dominate the response, so as a first approximation, paths that involve more than one nonlocal interaction are neglected, leaving a total of five distinguishable mechanisms for SHG. These five mechanisms can be represented as  $E1 + E1 \rightarrow E1$ ,  $E1 + E2 \rightarrow E1$ ,  $E1 + M1 \rightarrow E1$ ,  $E1 + E1 \rightarrow E2$ , and  $E1 + E1 \rightarrow M1$ . The  $E1 + E1 \rightarrow E1$  contribution should vanish when a sufficient number of randomly oriented particles are illuminated or for arrays made with centrosymmetric orientation.<sup>111</sup>

The truncated tetrahedral particles shown in Figure 4.2 comprise a lattice in which centrosymmetry of in-plane dipoles should result in cancellation of SHG when a sufficient number of particles are contained within the spot of the laser beam. The array can be considered to be made of particle pairs that have inversion symmetry, whereas individual particles do not have inversion symmetry. The symmetric character of the array, therefore, suppresses resonance enhancement from the in-plane dipolar mode, and no peak in the SHG efficiency is observed at

the extinction maximum in Figure 4.9 and 4.10. We might expect the  $E1 + E2 \rightarrow E1$  ( $E1 + E1 \rightarrow E2$ ) mechanism to contribute if input (or output) frequencies were in resonance with quadrupolar modes. However, the observations strongly suggest that the in-plane mode is not the main contribution to the observed SHG enhancement, so we do not assign the observed SHG enhancement to an in-plane quadrupole resonance. The polarization, orientation, and frequency dependence of the SHG enhancement is consistent with a weak out-of-plane dipolar resonance, which contributes through the  $E1 + E1 \rightarrow E1$  mechanism.

If the SHG enhancement is from the out-of-plane dipole mode, the position of this resonance should be sensitive to the particle height. The out-of-plane dipole mode is calculated by the DDA method and its resonant wavelength versus  $d_m$  is plotted in Figure 4.12 for  $D = 510$  nm and 590 nm samples. The resonant wavelength of the out-of-plane dipole mode red-shifts as  $d_m$  increases, and this trend is consistent with the  $d_m$  dependence of the SHG enhancement maximum that is shown in Figure 4.11. However, there is a large difference in their resonance wavelength. The SHG enhancement maximum is shown at a longer wavelength than the resonance of the out-of-plane dipole mode. The red-shift of the experimental observation from the theoretical calculation was also observed for in-plane dipole extinction measurements, so the water layer formation can be an explanation here, again.

#### 4.3.4 Polarization Dependent SHG

Polarized measurements made at a fixed input frequency were used to compare the tensorial response of the films to the nanoparticle arrays. Silver films of 50 nm height with no resonances at either the fundamental or SH frequencies and nanoparticle arrays of  $D = 390$  nm  $d_m = 50$  nm were studied. Typical polarization and orientation dependent results for both a film and an nanoparticle array are presented in Figure 4.13. The wavelength of the fundamental beam

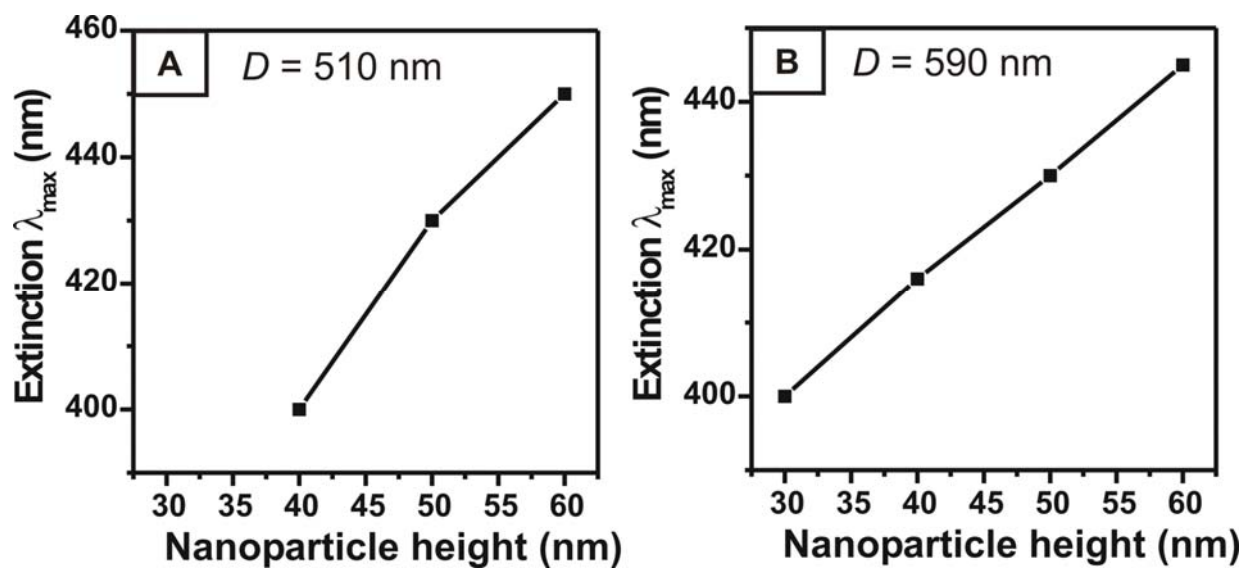


**Figure 4.12** Out-of-plane dipole resonance calculated by DDA method versus nanoparticle height ( $d_m$ ). Nanosphere diameter  $D$  was (A) 510 nm and (B) 590 nm.

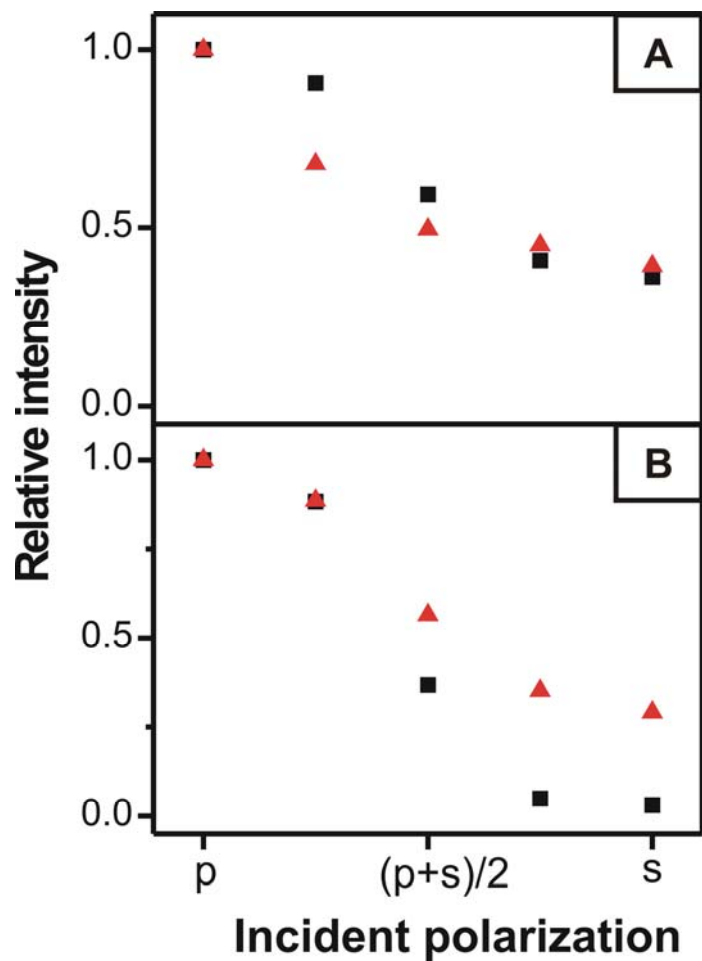


**Figure 4.13** Normalized SHG intensity detected in p polarization at (A) 10 and (B) 45° incidence for both the nanoparticle arrays (red triangles) and smooth film (black squares).

was 1300 nm and the peak extinction for this array was  $\sim 650$  nm; however, similar results were found with the same fundamental beam and a LSPR wavelength of 750 nm. The input polarization of the fundamental was varied from p to s with p-polarized SH detection. Results for s-polarized emission are too weak for peak integration, particularly in the case of the film. SHG from the silver film is highly sensitive to the out-of plane electric-field component of the fundamental beam, which is most easily seen for larger angles of incidence when the difference between p and s is most significant. In Figure 4.13, we see that at  $45^\circ$  the film shows a sharp decrease in p-polarized output when the input polarization varies from p to s, whereas at  $10^\circ$  the trend is the same but the variation is less severe. In contrast, SHG from the nanoparticle array is less sensitive to variation of the incidence angle and input polarization with the effect being most obvious at  $45^\circ$ .

The data can be interpreted with a model that was successfully applied to the magneto-optical Kerr effect.<sup>207,208</sup> This model provides a qualitative picture in which tensor elements are considered in terms of in-plane and out-of-plane matrix elements. We first write the  $i$ -polarized component SHG intensity as the square of the second-order polarization

$$I_i(2\omega; \omega) \approx \left| \vec{P}_i^{(2)}(2\omega) \right|^2. \quad (4.2)$$

The polarization,  $\vec{P}_i^{(2)}(2\omega)$ , can be expressed in terms of the second-order susceptibility tensor,

$\chi_{ijk}^{(2)}(2\omega; \omega)$ , and the fundamental local electric fields,  $\vec{E}_j(\omega)\vec{E}_k(\omega)$ , as

$$\vec{P}_i^{(2)}(2\omega) = \chi_{ijk}^{(2)}(2\omega; \omega)\vec{E}_j(\omega)\vec{E}_k(\omega). \quad (4.3)$$

The second-order susceptibility is written in a discrete basis truncated to include only conducting electrons<sup>208</sup>

$$\chi_{ijk}^{(2)}(2\omega; \omega) = \sum_{abc \in \text{cond. band}} \langle a | \hat{e}_i | b \rangle \langle b | \hat{e}_j | c \rangle \langle c | \hat{e}_k | a \rangle F_{abc}(\omega, 2\omega) \quad (4.4)$$

where  $F_{abc}(\omega, 2\omega)$  contains transmission and reflection coefficients as well as all energetic parameters and  $\hat{e}_i$  is an electric field component. Restriction of the sum over states to the conduction band is valid when the fundamental frequency is less than the difference between the Fermi energy and the d-band ( $\sim 4$  eV for silver). Predictions are intuitive in a tight-binding basis of atomic orbitals. The following rules may be applied to matrix elements for the film (coordinate system of Figure 4.5):

$$\langle a | \hat{e}_z | b \rangle \neq 0 \text{ and } \langle a | \hat{e}_x | b \rangle = \langle a | \hat{e}_y | b \rangle = 0. \quad (4.5)$$

These rules hold for all crystalline faces of silver and for an amorphous surface.

The dominance of out-of-plane emission for the film is consistent with predictions of the model, and this result is general for smooth noble metal surfaces. Results for the nanoparticle array reveal the sensitivity of SHG to the properties of individual particles even when the SHG is not resonant. The excitation profiles discussed in the previous section showed that the SHG resonance enhancement is related to an out-of-plane component, but Figure 4.13 suggests that the absolute emission intensity for the nanoparticle array possesses significant in-plane contributions as well. The rules outlined in Equation 4.5 cannot be applied to the nanoparticle array due to its finite nanoparticle height and spatial extent, a conclusion supported by these polarization measurements. This type of data would be especially useful for testing theoretical models when the orientations of individual particles have simpler symmetry and are uniform over the focus area. The nanoparticle arrays that are tested in this work have more complicated symmetry, and include defects that prevent azimuthal studies.

#### 4.4 Conclusion

Frequency-scanned excitation profiles of coherent SHG were measured for silver nanoparticle arrays prepared by nanosphere lithography. The maxima in the p:p SHG

efficiencies were observed in  $D = 510$  nm and 590 nm samples and they were blue-shifted from the peak of the in-plane dipolar LSPR. The SGH efficiency maxima red-shifted as the particle height increased, whereas the extinction maxima for normal incident beam blue-shifted. Those behaviors are consistent with the nanoparticle height dependent in-plane and out-of-plane dipolar LSPR that is calculated by DDA method. The discrepancy in measurement and calculation is explained by the water layer formation on the nanoparticle arrays. The data were interpreted by assuming that the purely in-plane dipolar emission mechanism is suppressed due to averaging over a centrosymmetric distribution of nanoparticles. Polarization and orientation dependent measurements suggest that the SHG is enhanced by a LSPR mode polarized out-of-plane, which was not observed in the linear spectrum due to its weak extinction. This is the first clear identification of such a resonance by nonlinear spectroscopy for shaped nanoparticles, and was only possible due to cancellation of in-plane dipolar emission. Unlike silver films, measurements of single-wavelength and polarization-controlled SHG intensity from nanoparticle arrays when the SHG was not resonant showed a moderate in-plane component from the nanoparticle array where this is forbidden. The experimental identification of out-of-plane dipolar LSPR will provide a key test of theoretical models for nanoparticle optical properties. Future work will probe quadrupole resonances to provide a full test of nanoparticle response theory for non-spherical nanoparticles.

## **Chapter 5**

### **Stability of Silver Nanoparticles Fabricated by Nanosphere Lithography and Atomic Layer Deposition to Femtosecond Laser Excitation**

## 5.1 Introduction

Noble metal nanoparticles have optical properties that are different from those of bulk. These properties originate from the localized surface plasmon resonance (LSPR), which is a collective oscillation of the conduction electrons that occurs when light impinges on a nanoparticle at a specific wavelength. The remarkable consequences of this optical phenomenon are enhanced light scattering and absorption and large local field enhancement near the nanoparticle surface at the resonant condition. The LSPR can be controlled by changing the size, shape, and composition of the nanoparticle<sup>4,21,147</sup> as well as the dielectric environment.<sup>134,141</sup> These features of LSPR have enabled the noble metal nanoparticles to be applied for a variety of applications, including bio/chemosensors,<sup>114-117</sup> optical filters,<sup>118,119</sup> plasmonic waveguides,<sup>23,120-122</sup> and surface-enhanced spectroscopy.<sup>5,123,124</sup>

Surface-enhanced Raman scattering (SERS) is one of the most studied surface-enhanced spectroscopic techniques to date.<sup>2,5,39,41</sup> Local field enhancements by the LSPR have been determined as the origin of the huge enhancement of Raman scattering from the molecules adsorbed on the noble metal nanoparticles or nanostructures. Recently, surface-enhanced nonlinear spectroscopic studies of molecules adsorbed on noble metal nanoparticles or nanostructures have also been reported including second harmonic generation,<sup>48,49,224</sup> sum frequency generation,<sup>88,225,226</sup> coherent anti-Stokes Raman scattering,<sup>227-230</sup> hyper-Raman scattering,<sup>43</sup> and two-photon absorption.<sup>50</sup>

Noble metal nanoparticles or nanostructures have been shown to be excellent substrates for surface-enhanced laser spectroscopy, and it is important to characterize the interaction between a laser pulse and the metal nanoparticles. There have been studies to explore the relaxation dynamics of noble metal nanoparticles that are excited by femtosecond laser pulses.

Electron-electron, electron-phonon, and phonon-phonon relaxation in gold and silver nanoparticles with various sizes and shapes have been studied by time-resolved pump-probe spectroscopy.<sup>231</sup> Coherent vibrational oscillation of the noble metal nanoparticles induced by femtosecond excitation also has been monitored by pump-probe transient spectroscopy. Hartland group and El-Sayed group monitored the transient absorption signal versus the delay time of the probe beam for colloidal gold nanoparticles<sup>232-234</sup> and gold nanoparticle arrays<sup>235</sup> fabricated by nanosphere lithography (NSL).<sup>4</sup> They monitored the oscillation of transient absorption signals with various probe beam wavelengths, and the oscillations that are monitored at blue and red side of the extinction maximum wavelength of the nanoparticle showed a 180° phase difference.

For nonlinear laser spectroscopies, sometimes, high laser intensity is required to obtain reasonable signal level. However, metal nanoparticles are susceptible to melting or deformation<sup>236-238</sup> by the heat induced through the relaxation process of hot electrons excited by high power ultrashort laser pulses that are used for nonlinear spectroscopic techniques. Furthermore, lowered melting temperature of the nanoparticle compared to bulk metal can accelerate the melting and deformation of the nanoparticles.<sup>221-223,239-241</sup>

Recently, Van Duyne and coworkers<sup>242</sup> demonstrated that the Al<sub>2</sub>O<sub>3</sub> film deposited on silver nanoparticle arrays by atomic layer deposition (ALD) can protect the nanoparticles from thermal deformation. They suggested the possibility of using the Al<sub>2</sub>O<sub>3</sub> coated silver nanoparticles as a substrate for operando SERS studies which require high temperatures and pressures employed in industrial catalytic reactions.<sup>242,243</sup> In this work, we present studies on the femtosecond laser power stability of NSL fabricated silver nanoparticles on glass substrates. Bare silver nanoparticles and nanoparticles coated with Al<sub>2</sub>O<sub>3</sub> film deposited by ALD were

irradiated by the femtosecond laser, and their LSPR shift was monitored by white light extinction measurement. The laser wavelengths were either resonant or off-resonant to the LSPR of the silver nanoparticles.  $\text{Al}_2\text{O}_3$  coated silver nanoparticles showed enhanced stability against the laser exposure, and it is proposed that  $\text{Al}_2\text{O}_3$  coated nanoparticles can be used as a stable platform for surface-enhanced laser spectroscopy including nonlinear spectroscopy.

## 5.2 Experimental Methods

### 5.2.1 Materials

Silver pellets (99.99%) were purchased from the Kurt J. Lesker Company (Pittsburgh, PA). Glass substrates (no. 2, 18 mm diameter cover slips) were purchased from Fisher Scientific (Hampton, NH). Surfactant free, white carboxyl-substituted polystyrene latex nanospheres with diameter ( $D$ ) = 390 nm were received as a suspension in water from Duke Scientific (Palo Alto, CA). Absolute ethanol was purchased from Pharmco (Brookfield, CT). Trimethylaluminum (TMA) for the fabrication of  $\text{Al}_2\text{O}_3$  atomic layers was purchased from Sigma Aldrich (Milwaukee, WI).

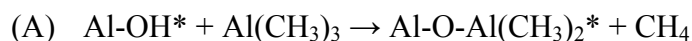
### 5.2.2 Preparation of Silver Nanoparticle Samples

Glass substrates were cleaned by immersion in a boiling piranha solution (3:1 concentrated  $\text{H}_2\text{SO}_4$ : 30%  $\text{H}_2\text{O}_2$ ) for 30 min. (CAUTION: *Piranha reacts violently with organic compounds and should be handled with great care.*) After cooling, the substrates were thoroughly rinsed repeatedly with  $18.2 \text{ M}\Omega \text{ cm}^{-1}$  Millipore water (Marlborough, MA). The substrates were then sonicated for 1 h in 5:1:1  $\text{H}_2\text{O}$ : $\text{NH}_4\text{OH}$ :30% $\text{H}_2\text{O}_2$ . Following sonication, the substrates were rinsed with copious amounts of Millipore water.

Single-layer, monodispersed silver nanoparticles were prepared with the NSL technique.<sup>3,4</sup> A suspension of nanospheres spontaneously self-assembled into hexagonally

closed-packed two dimensional arrays after being coated on a clean glass substrate. Silver was deposited at a rate of  $0.1 \text{ nm s}^{-1}$  with a Kurt J. Lesker Axxis electron beam deposition system (Pittsburgh, PA) with a base pressure of  $10^{-6}$  Torr. The deposited height ( $d_m$ ) was monitored with a Sigma Instruments 6 MHz gold plated quartz crystal microbalance (Fort Collins, CO). The nanosphere masks were removed from the substrate by sonication in absolute ethanol for approximately 5 min.

$\text{Al}_2\text{O}_3$  films were grown on NSL silver nanoparticles by ALD. The reactor utilized in these experiments is similar to one described in previous publications.<sup>244</sup> Trimethylaluminum (TMA) and deionized  $\text{H}_2\text{O}$  vapors were alternately dosed over the substrates in a nitrogen carrier stream at a mass flow rate of 360 sccm and a pressure of  $\sim 1$  Torr, using a growth temperature of  $50^\circ\text{C}$ .  $\text{Al}_2\text{O}_3$  ALD proceeds according to the following pair of self-limiting reactions, where the asterisks (\*) denote the surface species.<sup>245</sup>



One complete ALD cycle consists of four steps: (1) TMA reactant exposure time, 2 s; (2)  $\text{N}_2$  purge following TMA exposure, 10 s; (3)  $\text{H}_2\text{O}$  reactant exposure time, 2.5 s; (4)  $\text{N}_2$  purge following  $\text{H}_2\text{O}$  exposure, 30 s. Long purge times are necessary at low temperatures to prevent chemical vapor deposition of  $\text{Al}_2\text{O}_3$ .<sup>246</sup> In a previous study,  $\text{Al}_2\text{O}_3$  growth on silver surfaces by ALD was shown to proceed with an average growth rate of  $\sim 1 \text{ \AA/cycle}$ .<sup>247</sup>

For our experiments, 4 or 10 atomic layers of  $\text{Al}_2\text{O}_3$  that correspond to 0.4 nm and 1.0 nm layer thickness were deposited on silver nanoparticles.

### 5.2.3 Measurement of the Stability of Silver Nanoparticles upon Laser Exposure

Experiments were carried out with an amplified Ti:Sapphire laser system described in prior publications.<sup>137,213</sup> The output of the compressor is centered at 805 nm with a spectral bandwidth of 22 nm and pulse duration of 90 fs at 1 kHz. A tunable near-IR fundamental beam was generated with a laboratory-built optical parametric amplifier (OPA) pumped by 650  $\mu\text{J}/\text{pulse}$  of the amplified Ti:Sapphire laser beam. The total near-IR output of the OPA was 50  $\mu\text{J}/\text{pulse}$  (signal + idler). A polarizer separated the signal and idler pulses. The duration and bandwidth of the signal pulse are 125 fs and  $430\text{ cm}^{-1}$  (at  $1.3\ \mu\text{m}$ ), respectively.

The laser irradiation on the sample and the extinction measurements were performed using a laboratory-built microscope setup. Figure 5.1 shows the schematic diagram of the setup. The variable signal output of the OPA (tunable range of  $1.16 - 1.52\ \mu\text{m}$ ) was doubled by a 0.6 mm thickness type I  $\beta$ -barium borate (BBO) crystal and the fundamental near-IR beam was blocked by a short-pass color filter (Schott KG-3). The resulting visible beam was focused onto the sample by a +80 mm focal length  $\text{CaF}_2$  lens with a  $45^\circ$  incidence angle. Two different laser wavelengths were used for the laser power stability measurements of NSL-fabricated silver nanoparticles; one was the wavelength that corresponds to the LSPR wavelength maximum (LSPR  $\lambda_{\text{max}}$ ) of the nanoparticles, which will be called the resonant condition, and the other was the wavelength that is  $\sim 100\text{ nm}$  red from the LSPR  $\lambda_{\text{max}}$ , which will be called the off-resonant condition. The laser wavelengths tested were 630 nm and 730 nm for bare nanoparticles and 610 nm and 710 nm for nanoparticles coated with 0.4 nm and 1.0 nm of  $\text{Al}_2\text{O}_3$ . The spot size of the beam at the focus was  $25.2\ \mu\text{m}$  at full width at half-maximum (FWHM) along the long axis. The beam intensity was controlled with a round continuously variable neutral density filter.

Extinction spectra were collected on an Ocean Optics USB2000 fiber-coupled spectrometer. White light from a tungsten-halogen lamp was fiber-coupled with a  $100\ \mu\text{m}$  fiber

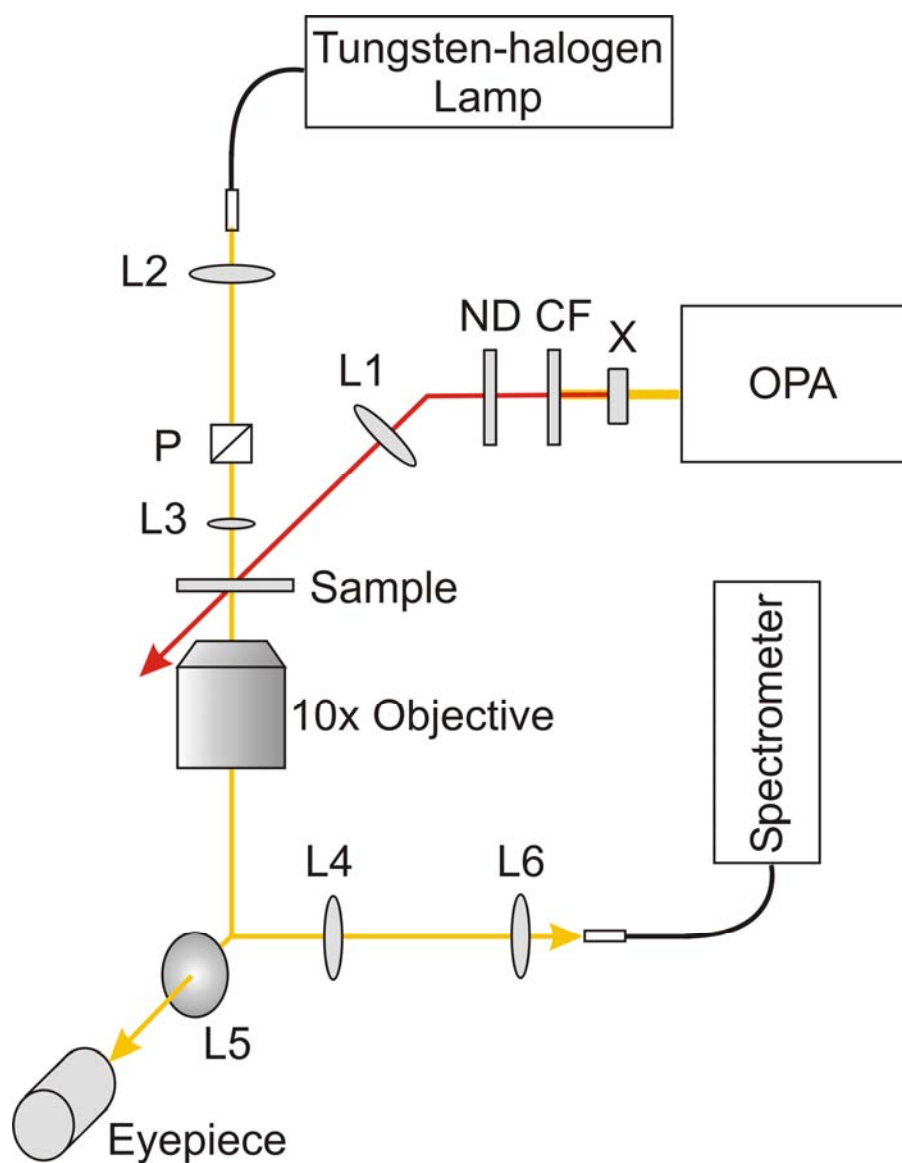


**Figure 5.1** Experimental setup used for laser irradiation and extinction measurements. Symbols represent L1: +80 mm  $\text{CaF}_2$  lens, L2: +40 mm achromatic lens, L3: +12.7 mm achromatic lens, L4 and L5: +200 mm achromatic lens (tube lens), L6: +30 mm achromatic lens, P: Glan-Taylor calcite polarizer, X: 0.6 mm type I BBO crystal, CF: short pass color filter, and ND: round continuously variable neutral density filter.

to a +40 mm focal length achromatic collimating lens. The collimated beam was then polarized by a Glan-Taylor calcite polarizer with 5 mm aperture and focused onto the sample by a +12.7 mm focal length achromatic lens with the optic axis normal to the sample surface. The beam was carefully aligned to monitor the spot of laser focus. The white light spot size on the sample was 20  $\mu\text{m}$  diameter at FWHM. Transmitted light was collected by an infinity-corrected 10 $\times$  Nikon microscope objective (NA = 0.30) at a working distance of 16.0 mm and directed to the spectrometer or an eyepiece by the choice of the mirror mounted after the objective. When the extinction was measured, the beam was focused into a 600  $\mu\text{m}$  fiber that couples into the spectrometer.

The extinction of NSL-fabricated silver nanoparticles sample was monitored during the laser irradiation. The extinction spectra were obtained before laser irradiation and at 30 sec intervals of laser exposure. While the extinction spectra were recorded, the laser beam was blocked in order to prevent the scattered laser light from entering the spectrometer.

### **5.3 Results and Discussion**

#### **5.3.1 Laser Induced LSPR Change of the Bare Silver Nanoparticles**

The LSPR of the NSL-fabricated silver nanoparticles is very sensitive to the particle size and tip sharpness.<sup>4,248</sup> For the NSL-fabricated silver nanoparticles, a blue shift of the LSPR wavelength maximum (LSPR  $\lambda_{\text{max}}$ ) has been observed when the tip of the nanoparticle is rounded by a solvent,<sup>248</sup> heat,<sup>146,242</sup> and electrochemical oxidation.<sup>249</sup> The same effect is predicted theoretically for the triangular nanoprisms.<sup>134</sup> Therefore any shape change in the nanoparticles from the laser irradiation can be monitored by the LSPR band shift.

Figure 5.2 shows the LSPR spectra of bare silver nanoparticles before and after laser exposure with different laser pulse intensities and exposure times. The NSL-fabricated

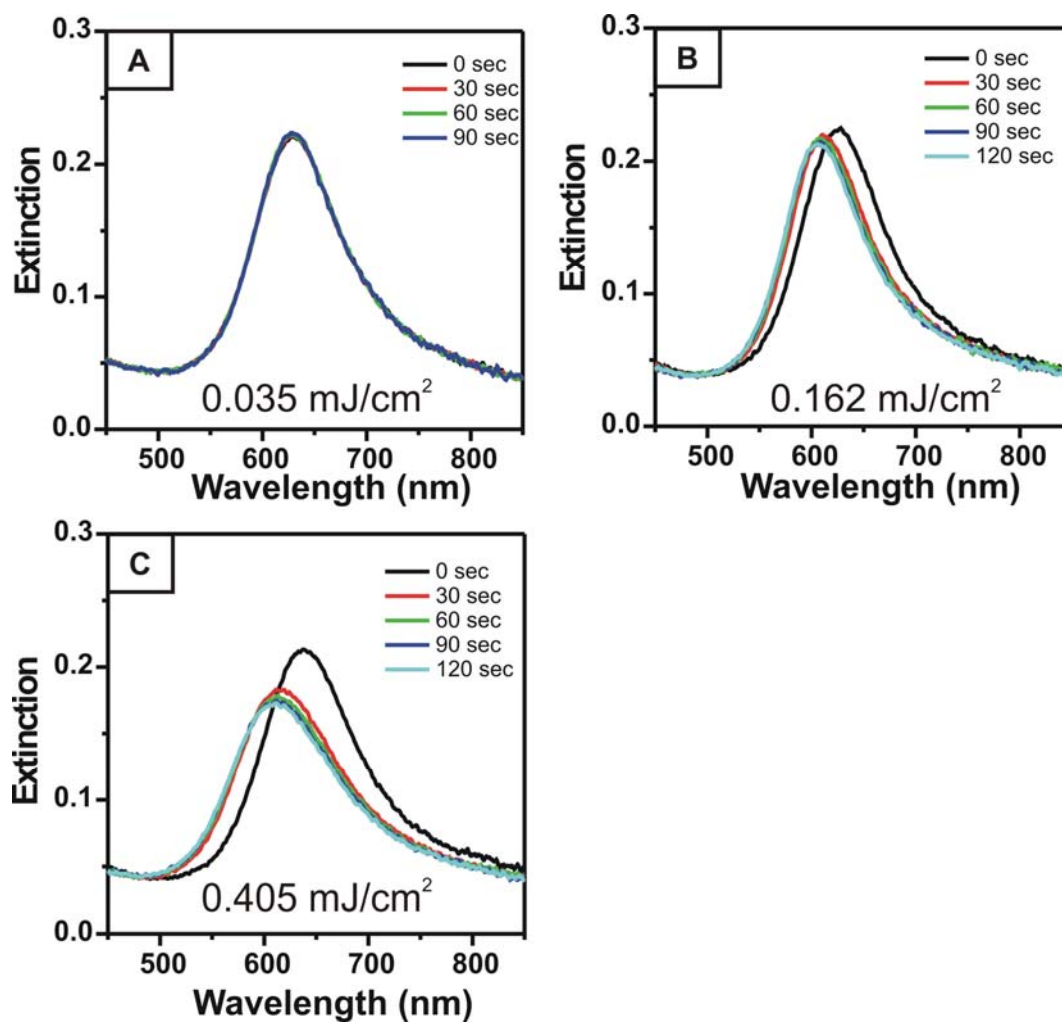


**Figure 5.2** LSPR change after the laser exposure to the bare silver nanoparticles ( $d_m = 30$  nm). Wavelength of incident laser was 630 nm. The laser pulse intensity was (A) 0.035 mJ cm<sup>-2</sup>, (B) 0.162 mJ cm<sup>-2</sup>, and (C) 0.405 mJ cm<sup>-2</sup>.

nanoparticles with  $D = 390$  nm and  $d_m = 30$  nm have an LSPR  $\lambda_{\max}$  at  $\sim 630$  nm, and the wavelength of laser was tuned to 630 nm. After laser exposure, the LSPR blue shifted. The same measurements with the 730 nm wavelength laser beam which is about 100 nm off-resonant from the LSPR  $\lambda_{\max}$  are shown in Figure 5.3. Again a blue-shift of the LSPR after laser exposure was observed. The LSPR shift versus laser exposure time is plotted in Figure 5.4. For both the resonant condition and off-resonant condition, the majority of the shift is observed with the first 30 sec laser exposure, and then the LSPR shift gradually saturates. The LSPR shift increased as the laser pulse intensity increased. The laser pulse intensity was calculated from the area within the radius of standard deviation of the Gaussian laser intensity profile. The standard deviation was  $10.7\mu\text{m}$  for the long axis of the beam spot and 68% of the total beam intensity is focused in the area.

The reshaping of the NSL-fabricated gold nanoparticles by a femtosecond laser pulse has been reported by El-Sayed and coworkers.<sup>222,223</sup> They excited gold nanoparticles with a 400 nm, 800 nm, and 700 nm laser that corresponded to interband/in-plane quadrupolar transition, dipolar transition, and both quadrupolar/dipolar transition, respectively. The LSPR and shape change of the gold nanoparticles were monitored by extinction spectra measurement and scanning electron microscopy (SEM). When dipolar transition was excited, which is the case for our experiments, a blue shift of the LSPR band was observed, which agrees with our results despite differences in detailed spectral features. El-Sayed and coworkers observed rounding of the tips for gold nanoparticles with  $3.0 \text{ mJ cm}^{-2}$  laser pulse intensity and the displacement or removal of the nanoparticles from the substrate with greater than  $5.0 \text{ mJ cm}^{-2}$  pulse intensities.<sup>222,223</sup> The rounded tips were explained by photothermal heating and the displacement of the nanoparticles for high power laser irradiation was explained by the flying of the nanoparticle of which kinetic

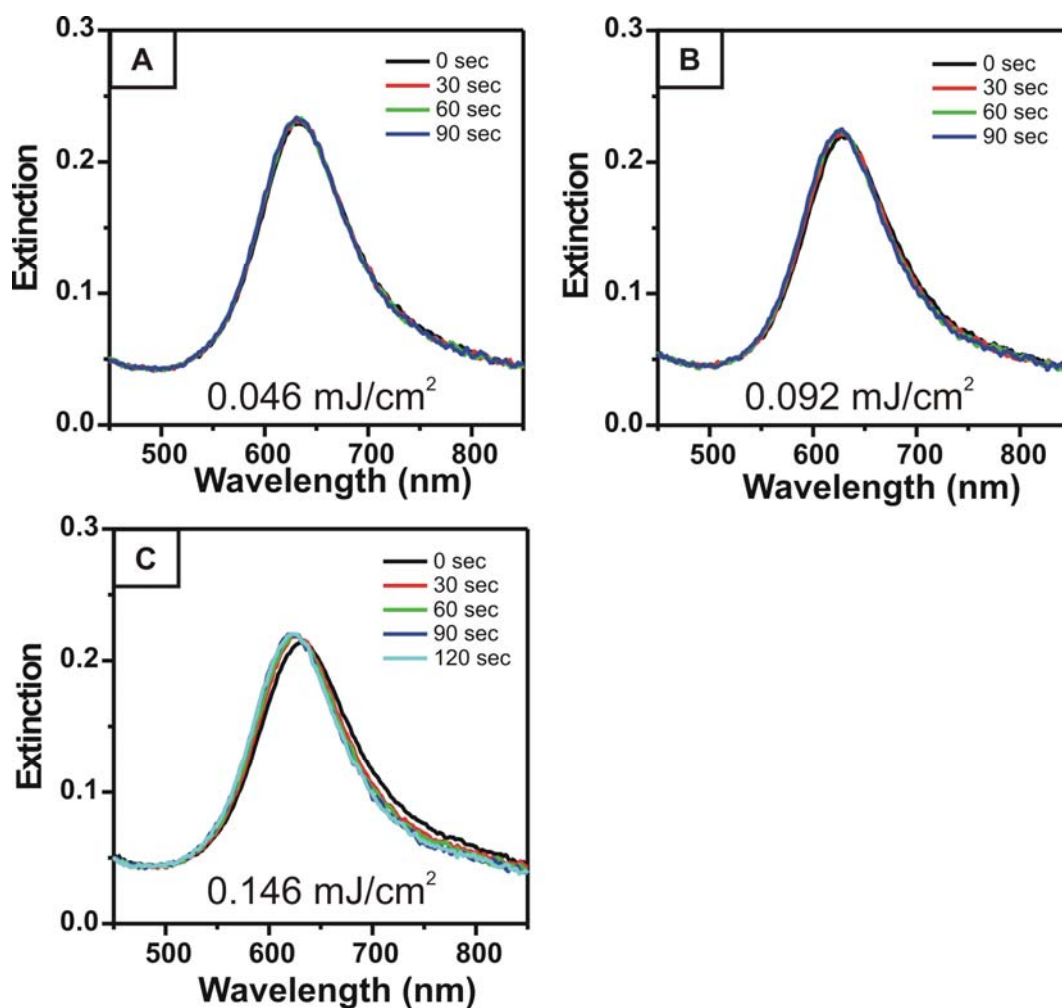


**Figure 5.3** LSPR change after the laser exposure to the bare silver nanoparticles ( $D = 390 \text{ nm}$ ,  $d_m = 30 \text{ nm}$ ). Wavelength of incident laser was  $730 \text{ nm}$ . The laser pulse intensity was (A)  $0.046 \text{ mJ cm}^{-2}$ , (B)  $0.092 \text{ mJ cm}^{-2}$ , and (C)  $0.146 \text{ mJ cm}^{-2}$ .

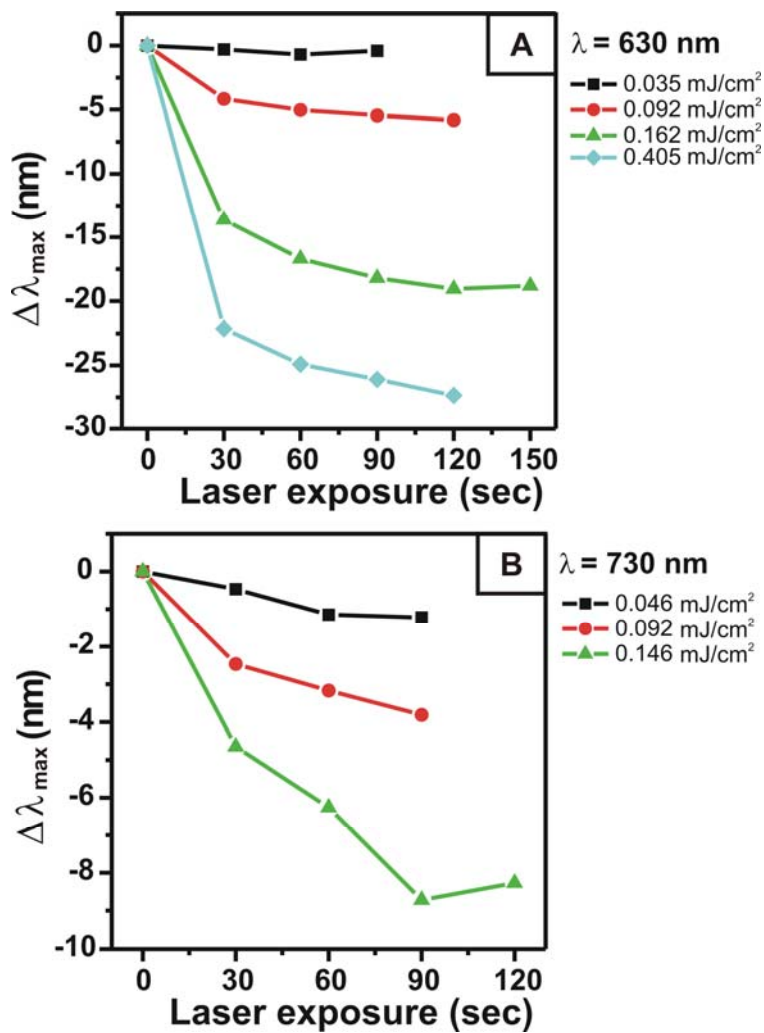


**Figure 5.4** LSPR shift versus laser exposure time for bare nanoparticles ( $D = 390 \text{ nm}$ ,  $d_m = 30 \text{ nm}$ ). Wavelength of incident laser was (A) 630 nm and (B) 730 nm.

energy was obtained by gold atom sublimation.<sup>222,223</sup> In our experiments, laser pulse intensities were lower than  $1 \text{ mJ cm}^{-2}$ , therefore displacement or removal of the nanoparticles is not expected.

When the conduction electrons in noble metal nanoparticle are excited by a femtosecond laser pulse, excited electrons undergo relaxation processes through electron-electron, electron-phonon, and phonon-phonon coupling.<sup>231</sup> Through the electron-phonon coupling, the energy is exchanged between the electrons and the lattice<sup>231</sup>, which results in lattice heating. The heat is dissipated through the phonon-phonon coupling between the nanoparticles and surrounding media. The time constant of the electron-electron relaxation is on the order of several hundred femtoseconds<sup>250,251</sup> and the electron-phonon relaxation is on the order of several picoseconds<sup>252</sup> which has a particle size dependence. The phonon-phonon relaxation is on the order of several hundred picoseconds,<sup>231,253,254</sup> revealing that the heat conductivity of the surrounding media is an important factor. In our experiment, the glass substrate serves as an energy sink. Once the nanoparticles are excited by a femtosecond pulse, all the relaxation processes are completed before the next laser pulse excites the nanoparticles again, since all the relaxation processes are faster than the 1 kHz of the laser repetition rate that was used for our experiment. Therefore, we can estimate the temperature of the silver nanoparticles right after exposure to the laser pulse.

In the case of the exposure to the 630 nm wavelength laser pulse, the energy absorbed by each nanoparticle is approximately  $6.83 \times 10^{-15} \text{ J}$ ,  $3.15 \times 10^{-14} \text{ J}$ , and  $7.88 \times 10^{-14} \text{ J}$  for a laser pulse intensity of  $0.035 \text{ mJ cm}^{-2}$ ,  $0.162 \text{ mJ cm}^{-2}$ , and  $0.405 \text{ mJ cm}^{-2}$ , respectively. The extinction of silver nanoparticles at 630 nm is approximated to be 0.2 (transmittance = 0.63) and according to the electrodynamics calculation of a silver nanoparticle with similar shape and size, the contribution of the absorption and scattering to the extinction is about 80 % and 20 %, respectively.

respectively. The calculated temperature of the silver nanoparticle based on energy absorbed is 308 K, 364 K and 467 K, respectively.  $25.35 \text{ J M}^{-1} \text{ K}^{-1}$  of silver heat capacity is used for the estimation, which is the value at 298.15 K. The heat capacity of silver varies less than 7 % until 600 K,<sup>255</sup> and therefore the estimation can be justified. The melting temperature of bulk silver is 1234.93 K. However the nanoparticle shows a large depression in the melting temperature with decreasing size, or radius, which is caused by the high surface tension of the nanoparticle.<sup>239,240,256</sup> Even though the melting temperature of our nanoparticle is close to that of the bulk, because of the large curvature at the tip area, the sharp tips can show low enough melting point to be melted by the energy provided by the laser pulse. The NSL silver nanoparticles fabricated using a sphere diameter less than 264 nm have been reported to undergo surface melting even at room temperature.<sup>188</sup> The rounded tip results in a blue shift of the LSPR band of the silver nanoparticles. SEM images were obtained for the nanoparticles with and without laser exposure, but no differences were observed within our resolution (data not shown). The LSPR of the nanoparticle array is very sensitive to the change of the tip geometry, therefore even a slight tip rounding that cannot be detected by SEM can cause a LSPR  $\lambda_{\text{max}}$  shift of  $\sim 25$  nm which was the maximum shift within our laser intensity.

In the case of the exposure to the 730 nm wavelength laser pulse, the energy absorbed by single nanoparticle is less than the case of the 630 nm because it corresponds to the tail of the LSPR band where the absorption is smaller. Therefore tip melting is not efficient at this condition, which leads to a smaller blue-shift than 630 nm laser pulse with similar laser pulse energy.

### **5.3.2 Laser Induced LSPR Change of ALD $\text{Al}_2\text{O}_3$ Coated Nanoparticles**

The LSPR changes induced by the laser pulse are monitored for the silver nanoparticles fabricated by NSL ( $D = 390$  nm and  $d_m = 50$  nm) and coated with 0.4 nm and 1.0 nm of  $\text{Al}_2\text{O}_3$  layers. Both samples show the LSPR  $\lambda_{\text{max}}$  at  $\sim 610$  nm, and the wavelength of the laser was tuned to 610 nm and 710 nm to test the laser power stability of the samples for the resonant and off-resonant conditions. Figure 5.5 and 5.6 show the LSPR shift versus laser exposure time for nanoparticles coated with 0.4 nm and 1.0 nm of  $\text{Al}_2\text{O}_3$ , respectively. For both the resonant condition and off-resonant condition, the majority of shift is observed with the first 30 sec laser exposure, and is then followed by a gradual saturation of the LSPR shift. This is similar to what was observed for the bare nanoparticles. The LSPR shift is larger for the 610 nm laser wavelength than the 710 nm laser wavelength with similar pulse intensities, and is also observed for the bare nanoparticles. However the absolute amount of the LSPR shift of the bare nanoparticle, nanoparticles with 0.4 nm of  $\text{Al}_2\text{O}_3$ , and nanoparticles with 1.0 nm of  $\text{Al}_2\text{O}_3$  for similar laser pulse intensities varies with respect to each other. Figure 5.7 shows the LSPR shift of bare nanoparticles (black squares) and nanoparticles with 0.4 nm (red circles) and 1.0 nm  $\text{Al}_2\text{O}_3$  (green triangles) after 120 sec laser exposure versus laser pulse intensity. The resonant condition is plotted with solid marks and the off-resonant condition is plotted with open marks. All the plots show the increase in LSPR shift as the laser pulse intensity increases. For the same laser pulse intensity, the bare nanoparticles undergo the largest LSPR shift and the nanoparticles with 1.0 nm of  $\text{Al}_2\text{O}_3$  shows the smallest shift against the laser exposure. The laser pulse energy of  $1.77 \text{ mJ cm}^{-2}$  that led to  $\sim 15$  nm LSPR shift of the sample with 1.0 nm of  $\text{Al}_2\text{O}_3$  in resonant condition can heat the nanoparticles up to 748 K. The LSPR shift is similar to the shift in bare nanoparticles induced by the pulse energy of  $0.162 \text{ mJ cm}^{-2}$  which can heat the nanoparticles only up to 422 K.

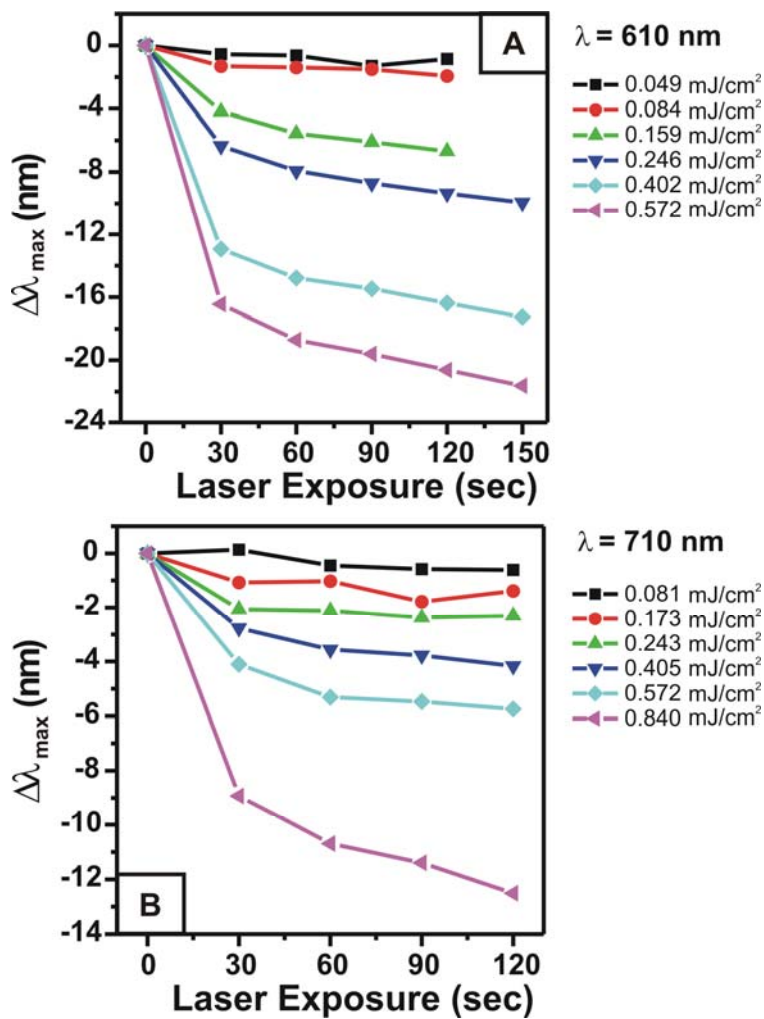


**Figure 5.5** LSPR shift versus laser exposure time for nanoparticles ( $D = 390$  nm,  $d_m = 50$  nm) coated with 0.4 nm of  $\text{Al}_2\text{O}_3$  layer. Wavelength of incident laser was (A) 610 nm and (B) 710 nm.

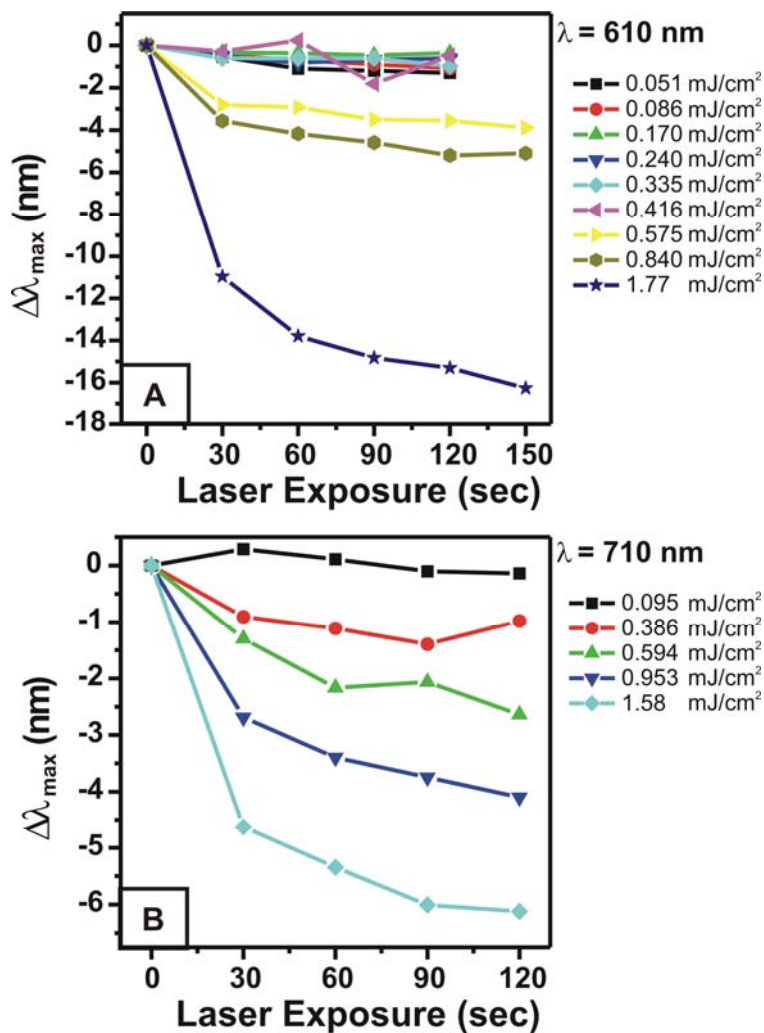


**Figure 5.6** LSPR shift versus laser exposure time for nanoparticles ( $D = 390$  nm,  $d_m = 50$  nm) coated with 1.0 nm of  $\text{Al}_2\text{O}_3$  layer. Wavelength of incident laser was (A) 610 nm and (B) 710 nm.

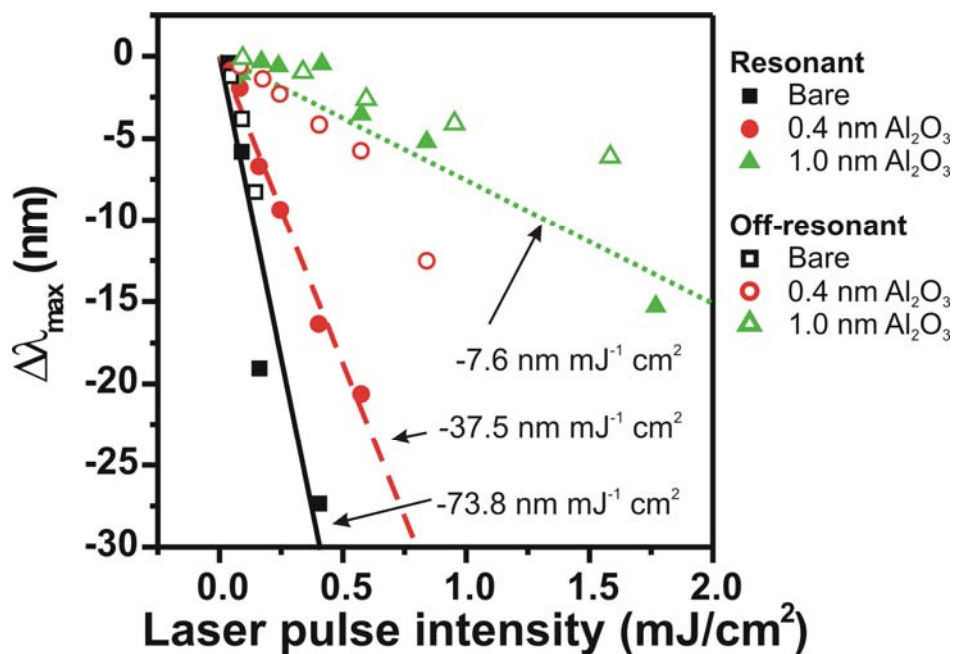


**Figure 5.7** LSPR shift after 120 sec laser exposure versus laser pulse intensity. The resonant condition is plotted with solid marks and the off-resonant condition is plotted with open marks. Linear fitting for the resonant condition is shown with solid black line, red dashed line, and green dotted line for bare particles, nanoparticles coated with 0.4 nm  $\text{Al}_2\text{O}_3$ , and 1.0 nm  $\text{Al}_2\text{O}_3$ , respectively. Slopes for each sample are  $-73.8 \text{ nm mJ}^{-1} \text{ cm}^2$ ,  $-37.5 \text{ nm mJ}^{-1} \text{ cm}^2$ , and  $-7.6 \text{ nm mJ}^{-1} \text{ cm}^2$  for resonant condition, and  $-50.8 \text{ nm mJ}^{-1} \text{ cm}^2$ ,  $-12.6 \text{ nm mJ}^{-1} \text{ cm}^2$ , and  $-4.0 \text{ nm mJ}^{-1} \text{ cm}^2$  for off-resonant condition.

The LSPR  $\lambda_{\max}$  shift shows an approximately linear relation to the laser pulse intensity within our intensity range. In the case of the resonant condition the slope is  $-73.8$ ,  $-37.5$ , and  $-7.6$  nm  $\text{mJ}^{-1}$   $\text{cm}^2$  for bare, nanoparticles with 0.4 nm of  $\text{Al}_2\text{O}_3$ , and 1.0 nm of  $\text{Al}_2\text{O}_3$ , respectively as shown in Figure 5.7. This means that if the nanoparticles coated with 1.0 nm of  $\text{Al}_2\text{O}_3$  are used as a substrate for laser spectroscopy, 10 times higher laser pulse intensity can be used compared to when the bare nanoparticles are used as substrates. In the case of off-resonant condition the slope is  $-50.8$ ,  $-12.6$ , and  $-4.0$  nm  $\text{mJ}^{-1}$   $\text{cm}^2$ , respectively.

As a mechanism of the protection from the laser deformation of  $\text{Al}_2\text{O}_3$  coated silver nanoparticles, it might be suggested that the  $\text{Al}_2\text{O}_3$  layers serve as an additional heat sink. In such a case, the suppression of the surface melting by the  $\text{Al}_2\text{O}_3$  layers can be explained by the increased electron-phonon and phonon-phonon relaxation time, which leads to the efficient cooling of the hot nanoparticles. Also it has been reported that molecules adsorbed on gold nanoshells can introduce an additional hot electron decay channel, which leads to a decreased relaxation time.<sup>257</sup> However, Whitney et. al. reported that  $\text{Al}_2\text{O}_3$  layers protect the silver nanoparticles from thermally induced deformation at the thermal equilibrium condition.<sup>242</sup> They compared the LSPR shift of bare silver nanoparticles and nanoparticles coated with  $\text{Al}_2\text{O}_3$  after heating at 100 – 500 °C for several hours and observed that the  $\text{Al}_2\text{O}_3$  coated nanoparticles showed greatly reduced LSPR shifts compared to the bare nanoparticles.<sup>242</sup> This was also verified by SEM imaging.<sup>242</sup> Their work implies that the increased relaxation rate is not the major factor in the protection of the silver nanoparticles from the laser induced surface melting for nanoparticles with  $\text{Al}_2\text{O}_3$  coating.

The surface melting in nanocrystals has been discussed by Shi<sup>239</sup> using the Lindemann criterion.<sup>258</sup> According to the Lindemann criterion, a crystal melts when the root mean-square

displacement of the atoms in the crystal exceeds a certain fraction of the interatomic distance.<sup>239</sup>

The melting temperature for a nanocrystal is given by<sup>239</sup>

$$\frac{T}{T_0} = \exp[-(\alpha - 1)n_s / n_v] \quad (5.1)$$

where  $T$  is melting temperature of nanocrystal,  $T_0$  is melting temperature of bulk, and  $n_s$  and  $n_v$  are the number of surface atoms and the number of atoms located within the particle, respectively. The ratio  $n_s / n_v$  implies the particle size dependence of the melting temperature. As the particle size reduces,  $n_s / n_v$  increases.  $\alpha$  is given by  $\sigma_s / \sigma_v$  where  $\sigma_s$  and  $\sigma_v$  are mean-square displacements of the atoms located on surface and within the particle, respectively. In most cases  $\sigma_s > \sigma_v$ , i.e.  $\alpha > 1$  because surface atoms are loosely bound compared to the bulk atoms. Therefore, as the particle size decreases, i.e.  $n_s / n_v$  increases,  $T$  decreases. As the  $\alpha$  approaches the value of 1, the particle size sensitivity of the melting temperature decreases, i.e. the melting temperature of the nanoparticle approaches that of bulk. In the case of the silver nanoparticles coated with  $\text{Al}_2\text{O}_3$ , the  $\text{Al}_2\text{O}_3$  layers serve as a rigid frame for the silver nanoparticles and suppress the thermal vibration of the surface atoms of the nanoparticles. As a result,  $\sigma_s$ , therefore  $\alpha$  of the  $\text{Al}_2\text{O}_3$  coated nanoparticles decreases compared to that of bare nanoparticles, which leads to the increased melting temperature of the  $\text{Al}_2\text{O}_3$  coated nanoparticles compared to the bare nanoparticles. This model provides a clear explanation for how the  $\text{Al}_2\text{O}_3$  layers protect the silver nanoparticles from the surface melting.

### 5.3.3 Change in LSPR Bandwidth after the Laser Exposure

After laser exposure, in addition to the LSPR shift, a corresponding change in the LSPR bandwidth was observed. For both the resonant and off-resonant condition, the LSPR  $\lambda_{\text{max}}$  blue

shifted after laser exposure. However the LSPR bandwidth increased for the resonant condition and it decreased for the off-resonant condition, which is shown in the Figure 5.2C and 5.3C.

In Figure 5.8, the percent change in LSPR bandwidth after 120 sec laser exposure is plotted versus laser pulse energy for the (A) resonant condition and (B) off-resonant condition. The percent change is defined as following:

$$\text{percent change} = \frac{w_0 - w_L}{w_0} \times 100 (\%) \quad (5.2)$$

where  $w_0$  is the FWHM of the LSPR band before laser exposure and  $w_L$  is after the 120 sec laser exposure. Both bandwidths are measured in energy units. As shown in Figure 5.8A, when the laser wavelength was close to the LSPR  $\lambda_{\text{max}}$  and the laser pulse intensity was larger than  $0.09 \text{ mJ cm}^{-2}$ , the LSPR bandwidth increased. However a slight decrease in bandwidth was observed when the laser pulse intensity was less than  $0.09 \text{ mJ cm}^{-2}$  for both bare and  $\text{Al}_2\text{O}_3$  coated nanoparticles. The percent change increases as the laser pulse intensity increases. The percent change in LSPR bandwidth when the laser wavelength was 100 nm apart from the LSPR  $\lambda_{\text{max}}$  is plotted in Figure 5.8B. The LSPR bandwidth was slightly decreased after laser exposure.

About 5,000 silver nanoparticles are within the region that is probed by the white light. The nanoparticle size shows a Gaussian distribution and its standard deviation is expected to be similar to the size distribution of the nanoparticles (standard deviation  $\sim 5 \text{ nm}$ ) that are used for NSL.<sup>188</sup> When the wavelength of the laser is longer than the LSPR  $\lambda_{\text{max}}$  by 100 nm (off-resonant condition), the nanoparticles cannot be heated efficiently by the laser, but the larger nanoparticles within the Gaussian distribution can be heated more efficiently than smaller nanoparticles because they have a longer LSPR wavelength. The LSPR of the redder particles blue-shifts while the bluer particles are unchanged, which leads to the blue shift and bandwidth narrowing of the overall LSPR band.

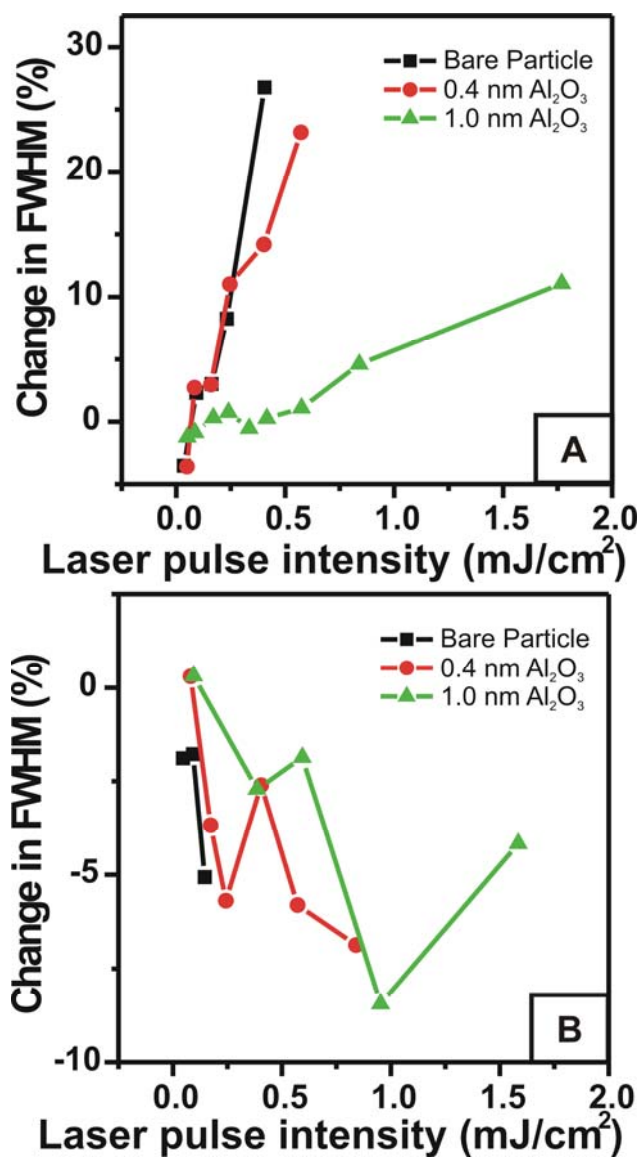


**Figure 5.8** Percent change in LSPR bandwidth after 120 sec laser exposure versus laser pulse intensity. (A) Resonant condition and (B) off-resonant condition.

In the case of the resonant condition, however, all the nanoparticles can be heated efficiently; therefore the bandwidth broadening after laser exposure cannot be explained by the argument above. When the laser is focused on the sample, the laser intensity shows a Gaussian profile, therefore the nanoparticles are heated inhomogeneously. Because the LSPR of the nanoparticles is monitored by white light having a spot size similar to the laser spot size, the resulting spectra is the average of all the nanoparticles with different amounts of shape deformation, which leads to the broadened overall LSPR band.

#### **5.4 Conclusion**

The laser induced LSPR change was monitored for NSL fabricated silver nanoparticles and silver nanoparticles coated with 0.4 nm and 1.0 nm of  $\text{Al}_2\text{O}_3$ . A blue shift of the LSPR band was observed after laser exposure, and this blue shift was explained by the rounded tips of the nanoparticles induced by laser heating. The blue shift of the LSPR became larger as the laser pulse energy increased both for the resonant and off-resonant conditions. The resonant condition showed a larger blue shift than the off-resonant condition for the same laser pulse energy because the laser energy can be more efficiently absorbed by the nanoparticles if the laser is resonant with the LSPR. The LSPR change after laser exposure was reduced when the silver nanoparticles were coated with ALD  $\text{Al}_2\text{O}_3$  layers, and coating with 1.0 nm of  $\text{Al}_2\text{O}_3$  showed enhanced protection compared with nanoparticles coated with 0.4 nm of  $\text{Al}_2\text{O}_3$ . The decreased LSPR shift of the nanoparticles coated with  $\text{Al}_2\text{O}_3$  compared to the bare nanoparticle was explained by increased surface melting temperature which results from the decreased mean-square displacement of the atoms located on the nanoparticle surface. The LSPR bandwidth was broadened for the resonant condition, while a slight narrowing of the LSPR band was observed for the off-resonant condition. The bandwidth broadening for the resonant condition was

explained by inhomogeneous sample heating caused by the Gaussian beam intensity profile. In the case of the off-resonant condition, more efficient heating for the redder sample led to bandwidth narrowing.

It is demonstrated that the ALD  $\text{Al}_2\text{O}_3$  layers provide enhanced stability of silver nanoparticles against the femtosecond laser exposure, and therefore the  $\text{Al}_2\text{O}_3$  coated nanoparticles can serve as a stable platform for surface-enhanced laser spectroscopy, including nonlinear spectroscopy. In the case of silver nanoparticles coated with 10 atomic layers of  $\text{Al}_2\text{O}_3$ , 10 times higher laser pulse intensity can be used compared to when the bare nanoparticles are used as substrates. However there is a trade off, because the local field enhancement by the nanoparticles drops quickly as the distance from the nanoparticle surface increases.<sup>210</sup> Therefore the thickness of the  $\text{Al}_2\text{O}_3$  layer should be carefully designed for the application as a substrate for laser spectroscopy. The work presented in this paper will provide criteria for selection of nanoparticle substrate and laser pulse intensity for various femtosecond laser spectroscopies.

Future work will be focused on testing the laser power stability of pre-annealed nanoparticles and such particles with  $\text{Al}_2\text{O}_3$  layers. The pre-annealing can be performed by moderate thermal heating<sup>242</sup> or incubation in organic solvents such as methanol,<sup>248</sup> and it is expected to reduce the sensitivity of the nanoparticle LSPR to laser exposure.

**References**

1. Fleischmann, M.; Hendra, P. J.; McQuillan, A. J. *Chem. Phys. Lett.* **1974**, *26*, 163.
2. Jeanmaire, D. L.; Van Duyne, R. P. *J. Electroanal. Chem.* **1977**, *84*, 1.
3. Hulteen, J. C.; Van Duyne, R. P. *J. Vac. Sci. Technol., A* **1995**, *13*, 1553.
4. Haynes, C. L.; Van Duyne, R. P. *J. Phys. Chem. B* **2001**, *105*, 5599.
5. McFarland, A. D.; Young, M. A.; Dieringer, J. A.; Van Duyne, R. P. *J. Phys. Chem. B* **2005**, *109*, 11279.
6. Yonzon, C. R.; Haynes, C. L.; Zhang, X.; Walsh, J. T.; Van Duyne, R. P. *Anal. Chem.* **2004**, *76*, 78.
7. Zhang, X.; Young, M. A.; Lyandres, O.; Van Duyne, R. P. *J. Am. Chem. Soc.* **2005**, *127*, 4484.
8. Haes, A. J.; Chang, L.; Klein, W. L.; Van Duyne, R. P. *J. Am. Chem. Soc.* **2005**, *127*, 2264.
9. Yonzon, C. R.; Jeoung, E.; Zou, S.; Schatz, G. C.; Mrksich, M.; Van Duyne, R. P. *J. Am. Chem. Soc.* **2004**, *126*, 12669.
10. Sherry, L. J.; Chang, S.-H.; Schatz, G. C.; Van Duyne, R. P.; Wiley, B. J.; Xia, Y. *Nano Lett.* **2005**, *5*, 2034.
11. Zou, S.; Janel, N.; Schatz, G. C. *J. Chem. Phys.* **2004**, *120*, 10871.
12. Zou, S.; Schatz, G. C. *J. Chem. Phys.* **2004**, *121*, 12606.
13. Zou, S.; Schatz, G. C. *Proc. SPIE-Int. Soc. Opt. Eng.* **2004**, *5513*, 22.
14. Hicks, E. M.; Zou, S.; Schatz, G. C.; Spears, K. G.; Van Duyne, R. P.; Gunnarsson, L.; Rindzevicius, T.; Kasemo, B.; Käll, M. *Nano Lett.* **2005**, *5*, 1065.
15. Walker, C. T.; Slack, G. A. *Am. J. Phys.* **1970**, *38*, 1380.
16. Ruthemann, G. *Ann. Phys.* **1948**, *2*, 107.
17. Lang, W. *Optik* **1948**, *3*, 233.
18. Watanabe, H. *J. Phys. Soc. Japan* **1956**, *11*, 112.
19. Ritchie, R. H. *Phys. Rev.* **1957**, *1*, 874.
20. Stern, E. A.; Ferrell, R. A. *Phys. Rev.* **1960**, *120*, 130.

21. Bohren, C. F.; Huffman, D. R. *Absorption and Scattering of Light by Small Particles*; WILEY-VCH: Weinheim, Germany, 2004.
22. Sambles, J. R.; Bradbery, G. W.; Yang, F. Z. *Contemp. Phys.* **1991**, *32*, 173.
23. Knoll, W. *Annu. Rev. Phys. Chem.* **1998**, *49*, 569.
24. Sarid, D. *Phys. Rev. Lett.* **1981**, *47*, 1927.
25. Burke, J. J.; Stegeman, G. I.; Tamir, T. *Phys. Rev. B* **1986**, *33*, 5186.
26. Okamoto, T.; H'Dhili, F.; Kawata, S. *Appl. Phys. Lett.* **2004**, *85*, 3968.
27. Winter, G.; Wedge, S.; Barnes, W. L. *New J. Phys.* **2006**, *8*, 1.
28. Mie, G. *Ann. Phys.* **1908**, *25*, 377.
29. van de Hulst, H. C. *Light Scattering by Small Particles*; Dover Publications, Inc.: Mineola, N.Y., 1981.
30. Papavassiliou, G. C. *Prog. Solid State Chem.* **1979**, *12*, 185.
31. Gans, R. *Ann. Phys.* **1912**, *37*, 881.
32. Haynes, C. L.; McFarland, A. D.; Zhao, L.; Van Duyne, R. P.; Schatz, G. C.; Gunnarsson, L.; Prikulis, J.; Kasemo, B.; Käll, M. *J. Phys. Chem. B* **2003**, *107*, 7337.
33. Lamprecht, B.; Schider, G.; Lechner, R. T.; Ditlbacher, H.; Krenn, J. R.; Leitner, A.; Aussenegg, F. R. *Phys. Rev. Lett.* **2000**, *84*, 4721.
34. Gunnarsson, L.; Rindzevicius, T.; Prikulis, J.; Kasemo, B.; Käll, M.; Zou, S.; Schatz, G. C. *J. Phys. Chem. B* **2005**, *109*, 1079.
35. Zhao, J.; Zhang, X.; Yonzon, C. R.; Haes, A. J.; Van Duyne, R. P. *Nanomedicine* **2006**, *1*, 219.
36. Willets, K. A.; Van Duyne, R. P. *Ann. Rev. Phys. Chem.* **2006**, *58*, 267.
37. Schatz, G. C.; Van Duyne, R. P. Electromagnetic mechanism of Surface-Enhanced Spectroscopy. In *Handbook of Vibrational Spectroscopy*; Chalmers, J. M., Griffiths, P. R., Eds.; John Wiley & Sons Ltd: Chichester, 2002; pp 759.
38. Albrecht, M. G.; Creighton, J. A. *J. Am. Chem. Soc.* **1977**, *99*, 5215.
39. Moskovits, M. *Rev. Mod. Phys.* **1985**, *57*, 783.
40. Haynes, C. L.; Van Duyne, R. P. *J. Phys. Chem. B* **2003**, *107*, 7426.
41. Nie, S.; Emory, S. R. *Science* **1997**, *275*, 1102.

42. Golab, J. T.; Sprague, J. R.; Carron, K. T.; Schatz, G. C.; Van Duyne, R. P. *J. Chem. Phys.* **1988**, *88*, 7942.
43. Hulteen, J. C.; Young, M. A.; Van Duyne, R. P. *Langmuir* **2006**, *22*, 10354.
44. Kneipp, K.; Kneipp, H.; Seifert, F. *Chem. Phys. Lett.* **1995**, *233*, 519.
45. Zhang, J.; Malicka, J.; Gryczynski, I.; Lakowicz, J. R. *J. Phys. Chem. B* **2005**, *109*, 7643.
46. Tovmachenko, O. G.; Graf, C.; van den Heuvel, D. J.; van Blaaderen, A.; Gerritsen, H. C. *Adv. Mater.* **2006**, *18*, 91.
47. Song, J.-H.; Atay, T.; Shi, S.; Urabe, H.; Nurmikko, A. V. *Nano Lett.* **2005**, *5*, 1557.
48. Clark, H. A.; Campagnola, P. J.; Wuskell, J. P.; Lewis, A.; Loew, L. M. *J. Am. Chem. Soc.* **2000**, *122*, 10234.
49. Chen, K.; Durak, C.; Heflin, J. R.; Robinson, H. D. *Nano Lett.* **2007**, *7*, 254.
50. Wenseleers, W.; Stellacci, F.; Meyer-Friedrichsen, T.; Mangel, T.; Bauer, C. A.; Pond, S. J. K.; Marder, S. R.; Perry, J. W. *J. Phys. Chem. B* **2002**, *106*, 6853.
51. Zhao, L.; Kelly, K. L.; Schatz, G. C. *J. Phys. Chem. B* **2003**, *107*, 7343.
52. Rechberger, W.; Hohenau, A.; Leitner, A.; Krenn, J. R.; Lamprecht, B.; Aussenegg, F. R. *Opt. Commun.* **2003**, *220*, 137.
53. Su, K.-H.; Wei, Q.-H.; Zhang, X.; Mock, J. J.; Smith, D. R.; Schultz, S. *Nano Lett.* **2003**, *3*, 1087.
54. Tamaru, H.; Kuwata, H.; Miyazaki, H. T.; Miyano, K. *Appl. Phys. Lett.* **2002**, *80*, 1826.
55. Atay, T.; Song, J.-H.; Nurmikko, A. V. *Nano Lett.* **2004**, *4*, 1627.
56. Maier, S. A.; Brongersma, M. L.; Kik, P. G.; Atwater, H. A. *Phys. Rev. B* **2002**, *65*, 193408.
57. Jensen, T.; Kelly, L.; Lazarides, A.; Schatz, G. C. *J. Cluster Sci.* **1999**, *10*, 295.
58. Ruppin, R. *Phys. Rev. B* **1982**, *26*, 3440.
59. Sönnichsen, C.; Reinhard, B. M.; Liphardt, J.; Alivisatos, A. P. *Nat. biotechnol.* **2005**, *23*, 741.
60. Reinhard, B. M.; Siu, M.; Agarwal, H.; Alivisatos, A. P.; Liphardt, J. *Nano Lett.* **2005**, *5*, 2246.
61. Zou, S.; Schatz, G. C. *Chem. Phys. Lett.* **2005**, *403*, 62.

62. Zhao, L.; Jensen, L.; Schatz, G. C. *J. Am. Chem. Soc.* **2006**, *128*, 2911.
63. Li, K.; Stockman, M. I.; Bergman, D. J. *Phys. Rev. Lett.* **2003**, *91*, 227402.
64. Qin, L.; Zou, S.; Xue, C.; Atkinson, A.; Schatz, G. C.; Mirkin, C. A. *Proc. Natl. Acad. Sci. U.S.A.* **2006**, *103*, 13300.
65. Sundaramurthy, A.; Crozier, K. B.; Kino, G. S.; Fromm, D. P.; Schuck, P. J.; Moerner, W. E. *Phys. Rev. B* **2005**, *72*, 165409.
66. Kumar, G. V. P.; Shruthi, S.; Vibha, B.; Reddy, B. A. A.; Kundu, T. K.; Narayana, C. J. *Phys. Chem. C* **2007**, *111*, 4388.
67. Lee, S. J.; Morrill, A. R.; Moskovits, M. J. *Am. Chem. Soc.* **2006**, *128*, 2200.
68. Xu, H.; Aizpurua, J.; Käll, M.; Apell, P. *Phys. Rev. E* **2000**, *62*, 4318.
69. Meier, M.; Wokaun, A.; Liao, P. F. *J. Opt. Soc. Am. B* **1985**, *2*, 931.
70. Carron, K. T.; Fluhr, W.; Meier, M.; Wokaun, A.; Lehmann, H. W. *J. Opt. Soc. Am. B* **1986**, *3*, 430.
71. Maiman, T. H. *Nature* **1960**, *187*, 493.
72. Collins, R. J.; Nelson, D. F.; Schawlow, A. L.; Bond, W.; Garrett, C. G. B.; Kaiser, W. *Phys. Rev. Lett.* **1960**, *5*, 303.
73. Shen, Y. R. *The Principles of Nonlinear Optics*; John Wiley & Sons, Inc.: Hoboken, NJ, 2003.
74. Franken, P. A.; Hill, A. E.; Peters, C. W.; Weinreich, G. *Phys. Rev. Lett.* **1961**, *7*, 118.
75. Boyd, R. W. *Nonlinear Optics*, 2nd ed.; Academic Press: San Diego, CA, 2003.
76. Mukamel, S. *Principles of Nonlinear Optical Spectroscopy*; Oxford University Press: New York, 1995.
77. Shen, Y. R. *Annu. Rev. Mater. Sci.* **1986**, *16*, 69.
78. Chen, C. K.; Heinz, T. F.; Ricard, D.; Shen, Y. R. *Phys. Rev. Lett.* **1981**, *46*, 1010.
79. Chen, C. K.; Heinz, T. F.; Ricard, D.; Shen, Y. R. *Phys. Rev. B* **1983**, *27*, 1965.
80. Heinz, T. F.; Chen, C. K.; Ricard, D.; Shen, Y. R. *Phys. Rev. Lett.* **1982**, *48*, 478.
81. Simpson, G. J.; Westerbuhr, S. G.; Rowlen, K. L. *Anal. Chem.* **2000**, *72*, 887.
82. Campagnola, P. J.; Wei, M.-d.; Lewis, A.; Loew, L. M. *Biophys. J.* **1999**, *77*, 3341.

83. Kim, J.; Somorjai, G. A. *J. Am. Chem. Soc.* **2003**, *125*, 3150.
84. Dombeck, D. A.; Kasischke, K. A.; Vishwasrao, H. D.; Ingelsson, M.; Hyman, B. T.; Webb, W. W. *Proc. Natl. Acad. Sci. U.S.A.* **2003**, *100*, 7081.
85. Schaller, R. D.; Johnson, J. C.; Wilson, K. R.; Lee, L. F.; Haber, L. H.; Saykally, R. J. *J. Phys. Chem. B* **2002**, *106*, 5143.
86. Miranda, P. B.; Shen, Y. R. *J. Phys. Chem. B* **1999**, *103*, 3292.
87. Buck, M.; Himmelhaus, M. *J. Vac. Sci. Technol., A* **2001**, *19*, 2717.
88. Baldelli, S.; Eppler, A. S.; Anderson, E.; Shen, Y. R.; Somorjai, G. A. *J. Chem. Phys.* **2000**, *113*, 5432.
89. Stokes, G. Y.; Gibbs-Davis, J. M.; Boman, F. C.; Stepp, B. R.; Condie, A. G.; Nguyen, S. T.; Geiger, F. M. *J. Am. Chem. Soc.* **2007**, *129*, 7492.
90. Belkin, M. A.; Shen, Y. R. *Int. Rev. Phys. Chem.* **2005**, *24*, 257.
91. Mao, M. Y.; Miranda, P. B.; Kim, D. S.; Shen, Y. R. *Phys. Rev. B* **2001**, *6403*, 035415.
92. Mifflin, A. L.; Gerth, K. A.; Geiger, F. M. *J. Phys. Chem. A* **2003**, *107*, 9620.
93. Heinz, T. F.; Loy, M. M. T.; Thompson, W. A. *Phys. Rev. Lett.* **1985**, *54*, 63.
94. Murphy, R.; Yeganeh, M.; Song, K. J.; Plummer, E. W. *Phys. Rev. Lett.* **1989**, *63*, 318.
95. Wong, E. K. L.; Richmond, G. L. *J. Chem. Phys.* **1993**, *99*, 5500.
96. Yan, E. C. Y.; Liu, Y.; Eisenthal, K. B. *J. Phys. Chem. B* **1998**, *102*, 6331.
97. Peleg, G.; Lewis, A.; Linial, M.; Loew, L. M. *Proc. Natl. Acad. Sci. U.S.A.* **1999**, *96*, 6700.
98. Chen, C. K.; de Castro, A. R. B.; Shen, Y. R. *Phys. Rev. Lett.* **1981**, *46*, 145.
99. Boyd, G. T.; Rasing, T.; Leite, J. R. R.; Shen, Y. R. *Phys. Rev. B* **1984**, *30*, 519.
100. Wokaun, A.; Bergman, J. G.; Heritage, J. P.; Glass, A. M.; Liao, P. F.; Olson, D. H. *Phys. Rev. B* **1981**, *24*, 849.
101. Sandrock, M. L.; Pibel, C. D.; Geiger, F. M.; Foss, C. A. *J. Phys. Chem. B* **1999**, *103*, 2668.
102. Podlipensky, A.; Lange, J.; Seifert, G.; Graener, H.; Cravetchi, I. *Opt. Lett.* **2003**, *28*, 716.
103. Antoine, R.; Brevet, P. F.; Girault, H. H.; Bethell, D.; Schiffrin, D. J. *Chem. Commun.* **1997**, 1901.

104. Antoine, R.; Pellarin, M.; Palpant, B.; Broyer, M.; Prével, B.; Galletto, P.; Brevet, P. F.; Girault, H. H. *J. Appl. Phys.* **1998**, *84*, 4532.
105. Hao, E. C.; Schatz, G. C.; Johnson, R. C.; Hupp, J. T. *J. Chem. Phys.* **2002**, *117*, 5963.
106. Johnson, R. C.; Li, J. T.; Hupp, J. T.; Schatz, G. C. *Chem. Phys. Lett.* **2002**, *356*, 534.
107. Vance, F. W.; Lemon, B. I.; Hupp, J. T. *J. Phys. Chem. B* **1998**, *102*, 10091.
108. Russier-Antoine, I.; Jonin, C.; Nappa, J.; Bénichou, E.; Brevet, P.-F. *J. Chem. Phys.* **2004**, *120*, 10748.
109. Jin, R.; Jureller, J. E.; Kim, H. Y.; Scherer, N. F. *J. Am. Chem. Soc.* **2005**, *127*, 12482.
110. Lamprecht, B.; Leitner, A.; Aussenegg, F. R. *Appl. Phys. B* **1997**, *64*, 269.
111. Lamprecht, B.; Leitner, A.; Aussenegg, F. R. *Appl. Phys. B* **1999**, *68*, 419.
112. Lamprecht, B.; Krenn, J. R.; Leitner, A.; Aussenegg, F. R. *Appl. Phys. B* **1999**, *69*, 223.
113. Canfield, B. K.; Kujala, S.; Laiho, K.; Jefimovs, K.; Turunen, J.; Kauranen, M. *Opt. Express* **2006**, *14*, 950.
114. Haes, A. J.; Van Duyne, R. P. *J. Am. Chem. Soc.* **2002**, *124*, 10596.
115. Zhao, J.; Das, A.; Zhang, X.; Schatz, G. C.; Sligar, S. G.; Van Duyne, R. P. *J. Am. Chem. Soc.* **2006**, *128*, 11004.
116. Henglein, A.; Meisel, D. *J. Phys. Chem. B* **1998**, *102*, 8364.
117. Elghanian, R.; Storhoff, J. J.; Mucic, R. C.; Letsinger, R. L.; Mirkin, C. A. *Science* **1997**, *277*, 1078.
118. Dirix, Y.; Bastiaansen, C.; Caseri, W.; Smith, P. *Adv. Mater.* **1999**, *11*, 223.
119. Ebbesen, T. W.; Lezec, H. J.; Ghaemi, H. F.; Thio, T.; Wolff, P. A. *Nature* **1998**, *391*, 667.
120. Quinten, M.; Leitner, A.; Krenn, J. R.; Aussenegg, F. R. *Opt. Lett.* **1998**, *23*, 1331.
121. Brongersma, M. L.; Hartman, J. W.; Atwater, H. A. *Phys. Rev. B* **2000**, *62*, R16356.
122. Egusa, S.; Liau, Y. H.; Scherer, N. F. *Appl. Phys. Lett.* **2004**, *84*, 1257.
123. Freeman, R. G.; Grabar, K. C.; Allison, K. J.; Bright, R. M.; Davis, J. A.; Guthrie, A. P.; Hommer, M. B.; Jackson, M. A.; Smith, P. C.; Walter, D. G.; Natan, M. J. *Science* **1995**, *267*, 1629.
124. Kahl, M.; Voges, E.; Kostrewa, S.; Viets, C.; Hill, W. *Sens. Actuators, B* **1998**, *51*, 285.

125. Wallraff, G. M.; Hinsberg, W. D. *Chem. Rev.* **1999**, *99*, 1801.
126. Ito, T.; Okazaki, S. *Nature* **2000**, *406*, 1027.
127. Craighead, H. G.; Niklasson, G. A. *Appl. Phys. Lett.* **1984**, *44*, 1134.
128. Piner, R. D.; Zhu, J.; Xu, F.; Hong, S.; Mirkin, C. A. *Science* **1999**, *283*, 661.
129. Canfield, B. K.; Kujala, S.; Jefimovs, K.; Vallius, T.; Turunen, J.; Kauranen, M. *J. Opt. A: Pure Appl. Opt.* **2005**, *7*, S110.
130. Bouhelier, A.; Bachelot, R.; Im, J. S.; Wiederrecht, G. P.; Lerondel, G.; Kostcheev, S.; Royer, P. *J. Phys. Chem. B* **2005**, *109*, 3195.
131. Félidj, N.; Aubard, J.; Lévi, G.; Krenn, J. R.; Schider, G.; Leitner, A.; Aussenegg, F. R. *Phys. Rev. B* **2002**, *66*, 245407.
132. Félidj, N.; Laurent, G.; Aubard, J.; Lévi, G.; Hohenau, A.; Krenn, J. R.; Aussenegg, F. R. *J. Chem. Phys.* **2005**, *123*, 221103.
133. Schider, G.; Krenn, J. R.; Gotschy, W.; Lamprecht, B.; Ditlbacher, H.; Leitner, A.; Aussenegg, F. R. *J. Appl. Phys.* **2001**, *90*, 3825.
134. Kelly, K. L.; Coronado, E.; Zhao, L.; Schatz, G. C. *J. Phys. Chem. B* **2003**, *107*, 668.
135. Malynych, S.; Chumanov, G. *J. Am. Chem. Soc.* **2003**, *125*, 2896.
136. Taleb, A.; Russier, V.; Courty, A.; Pileni, M. P. *Phys. Rev. B* **1999**, *59*, 13350.
137. Moran, A. M.; Sung, J.; Hicks, E. M.; Van Duyne, R. P.; Spears, K. G. *J. Phys. Chem. B* **2005**, *109*, 4501.
138. Canfield, B. K.; Kujala, S.; Jefimovs, K.; Turunen, J.; Kauranen, M. *Opt. Express* **2004**, *12*, 5418.
139. Tuovinen, H.; Kauranen, M.; Jefimovs, K.; Vahimaa, P.; Vallius, T.; Turunen, J.; Tkachenko, N. V.; Lemmetyinen, H. *J. Nonlinear Opt. Phys. Mater.* **2002**, *11*, 421.
140. Zou, S.; Schatz, G. C. *J. Chem. Phys.* **2005**, *122*, 097102.
141. Jensen, T. R.; Duval, M. L.; Kelly, K. L.; Lazarides, A. A.; Schatz, G. C.; Van Duyne, R. P. *J. Phys. Chem. B* **1999**, *103*, 9846.
142. Kreibig, U.; Vollmer, M. *Optical Properties of Metal Clusters*; Springer-Valag: Heidelberg, Germany, 1995; Vol. 25.
143. Linden, S.; Christ, A.; Kuhl, J.; Giessen, H. *Appl. Phys. B* **2001**, *73*, 311.
144. Linden, S.; Kuhl, J.; Giessen, H. *Phys. Rev. Lett.* **2001**, *86*, 4688.

145. Canfield, B. K.; Kujala, S.; Kauranen, M.; Jefimovs, K.; Vallius, T.; Turunen, J. *Appl. Phys. Lett.* **2005**, *86*, 183109.
146. Jensen, T. R.; Malinsky, M. D.; Haynes, C. L.; Van Duyne, R. P. *J. Phys. Chem. B* **2000**, *104*, 10549.
147. Chan, G. H.; Zhao, J.; Hicks, E. M.; Schatz, G. C.; Van Duyne, R. P. *Nano Lett.* **2007**, *7*, 1947.
148. Scime, E. E.; Anderson, E. H.; McComas, D. J.; Schattenburg, M. L. *Appl. Optics* **1995**, *34*, 648.
149. Schnabel, B.; Kley, E.-B.; Wyrowski, F. *Opt. Eng.* **1999**, *38*, 220.
150. Yu, Z.; Deshpande, P.; Wu, W.; Wang, J.; Chou, S. Y. *Appl. Phys. Lett.* **2000**, *77*, 927.
151. Gruntman, M. *Appl. Optics* **1995**, *34*, 5732.
152. Ono, Y.; Kimura, Y.; Ohta, Y.; Nishida, N. *Appl. Optics* **1987**, *26*, 1142.
153. Smith, R. E.; Warren, M. E.; Wendt, J. R.; Vawter, G. A. *Opt. Lett.* **1996**, *21*, 1201.
154. Enger, R. C.; Case, S. K. *Appl. Optics* **1983**, *22*, 3220.
155. Cescato, L. H.; Gluch, E.; Streibl, N. *Appl. Optics* **1990**, *29*, 3286.
156. Wendt, J. R.; Vawter, G. A.; Smith, R. E.; Warren, M. E. *J. Vac. Sci. Technol. B* **1997**, *15*, 2946.
157. Born, M.; Wolf, E. *Principles of Optics*, 6th ed.; Cambridge University Press: Cambridge, UK, 1997.
158. Yariv, A.; Yeh, P. *J. Opt. Soc. Am.* **1977**, *67*, 438.
159. Flanders, D. C. *Appl. Phys. Lett.* **1983**, *42*, 492.
160. Glytsis, E. N.; Gaylord, T. K. *Appl. Optics* **1992**, *31*, 4459.
161. Richter, I.; Sun, P.-C.; Xu, F.; Fainman, Y. *Appl. Optics* **1995**, *34*, 2421.
162. Xu, F.; Tyan, R.-C.; Sun, P.-C.; Fainman, Y.; Cheng, C.-C.; Scherer, A. *Opt. Lett.* **1995**, *20*, 2457.
163. Brundrett, D. L.; Gaylord, T. K.; Glytsis, E. N. *Appl. Optics* **1998**, *37*, 2534.
164. Shiraishi, K.; Sato, T.; Kawakami, S. *Appl. Phys. Lett.* **1991**, *58*, 211.
165. Yeh, P. *Opt. Commun.* **1978**, *26*, 289.

166. Tamada, H.; Doumuki, T.; Yamaguchi, T.; Matsumoto, S. *Opt. Lett.* **1997**, *22*, 419.
167. Chen, E.; Chou, S. Y. *Appl. Phys. Lett.* **1997**, *70*, 2673.
168. Genet, C.; Ebbesen, T. W. *Nature* **2007**, *445*, 39.
169. Barnes, W. L.; Dereux, A.; Ebbesen, T. W. *Nature* **2003**, *424*, 824.
170. Lord Rayleigh, O. M., F.R.S. *Philos. Mag.* **1918**, *35*, 373.
171. Kerker, M.; La Mer, V. K. *J. Am. Chem. Soc.* **1950**, *72*, 3516.
172. Heller, W.; Nakagaki, M. *Journal of Chemical Physics* **1974**, *61*, 3619.
173. Yang, H. *J. Phys. Chem. A* **2007**, *111*, 4987.
174. Bazhan, W.; Kolwas, K.; Kolwas, M. *Opt. Commun.* **2002**, *211*, 171.
175. Gryczynski, Z.; Lukomska, J.; Lakowicz, J. R.; Matveeva, E. G.; Gryczynski, I. *Chem. Phys. Lett.* **2006**, *421*, 189.
176. Klitgaard, S.; Shtoyko, T.; Calander, N.; Gryczynski, I.; Matveeva, E. G.; Borejdo, J.; Neves-Petersen, M. T.; Petersen, S. B.; Gryczynski, Z. *Chem. Phys. Lett.* **2007**, *443*, 1.
177. Calander, N.; Gryczynski, I.; Gryczynski, Z. *Chem. Phys. Lett.* **2007**, *434*, 326.
178. Khlebtsov, N. G.; Melnikov, A. G.; Bogatyrev, V. A.; Dykman, L. A.; Alekseeva, A. V.; Trachuk, L. A.; Khlebtsov, B. N. *J. Phys. Chem. B* **2005**, *109*, 13578.
179. Alekseeva, A. V.; Bogatyrev, V. A.; Dykman, L. A.; Khlebtsov, B. N.; Trachuk, L. A.; Melnikov, A. G.; Khlebtsov, N. G. *Appl. Optics* **2005**, *44*, 6285.
180. Sung, J.; Hicks, E. M.; Van Duyne, R. P.; Spears, K. G. *J. Phys. Chem. C* **2007**, *111*, 10368.
181. Hecht, E. *Optics*, 4th ed.; Addison Wesley: San Francisco, CA, 2002.
182. Fowles, G. R. *Introduction to Modern Optics*, 2nd ed.; Dover Publications, Inc.: Mineola, NY, 1989.
183. Lee, S.-M.; Jun, Y.-W.; Cho, S.-N.; Cheon, J. *J. Am. Chem. Soc.* **2002**, *124*, 11244.
184. Petroski, J. M.; Green, T. C.; El-Sayed, M. A. *J. Phys. Chem. A* **2001**, *105*, 5542.
185. Jana, N. R.; Gearheart, L.; Murphy, C. J. *J. Phys. Chem. B* **2001**, *105*, 4065.
186. Kim, F.; Song, J. H.; Yang, P. *J. Am. Chem. Soc.* **2002**, *124*, 14316.

187. Jin, R.; Cao, Y.; Mirkin, C. A.; Kelly, K. L.; Schatz, G. C.; Zheng, J. G. *Science* **2001**, *294*, 1901.
188. Hulteen, J. C.; Treichel, D. A.; Smith, M. T.; Duval, M. L.; Jensen, T. R.; Van Duyne, R. P. *J. Phys. Chem. B* **1999**, *103*, 3854.
189. Santos, B. S.; Pereira, G. A. L.; Petrov, D. V.; de Mello Donegá, C. *Opt. Commun.* **2000**, *178*, 187.
190. Jacobsohn, M.; Banin, U. *J. Phys. Chem. B* **2000**, *104*, 1.
191. Bavli, R.; Yogev, D.; Efrima, S.; Berkovic, G. *J. Phys. Chem.* **1991**, *95*, 7422.
192. Götz, T.; Buck, M.; Dressler, C.; Eisert, F.; Träger, F. *Appl. Phys. A* **1995**, *60*, 607.
193. Simon, M.; Träger, F.; Assion, A.; Lang, B.; Voll, S.; Gerber, G. *Chem. Phys. Lett.* **1998**, *296*, 579.
194. Müller, T.; Vaccaro, P. H.; Balzer, F.; Rubahn, H. G. *Opt. Commun.* **1997**, *135*, 103.
195. Srinivasan, R.; Tian, Y.; Suni, I. I. *Surf. Sci.* **2001**, *490*, 308.
196. Hayakawa, T.; Usui, Y.; Bharathi, S.; Nogami, M. *Adv. Mater.* **2004**, *16*, 1408.
197. Bloembergen, N.; Chang, R. K.; Jha, S. S.; Lee, C. H. *Phys. Rev.* **1968**, *174*, 813.
198. Hua, X. M.; Gersten, J. I. *Phys. Rev. B* **1986**, *33*, 3756.
199. Lo, K. Y.; Lue, J. T. *Phys. Rev. B* **1995**, *51*, 2467.
200. Dewitz, J. P.; Hübner, W.; Bennemann, K. H. *Z. Phys. D* **1996**, *37*, 75.
201. Zheludev, N. I.; Emel'yanov, V. I. *J. Opt. A: Pure Appl. Opt.* **2004**, *6*, 26.
202. Dadap, J. I.; Shan, J.; Eisenthal, K. B.; Heinz, T. F. *Phys. Rev. Lett.* **1999**, *83*, 4045.
203. Dadap, J. I.; Shan, J.; Heinz, T. F. *J. Opt. Soc. Am. B* **2004**, *21*, 1328.
204. Mendoza, B. S.; Mochán, W. L. *Phys. Rev. B* **1996**, *53*, 4999.
205. Brudny, V. L.; Mendoza, B. S.; Mochán, W. L. *Physical Review B* **2000**, *62*, 11152.
206. Pustogowa, U.; Hübner, W.; Bennemann, K. H. *Phys. Rev. B* **1993**, *48*, 8607.
207. Hübner, W. *Phys. Rev. B* **1990**, *42*, 11553.
208. Hübner, W.; Bennemann, K. H.; Böhmer, K. *Phys. Rev. B* **1994**, *50*, 17597.

209. Haynes, C. L.; McFarland, A. D.; Smith, M. T.; Hulteen, J. C.; Van Duyne, R. P. *J. Phys. Chem. B* **2002**, *106*, 1898.
210. Dieringer, J. A.; McFarland, A. D.; Shah, N. C.; Stuart, D. A.; Whitney, A. V.; Yonzon, C. R.; Young, M. A.; Zhang, X.; Van Duyne, R. P. *Faraday Discuss.* **2006**, *132*, 9.
211. Hao, E.; Schatz, G. C. *J. Chem. Phys.* **2004**, *120*, 357.
212. Rossi, R. C.; Lewis, N. S. *J. Phys. Chem. B* **2001**, *105*, 12303.
213. Marin, T. W.; Homoelle, B. J.; Spears, K. G.; Hupp, J. T.; Spreer, L. O. *J. Phys. Chem. A* **2002**, *106*, 1131.
214. Huang, C.-P.; Kapteyn, H. C.; McIntosh, J. W.; Murnane, M. M. *Opt. Lett.* **1992**, *17*, 139.
215. Squier, J.; Korn, G.; Mourou, G.; Vaillancourt, G.; Bouvier, M. *Opt. Lett.* **1993**, *18*, 625.
216. Akhremitchev, B.; Wang, C.; Walker, G. C. *Rev. Sci. Instrum.* **1996**, *67*, 3799.
217. Draine, B. T.; Flatau, P. J. *J. Opt. Soc. Am. A* **1994**, *11*, 1491.
218. Yang, W. H.; Schatz, G. C.; Van Duyne, R. P. *J. Chem. Phys.* **1995**, *103*, 869.
219. Malinsky, M. D.; Kelly, K. L.; Schatz, G. C.; Van Duyne, R. P. *J. Phys. Chem. B* **2001**, *105*, 2343.
220. Kawasaki, M.; Hori, M. *J. Phys. Chem. B* **2003**, *107*, 6760.
221. Link, S.; Burda, C.; Mohamed, M. B.; Nikoobakht, B.; El-Sayed, M. A. *J. Phys. Chem. A* **1999**, *103*, 1165.
222. Huang, W.; Qian, W.; El-Sayed, M. A. *J. Am. Chem. Soc.* **2006**, *128*, 13330.
223. Huang, W.; Qian, W.; El-Sayed, M. A. *J. Appl. Phys.* **2005**, *98*, 114301.
224. Eisenthal, K. B. *Chem. Rev.* **2006**, *106*, 1462.
225. Kweskin, S. J.; Rioux, R. M.; Habas, S. E.; Komvopoulos, K.; Yang, P.; Somorjai, G. A. *J. Phys. Chem. B* **2006**, *110*, 15920.
226. Kawai, T.; Neivandt, D. J.; Davies, P. B. *J. Am. Chem. Soc.* **2000**, *122*, 12031.
227. Liang, E. J.; Weippert, A.; Funk, J.-M.; Materny, A.; Kiefer, W. *Chem. Phys. Lett.* **1994**, *227*, 115.
228. Koo, T.-W.; Chan, S.; Berlin, A. A. *Opt. Lett.* **2005**, *30*, 1024.
229. Ichimura, T.; Hayazawa, N.; Hashimoto, M.; Inouye, Y.; Kawata, S. *J. Raman Spectrosc.* **2003**, *34*, 651.

230. Hayazawa, N.; Ichimura, T.; Hashimoto, M.; Inouye, Y.; Kawata, S. *J. Appl. Phys.* **2004**, *95*, 2676.
231. Link, S.; Ei-Sayed, M. A. *Annu. Rev. Phys. Chem.* **2003**, *54*, 331.
232. Hartland, G. V. *J. Chem. Phys.* **2002**, *116*, 8048.
233. Hodak, J. H.; Henglein, A.; Hartland, G. V. *J. Phys. Chem. B* **2000**, *104*, 9954.
234. Hu, M.; Wang, X.; Hartland, G. V.; Mulvaney, P.; Juste, J. P.; Sader, J. E. *J. Am. Chem. Soc.* **2003**, *125*, 14925.
235. Huang, W.; Qian, W.; El-Sayed, M. A. *Nano Lett.* **2004**, *4*, 1741.
236. Habenicht, A.; Olapinski, M.; Burmeister, F.; Leiderer, P.; Boneberg, J. *Science* **2005**, *309*, 2043.
237. Kaempfe, M.; Rainer, T.; Berg, K.-J.; Seifert, G.; Graener, H. *Appl. Phys. Lett.* **1999**, *74*, 1200.
238. Miranda, M. H. G.; Falcão-Filho, E. L.; Rodrigues, J. J.; de Araújo, C. B.; Acioli, L. H. *Phys. Rev. B* **2004**, *70*, 161401.
239. Shi, F. G. *J. Mater. Res.* **1994**, *9*, 1307.
240. Buffat, P.; Borel, J.-P. *Phys. Rev. A* **1976**, *13*, 2287.
241. Dick, K.; Dhanasekaran, T.; Zhang, Z.; Meisel, D. *J. Am. Chem. Soc.* **2002**, *124*, 2312.
242. Whitney, A. V.; Elam, J. W.; Stair, P. C.; Van Duyne, R. P. *J. Phys. Chem. B* **2007**, accepted.
243. Bañares, M. A. *Catal. Today* **2005**, *100*, 71.
244. Elam, J. W.; Groner, M. D.; George, S. M. *Rev. Sci. Instrum.* **2002**, *73*, 2981.
245. Ott, A. W.; Klaus, J. W.; Johnson, J. M.; George, S. M. *Thin Solid Films* **1997**, *292*, 135.
246. Groner, M. D.; Fabreguette, F. H.; Elam, J. W.; George, S. M. *Chem. Mater.* **2004**, *16*, 639.
247. Whitney, A. V.; Elam, J. W.; Zou, S.; Zinovev, A. V.; Stair, P. C.; Schatz, G. C.; Van Duyne, R. P. *J. Phys. Chem. B* **2005**, *109*, 20522.
248. Malinsky, M. D.; Kelly, K. L.; Schatz, G. C.; Van Duyne, R. P. *J. Am. Chem. Soc.* **2001**, *123*, 1471.
249. Zhang, X.; Hicks, E. M.; Zhao, J.; Schatz, G. C.; Van Duyne, R. P. *Nano Lett.* **2005**, *5*, 1503.

250. Del Fatti, N.; Voisin, C.; Achermann, M.; Tzortzakis, S.; Christofilos, D.; Vallée, F. *Phys. Rev. B* **2000**, *61*, 16956.
251. Voisin, C.; Christofilos, D.; Del Fatti, N.; Vallée, F.; Prével, B.; Cottancin, E.; Lermé, J.; Pellarin, M.; Broyer, M. *Phys. Rev. Lett.* **2000**, *85*, 2200.
252. Hodak, J. H.; Martini, I.; Hartland, G. V. *J. Phys. Chem. B* **1998**, *102*, 6958.
253. Link, S.; Burda, C.; Nikoobakht, B.; El-Sayed, M. A. *Chem. Phys. Lett.* **1999**, *315*, 12.
254. Link, S.; Hathcock, D. J.; Nikoobakht, B.; El-Sayed, M. A. *Adv. Meter.* **2003**, *15*, 393.
255. *CRC Handbook of Chemistry and Physics*, 82nd ed.; CRC Press: Boca Raton, FL, 2001.
256. Link, S.; El-Sayed, M. A. *J. Phys. Chem. B* **1999**, *103*, 8410.
257. Westcott, S. L.; Averitt, R. D.; Wolfgang, J. A.; Nordlander, P.; Halas, N. J. *J. Phys. Chem. B* **2001**, *105*, 9913.
258. Lindemann, F. A. *Phys. Z.* **1910**, *11*, 609.
259. McFarland, E. W.; Tang, J. *Nature* **2003**, *421*, 616.
260. Zhang, C.; Du, M.-H.; Cheng, H.-P.; Zhang, X.-G.; Roitberg, A. E.; Krause, J. L. *Phys. Rev. Lett* **2004**, *92*, 158301.
261. Reed, M. A.; Zhou, C.; Muller, C. J.; Burgin, T. P.; Tour, J. M. *Science* **1997**, *278*, 252.
262. Nitzan, A. *Annu. Rev. Phys. Chem.* **2001**, *52*, 681.
263. Nitzan, A.; Ratner, M. A. *Science* **2003**, *300*, 1384.
264. Bumm, L. A.; Arnold, J. J.; Cygan, M. T.; Dunbar, T. D.; Burgin, T. P.; Jones II, L.; Allara, D. L.; Tour, J. M.; Weiss, P. S. *Science* **1996**, *271*, 1705.
265. Petek, H.; Ogawa, S. *Prog. Surf. Sci.* **1997**, *56*, 239.
266. Zhu, X. Y. *Surf. Sci. Rep.* **2004**, *56*, 1.
267. Netzer, F. P.; Bertel, E.; Matthew, J. A. D. *Surf. Sci.* **1980**, *92*, 43.
268. Avouris, P.; Demuth, J. E. *J. Chem. Phys.* **1981**, *75*, 4783.
269. Harris, C. B.; Zwemer, D. A.; Gallo, A. R.; Robota, H. J. *Surf. Sci* **1979**, *85*, L205.
270. Robota, H. J.; Whitmore, P. M.; Harris, C. B. *J. Chem. Phys* **1982**, *76*, 1692.
271. Glass, A. M.; Liao, P. F.; Bergman, J. G.; Olson, D. H. *Opt. Lett.* **1980**, *5*, 368.

272. Haes, A. J.; Zou, S.; Zhao, J.; Schatz, G. C.; Van Duyne, R. P. *J. Am. Chem. Soc* **2006**, *128*, 10905.
273. Zhao, J.; Jensen, L.; Sung, J.; Zou, S.; Schatz, G. C.; Van Duyne, R. P. *J. Am. Chem. Soc* **2007**, *129*, 7647.
274. Labsphere Technical Guide *A Guide to Integrating Sphere Theory and Application*; Labsphere, Inc. Publication, 1997.
275. Labsphere Technical Guide *A Guide to Integrating Sphere Radiometry and Photometry*; Labsphere, Inc. Publication.
276. Goebel, D. G. *Appl. Optics* **1967**, *6*, 125.
277. Tai, W.-P. *Mater. Lett.* **2001**, *51*, 451.
278. Nordlander, P.; Prodan, E. *Nano Lett.* **2004**, *4*, 2209.
279. Hohenester, U.; Krenn, J. *Phys. Rev. B* **2005**, *72*, 195429.
280. Schmeits, M.; Dambly, L. *Phys. Rev. B* **1991**, *44*, 12706.
281. Sweatlock, L. A.; Maier, S. A.; Atwater, H. A.; Penninkhof, J. J.; Polman, A. *Phys. Rev. B* **2005**, *71*, 235408.
282. Maier, S. A.; Kik, P. G.; Atwater, H. A. *Appl. Phys. Lett.* **2002**, *81*, 1714.
283. Wei, Q.-H.; Su, K.-H.; Durant, S.; Zhang, X. *Nano Lett.* **2004**, *4*, 1067.
284. Ng, M.-Y.; Liu, W.-C. *Opt. Express* **2006**, *14*, 4504.

## **Appendix 1**

### **Absorption Measurement of Dyes Adsorbed on Silver Film**

## A1.1 Introduction

When organic chromophores are adsorbed on a metal surface, their electronic levels couple to the metal conduction level, therefore the optical property of the molecule adsorbed on metal is altered from that of isolated or solvated molecule. There have been attempts to introduce organic molecules to electronic, optoelectronic and photovoltaic devices.<sup>259-261</sup> The electronic coupling in molecule-metal junction plays a key role in the electrical conductance,<sup>261-263</sup> therefore, understanding the electronic structure of the molecules in contact with the metal is essential for development of such devices. There have been several approaches to investigate the molecular electronic structure adsorbed on metal. From scanning tunneling microscope (STM) experiments, conductivity information can be obtained.<sup>264</sup> Two-photon photoemission (2PPE) spectroscopy is a strong tool for quantitative determination of the electronic structure, such as the highest occupied molecular orbital (HOMO) and the lowest unoccupied molecular orbital (LUMO) of adsorbate-substrate system.<sup>265,266</sup> Electronic excitations of the molecules adsorbed on metal surfaces have been studied by electron energy loss spectroscopy (EELS) also. Netzer et al. studied the electronic excitation of benzene and pyridine on Ir(111) surface by EELS method.<sup>267</sup> Avouris et al. studied benzene, pyridine, and pyrazine adsorbed on Ag(111) surface by the same method,<sup>268</sup> and they reported the 0.1 – 0.2 eV shift of molecular electronic excitation energy upon adsorption on the silver surface. Absorbance measurements on surface adsorbed molecules have been performed by several methods. Harris and coworkers reported the absorbance spectra of the aromatic hydrocarbons, such as pyrazine, pyridine, benzene and naphthalene adsorbed on Ni(111) surface obtained by UV-vis spectroscopic ellipsometry.<sup>269,270</sup> McFarland et al. obtained the absorbance spectra of merbromin adsorbed on gold film by an integrating sphere.<sup>259</sup>

The coupling between the dye resonance and metal surface plasmon has also been studied. Glass et al.<sup>271</sup> reported that when dye molecules are adsorbed on a silver island film, their electronic resonance couples strongly with the plasmon resonance of the metal. When a rhodamine B ethanol solution was spin-coated on a silver island film, the plasmon resonance of the film showed a large shift even though the absorption of the dye alone was quite weak. Recently, Van Duyne and coworkers<sup>272,273</sup> fabricated silver nanoparticle arrays with various localized surface plasmon resonance (LSPR) position by nanosphere lithography (NSL),<sup>4</sup> and plotted the LSPR shift before and after dye adsorption versus the LSPR of the bare nanoparticle array. Rhodamine 6G, [2,3,7,8,12,13,17,18-Octakis-(propyl)porphyrinato]magnesium(II), and iron(II) tris-2,2'-bipyridine were tested in their study. They reported that the LSPR shift of the silver nanoparticle array after the dye adsorption is extremely sensitive to the molecular resonance of the dye molecule.<sup>272,273</sup> They tried to explain the observed derivative-like behavior of the LSPR shift by several approaches, including Kramers-Kronig analysis. The real part of the refractive index of the dye layer is calculated from the Kramers-Kronig transformation of the imaginary counter part derived from absorption measurement, and it is compared with the LSPR shift profile. Absorption spectrum of the dye adsorbed on silver nanoparticle is different from that of a hydrated dye; therefore obtaining the spectrum of the dye on the silver surface is essential for the precise analysis of the data. In their study, the absorption spectra of a dye adsorbed on a silver film was measured by an integrating sphere. Ideally, the absorbance of dye adsorbed on the silver nanoparticle array should be measured, however, the silver film was used as a substrate because the LSPR of the nanoparticle array interferes with the absorption measurement.<sup>273</sup>

This chapter will focus on describing the absorption measurement procedure using an integrating sphere. An integrating sphere consists of a hollow sphere of which interior is coated with a diffuse reflective material with high reflectance. There are small holes which act as input and output ports. Inside the integrating sphere, the fraction of radiant flux received by a certain area is the same for any radiating point on the sphere surface and fraction of radiant flux received by the certain area from a radiating point is the fractional surface area of the certain area consumes within a sphere.<sup>274</sup> It is the key feature of the integrating sphere. The integrating sphere is used for various optical, radiometry, and photometry measurements, such as reflectance measurement on a surface, transmittance measurement for a turbid sample, measurement of total geometric luminous flux from electric lamps, and laser power measurement.<sup>274,275</sup>

The basic theory and geometry of the integrating sphere is introduced in the following section. Sample preparation and the modified integrating sphere setup for fiber optic coupling are presented in section A1.3, and results and conclusion are provided in section A1.4 and A1.5 respectively.

## A1.2 Integrating Sphere Theory

### A1.2.1 Radiance Equation

Inside the integrating sphere, the radiance increases due to multiple reflections of the incident light.<sup>274</sup> When the integrating sphere is illuminated by an input flux  $\Phi_i$ , the input flux is perfectly diffused by the initial reflection. The amount of flux incident on the entire sphere surface for this initial reflection is<sup>274</sup>

$$\Phi_1 = \Phi_i \rho \left( \frac{A_s - A_i - A_e}{A_s} \right) = \Phi_i \rho (1 - f), \quad (\text{A1.1})$$

where  $\rho$  is the reflectance of the surface,  $A_s$ ,  $A_i$ , and  $A_e$  are the area of the entire integrating sphere, input port, and output port, respectively.  $f$  is the port fraction given by  $f = (A_i + A_e) / A_s$ .

If there are more ports other than the input and output ports, they also need be considered. After the infinite number of reflections the total flux incident over the entire integrating sphere surface becomes<sup>274</sup>

$$\Phi = \frac{\Phi_i \rho (1 - f)}{1 - \rho (1 - f)}, \quad (\text{A1.2})$$

and it indicates that after multiple reflections, the total flux incident on the sphere surface ( $\Phi$ ) is higher than the input flux ( $\Phi_i$ ). The sphere surface radiance is given by<sup>274</sup>

$$L_s = \frac{\Phi_i}{\Omega A_s} \frac{\rho}{1 - \rho (1 - f)}, \quad (\text{A1.3})$$

where  $\Omega$  is the total projected solid angle from the surface. The second part of the Equation A1.3 is a unitless quantity that is defined as the sphere multiplier,  $M$ .<sup>274</sup>

$$M = \frac{\rho}{1 - \rho (1 - f)} \quad (\text{A1.4})$$

The sphere multiplier accounts for the increase in radiance within the sphere due to multiple reflections, and it is sensitive to the port fraction,  $f$ , and the sphere surface reflectance,  $\rho$ . If the reflectance of the integrating sphere is not homogeneous, the above equations need to be modified. A general expression for  $M$  is<sup>274,276</sup>

$$M = \frac{\rho_0}{1 - \rho_w \left( 1 - \sum_i f_i \right) - \sum_i \rho_i f_i} = \frac{\rho_0}{1 - \bar{\rho}}, \quad (\text{A1.5})$$

where  $\rho_0$  is the initial reflectance for incident flux,  $\rho_w$  is the reflectance of the sphere wall,  $\rho_i$  is the reflectance of port opening  $i$ , and  $f_i$  is the fractional port area of the port opening  $i$ .  $\bar{\rho}$  is the average reflectance given by  $\bar{\rho} = \rho_w \left(1 - \sum_i f_i\right) + \sum_i \rho_i f_i$ .

### A1.2.2 Reflectance Measurement – Substitution and Comparison Methods

The reflectance of a sample can be obtained by measuring the flux in the sphere with the sample mounted on the sample port and comparing it with the measurement with the standard material. There are two reflectance measurement methods; substitution method and comparison method. Figure A1.1 shows the measurement by the substitution method. The radiance is measured with a reference and sample separately. From the Equation A1.3 and A1.5, the ratio of the radiance with the sample to the reference is<sup>274</sup>

$$\frac{L_s}{L_r} = \frac{\rho_s}{\rho_r} \frac{1 - \bar{\rho}_r}{1 - \bar{\rho}_s}, \quad (\text{A1.6})$$

where  $\bar{\rho}_s$  is average wall reflectance with the sample and  $\bar{\rho}_r$  is average reflectance with the reference.  $L_s$  and  $L_r$  are experimentally measurable parameters and  $\rho_r$  and  $\bar{\rho}_r$  are known properties. However,  $\bar{\rho}_s$  is dependent on  $\rho_s$  which is the parameter that we want to obtain through this measurement, so it cannot be easily determined. Therefore the substitution method results in inherent error.

The comparison method mounts both the sample and reference simultaneously to the ports in the integrating spheres (Figure A1.2).<sup>274</sup> The average wall reflectance is the same for both  $L_r$  and  $L_s$  measurement, i.e.  $\bar{\rho}_r = \bar{\rho}_s$ , therefore Equation A1.6 becomes

$$\frac{L_s}{L_r} = \frac{\rho_s}{\rho_r}. \quad (\text{A1.7})$$

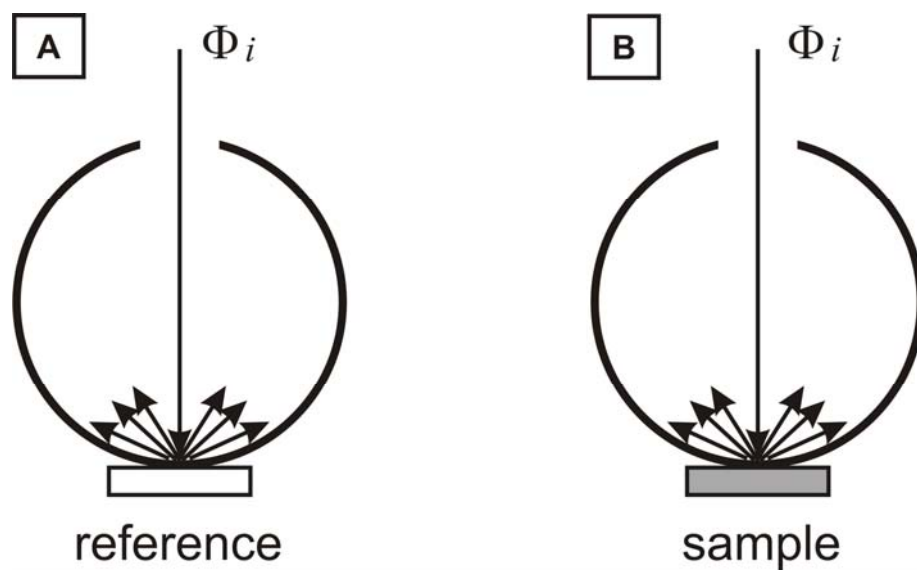


**Figure A1.1** Substitution method. Reflectance measurement of (A) reference and (B) sample.

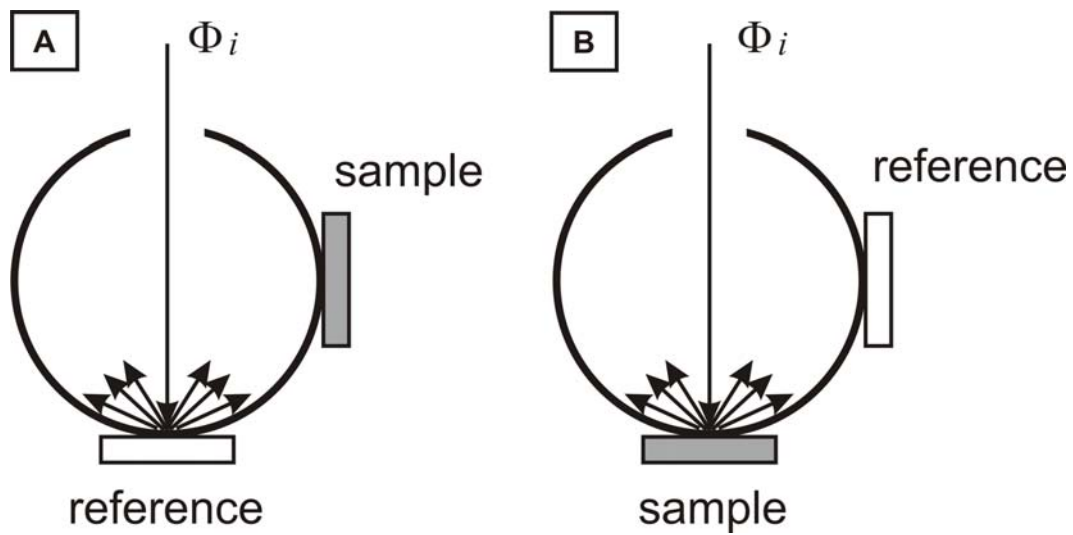


**Figure A1.2** Comparison method. Reflectance measurement of (A) reference and (B) sample.

$\rho_s$  can be obtained by Equation A1.7 with measured and known parameters.

### A1.2.3 Reflectance Measurement Geometry

In the reflectance measurement discussed in the previous section, the sample or the reference is illuminated by normal incident directional flux. After the interaction with the sample or reference, hemispherical collection is subjected (Figure A1.3A). Such geometry is represented by  $0^\circ/d$  or  $0^\circ/\text{hemispherical}$ .  $0^\circ$  refers to the normal incidence and  $d$  refers to diffuse collection. On the other hand, a reciprocal geometry can be used. Here, the sample is illuminated by diffuse flux of light and the only directional output flux from the sample is collected (Figure A1.3B,C). The collection direction can be normal to the sample (Figure A1.3B) or at some angle such as  $8^\circ$  (Figure A1.3C). The former is represented by  $d/0^\circ$  or  $\text{hemispherical}/0^\circ$  and the latter is represented by  $d/8^\circ$  or  $\text{hemispherical}/8^\circ$ . The advantage of the  $d/0^\circ$  geometry compared to the  $0^\circ/d$  geometry is that the incident flux is greater for  $d/0^\circ$  since integrating spheres provide total light collection, which leads to the increased signal-to-noise ratio.<sup>274</sup> The advantage of the  $0^\circ/d$  geometry is reduced sample heating that can cause thermochromic effect.<sup>274</sup>

The integrating sphere model RSA-HP-84 (labsphere) that is used for our measurement provides  $d/0^\circ$  and  $d/8^\circ$  geometry. The  $d/8^\circ$  geometry is used for reflectance measurement with specular reflectance included. If the reflectance is measured with  $d/0^\circ$  geometry (Figure A1.3B), specular reflectance is excluded. In the case of  $d/0^\circ$  geometry, in order to form a specular reflection toward the exit port, there should be a normal component in the incident beam to the sample. However, there cannot be a normal component because exit port is located normal to the sample, from where no beam can enter. Therefore the specular reflectance is excluded in the  $d/0^\circ$  geometry.

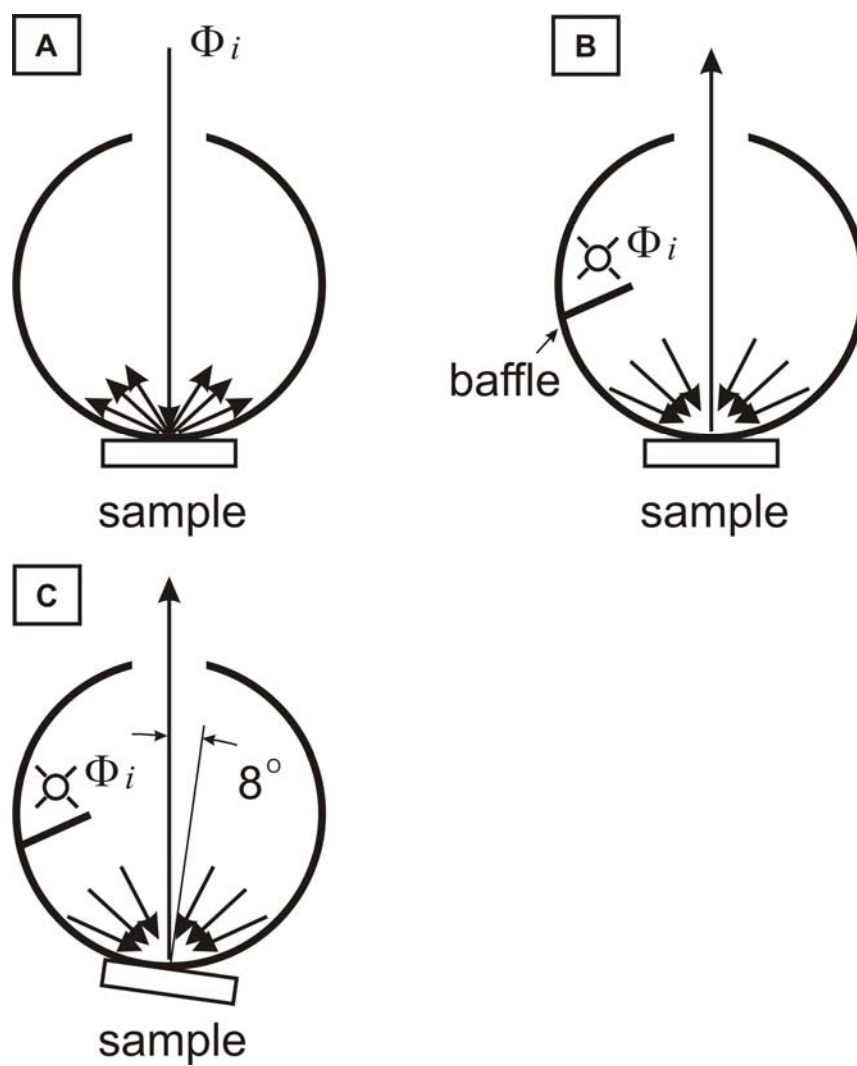


**Figure A1.3** Measurement geometry. (A)  $0^\circ/d$ , (B)  $d/0^\circ$ , and (C)  $d/8^\circ$ .

### A1.3 Experimental Methods

#### A1.3.1 Sample Preparation

Fisher brand no. 1, 25 mm diameter glass coverslips (Fisher Scientific, Fairlawn, VA) were cleaned by immersion in a boiling piranha solution (3:1 concentrated  $\text{H}_2\text{SO}_4$ : 30%  $\text{H}_2\text{O}_2$ ) for 30 min. After cooling, the substrates were thoroughly rinsed repeatedly with  $19.2 \text{ M}\Omega \text{ cm}^{-1}$  Millipore water (Marlborough, MA). Silver film of 200 nm or 270 nm height was deposited at a rate of  $0.1 - 0.3 \text{ nm s}^{-1}$  with a Kurt J. Lesker Axxis electron beam deposition system (Pittsburg, PA) or Consolidated Vacuum Corporation (Rochester, NY) deposition system with a base pressure of  $10^{-6}$  torr. The deposition height and deposition rate were monitored with a quartz crystal microbalance.

2',7'-Dibromo-5'-(hydroxymercurio)fluorescein disodium salt (merbromin), rhodamine 6G (R6G), and tris(2,2'-bipyridyl)dichlororuthenium(II) hexahydrate ( $\text{Ru}(\text{bpy})_3^{2+}$ ) were purchased from Sigma Aldrich (St. Louise, MO). [2,3,7,8,12,13,17,18-Octakis-(propyl)porphyrizinato]magnesium(II) (MgPz) was received from Brian Hoffman's group (Northwestern University). Absolute ethanol was purchased from Pharmco (Brookfield, CT).

5 mM merbromin aqueous solution, 0.1 mM R6G ethanol solution, 50  $\mu\text{M}$  MgPz ethanol solution, and 2 mM  $\text{Ru}(\text{bpy})_3^{2+}$  ethanol solution were prepared. Dye molecules were adsorbed on a silver film by incubating the film in each solution at room temperature. Incubation time was 30 min for  $\text{Ru}(\text{bpy})_3^{2+}$  solution and 12 h for the other solutions. All the films were rinsed thoroughly with the corresponding solvent after the incubation and dried under gentle nitrogen flow.

#### A1.3.2 Geometry of Integrating Sphere

UV-vis surface absorption spectra of merbromin, R6G,  $\text{Ru}(\text{bpy})_3^{2+}$ , and MgPz adsorbed on silver film were collected by an integrating sphere model RSA-HP-84 (labsphere). The geometry of the integrating sphere is illustrated in Figure A1.4. The surface of the integrating sphere is coated with a diffuse reflective material, Spectralon. There are three port openings labeled as reflectance sample port, transmittance port, and dummy port. Transfer optics consists of two mirrors and a lens assembly in order to direct the beam towards the detector. A lamp is installed on top of the sphere, and a baffle is placed in order to prevent direct illumination of the sample.

The integrating sphere provides  $d/0^\circ$  and  $d/8^\circ$  geometry and the geometry can be selected by mounting an appropriate sample holder on the reflectance sample port. All the reflectance measurements were performed with  $d/8^\circ$  geometry as shown in Figure A1.4 in order to include specular reflectance factors.

The integrating sphere also provides the selection between substitution and comparison method. For the substitution method, a diffuse reflectance standard material is mounted on the dummy port and the reflectance of the reference and sample are measured by mounting them on the reflectance sample port as shown in Figure A1.1. For the comparison method, one of the reference and sample of which reflectance will be measured is mounted on the reflectance sample port and the other is mounted on the dummy port as shown in Figure A1.2. In our measurements, the substitution method was used instead of the comparison method. The substitution method causes inherent error, called substitution error, because the average reflectance with reference ( $\bar{\rho}_r$ ) and with sample ( $\bar{\rho}_s$ ) are different each other as discussed in section A.2.2. However, the reflectance of our sample and reference are similar as can be seen in the results section. If we assume that the sample absorbance is 0.01 and the port opening is 2.5

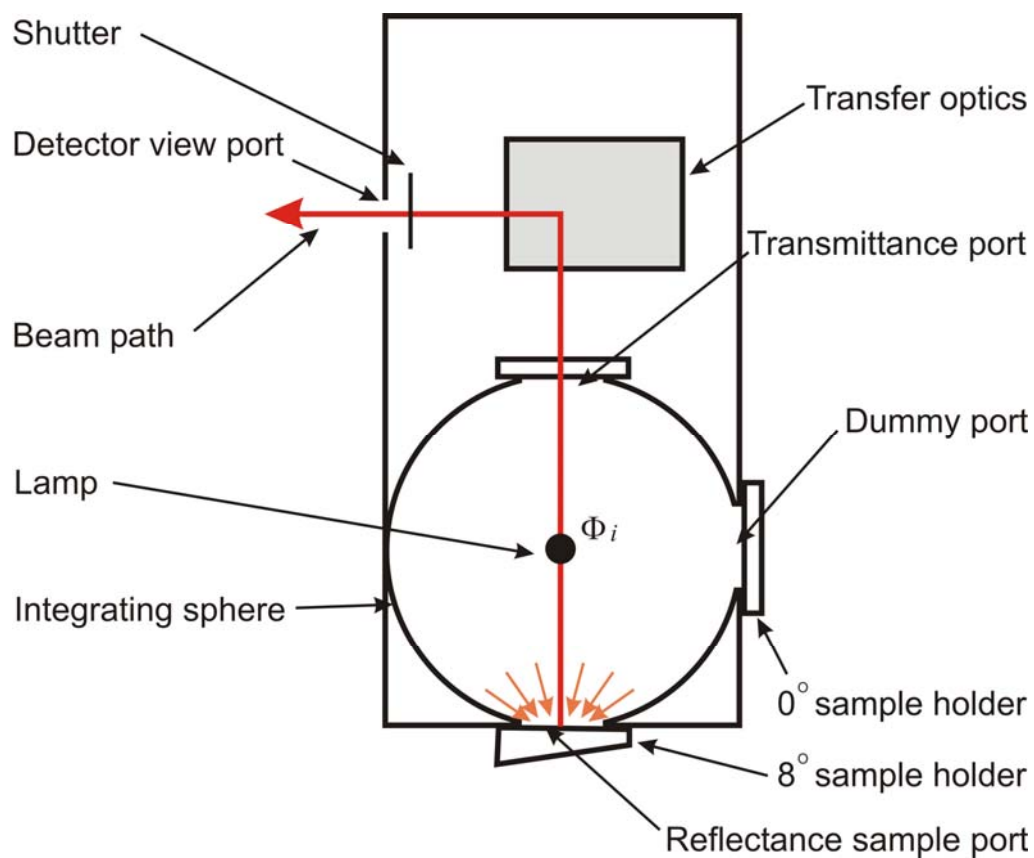


**Figure A1.4** Integrating sphere model RSA-HP-84 (labsphere).

% of the integrating sphere surface area, then the substitution error is  $\sim 0.06\%$ . Therefore in our system,  $\bar{\rho}_r \sim \bar{\rho}_s$ , and it can be assumed that

$$\frac{L_s}{L_r} \sim \frac{\rho_s}{\rho_r}. \quad (\text{A1.8})$$

### A1.3.3 Collection Optics Alignment

The integrating sphere model RSA-HP-84 is designed as an accessory for the Hewlett-Packard HP8452A diode-array spectrophotometer. However in our measurements, fiber optic coupled spectrometer (USB2000, Ocean Optics) with a charge-coupled device (CCD) detector was used instead of the spectrophotometer. In order to couple the integrating sphere output to the 400  $\mu\text{m}$  fiber, additional collection optics were required. Figure A1.5 shows the alignment of collection optics. For the reflectance measurements, the signal that comes only from the reflectance sample port should be collected and as much of that signal should be collected for a high signal level. With a lens combination, the image of the reflectance sample port can be formed on an image plane. The goal of this alignment is to reduce the image size in order to achieve maximum signal coupling into the optical fiber. If the reflectance sample port is opened, at the image plane, the image of the port appears as a dark spot with bright background that comes from the inner wall of the integrating sphere near the port (see blue box in Figure A1.5). About 2 mm diameter of the port image could be achieved with a +76.2 mm achromatic lens and a 10 $\times$  microscope objective at  $\sim 10$  mm downstream of the microscope objective as shown in Figure A1.5. However, the image diameter was 5 times larger than the diameter of optical fiber; therefore collection efficiency was still very low. If an achromatic lens with shorter focal length is used, a reduced image spot size is expected, which will lead to an increase in signal level.

A shutter before the detector view port (Figure A1.4) was fixed with a piece of adhesive tape to open in order not to block the beam path.

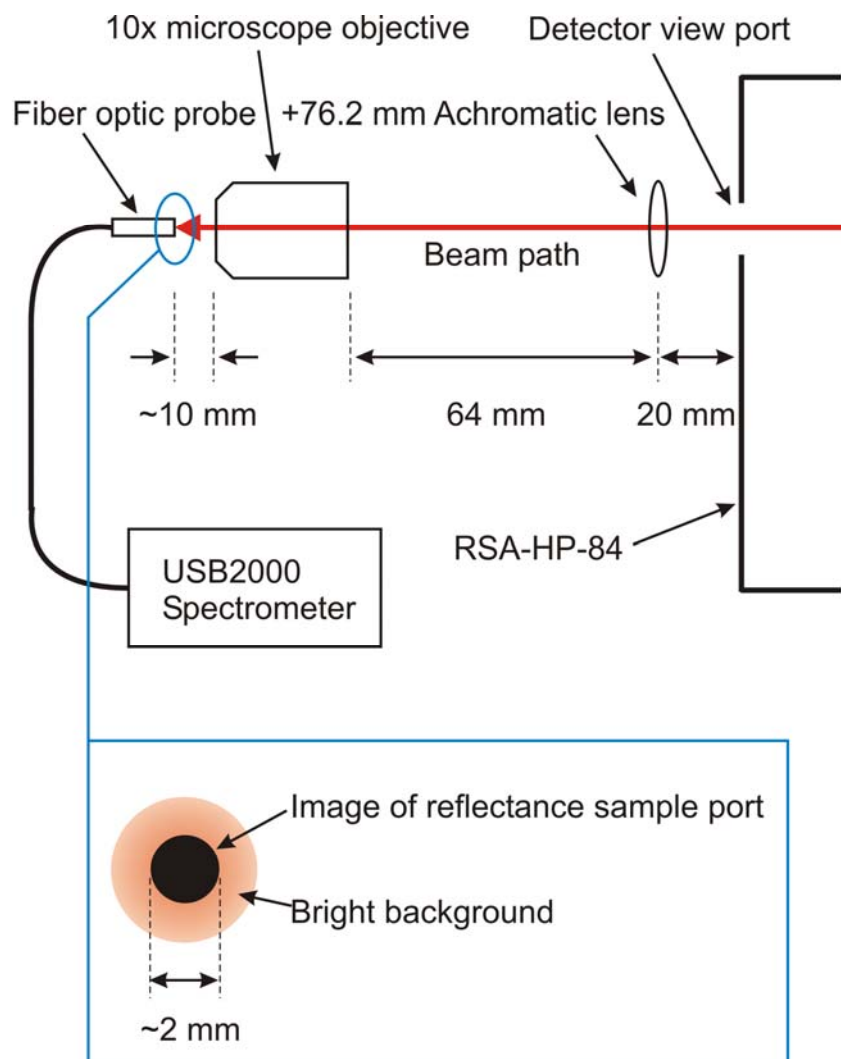


**Figure A1.5** Collection optics alignment. The image of reflectance sample port is formed ~10 mm downstream of the 10× objective as shown in the box.

### A1.3.4 Surface Absorption Measurement

Standard procedure of the comparison method for  $d/8^\circ$  reflectance factor measurement as described in the RSA-HP-84 instruction manual was followed for the surface reflectance measurement. An  $8^\circ$  sample holder was attached to the reflectance sample port and a  $0^\circ$  sample holder was attached to the dummy port as shown in Figure A1.4. An SRS-99-010 diffuse reflectance standard was mounted on the dummy port for all measurements. The room was maintained dark.

A blank scan was performed with the reflectance sample port open, and the signal was stored as “*dark*”. Bright beam came out from the port during this measurement, and care was taken to prevent any scattered light from the beam entering back into the integrating sphere. After the blank scan, the reference (bare silver film) was mounted to the reflectance sample port and the signal was saved as “*reference*”. A similar measurement was performed for the sample (dye adsorbed silver film), and it was saved as “*sample*”. The surface absorption spectrum ( $A_{surf}$ ) was obtained as follows:

$$A_{surf} = -\log_{10} \frac{sample - dark}{reference - dark}. \quad (A1.9)$$

The program OOIBase32 that was provided with Ocean Optics spectrometer supports the function of storing dark and reference to display absorbance directly after the sample measurement. However, it is recommended to save the sample and reference data separately rather than saving only “absorbance”. When the absorbance is saved by the OOIBase32 program (version 2.0.1.4), it is rounded to three decimal places. Surface absorbance in our experiment was mostly less than 0.01; therefore saved absorbance spectra by the program cannot retain detailed spectral features.

### A1.3.5 Solution Absorption Measurement

Absorption spectra of each dye solution are obtained by an Ocean Optics USB2000 or SD2000 fiber optic coupled spectrometer with a CCD detector.

## **A1.4 Results**

### **A1.4.1 2',7'-Dibromo-5'-(hydroxymercurio)fluorescein disodium salt (merbromin)**

Figure A1.6A shows the molecular structure of merbromin and Figure A1.6B shows the absorption spectra of merbromin aqueous solution (red plot), merbromin adsorbed on 200 nm silver film (black plot), and on 50 nm gold film (green plot). In solution, a main peak is observed at 505 nm and a small shoulder is at high energy side. However, in surface adsorbed merbromin absorption spectra, two bands with comparable intensity are observed and they are red-shifted from the solution peak. The peak positions are 542 nm and 524 nm on gold and 538 nm and 506 nm on silver. The surface absorption spectra are broader than the solvent spectrum and the merbromin adsorbed on silver film shows the most broadened feature. This observation is similar to previous absorption measurements done on gold and SnO<sub>2</sub> surfaces.<sup>259,277</sup> Both our measurement and previously reported spectra show a broadened absorption peak for surface adsorbed merbromin, but the peak position is slightly different from each other.

### **A1.4.2 Rhodamine 6G (R6G)**

Figure A1.7A shows the molecular structure of R6G and Figure A1.7B shows the absorption spectra of R6G ethanol solution (red plot) and R6G adsorbed on 200 nm silver film (black plot). In the ethanol solution, a main peak originated from S<sub>0</sub>-S<sub>1</sub> electronic transition is shown at 530 nm. A shoulder at 495 nm is the vibronic S<sub>0</sub>-S<sub>1</sub> transition band. The spectrum of R6G adsorbed on silver shows a red-shifted and broadened feature. Zhao et al.<sup>273</sup> deconvoluted this band into three Gaussian bands centered at 502 nm, 539 nm, and 572 nm. Each band was assigned as H-dimer, monomer, and J-dimer band, respectively.

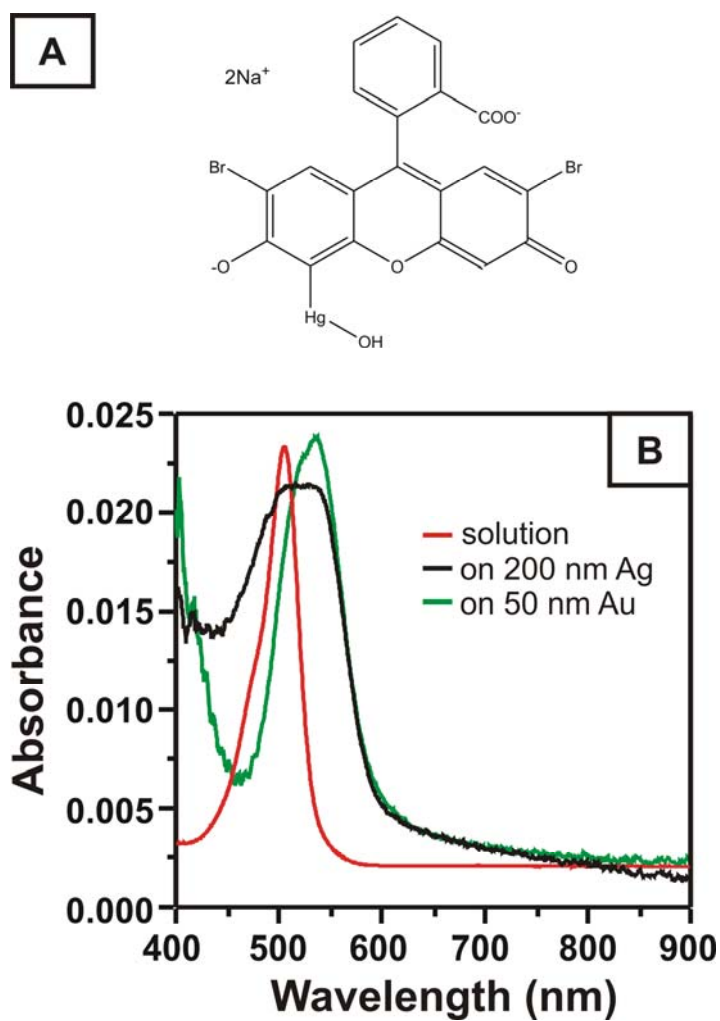


**Figure A1.6** (A) Molecular structure of merbromin. (B) Absorption spectra of merbromin aqueous solution (red plot), merbromin adsorbed on 200 nm Ag film (black plot), and merbromin adsorbed on 50 nm Au film (green plot). The solution spectrum is arbitrarily scaled.

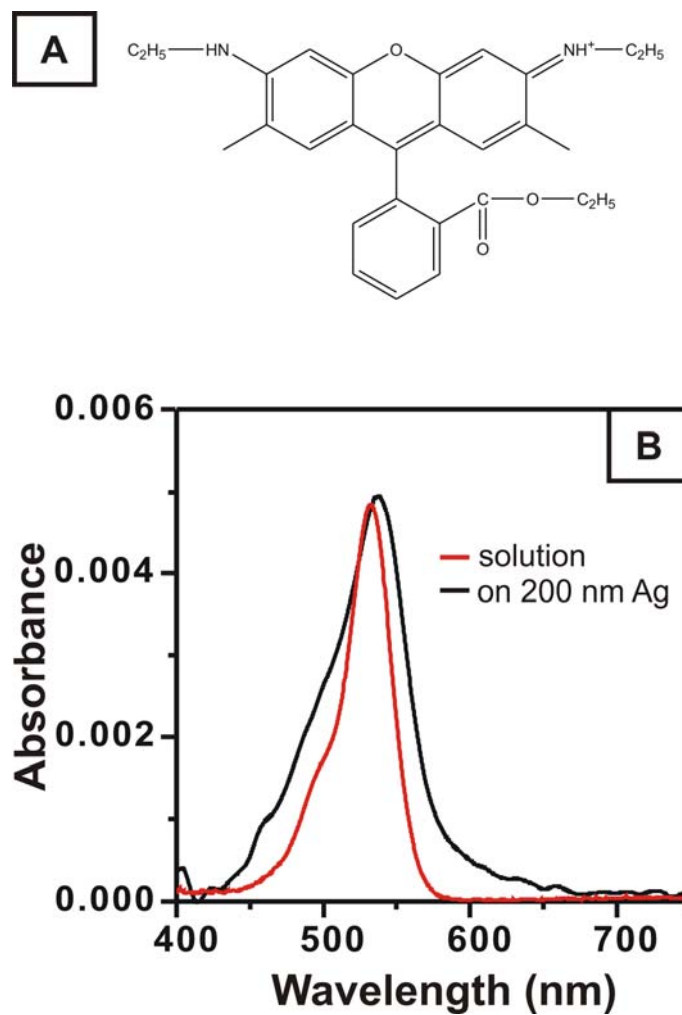


**Figure A1.7** (A) Molecular structure of R6G. (B) Absorption spectra of R6G ethanol solution (red plot) and R6G adsorbed on 200 nm Ag film (black plot). The solution spectrum is arbitrarily scaled.

#### A1.4.3 [2,3,7,8,12,13,17,18-Octakis-(propyl)porphyrinato]magnesium(II) (MgPz)

Figure A1.8A shows the molecular structure of MgPz. This molecule has  $D_{4h}$  symmetry and adsorbs to a silver surface with an orientation parallel to the surface.<sup>272</sup> The red plot in Figure A1.8B is the absorption spectrum of MgPz ethanol solution. The spectrum contains two features; a strong low-energy transition at 598 nm and a weak high-energy transition at 548 nm. Haes et al. assigned these peaks as a split Q-band ( $\pi - \pi^*$  transition).<sup>272</sup> The black plot in Figure A1.8B is the absorption spectrum of MgPz adsorbed on 200 nm silver film. The peak is slightly red-shifted ( $\lambda_{\text{max}} = 601$  nm) and band width is slightly broadened compared to the solution spectrum.

#### A1.4.4 Tris(2,2'-bipyridyl)dichlororuthenium(II) Hexahydrate ( $\text{Ru}(\text{bpy})_3^{2+}$ )

Figure A1.9A shows the molecular structure of  $\text{Ru}(\text{bpy})_3^{2+}$ . This molecule has  $D_{3d}$  symmetry. The red plot in figure A1.9B shows the absorption spectra of  $\text{Ru}(\text{bpy})_3^{2+}$  aqueous solution. A strong transition is shown at 456 nm and a shoulder is at the high energy side of the peak.  $\text{Ru}(\text{bpy})_3^{2+}$  adsorbed on 270 nm silver film is shown with black plot. It is clear that the band is broadened compared to the solution spectrum; however the band location is not well resolved because of low signal-to-noise ratio. The intensity of the light source installed in the integrating sphere drops quickly below 500 nm, therefore it was difficult to obtain low intensity spectral features below 500 nm wavelength with the integrating sphere.

### A1.5 Conclusion

The absorption spectra of various dyes adsorbed on a silver film were obtained by an integrating sphere. The substitution method with  $d/8^\circ$  geometry was used. The surface spectra were compared with the solution spectra. Surface absorption spectra of merbromin, R6G, and MgPz were obtained successfully. All the spectra showed red-shifted and broadened feature

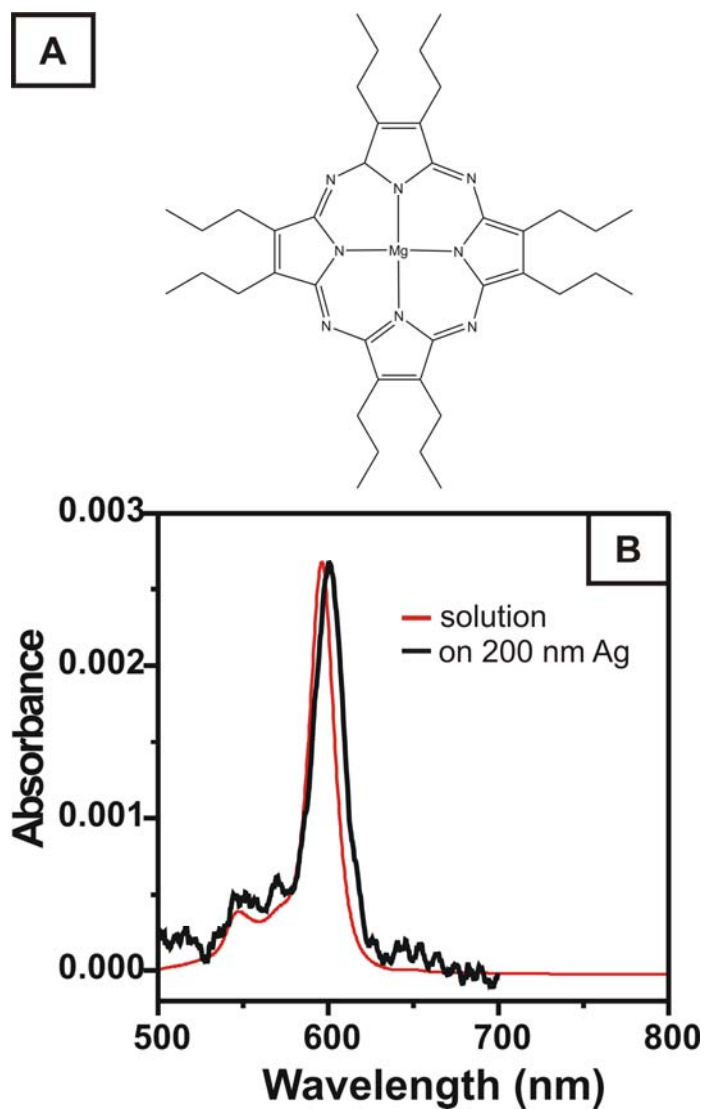


**Figure A1.8** (A) Molecular structure of MgPz. (B) Absorption spectra of MgPz ethanol solution (red plot) and MgPz adsorbed on 200 nm Ag film (black plot). The two spectra are arbitrarily scaled.

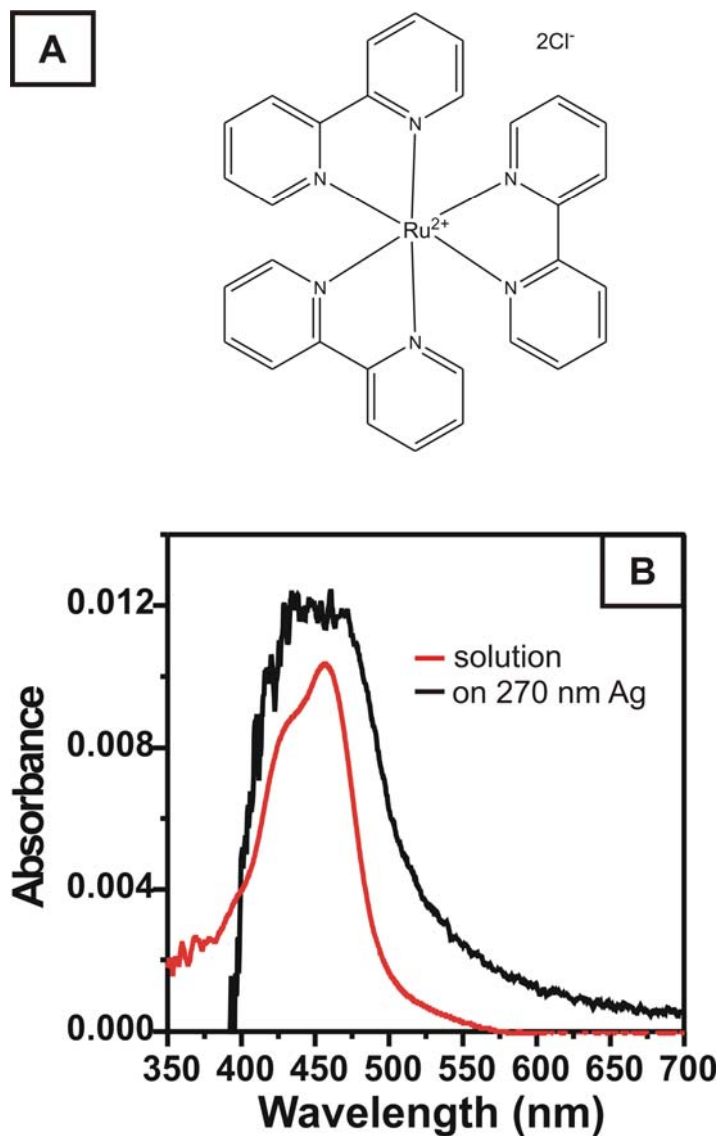


**Figure A1.9** (A) Molecular structure of  $\text{Ru}(\text{bpy})_3^{2+}$ . (B) Absorption spectra of  $\text{Ru}(\text{bpy})_3^{2+}$  aqueous solution (red plot) and  $\text{Ru}(\text{bpy})_3^{2+}$  adsorbed on 270 nm Ag film (black plot). The solution spectrum is arbitrarily scaled.

compared to the corresponding solution spectra. However, the surface absorption spectra of  $\text{Ru}(\text{bpy})_3^{2+}$  could not be taken with reasonable signal-to-noise ratio. In aqueous solution the vibronic transition of  $\text{Ru}(\text{bpy})_3^{2+}$  is located at 456 nm and below, and the low intensity of integrating sphere light source in the wavelength region limited the absorption measurement with the instrument. This limitation might be improved by increasing collection efficiency. In section A3.3, it was discussed that the signal coupling to the fiber optic probe was not efficient. Another option could be using a photodiode array detector instead of a CCD detector in order to reduce shot noise. An improved signal collection scheme is required to obtain surface absorption spectra with the current integrating sphere setup, especially for a dye with a vibronic transition wavelength shorter than 500 nm.

## **Appendix 2**

### **Plasmon Coupling in Finite Two-Dimensional Arrays of Cylindrical Silver Nanoparticles – Effect of Number of Interacting Nanoparticles**

## A2.1 Introduction

The optical properties of nanofabricated noble metal nanoparticles have drawn particular interest because of their importance in applications including bio/chemosensors,<sup>114-117</sup> optical filters,<sup>118,119</sup> plasmonic waveguides,<sup>23,120-122</sup> and substrates for surface-enhanced spectroscopy.<sup>5,123,124</sup> The unique optical properties of the nanoparticles that are distinguished from those of bulk originate from the localized surface plasmon resonance (LSPR), which is a collective oscillation of the conduction electrons that occurs when light impinges on a nanoparticle at a specific wavelength. The LSPR can be controlled by changing the size, shape, composition,<sup>4,21,147</sup> and the dielectric environment of the nanoparticle.<sup>134,141</sup> In the case of nanoparticle clusters and nanoparticle arrays, electromagnetic coupling between nanoparticles is also an important factor that determines the overall plasmon resonance of the system.

Two adjacent nanoparticles with various particle spacing have been fabricated by electron beam lithography (EBL) and their optical properties have been explored by various research groups.<sup>34,52-55</sup> They monitored the resonance wavelength of the system while the particle spacing was tuned and they observed that for the incident beam polarization parallel to the array axis (longitudinal excitation), the resonance of the system red-shifts as particles get closer, and for the incident beam polarization perpendicular to the array axis (transverse excitation), the resonance blue-shifts as particles get closer. Those observations also have been explained by various theoretical models.<sup>34,278-280</sup> A molecular ruler utilizing this sensitivity of resonance to the particle spacing has been demonstrated by Alivisatos and coworkers.<sup>59,60</sup>

The optical properties of more extended systems, such as one-dimensional (1D)<sup>14,56,281</sup> and two-dimensional (2D)<sup>32,33,132,180</sup> semi-infinite arrays, have been studied experimentally and their observations were rationalized by theoretical studies.<sup>11,12,51,69,282</sup> Particle spacing and

incident beam polarization dependence was studied for various shapes of nanoparticles. Aussenegg and coworkers have studied grid spacing dependent extinction spectra and plasmon lifetime of 2D gold cylinder and nanorod arrays.<sup>33,132</sup> Van Duyne and coworkers studied short range coupling effects in hexagonal and square arrays of triangular and cylinder gold and silver nanoparticles.<sup>32</sup> Grid spacing dependent extinction spectra of 2D L-shaped nanoparticle arrays also studied by Spears and coworkers.<sup>180</sup>

The effect of the number of nanoparticles on the plasmon resonance has been studied on a finite 1D chain with small numbers of nanoparticles. Atwater and coworkers<sup>282</sup> measured the far-field extinction spectra of a 1D chain of cylindrical gold nanoparticles with illumination for both longitudinal and transverse polarization. The number of nanoparticles in single chain was varied from 3 to 80 particles and they observed that the plasmon resonance red-shifts monotonically for longitudinal excitation and blue-shifts for transverse excitation as the number of nanoparticles increases. They also performed finite-difference time-domain (FDTD) simulations<sup>282</sup> and three-dimensional full-field electromagnetic simulations<sup>281</sup> for their system, and verified their results. On the other hand, Zhang and coworkers studied a 1D chain of 1 – 6 gold nanoparticles experimentally and theoretically, and they observed nonmonotonic behavior of the plasmon resonance shift for the condition where the phase retardation effect affects the resonance wavelength.<sup>283</sup> Bouhelier et al. studied the effect of particle size, grid spacing and number of particles on the resonant wavelength and bandwidth of 1D chain of gold nanoparticles.<sup>130</sup>

In the case of finite 2D arrays with a small number of nanoparticles, Ng and Liu<sup>284</sup> studied the optical properties of  $2 \times 3$  (6 particles arranged in 2 rows and 3 columns) cylindrical nanoparticles with fixed interparticle distance while the size of the particle was varied. However,

there have been no systematic studies about the effect of number of nanoparticles on the optical properties of finite 2D arrays, other than our work on 2D L-shaped nanoparticles for one particle size and grid spacing.<sup>180</sup> In order to develop miniaturized LSPR biosensor chip, it is important to know how many particles/pixel is required to get narrow LSPR bandwidth and desired LSPR wavelength. Therefore, the systematic study is essential for designing biosensor chip with minimum pixel size.

In this work, we extend our previous study to arrays of two different particle sizes. Finite 2D arrays of cylinders (diameter = 339 nm and 163 nm) with various numbers of nanoparticles were fabricated by EBL, and their optical properties were obtained by far-field extinction measurements. Grid spacing was 400 nm and 450 nm for large cylinders and 450 nm for small cylinders. The optical properties of finite 2D arrays were compared with that of isolated nanoparticles and semi-infinite 2D nanoparticle arrays.

## **A2.2 Experimental Methods**

### **A2.2.1 Sample Fabrication and Structural Characterization**

The nanoparticle arrays were fabricated on an indium-tin oxide (ITO) conducting layer of 40 nm on 750  $\mu\text{m}$  thick glass substrate. Each sample was fabricated over the area of  $100 \times 100 \mu\text{m}^2$  and they were separated by 1 or 2 mm. As a guidance for finding sample,  $50 \times 50 \mu\text{m}^2$  and  $500 \times 500 \mu\text{m}^2$  silver films were fabricated as markers within each sample and at the beginning and ending of each row of samples, respectively. Samples were fabricated at the Michigan Nanofabrication Facility (MNF) which is part of the National Nanotechnology Infrastructure Network (NNIN).

Exposure of the patterns was done in a two step process. The markers were fabricated on the substrate using photolithography. The substrate was prebaked at 130 °C for 10 min to

remove any excess moisture on the surface. S1813 (Microchem) was then spun on the surface at 4000 rpm for 30 sec. A post spin bake at 115 °C for 60 min was then performed. The mask was then exposed for 6 sec in a MA-6 aligner. The pattern was developed in MIF 319 (Microchem) for 30 sec and rinsed in water and dried in nitrogen. The substrate was then mounted in a Cooke evaporator and 30 nm of silver was deposited. Excess resist was removed via an overnight soak in acetone. Subsequent preparation of the nanoparticle arrays was performed using EBL. A RAITH 150, employing an accelerating voltage of 20 kV, aperture of 20  $\mu\text{m}$ , and a working distance of 7 mm was used. 950k PMMA A4 (Microchem) was spun onto of the existing pattern at 4000 rpm for 45 sec. The substrate was then soft baked at 170 °C overnight. After exposure, the patterns were then developed in for 2 min in a 3:1 mixture of isopropyl alcohol (IPA) and methyl isobutyl ketone (MIBK). 30 nm of silver was then deposited (Cooke evaporator) over both the pattern and resist and subsequently removed, leaving patterned nanoparticles behind. This was accomplished by slightly over-developing the resist.

Scanning electron microscopic (SEM) images of the nanoparticle shape and array structure are shown in Figure A2.1. SEM Imaging was performed in the EPIC center at Northwestern University with a Hitachi 4500. The diameter ( $d$ ) of nanoparticle is  $339 \pm 6$  nm for large cylinder (Figure A2.1A) and  $163 \pm 4$  nm for small cylinder (Figure A2.1B). The height of cylinders is 30 nm. Two different types of arrays were fabricated for both large and small cylinders; one is semi-infinite arrays and the other is gap arrays. In the case of semi-infinite arrays, continuous square arrays of nanoparticles were fabricated within  $100 \times 100 \mu\text{m}^2$  area with various grid spacings ( $D$ ). Table A2.1 summarizes all the semi-infinite arrays fabricated for this study. Nanoparticle arrays with 5  $\mu\text{m}$  grid spacing were also fabricated in order to obtain optical properties of “isolated” nanoparticles. At this grid spacing, dipole interaction between

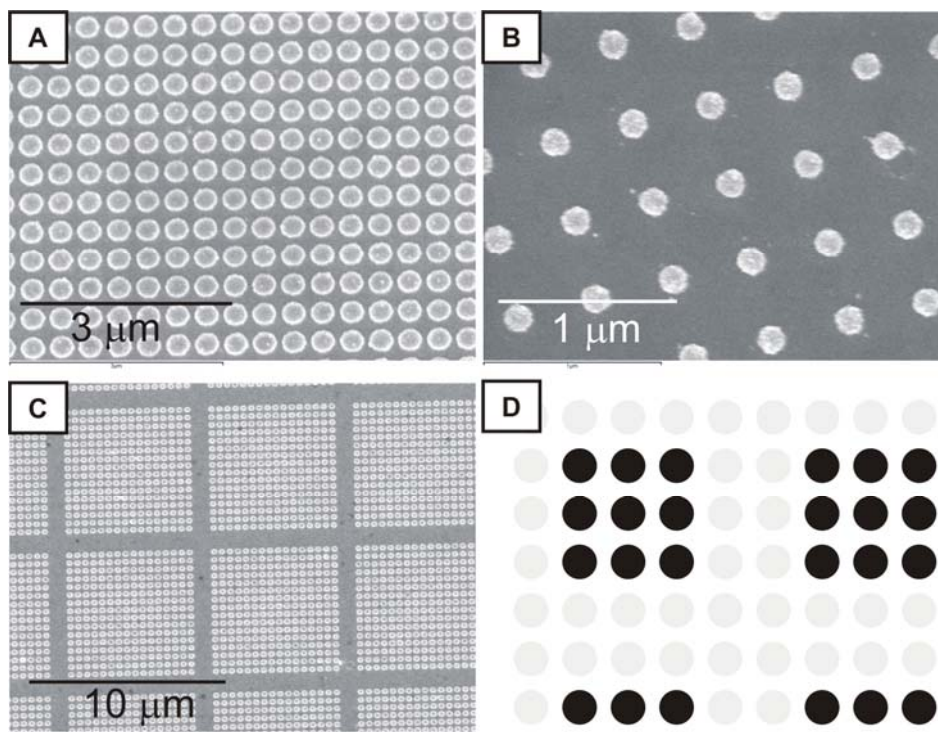


**Figure A2.1** SEM images of two-dimensional square arrays of cylindrical nanoparticles. (A)  $d = 339$  nm nanoparticles. (B)  $d = 163$  nm nanoparticles. (C) Gap array of  $d = 339$  nm nanoparticles (16 particles per block edge and gap of 2 particles). (D) Diagram of gap arrays with  $3 \times 3$  blocks and gap size of 2. Gray particles in the diagram stand for vacant sites.

diameter (nm)	grid spacing (nm)
339 <sup>a</sup>	400, 450, 475, 500, 525, 550, 600, 650, 700, 800, 900, 5000
163 <sup>b</sup>	450, 475, 500, 525, 550, 600, 800, 900

<sup>a</sup> Error is  $\pm 6$  nm

<sup>b</sup> Error is  $\pm 4$  nm

**Table A2.1** Characteristics of semi-infinite square arrays

nanoparticles is negligible. In the case of the gap array, vacant sites were introduced within  $100 \times 100 \mu\text{m}^2$  square array of the nanoparticles as shown in Figure A2.1C. In the gap arrays, each unit block consists of certain number of nanoparticles with fixed grid spacing, and they are separated by a certain gap dimension. Figure A2.1D shows the diagram of gap arrays with  $3 \times 3$  blocks (3 particles per block edge) and gap size of 2. Gray particles in the diagram stand for vacant sites. For the large cylinder, gap arrays of 400 nm and 450 nm grid spacing were fabricated (gap array 1) and for the small cylinder, gap arrays of 450 nm grid spacing were fabricated (gap array 2). Various numbers of particles in single block and various gap sizes were fabricated for both large and small cylinders. All the gap arrays reported in this paper are summarized in Table A2.2.

### **A2.2.2 Extinction Measurements**

Extinction spectra were collected on an Ocean Optics USB2000 fiber-coupled spectrometer for the 400 – 1000 nm region and a fiber-coupled near-IR spectrometer (NIR 128L-1.7T1-USB, Control Development) for the 900 – 1700 nm region. The spectra over this wide region have a slight mismatch near 900 nm, signifying where one spectrometer ends and the other begins. The experimental setup for the extinction measurements is described in detail elsewhere.<sup>180</sup> Briefly, white light from a tungsten-halogen lamp light source was fiber-coupled with a 100  $\mu\text{m}$  fiber to a +40 mm focal length achromatic collimating lens. The collimated beam was then polarized by a Glan-Taylor calcite polarizer with 5 mm aperture and focused onto the sample by a +12.7 mm focal length achromatic lens with the optic axis normal to the sample surface. Transmitted light was collected by an infinity corrected 10 $\times$  Nikon microscope objective (NA = 0.30) at a working distance of 16.0 mm and focused into a 600  $\mu\text{m}$  fiber that couples into the spectrometer. The white light spot size on the sample was scanned with a

diameter (nm)	grid spacing (nm)	block size <sup>a</sup>	gap size <sup>a</sup>
339 <sup>b</sup>	400, 450	2×2, 3×3, 4×4	1, 2
339 <sup>b</sup>	400, 450	8×8, 16×16, 24×24	1, 2, 8
339 <sup>b</sup>	400, 450	40×40	1
339 <sup>b</sup>	5000	1×1	N/A
339 <sup>b</sup>	400 / 450	semi-infinite (250×250 / 222×222)	0
163 <sup>c</sup>	450	2×2, 3×3, 4×4	1, 2
163 <sup>c</sup>	450	8×8, 16×16, 24×24	1, 2, 8
163 <sup>c</sup>	450	40×40	1
163 <sup>c</sup>	450	semi-infinite (222×222)	0

<sup>a</sup> Number of particles

<sup>b</sup> Error is ± 6 nm, gap array 1

<sup>c</sup> Error is ± 4 nm, gap array 2

**Table A2.2** Characteristics of gap arrays

straight edge and was close to Gaussian with a 20  $\mu\text{m}$  diameter at full width at half-maximum (FWHM).

The sample was mounted on two computer-controlled microtranslational stages (M-111.1DG, Physik Instrumente) to form an x–y system with a 50 nm step size. The x–y stage system is fixed on the manual vertical linear stage (MVN50, Newport Corp.) and manual rotational stage (M-UTR120A, Newport Corp.). All the samples were studied under a stream of dry nitrogen. The reference measurement was obtained by scanning into a nearby region of the glass substrate.

## A2.3 Results and Discussion

### A2.3.1 Semi-Infinite Arrays

The extinction spectra of semi-infinite 2D arrays of large cylinders ( $d = 339$  nm) with various grid spacings are depicted in Figure A2.2. The resonant wavelength and bandwidth of the arrays vary with grid spacing. The resonant wavelength is plotted versus grid spacing in Figure A2.3A. Multiple plots for each grid spacing are the data obtained from multiple pads that were fabricated with the same grid spacing. The resonant wavelength red-shifts as the grid spacing increases until 700 nm where it shows maximum red shift. This grid spacing will be called critical grid spacing ( $D_{\text{crit}}$ ). After the  $D_{\text{crit}}$ , the resonant wavelength blue-shifts and converges to that of isolated nanoparticle. As shown in Figure A2.3A, the  $D_{\text{crit}}$  is observed where the plot of resonant wavelength versus grid spacing intersects with the light line given by  $\lambda = Dn_{\text{glass}}$ , where  $\lambda$  is wavelength and  $n_{\text{glass}}$  is the refractive index of glass substrate ( $n_{\text{glass}} = 1.5$ ). The bandwidth of the plasmon resonance is plotted versus grid spacing in Figure A2.3B. The minimum bandwidth of  $806\text{ cm}^{-1}$  is shown at 650 nm grid spacing that is 50 nm apart from the  $D_{\text{crit}}$ . This bandwidth corresponds to a plasmon lifetime of 6.6 fs. All these observations are

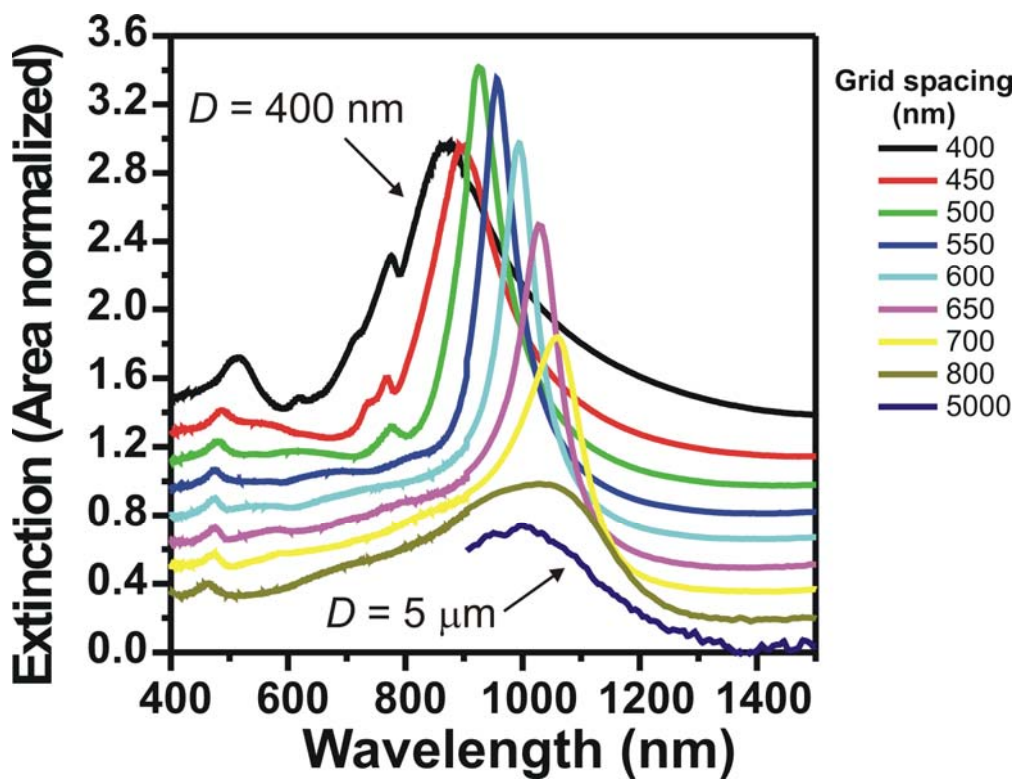


**Figure A2.2** Nanoparticle area normalized extinction spectra of 2D square arrays of  $d = 339$  nm nanoparticles (large cylinders). Grid spacing ranges from 400 nm to 5  $\mu\text{m}$  from top to bottom. All spectra are shown with an offset of 0.15 for clarity. In the case of isolated particle ( $D = 5 \mu\text{m}$ ), only the spectrum obtained by near-IR spectrometer is available.

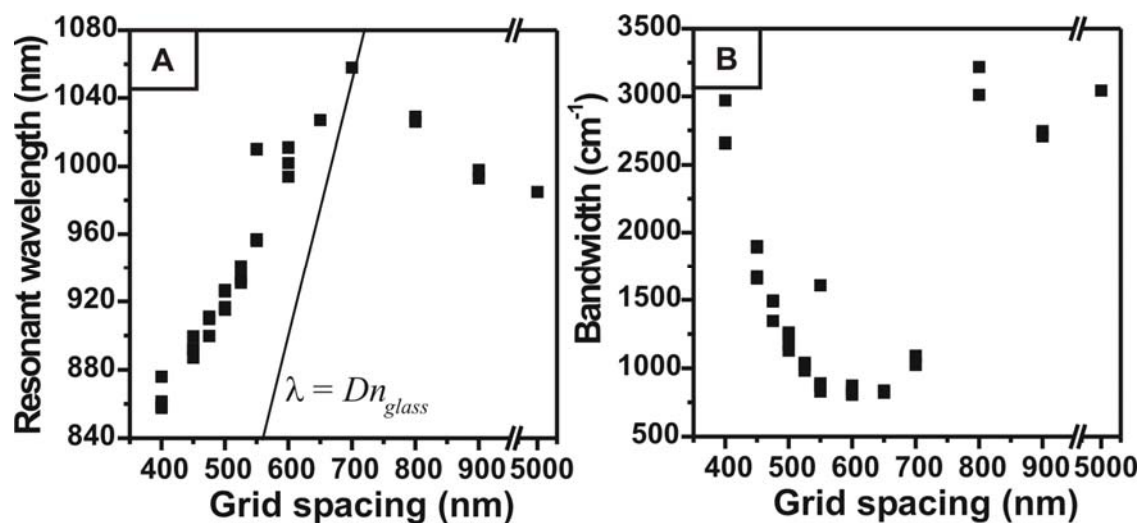


**Figure A2.3** (A) Resonant wavelength and (B) bandwidth versus grid spacing for 2D semi-infinite arrays of  $d = 339$  nm nanoparticles (large cylinders). The light line  $\lambda = Dn_{glass}$  is shown with a black solid line in panel A.  $\lambda$  is wavelength,  $D$  is grid spacing and  $n_{glass}$  is refractive index of glass ( $n_{glass} = 1.5$ ).

consistent with the previous reports for cylindrical nanoparticle arrays<sup>33</sup> and L-shaped nanoparticle arrays.<sup>180</sup> Aussenegg and coworkers<sup>33</sup> explained the observation with the model proposed by Meier et al.<sup>69</sup> The red shift of the plasmon resonance at the grid spacing slightly smaller than  $D_{\text{crit}}$  was explained by the large local optical fields due to an almost in-phase addition of the scattered light fields of neighboring particles while the grating order is evanescent.<sup>33</sup> At the  $D_{\text{crit}}$ , the grating order changes from evanescent to radiating at grazing angle, where strong damping occurs, which broadens the bandwidth.<sup>33</sup>

Some additional features are shown in the extinction spectra of Figure A2.2. There is a small band at the 460 – 520 nm region, and it can be a quadrupole or higher order multipole band. At the closest grid spacing, the band red-shifts and intensity increases, which is consistent with the previous observation for L-shaped nanoparticle arrays.<sup>180</sup> In the case of grid spacings smaller than 550 nm, a small additional band is observed at the 770 – 780 nm region, but the origin of this band is not clear.

The resonant wavelength and bandwidth of the dipole band of small cylinder arrays ( $d = 163$  nm) are plotted versus grid spacing in Figure A2.4A and A2.4B, respectively. In the case of small cylinders,  $D_{\text{crit}}$  is about 475 – 500 nm and it is smaller than  $D_{\text{crit}}$  of large cylinder arrays (700 nm); this shift is because the resonant wavelength of the small cylinder is shifted to the blue of the large cylinder. The resonant wavelength of isolated nanoparticle is 985 nm for the large cylinder. In the case of the small cylinder, an isolated nanoparticle array did not survive the fabrication process. However, if we assume that the optical properties of a 900 nm grid spacing array approaches to that of isolated nanoparticle sufficiently, the resonant wavelength of the isolated particle is about 545 nm.

### **A2.3.2 Gap Arrays**

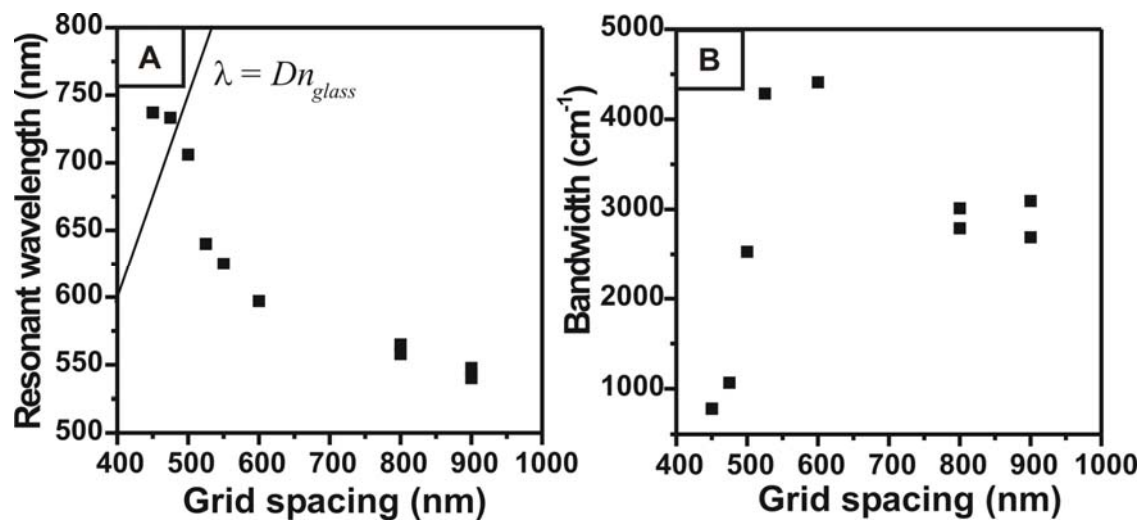


**Figure A2.4** (A) Resonant wavelength and (B) bandwidth versus grid spacing for 2D semi-infinite arrays of  $d = 163$  nm nanoparticles (small cylinders). The light line  $\lambda = Dn_{glass}$  is shown with a black solid line in panel A.  $\lambda$  is wavelength,  $D$  is grid spacing and  $n_{glass}$  is refractive index of glass ( $n_{glass} = 1.5$ ).

In order to monitor how the number of interacting particles affects the optical properties of finite 2D arrays, we fabricated two different types of gap arrays. One gap array consists of large cylinders with 400 and 450 nm grid spacing (gap array 1 in Table A2.2) and the other gap array consists of small cylinders with 400 nm grid spacing (gap array 2 in Table A2.2). In the case of gap arrays 1, their grid spacing is much smaller than  $D_{\text{crit}}$  of the semi-infinite array with same nanoparticle size as shown in Figure A2.3, where the  $D_{\text{crit}}$  of the semi-infinite array is 700 nm. In the case of gap arrays 2, their grid spacing is still smaller than  $D_{\text{crit}}$  of the semi-infinite array with the same nanoparticle size, but they are very close. The  $D_{\text{crit}}$  of the semi-infinite array is about 475 – 500 nm as shown in Figure A2.4. Since the grid spacing is smaller than  $D_{\text{crit}}$  for both arrays, their grating order is evanescent, i.e. the reciprocal lattice vector ( $2\pi/D$ ) is larger than the wavevector of the resonant wavelength within a glass medium ( $2\pi n_{\text{glass}}/\lambda$ ). However, in the case of the semi-infinite array of large cylinders with  $D = 400$  nm and 450 nm, the resonant wavelength is blue-shifted from the corresponding isolated nanoparticle resonance (Figure A2.3A), whereas in the case of small cylinder arrays with  $D = 450$  nm, the resonant wavelength is red-shifted from the corresponding isolated nanoparticle resonance (Figure A2.4A). The latter effect appears to arise from the large local optical fields due to an almost in-phase addition of the scattered light fields of neighboring particles. For the two different cases, we constructed 2D square arrays with finite nanoparticle number. The numbers of nanoparticles were varied from an isolated nanoparticle (particle number = 1) to the semi-infinite arrays (particle number =  $250 \times 250$  for  $D = 400$  nm,  $222 \times 222$  for  $D = 450$  nm) as summarized in Table A2.2, and we monitored the modification of optical properties. The data for an isolated nanoparticle for the small cylinder was not available, therefore the data of the semi-infinite array with  $D = 900$  nm will approximate the isolated particle data in our discussion.

The extinction spectra of selected arrays from gap array 1 with large particles ( $d = 339$  nm) and  $D = 400$  nm and  $D = 450$  nm are depicted in Figure A2.5A and A2.5B, respectively. The extinction spectra of isolated particle,  $2 \times 2$ ,  $3 \times 3$ ,  $8 \times 8$ ,  $16 \times 16$  blocks with gap dimension of 1, and semi-infinite arrays are plotted with black, red, green, blue, cyan, and purple lines, respectively. Each spectrum is normalized to the height of the extinction maximum. The resonant wavelength blue-shifts as the number of nanoparticles in the block increases for both  $D = 400$  nm and  $D = 450$  nm arrays. The resonant wavelengths of gap array 1 with  $D = 400$  nm and  $D = 450$  nm are shown in Figure A2.6A and A2.6C, respectively. The resonant wavelength of the isolated nanoparticle is 955 – 965 nm and that of the semi-infinite array is 856 nm for  $D = 400$  nm and 874 – 884 nm for  $D = 450$  nm. The slight difference in resonance position with the data in Figure A2.4 might be because of the small difference in each sample that comes from the imperfection of the fabrication. As the number of particles increases, the resonant wavelength blue-shifts and it approaches that of the semi-infinite array. The formation of a  $2 \times 2$  block induces a large blue shift from the isolated nanoparticle resonance,  $\sim 60$  nm for  $D = 400$  nm and  $\sim 40$  nm for  $D = 450$  nm, followed by a gradual blue shift approaching to the semi-infinite array resonance as the number of nanoparticles increases. The resonance of  $16 \times 16$  nanoparticles approached that of semi-infinite array and there is almost no change in resonant wavelength for larger blocks. However, the size of gap does not seem to play a significant role in the resonant wavelength. Except for the  $2 \times 2$  block with  $D = 400$  nm, the other blocks shows similar resonant wavelength for different gap dimensions.

The extinction spectra of selected arrays from gap array 2 with smaller particles ( $d = 163$  nm) are depicted in Figure A2.7. The extinction spectra of the isolated particle,  $2 \times 2$ ,  $3 \times 3$ ,  $8 \times 8$ ,  $16 \times 16$  blocks with gap dimension of 1, and semi-infinite arrays are plotted with black, red,

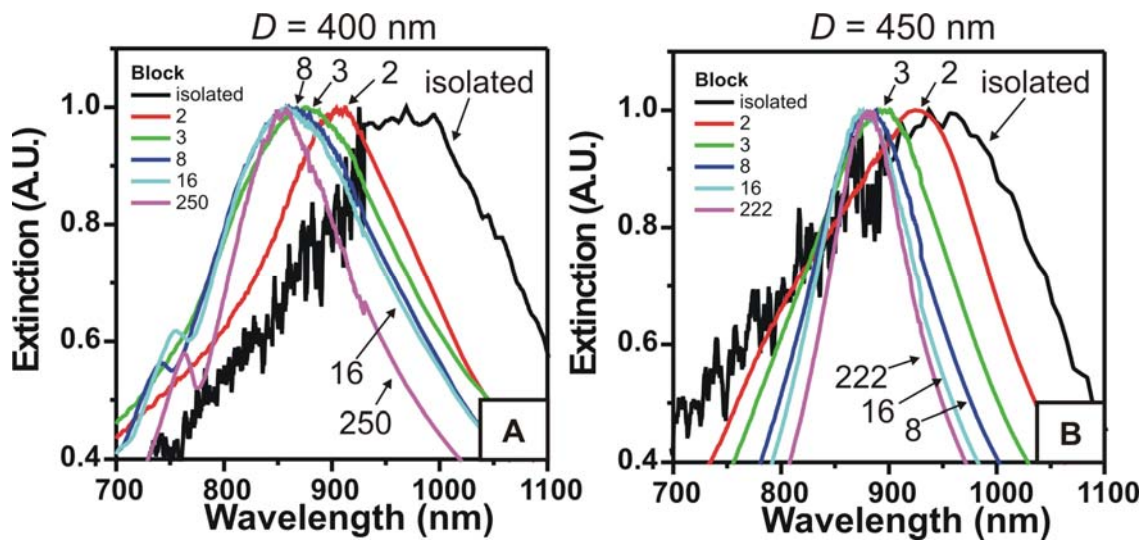


**Figure A2.5** Extinction spectra of gap array 1 ( $d = 339 \text{ nm}$ ) for (A)  $D = 400 \text{ nm}$  and (B)  $D = 450 \text{ nm}$ . Extinction spectra of isolated particle,  $2 \times 2$ ,  $3 \times 3$ ,  $8 \times 8$ ,  $16 \times 16$  blocks with gap dimension of 1, and semi-infinite arrays are plotted with black, red, green, blue, cyan, and purple lines, respectively. Each spectrum is normalized to the height of the extinction maximum.

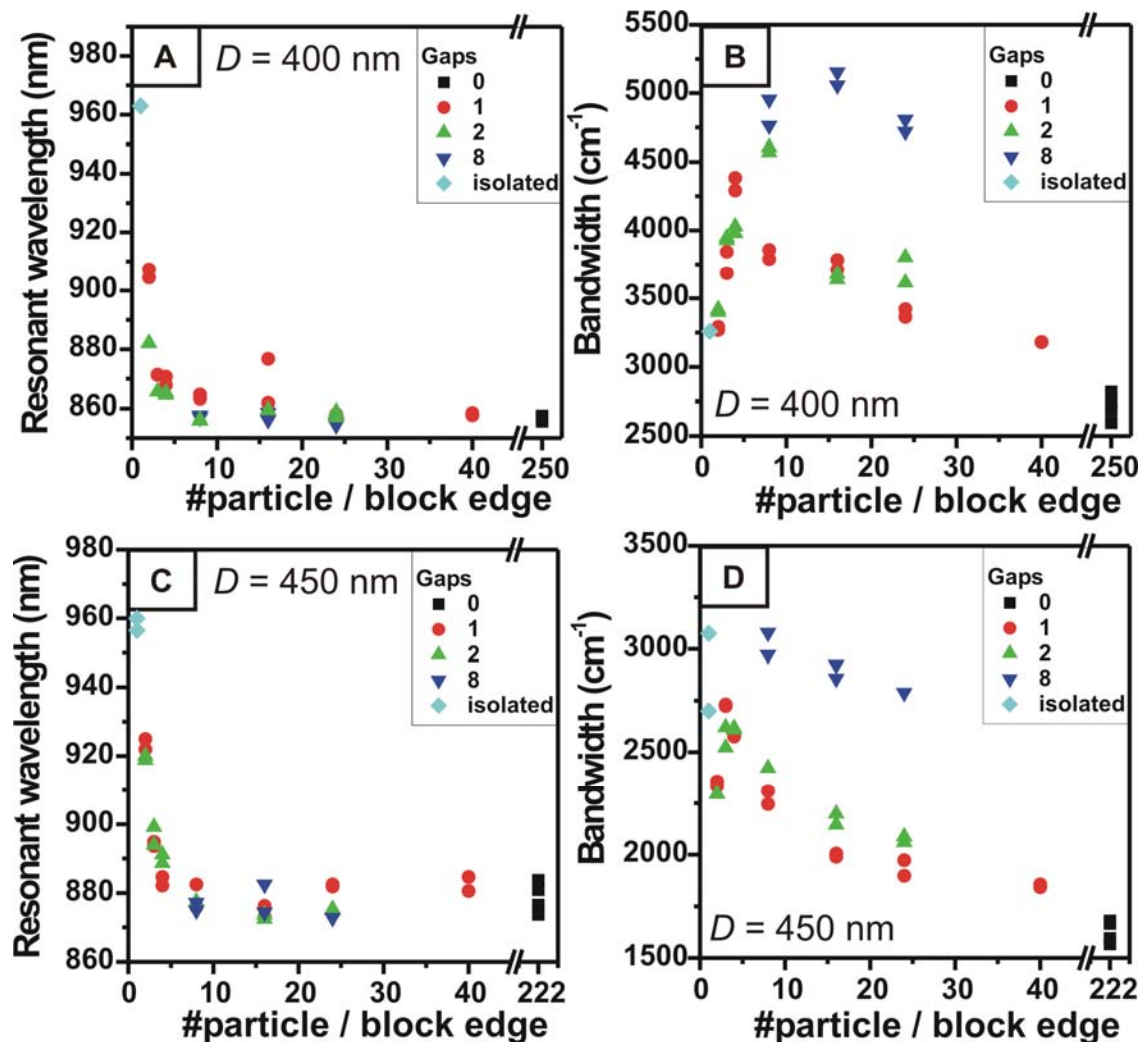


**Figure A2.6** Resonant wavelength and band width of gap array 1 samples ( $d = 339$  nm) versus the number of particles per block edge. Panels A and B are for gap arrays with  $D = 400$  nm and panels C and D are for gap arrays with  $D = 450$  nm. Data for semi-infinite particle arrays are plotted with black squares and data with gaps corresponding to 1, 2, and 8 particles are plotted with red circles, green triangles and blue inverted triangles, respectively. Data for isolated particles are plotted with cyan diamonds.

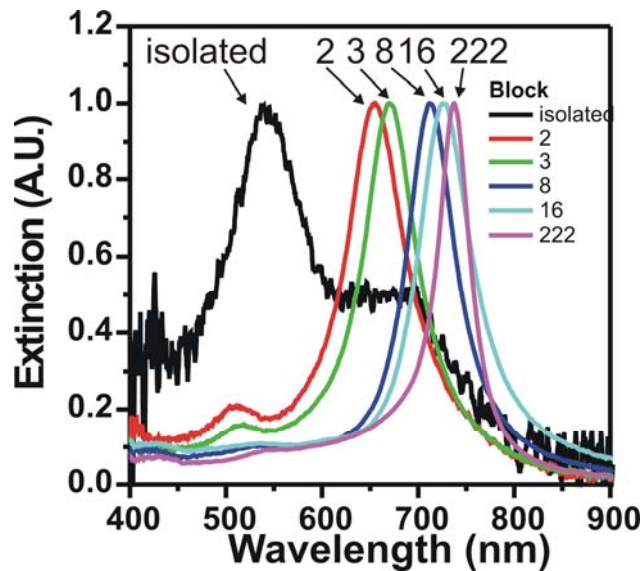


**Figure A2.7** Extinction spectra of gap array 2 ( $d = 163$  nm). Extinction spectra of isolated particle,  $2 \times 2$ ,  $3 \times 3$ ,  $8 \times 8$ ,  $16 \times 16$  blocks with gap dimension of 1, and semi-infinite arrays are plotted with black, red, green, blue, cyan, and purple lines, respectively. Each spectrum is normalized to the height of the extinction maximum.

green, blue, cyan, and purple lines, respectively. The resonant wavelength red-shifts as the number of nanoparticles in the block increases. The resonant wavelengths of gap array 2 are plotted in Figure A2.8A. The resonant wavelength of the approximately isolated nanoparticle is 540 – 548 nm and that of semi-infinite array is 737 – 771 nm. As the number of particles increases the resonant wavelength red-shifts and it approaches that of the semi-infinite array. A red shift of 140 nm from the isolated nanoparticle resonance is observed with the formation of a  $2 \times 2$  block, followed by a gradual red shift approaching the semi-infinite array resonance as the number of nanoparticles increases. Here again, the resonance of  $16 \times 16$  nanoparticles approached that of semi-infinite array and the size of gap does not play a significant role in the resonant wavelength.

The bandwidth of the gap array shows complicated behaviors. The plasmon bandwidth of gap array 1 with  $D = 400$  nm and  $D = 450$  nm are shown in Figure A2.6B and A2.6D, respectively. For a fixed gap dimension, the bandwidth increases as the number of nanoparticles increases until certain block dimension, and then it decreases and approaches that of semi-infinite array; at no spacing is the bandwidth less than the semi-infinite array. In the case of the  $D = 400$  nm sample, the maximum bandwidth is observed at  $4 \times 4$ ,  $8 \times 8$ , and  $16 \times 16$  blocks for gap dimension of 1, 2, and 8, respectively and in the case of  $D = 450$  nm sample, the maximum bandwidth is observed at  $3 \times 3$  and  $4 \times 4$  blocks for gap dimension of 1 and 2, respectively. For a fixed block dimension, a large gap results in broader bandwidth with some exceptions. The blocks with gap dimension of 8 shows large bandwidth compared to those with gap dimension of 1 and 2 for both  $D = 400$  nm and  $D = 450$  nm. They are fabricated on different substrates from the other gap arrays, therefore a slight variation of nanoparticles that came from the imperfection of the sample fabrication might cause the large deviation in bandwidth.

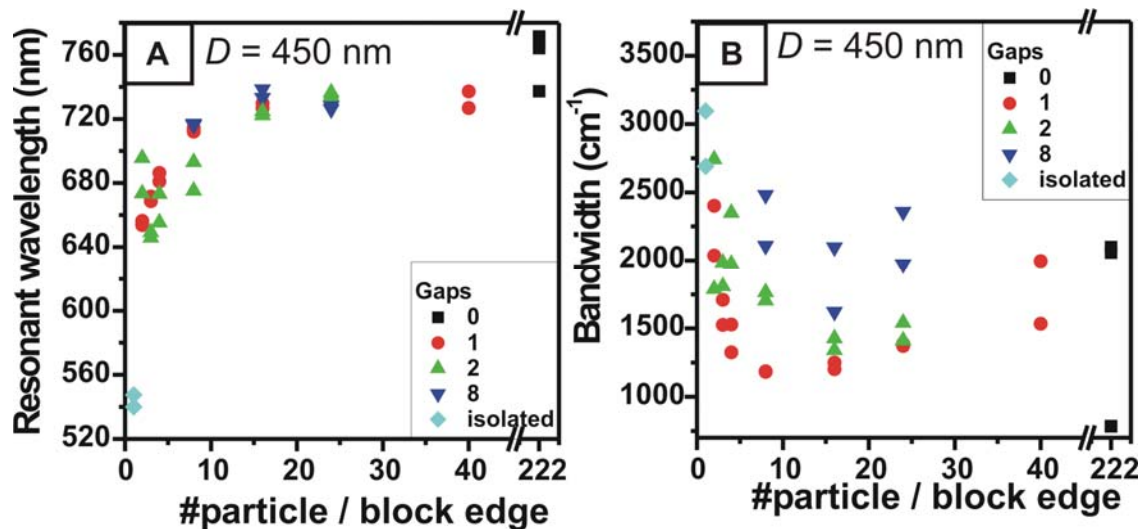


**Figure A2.8** (A) Resonant wavelength and (B) band width of gap array 2 samples ( $d = 163$  nm,  $D = 450$  nm) versus the number of particles per block edge. Data for semi-infinite particle arrays are plotted with black squares and data with gaps corresponding to 1, 2, and 8 particles are plotted with red circles, green triangles and blue inverted triangles, respectively. Data for isolated particles are plotted with cyan diamonds.

Generally, for the samples prepared with identical geometric parameters, the bandwidth shows larger deviation than the resonance wavelength. However, it is still possible that the observation is real, not an artifact. For the large gap of 8, each block is isolated and there is no interaction between blocks. On the other hand, in the case of small gap of 1 and 2, each block is quite close and the dipole interactions among those blocks are possible because of the high polarizability of the large nanoparticles, which narrows the bandwidth. In order to verify this hypothesis, more samples with various gap dimensions between 2 and 8 should be tested.

In the case of gap array 2, the sample with gap dimension of 8 is fabricated on a different substrate. Semi-infinite arrays show large deviation in bandwidth; samples for  $\sim 2100 \text{ cm}^{-1}$  bandwidth is fabricated in same substrate with the other gap array 2 samples and sample for  $\sim 790 \text{ cm}^{-1}$  bandwidth is fabricated in the substrate for the semi-infinite arrays. If we ignore the semi-infinite array sample with narrowest bandwidth, the bandwidth versus block dimension shows minimum for each gap dimension,  $8 \times 8$  for 1 gap and  $16 \times 16$  for 2 and 8 gaps. However gap array 2 samples showed large deviation in bandwidth between sample to sample and even within the same sample in different spot that is monitored with white light, so to confirm this observation is real, more experiments should be performed with new samples having fewer artifacts.

Unlike the case of resonant wavelength, bandwidth data shows large noise both for gap array 1 and gap array 2, and there is difficulty in interpretation of the data, especially for gap array 2. More experiments and theoretical modeling are required to explore the effect on the plasmon bandwidth more precisely.

#### **A2.4 Conclusion**

We measured the optical properties of finite 2D arrays of silver cylindrical nanoparticles and studied the effect of the number of interacting nanoparticles. In the case of gap array 1 of large diameter nanoparticles, where the near-field interaction is dominant, the resonant wavelength of the  $2 \times 2$  particles block blue-shifted from that of isolated particles, and as the block dimension increases, the resonant wavelength keeps blue-shifting and converges to that of semi-infinite array. On the contrary, in the case of the gap array 2 of small diameter nanoparticles, where the far-field interaction is also important, the resonant wavelength of the  $2 \times 2$  particles block red-shifted from that of isolated particles, and as the block dimension increases, the resonant wavelength keeps red-shifting and converges to that of semi-infinite array. In both cases, the size of gap does not seem to play a significant role in the resonant wavelength, although the noise of the data might be obscuring trends. In the case of gap array 1, as the number of nanoparticle in the block increases, the bandwidth of the block resonance increases until certain block dimension and then decreases to converge to the bandwidth of semi-infinite array resonance. Larger gaps show larger bandwidth for the fixed block dimension, but more study is required to explore the effect of gap dimension on the bandwidth of the array resonance more in detail.

This study is expected to provide better understanding of plasmon coupling in finite 2D arrays and also to present fundamental experimental data that is required for further theoretical study.

**Jiha Sung**

---

Department of Chemistry  
Northwestern University  
2145 Sheridan Road  
Evanston, IL 60208-3113 USA  
j-sung2@northwestern.edu  
Phone: (847) 491-2954

**Education**

---

- 2007 (expected)    **Ph. D., Department of Chemistry, Northwestern University**  
Advisors: Professor Richard P. Van Duyne and Professor Kenneth G. Spears  
Thesis Title: Linear and Nonlinear Optical Spectroscopy on Two-Dimensional Arrays of Silver Nanoparticles
- 2002                **M.S., Department of Chemistry, Seoul National University, Korea**  
Advisor: Professor Seong Keun Kim  
Thesis Title: Spectroscopic Study of Jet-cooled Phenylalanine and Its Hydrated Clusters Using Laser and Synchrotron Radiation
- 1999                **B.S., Department of Chemistry, Seoul National University, Korea**  
Honor of Cum Laude

**Research Experience**

---

- 2002-Present    **Northwestern University**  
Studied linear and nonlinear optical properties of Ag nanoparticle arrays by extinction, dark field scattering and second harmonic generation (SHG) measurements.  
Managed amplified femtosecond laser system.
- 2001                **Pohang Accelerator Laboratory (PAL)**  
**3B1 Gas-Phase/Reflectivity/ARUPS Beamline**  
Studied jet-cooled phenylalanine and its hydrated clusters by photoelectron-photoion coincidence (PEPICO) method.
- 2000-2002        **Seoul National University**  
Studied jet-cooled adenine and phenylalanine by resonant two-photon ionization (R2PI) and mass-analyzed threshold ionization (MATI) method.

**Teaching Experience**

---

- 2002-2004        **Northwestern University**  
Teaching Assistant for General Chemistry labs, Advanced Laboratory Course, and Graduate Quantum Chemistry 2 Course.  
Donald E. Smith Award for Excellence in 400-Level teaching (2005)

2000-2001

**Seoul National University**

Teaching Assistant for General Chemistry labs and Exercises in General Chemistry.

**Publications**

---

- **Sung, J.**; Hicks, E. M.; Van Duyne, R. P.; Spears, K. G., Nanoparticle Spectroscopy: Dipole Coupling in Two-Dimensional Arrays of L-Shaped Silver Nanoparticles. *Journal of Physical Chemistry C* **111**, 10368-10376 (2007).
- Zhao, J.; Jensen, L.; **Sung, J.**; Zou, S.; Schatz, G. C.; Van Duyne, R. P., Interaction of Plasmon and Molecular Resonances for Rhodamine 6G Adsorbed on Silver Nanoparticles. *Journal of the American Chemical Society* **129**, 7647-7656 (2007).
- Ponnu, A.; **Sung, J.**; Spears, K. G., Ultrafast Electron-Transfer and Solvent Adiabaticity Effects in Viologen Charge-Transfer Complexes. *Journal of Physical Chemistry A* **110**, 12372-12384 (2006).
- Moran, A. M.; **Sung, J.**; Hicks, E. M.; Van Duyne, R. P.; Spears, K. G., Second Harmonic Excitation Spectroscopy of Silver Nanoparticle Arrays. *Journal of Physical Chemistry B* **109**, 4501-4506 (2005).
- Lee, K. T.; **Sung, J.**; Lee, K. J.; Kim, H. M.; Han, K. Y.; Park, Y. D.; Kim, S. K., Comparative study of charge division in substituted benzene cations. *Journal of Chemical Physics* **126**, 224306/1-224306/5 (2007).
- Lee, K. T.; Kim, H. M.; Han, K. Y.; **Sung, J.**; Lee, K. J.; Kim, S. K., Spectroscopic Observation of Conformation-Dependent Charge Distribution in a Molecular Cation. *Journal of the American Chemical Society* **129**, 2588-2592 (2007).
- Lee, K. T.; **Sung, J.**; Lee, K. J.; Kim, S. K.; Park, Y. D., Conformation-dependent ionization of L-phenylalanine: structures and energetics of cationic conformers. *Chemical Physics Letters* **368**, 262-268 (2002).
- Lee, K. T.; **Sung, J.**; Lee, K. J.; Park, Y. D.; Kim, S. K., Conformation-Dependent Ionization Energies of L-Phenylalanine. *Angewandte Chemie, International Edition* **41**, 4114-4117 (2002).
- Lee, K. T.; **Sung, J.**; Lee, K. J.; Kim, S. K.; Park, Y. D., Resonant two-photon ionization study of jet-cooled amino acid: L-phenylalanine and its monohydrated complex. *Journal of Chemical Physics* **116**, 8251-8254 (2002).
- Kim, N. J.; Jeong, G.; Kim, Y. S.; **Sung, J.**; Kim, S. K.; Park, Y. D., Resonant two-photon ionization and laser induced fluorescence spectroscopy of jet-cooled adenine. *Journal of Chemical Physics* **113**, 10051-10055 (2000).

**Presentations**

---

- **Sung, J.**; McLellan, E. C.; Van Duyne, R. P.; Spears, K. G., “Localized surface plasmon resonance modifications by dipole coupling in 2-D silver nanoparticle arrays”, 233rd American Chemical Society (ACS) National Meeting, Chicago, IL, United States, March 25-29, 2007, PHYS-302 (Poster).
- Lee, K. T.; **Sung, J.**; Lee, K. J.; Kim, C.; Kim, S. K., “Amino Acid in Gas Phase : Spectroscopy of Phenylalanine and Its Hydrated Clusters”, 85th Annual Meeting of the Korean Chemical Society, Seoul, Korea, April 21-22, 2001, S15P10Po (Poster).

**Affiliation**

---

American Chemical Society